BINDING AND TRANSPORT OF RADIONUCLIDES IN NATURAL AND SYNTHETIC ENVIRONMENT - A COMPUTATIONAL STUDY

By

Biswajit Sadhu
CHEM01201304002
Bhabha Atomic Research Centre, Mumbai

A thesis submitted to the Board of Studies in

Chemical Sciences

In partial fulfillment of requirements for the

Degree of

DOCTOR OF PHILOSOPHY

of

HOMI BHABHA NATIONAL INSTITUTE

March, 2017

Homi Bhabha National Institute

Recommendations of the Viva Voce Committee

As members of the Viva Voce Committee, we certify that we have read the dissertation prepared by **Biswajit Sadhu** entitled "Binding and Transport of Radionuclides in Natural and Synthetic Environment- A computational study" and recommend that it may be accepted as fulfilling the thesis requirement for the award of Degree of Doctor of Philosophy.

Chairman - Prof. Chandra. N. Patra		**Date:** 23-03-17
Guide / Convener - Prof. Tusar Bandyopadhyay	Tusar Bandyopadhyay	**Date:** 23-3-17
Co-guide – Dr. Mahesh Sundararajan		**Date:** 23/3/17
Examiner - Prof. Amalendu Chandra		**Date:** 23/3/17
Member 1- Prof. S. K. Ghosh		**Date:** 23/3/17.
Member 2- Prof. C. Majumdar		**Date:** 23/3/17

Final approval and acceptance of this thesis is contingent upon the candidate's submission of the final copies of the thesis to HBNI.

We hereby certify that we have read this thesis prepared under our direction and recommend that it may be accepted as fulfilling the thesis requirement.

Date: 23-03-2017

Place: Mumbai

	Tusar Bandyopadhyay
Co-guide	**Guide**

STATEMENT BY AUTHOR

This dissertation has been submitted in partial fulfillment of requirements for an advanced degree at Homi Bhabha National Institute (HBNI) and is deposited in the Library to be made available to borrowers under rules of the HBNI.

Brief quotations from this dissertation are allowable without special permission, provided that accurate acknowledgement of source is made. Requests for permission for extended quotation from or reproduction of this manuscript in whole or in part may be granted by the Competent Authority of HBNI when in his or her judgment the proposed use of the material is in the interests of scholarship. In all other instances, however, permission must be obtained from the author.

Biswajit Sadhu

Biswajit Sadhu

DECLARATION

I, hereby declare that the investigation presented in the thesis has been carried out by me. The work is original and has not been submitted earlier as a whole or in part for a degree / diploma at this or any other Institution / University.

Biswajit Sadhu

Biswajit Sadhu

List of Publications arising from the thesis

Journal

1. "Water-Mediated Differential Binding of Strontium and Cesium Cations in Fulvic Acid." **B. Sadhu,** M. Sundararajan and T. Bandyopadhyay, *Journal of physical chemistry B,* **2015**, *119*, 10989–10997.

2. "Selectivity of Singly Permeating Ion in Nonselective NaK Channel: A Combined QM and MD Based Investigations." **B. Sadhu,** M. Sundararajan and T. Bandyopadhyay, *The Journal of Physical Chemistry B,* **2015**, *119*, 12783-12797.

3. "Elucidating the Structures and Cooperative Binding Mechanism of Cesium Salts to Multitopic Ion-Pair Receptor through Density Functional Theory Calculations." **B. Sadhu,** M. Sundararajan, G. Velmurugan, P. Venuvanalingam, *Dalton Transactions,* **2015**, *44*, 15450-15462.

4. "Efficient Separation Of Europium Over Americium Using Cucurbit-[5]-uril Supramolecule: A Relativistic DFT Based investigation." **B. Sadhu,** M. Sundararajan and T. Bandyopadhyay, *Inorganic chemistry,* **2016**, *55*, 598-609.

5. "Translocation Energetics and Selectivity of Divalent ions (Ca^{2+} , Sr^{2+} and Ba^{2+}) in Nonselective NaK Channel." **B. Sadhu,** M. Sundararajan and T. Bandyopadhyay (*To be communicated).*

6. "Selective Separation of Strontium with multitopic ion-pair receptor: A DFT exploration." **B. Sadhu,** M. Sundararajan and T. Bandyopadhyay (*To be communicated).*

Other publications

7. "Modulation of Protonation–Deprotonation Processes of 2-(4′-Pyridyl) benzimidazole in Its Inclusion Complexes with Cyclodextrins." V. Khorwal, **B. Sadhu,** A. Dey, M. Sundararajan, and A Datta, *The Journal of Physical Chemistry B,* **2013,** *117,* 8603-8610.

8. "An insight into third-phase formation during the extraction of thorium nitrate: evidence for aggregate formation from small-angle neutron scattering and validation by computational studies." P. K. Verma, P. N. Pathak, P. K. Mohapatra, V. K. Aswal, **B. Sadhu**, M. Sundararajan.. *The Journal of Physical Chemistry B,* **2013**, *117,* 9821-9828.

9. "Effect of Successive Alkylation of N, N-Dialkyl Amides on the Complexation Behavior of Uranium and Thorium: Solvent Extraction, Small Angle Neutron Scattering and Computational Studies." P. K. Verma, P. N. Pathak, N. Kumari, **B. Sadhu,** M. Sundararajan, V. K. Aswal, P. K. Mohapatra, *The Journal of Physical Chemistry B,* **2014**, *118,*14388-14396.

10. "Investigations on preferential Pu (IV) extraction over U (VI) by N, N-dihexyloctanamide versus tri-n-butyl phosphate: evidence through small angle neutron scattering and DFT studies." P. K. Verma, N. Kumari, P. N. Pathak, **B. Sadhu,** M. Sundararajan, V. K. Aswal and P. K. Mohapatra, *The Journal of Physical Chemistry A***,** **2014**, *118*, 3996-4004.

11. "Gas phase Reactions of Uranyl with α-Hydroxyisobutyric Acid using Electrospray Ionization Mass Spectrometry and Density Functional Theory." P. Kumar, P. G. Jaison, V. M. Telmore, D. Alamelu, S. K. Aggarwal, **B. Sadhu,** M. Sundararajan, *Journal of Radioanalytical and Nuclear Chemistry,* **2016**. *308,* 303-310.

12. "Selective Recognition of Uranyl ion from Bulk of Thorium (IV) and Lanthanide(III) ions by tetraalkyl Urea: A Combined Experimental and Quantum Chemical Study." B. G. Vats, D. Das, **B. Sadhu**, I. C. Pius, D. Noronha, S. Kannan, M. Sundararajan, *Dalton transactions,* **2016,** *45,*10319-10325.

13. "Asn47 and Phe114 Modulates the Inner Sphere Reorganization Energies of Type Zero Copper Proteins: Insights from Quantum Chemical Calculations." **B. Sadhu**, M. Sundararajan, *Physical Chemistry Chemical Physics,* **2016,** *18*, 16748-16756.

14. "A projected amyloid marker, Auramine O, interacts significantly with the native form of the protein itself." N. Mudliar, **B. Sadhu,** P. K. Singh, *The Journal of Physical Chemistry B* **2016**, ASAP.

15. "Achieving Highly Efficient and Selective Cesium Extraction using 1,3 di-octyloxycalix [4]arene-crown-6 in n-octanol based Solvent System: Experimental and DFT Investigation." K. Patra, **B. Sadhu**, C. P. Kaushik, A. Sengupta, A. Kumar, R K Mishra, U. V. Deokar and R. Singh (to be communicated).

16. "Speciation of Uranium-Mandelic Acid Complexes using Electrospray Ionization Mass Spectrometry and Density Functional Theory" P. Kumar, P.G. Jaison, V. M. Telmore, **B. Sadhu** and M. Sundararajan (to be communicated).

17. "Novel Strategy for Enhanced Cucurbit[7]uril Synthesis: Experimental and Theoretical investigations" D. R. Boraste, **B. Sadhu**, P. Borase, P. V. Ghorpade, M. Sundararajan, G. S. Shankarling (to be communicated).

Biswajit Sadhu

“My big thesis is that although the world looks messy and chaotic, if you translate it into the world of numbers and shapes, patterns emerge and you start to understand why things are the way they are.”

-Marcus du Sautoy

Dedicated to my lovely wife and my dear parents

ACKNOWLEDGEMENTS

I can see that my childhood dream is getting shaped as I approach toward the end of my Ph.D journey. This would have never been possible without the immense help and supports from so many beautiful persons in various parts of my endeavors. I would like to express my sincere acknowledgement to all of them for encouraging and motivating me all the way.

At first, it is my great privilege to acknowledge **Dr. K. S. Pradeepkumar**, Associate Director, Health, Safety and Environment Group for motivating me and seeding the thought of pursuing Ph.D in the field of computational modeling into my mind.

This day would not have come without the esteemed guidance and support from my guide **Dr. Tusar Bandyopadhyay** and Technology advisor **Dr. Mahesh Sundararajan**. I am sincerely thankful to both of them for introducing me to the field of metadynamics and quantum mechanics and teaching me the science patiently. Their guidance both at personal and professional level kept me always motivated and immensely helped me to pursue my dreams. I will be forever in debt to them for providing their precious time to listen my ideas and always putting thoughts for improvements.

I would like to take this opportunity to thank **Dr. H. N. Ghosh**, RPCD, BARC for his moral support and continuous encouragement. His infectious enthusiasm and unlimited zeal have been the major driving force and source of inspiration throughout my career.

The availability of ANUPAM parallel computing facility in BARC is also highly acknowledged. Special thanks to **Shri Kislay Bhatt** and **Shri Vaibhav Kumar** for their spontaneous software related help. I also sincerely acknowledge the respected members of doctoral committee for their critical comments during annual review and pre-synopsis presentation, which immensely helped me to upgrade the level of research work.

I feel extremely fortunate and thankful to **Shri Nitin A. Bhosale** for creating the beautiful working environment in the lab and for providing his positive thoughts and presence to make the journey enjoyable. It is an honor for me to thank **Shri Rajvir Singh**, **Shri Probal Chowdhury**, **Dr. Anil Kumar** for their selfless moral support throughout my thesis work.

I am very thankful to my dear friends **Quazi, Susanta, Goutam**, **Malay, Bipattaran, Kousiki, Tushar** and my seniors, **Dr. Soumitra Das, Dr. P. K. Singh, Dr. Brindaban Modak**, and **Dr. Pranaw Kumar** for being a pillar of support as I crossed the highway towards Ph.D.

I would like to express my heartiest gratitude to my parents **Mr. Pankaj Sadhu and Mrs. Pratima Sadhu** for their endless love and blessings which helped me to keep focus on my life goal. Their inspiring words "*Shoot for the moon. Even if you miss, you'll land among the stars.*" have been a source of motivation throughout my professional career. My special thanks to my wife **Riya** for being with me with patience and make me confident enough to pursue my dreams. I thank my dearest brother **Trijit** who always remains beside me as a friend, philosopher and guide in my hardest days of research work.

Last but not the least; I thank the beautiful and soulful presence of almighty God in my life for everything.

...Biswajit

Contents

Chapter 1: Introduction to Natural and Synthetic receptors/binders and Computational Methodology

Chapter 2: Differential Binding of Cesium and Strontium with Ecological Receptor (Fulvic Acid)

Chapter 3: Permeation of Cesium and Other Monovalent Ions through Non-selective NaK Ion Channel of Soil Dwelling Bacteria

Chapter 4: Permeation of Strontium and Other Divalent Ions through Non-selective NaK Ion Channel

Chapter 5: Structure and Cooperative Binding Mechanism of Cesium Salts with Multitopic Ion-pair Receptor

Chapter 6: Selective Separation of Strontium with multitopic ion-pair receptor: A DFT exploration

Chapter 7: Efficient Separation of Europium over Americium using Cucurbit-[5]-uril

SYNOPSIS

Once they are released into the environment, radioactive fission products can present a potential biological threat to human health. The dominant sources for these releases are from nuclear reactor accidents,[1] nuclear weapon tests,[2] and fuel reprocessing plants.[3-4] In the back end of the nuclear fuel cycle, enormous efforts are devoted to reprocess the spent fuel of high level liquid waste (HLLW) for subsequent safe disposal and for nuclear waste recycling. In order to regulate/mitigate the radionuclide migration, chemical structures present in natural as well as in synthetic media play a major role to bind a specific substrate. Naturally occurring various soil organic matter (SOM) or else the cell/protein surface of soil dwelling bacteria can act as binder to the radionuclides. The synthetic binders represent a particular variety, which are laboratory-synthesized to achieve a specific binding feature. Any accidentally released radionuclides are expected to migrate in natural environmental sub-systems, such as, soil and water. Upon deposition into soil, the SOM tunes the migration behaviour of the radionuclides, which in turn influence the dynamic transport processes of radionuclides from soil to water or vice versa and finally might enter into the food chains through the plants. Similar to this, separating the long-lived minor actinides (MA) from other fission products and subsequent transmutation to generate short-lived radionuclides is expected to be a viable solution to long-standing disposal associated problems.[5] However, the selective extraction of MAs from HLLW poses a formidable challenge due to the presence of chemically similar 4*f*-lanthanide congeners such as Eu^{3+}.Thus, design of ion selective structures to achieve a desirable separation factor (SF) between 4*f*- and 5*f*-elements is a primary objective towards reprocessing the spent fuel. Being radioactive in nature, any experimental studies directed towards understanding the structure and dynamics of radionuclides' interactions with natural/synthetic structures poses a formidable challenge. In Silico studies of binding and transport of radionuclides is an alternative lucrative option towards this goal. Additionally, computational study can decipher the molecular mechanisms on how such regulation and capture occurs, which has been a topic of many active research interests in recent days. The contents of the works of the present thesis primarily aims at providing microscopic insight on the migration mechanism and binding aspects of radionuclides to the representatives of two distinct classes of structures. The thesis will also make modest attempts to unravel mechanistic issues, at the molecular level, of much of these processes that remained elusive till today.

The above aspects have been studied by treating the problem at hand in light of the features associated with multiple scales of time and/or space. In particular, the multiscale modeling approach is adopted in which calculation of material properties or system behavior on one level is obtained using information or models from different levels. On each level, particular approaches are used for description of a system. Throughout the thesis, the following levels are adopted: level of quantum mechanical (QM) models (information about electrons is included), level of conventional molecular dynamics (MD) models (information about individual atoms is included at the equilibrium condition), level of biased MD, such as, metadynamics (MtD) (information about atoms and/or groups of atoms is included at non-equilibrium condition). Together they provide rich structural/dynamical information on the studied systems, which were hitherto unknown. In Chapter 1, general remarks about these theoretical approaches are presented. Also discussed are their success and limitations in these studies. This clear overview is presented starting with the very basic principles. This chapter provides the necessary background of natural and synthetic receptor/binder to appreciate and interpret the results reported in subsequent chapters.

The ecological receptor such as SOM, which contains Humic acid (HA) and fulvic acids (FA) can potentially bind various radionuclides (^{137}Cs, ^{90}Sr) *via* its various functional groups (carboxyl, quinone and phenolate) to restrict their migration to biological entities and as well as into the aqueous phase. Several experimental investigations[6-8] were carried out in order to gain insight on the radionuclide translocation behaviour. Majority of them were, however, mainly focused to evaluate SOM influence on radionuclide sorption into mineral layers, while experiments on the direct interaction of Cs^+ and Sr^{2+} with FA are limited. Like its group congeners (K^+ and Ca^{2+}), Cs^+ and Sr^{2+} might also be absorbed by plants and enter into the human food chains. As is evident from numerous experimental investigations,[9-10] the interaction of metal cations with SOM is non-specific in nature. The binding of radionuclide cation to SOM consist of many steps as it approaches from solution (dissolved phase) to surface of SOM (particulate phase). The non-specificity and neighbouring group participation can lead to major problem on simulating the actual binding phenomena. Dynamic nature of binding and equilibrium selectivity at non-specific binding sites can be appropriately understood with the help of multiscale modelling techniques, such as quantum mechanics (QM), Molecular Dynamics (MD) and metadynamics (MtD). Chapter 2 of the present thesis aims at understanding the binding of aforementioned radionuclides with FA, a representative of SOM, using multiscale modelling approach.

In addition to aforementioned soil components, soil dwelling microorganisms and plants also play a direct role on transporting radionuclides through various ion channel routes. This can eventually lead to the entry of the radionuclides into the food chain.[11] The selective transport of these cations from extracellular surface to intracellular medium *via* selectivity filter (SF) of ion channel is a complex phenomenon and unravelling the mechanistic riddle of such translocation has been a topic of intense debate for last two decades.[12-13] Several theories have been postulated and tested till date. In 1962, Eisenman[14] proposed "field strength hypothesis" to explain the cation selectivity in glass electrode and found that the field strength and type of interacting ligands were shown to play crucial role to achieve the cation selectivity. A decade later in "snug-fit hypothesis",[15] it was proposed that the protein ligand inside SF form a rigid scaffold, wherein a particular size of ion can bind preferably. However, this theory was later criticized as the experimentally obtained crystallographic B factor for ion channel suggested that the atoms of SF fluctuates more than 4 Å in physiological temperature,[16] which indicated SF does not remain rigid during permeation. Experimental monitoring of the dynamic phenomena at molecular level is always an uphill task considering the limitation of available experimental techniques. Hence, use of computational techniques became widely popular to provide insights. In 2004, based on molecular dynamics investigations, Noskov et al.[17] reiterated the importance of "field strength hypothesis" and also projected that the orientation, number of interacting carbonyl ligands attribute to the origin of selectivity in K^+ ion channel. In a more accepted "over-coordination hypothesis",[18] it was demonstrated that the coordination number of cation at SF is higher as compared to bulk. Thus, rather than the type of ligand it is the number of coordinating ligands around metal maintains the selectivity. Such specific arrangement is provided by the acting "topological constraint" in SF.[19]

Among these diverse, however inter-related hypotheses, the researcher community remained largely divided,[13] pointing towards the fact that many more investigations are indeed needed to achieve a consensus on these ion translocation mechanism. In contrast to Na^+ and K^+ channel, recently reported NaK ion channel[20] (to which a large portion of thesis is devoted to) is an exception as it is shown to permeate all the monovalent alkali metal ion (Na^+, K^+ and Rb^+) including Cs^+ and few divalent alkaline earth metal ions (Ca^{2+} and Ba^{2+}). The charge soaking experiment on this ion channel demonstrated the binding sites for different cations inside SF.[21] This ignited many important questions such as a) whether ion-selectivity exists inside different binding sites of NaK ion channel? b) If yes. How such selectivity arises at the molecular level? c) Whether translocation of radionuclide cations like, Cs^+ and Sr^{2+} through the ion channel is energetically feasible? And, d) how closely the permeation events are related to different monovalent as well as divalent cations? Chapters 3 and 4 of the present thesis are mainly focused to provide possible answers to these intriguing questions for monovalent and divalent cations, respectively.

Unlike naturally existing binders or receptors, synthetic ones are aimed to achieve controlled binding motif for metal ions. Commonly used synthetic receptors for nuclear separation processes are of macrocyclic in nature. These are extensively used in nuclear reprocessing plants to achieve selective separation of radionuclides from generated nuclear waste for various purposes. Broadly, nuclear waste can be categorized in different class based on the activity level. High level nuclear waste (HLW) in general contains unextracted uranium (^{235}U, ^{238}U), plutonium (^{239}Pu) along with many other fission products like cesium (^{137}Cs), strontium (^{89}Sr, ^{90}Sr) and lanthanides (^{155}Eu) and minor actinides (MAs)) such as americium (^{241}Am, ^{243}Am) and curium (^{245}Cm). Due to diverse nature of elements present in HLW and many of having close chemical resemblance (such as Am^{3+}/Eu^{3+}); achieving high separation factor for a particular radionuclide has always been a bottleneck in the back-end fuel cycle. Recent advancement on crown ether based ligand led us to understand the importance of counter ions in enhancing the metal binding processes. For instance, Sessler et al. synthesized new class of ion-pair receptors which can sequentially or concurrently bind both metal and counter ion to provide better binding affinities.[22-23] How such assistance are rendered at microscopic level is, however, not understood conclusively and further investigations are indeed required. Deciphering the acting mechanism will not only help in tuning metal binding at the host but also to design futuristic ion-probes for chemical extraction processes. Chapters 5, 6 and 7 of the present thesis are devoted to understand the host-guest binding mechanisms for a variety of radionuclides at the atomic level using density functional theory (DFT) based calculations.

To summarize (Chapter 8), in the present thesis work, we have mainly focused to elucidate the binding and transport mechanism of various important radionuclides in natural and synthetic environments. Soil organic matter and soil dwelling bacteria are considered as representative of natural binders, while newly reported multitopic ion-pair and cucurbit-[5]-uril ligand are taken as synthetic binders. Multi-scale modeling techniques (MtD, MD and DFT) are used to decipher the dynamic and static feature of acting binding mechanisms prevailing in natural environment. For synthetic counterpart, DFT based calculations are carried out to accurately predict the binding and selectivity of radionuclides toward the host molecule. The overall thesis is composed of eight chapters. The content of each chapter is briefly presented below.

Chapter 1: Introduction to Natural and Synthetic receptors/binders and Computational Methodology

This chapter provides a brief introduction on the importance and relevance of natural and synthetic receptors/binders in the context of radionuclide migration. Popular modes of investigations to study the binding behaviour to these receptors are also elaborated. Later, a general outline of different theoretical and computational techniques used in this thesis is described. The theory behind DFT and importance of its different input parameters such as basis set, effective core potential (ECP), need of dispersion and solvation effects are mainly emphasized. A brief background on working principle of classical MD and non-equilibrium MtD simulations are also delineated in this chapter. Finally, objective and goal of the present thesis are discussed.

Chapter 2: Differential Binding of Cesium and Strontium with Ecological Receptor (Fulvic Acid)

This chapter deals with the studies on the binding mechanism of ^{137}Cs and ^{90}Sr with fulvic acid (FA), a representative of SOM. Migration of these potentially harmful radionuclides in soil is governed by the chemical and biological reactivity of soil components. FA is known to alter the mobility of radionuclide cations, Cs^{+} and Sr^{2+}. Shedding light on the possible interaction mechanisms at the atomic level of these two ions with FA is thus vital to explain their transport behavior and, for the design of new ligands for the efficient extraction of radionuclides. Here, multiscale modeling technique such as MD, MtD simulations and DFT based calculations are performed on radionuclide-FA-water based system which predicts that interaction of Cs^+ to FA is very weak as compared to Sr^{2+} while the water-FA interaction is largely responsible for the weak binding of Cs^+ to FA leading to the outer sphere complexation of the ion with FA; the interaction between Sr^{2+} and FA is stronger and thus can surpass the existing secondary non-bonding interaction between coordinated waters and FA leading to inner sphere complexation of the ion with FA. DFT studies pointed that entropy plays a dominant role for Cs^+ binding to FA, whereas Sr^{2+} binding is an enthalpy driven process. The predicted results[24] are found to be in excellent agreement with the available experimental data on complexation of Cs^+ and Sr^{2+} with SOM.

Chapter 3: Permeation of Cesium and Other Monovalent Ions through Non-selective NaK Ion Channel of Soil Dwelling Bacteria

In this chapter, we have detailed our findings on binding, selectivity and transport mechanism of Cs^+ and other interfering monovalent ions (Na^+ and K^+) through non-selective NaK ion-channel of soil dwelling bacteria *bacillus cereus*.[25] Recently reported NaK ion channel, in contrary to K^+ channel, seems to be an exception, as it is observed to permeate most of the group IA alkali metal cations and hence suggested to be nonselective in nature.[20] This ignited the notion that radionuclide like ^{137}Cs can also possibly permeate through the pore and use it as a transport route to enter into the biological life cycle. We have adopted extensive multiscale modeling approach (DFT, MD and MtD method) to elucidate the equilibrium selectivity of metal ions at various binding sites and also have constructed free energy pathway of single ion translocation, free from 'contamination' due to the absence any other 'rivalry' cations. Among the all possible binding sites, vestibule is noticed to be nonselective and seen to act as probable binding site only in presence of multiple ions. Binding sites, S3 and S4 are found to be selective for K^+ and Na^+, respectively. Cs^+ permeation through the pore was noted to be favorable however, the rate of permeation is expected to be smaller as compared to Na^+

and K^+. As an important observation, we find that calculations on over simplified models using an isolated ion binding site may lead to erroneous selectivity trend as it neglects the synergetic of consecutive binding sites on the final outcome. Energy decomposition analysis revealed ion-dipole electrostatics as the major contributing interaction in metal-bound binding sites. Our investigations find that although NaK is permeable to monovalent alkali metal ions, strongly ‘site specific’ selectivity does exist at the three well-defined non-contiguous binding sites of the SF. Different important physico-mechanical parameters (such as ligating environment, synergistic influence of binding sites and topological constraints) were found to be the determining factor to induce the ‘site specific’ selectivity of ions during translocation. Wherever possible our computed results are compared with the available experimental findings.

Chapter 4: Permeation of Strontium and Other Divalent Ions through Non-selective NaK Ion Channel

This chapter elaborates our findings on translocation mechanism of Sr^{2+} and other important divalent metal ions (Ca^{2+} and Ba^{2+}) through NaK ion channel with multiscale modeling approach. To construct the free energy pathway of ion translocation, mean-field polarizable (MFP) model of water is used, while for metals electronic polarization effects are included with ionic charge rescalling. Further, DFT was applied to determine the ionic equilibrium selectivity at different binding sites of SF. Similar to previouly reported experimental results, we find that during permeation, divalent metals faces higher energy barrier as compared to K^+. Moreover, DFT and MD results suggested that all divalent metals have strong preference at S3 site of SF while S4 site does not act as a binding site for the same. Due to stronger binding at S3, divalent ions can subsitute K^+ which is in close aggrement with the charge soaking experimental results. As an important conclusion, obtained results indicated that use of non-polarizable model of water and absence of ionic charge rescalling in MD simulatiuon can led to underestimation of the ion-protein binding and can fail to produce good match with the reported experimental results. Thus, it emphasizes the importance of electronic polarization factor in depicting such ion translocation phenomena.

Chapter 5: Structure and Cooperative Binding Mechanism of Cesium Salts with Multitopic Ion-pair Receptor

This chapter delineates the results on structure and binding of various cesium salts with an ion-pair receptor. Designing new and innovative receptors for the selective binding of radionuclides is central to nuclear waste management processes. Recently, a new multitopic ion-pair receptor was reported which binds a variety of cesium salts.[22] Due to the large size of the receptor; quantum chemical calculations on the full ion-pair receptors are pretty limited.Thus the binding mechanisms are not well understood at the molecular level in full detail. Here, we have assessed the binding strengths of various cesium salts to recently synthesized multi-topic ion-pair receptor molecule using DFT based calculations without any truncation of the system. Calculated results predict that the binding of cesium salts to the receptor is predominantly occurs via cooperative binding mechanism. Cesium and anion synergistically assist each other to bind favourably inside the receptor. Energy decomposition analysis on the ion-pair complexes shows that the Cs salts are bound to the receptor mainly through electrostatic interactions with small contribution from covalent interactions for large ionic radii anions. Further, Quantum Theory of Atoms In Molecules (QTAIM) analysis is performed to characterize the importance of different inter-molecular interactions between the ions and the receptor inside the ion-pair complexes. Unlike the recent molecular mechanics (MM) calculations, our calculated binding affinity trends for various Cs ion-pair complexes (CsF, CsCl and CsNO3) are now in excellent agreement to the experimental binding affinity trends.[22,23] Thus the applied computational methodology can be regarded as a benchmark for this class of calculations.[26]

Chapter 6: Selective Separation of Strontium with multitopic ion-pair receptor: A DFT exploration

In this chapter, we have proposed two steps Sr^{2+} extraction methodology in nitrate media using a multi-topic ion-pair receptor which was earlier reported to be strongly selective for K^+. Free energy corrected DFT calculations are used to evaluate the thermodynamics of the extraction processes. Effects of different solvents (ether, acetonitrile and aqueous) are incorporated using COSMO continuum model. Binding energy calculations predicted a selectivity order $K^+ > Sr^{2+} > Ca^{2+}$. The most preferable binding mode of KNO_3 in receptor is noted to be different from divalent metal-nitrate salts. In case of KNO_3, K^+ is seen to bind preferably at the crown site (C) while NO_3^- binds at pyrrole site (P). On the contrary, for divalent metals, apart from 'P' site, NO_3^- can also simultaneously bind at the outer sphere of 'C' site to coordinate the metal *via* monodentate motif. Our results on free energy of extraction predict that selective separation of chemically alike Ca^{2+}/Sr^{2+} pair is indeed achievable using this host. Once extracted in organic media, KNO_3 solution can be used to back strip Sr^{2+} to the aqueous phase. In this study, all possible binding sites for metal-nitrate salts of these aforementioned cations have been identified that shed light on probable crystal structures of divalent metal nitrates with the ion-pair receptor. Moreover, influence of different solvents during phase transfer equilibrium has been assessed through calculation of extraction free energy.

Chapter 7: Efficient Separation of Europium over Americium using Cucurbit-[5]-uril

In this chapter, we have discussed the results on possible separation of Eu/Am pair using cucurbit-[5]-uril, a macrocycle from cucurbit-[n]-uril family using relativistic density functional theory (DFT) based calculations.[27] Achieving an efficient separation of chemically similar Am^{3+}/Eu^{3+} pair in high level liquid waste treatment is crucial for managing the long term nuclear waste disposal issues. We have explored the structures, binding and energetics of metal-CB[5] complexation with and without the presence of counter-ions. Our study reveals an excellent selectivity of Eu^{3+} over Am^{3+} with CB[5] (ion exchange free energy, $\Delta\Delta G_{Am/Eu} > 10$ kcal mol^{-1}). Both metals bind with the carbonyl portals via μ^5 coordination arrangement with further involvement of three external water molecules. It is noted that the presence of counter-ions, particularly nitrate, inside the hydrophobic cavity of CB[5] induces a cooperative cation-anion binding, resulting into enhancement of metal binding at the host. The overall binding process is found to be entropy driven, resembling the recent experimental observations.[28] The optimized structural parameters for Eu^{3+}-CB[5] complexes are found to be in excellent agreement with the available experimental information. To rationalize the computed selectivity trend, we further scrutinized the electronic structures using energy decomposition analysis (EDA), QTAIM, Mülliken population analysis (MPA), Nalewajski-Mrojek (N-M) bond order and molecular orbital analyses. Strong electrostatic ion-dipole interaction along with efficient charge transfer between CB[5] and Eu^{3+} are found to outweighs the better degree of covalency between CB[5] and Am^{3+},which led to superior selectivity of Eu^{3+} over Am^{3+}.

Chapter 8: Summary and Outlook

This is the concluding chapter of thesis. Here, we have summarized the goals and finding of the present thesis. We have also discussed how the findings of present thesis can in principle be useful to aid information/knowledge, which further can led to many interesting development in this field in future. As evident, the present thesis is aimed at providing knowledge on diversity of binding mechanisms of radionuclide with natural or synthetic binders. Using its own way, nature distinctly controls the ionic balance either in cell or in environmental sub-systems. Understanding the unique controlling factors of such processes and implementing the knowledge to design synthetic analogue for societal application can be considered as the futuristic goal of the thesis.

References:

1. Stohl, A.; Seibert, P.; Wotawa, G.; Arnold, D.; Burkhart, J. F.; Eckhardt, S.; Tapia, C.; Vargas, A.; Yasunari, T. J. *Atmos. Chem. Phys.* 2011, *11*, 28319.
2. Aarkrog, A. *J. Environ. Radioact.* 1988, *6*, 151.
3. Adriano, D. C.; Hoyt, G. D.; Pinder, J. E. *Health Phys.* 1981, *40*, 369.
4. Carlton, H. B., L. R.; Evans, A. B.; Beary, L. A.; Murphy, C. E.; Pinder, J. E.; Strom, R. N. Cesium in the Savannah River Site Environment; WSRC-RP-92-250; Westinghouse Savannah River Company: Aiken, SC,1992.
5. Tsujimoto, K.; Sasa, T.; Nishihara, K.; Oigawa, H.; Takano, H. *J. Nucl. Sci. Technol.* 2004, *41*, 21.
6. Maguire, S.; Pulford, I. D.; Cook, G. T.; Mackenzie, A. B. *J. Soil Sci.* 1992, *43*, 689.
7. Shaban, I. S.; Macasek, F. *J. Radioanal. Nucl. Chem.* 1998, *229*, 73.
8. Kumar, S.; Tomar, B. S.; Ramanathan, S.; Manchanda, V. K. *Radiochim. Acta* 2006, *94*, 369.
9. Benedetti, M. F.; Riemsdijk, W. H. V.; Koopal, L. K.; Kinniburgh, D. G.; Gooddy, D. C.; Milne, C. J. *Geochim. Cosmochim. Acta* 1996, *60*, 2503.
10. Rigol, A.; Vidal, M.; Rauret, G. *J. Environ. Radioact.* 2002, *58*, 191.
11. Zhu, Y. G.; Smolders, E. *J. Exp. Bot.* 2000, *51*, 1635.
12. Alam, A.; Jiang, Y. *The Journal of General Physiology* 2011, *137*, 397-403.
13. Fowler, P. W.; Tai, K.; Sansom, M. S. P. *Biophys. J.* 2008, *95*, 5062.
14. Eisenman, G. *Biophys. J.* 1962, *2*, 259.
15. Bezanilla, F.; Armstrong, C. M. *The Journal of General Physiology* 1972, *60*, 588-608.
16. Allen, T. W.; Andersen, O. S.; Roux, B. *The Journal of General Physiology* 2004, *124* (6), 679-690.
17. Noskov, S. Y.; Berneche, S.; Roux, B. *Nature* 2004, *431*, 830.
18. Varma, S.; Rempe, S. B. *Biophys. J.* 2007, *93*, 1093.
19. Bostick, D. L.; Brooks, C. L. *Proc. Natl. Acad. Sci. U. S. A.* 2007, *104*, 9260.
20. Shi, N.; Ye, S.; Alam, A.; Chen, L.; Jiang, Y. *Nature* 2006, *440*, 570.
21. Alam, A.; Jiang, Y. *Nat. Struct. Mol. Biol.* 2009, *16*, 35.
22. Kim, S. K.; Vargas-Zúñiga, G. I.; Hay, B. P.; Young, N. J.; Delmau, L. H.; Masselin, C.; Lee, C.-H.; Kim, J. S.; Lynch, V. M.; Moyer, B. A.; Sessler, J. L. *Journal of the American Chemical Society* 2012, *134*, 1782-1792.
23. Kim, S. K.; Lynch, V. M.; Young, N. J.; Hay, B. P.; Lee, C.-H.; Kim, J. S.; Moyer, B.

A.; Sessler, J. L. *Journal of the American Chemical Society* 2012, *134* (51), 20837-20843.

24. Sadhu, B.; Sundararajan, M.; Bandyopadhyay, T. *J. Phys. Chem. B* 2015, *119*, 10989.

25. Sadhu, B.; Sundararajan, M.; Bandyopadhyay, T. *The Journal of Physical Chemistry B* 2015, *119* (40), 12783-12797.

26. Sadhu, B.; Sundararajan, M.; Velmurugan, G.; Venuvanalingam, P. *Dalton Trans.* 2015, *44*, 15450.

27. Sadhu, B.; Sundararajan, M.; Bandyopadhyay, T. *Inorganic Chemistry* 2016, *55*, 598-609.

28. Rawat, N.; Kar, A.; Bhattacharyya, A.; Rao, A.; Nayak, S. K.; Nayak, C.; Jha, S. N.; Bhattacharyya, D.; Tomar, B. S. *Dalton Trans.* 2015, *44*, 4246.

List of Abbreviations

BCP	Bond Critical Point
BFE	Binding Free Energy
C/C	Crown/Crown
C/CP	Crown/Crown-Pyrrole
C/P	Crown/Pyrrole
CB	Cucurbit-uril
CGP	Cage Critical Point
CN	Coordination Number
COM	Centre of Mass
CSSX	Caustic-side Solvent Extraction
DFT	Density Functional Theory
ECP	Effective Core Potential
EDA	Energy Decomposition Analysis
FA	Fulvic Acid
FES	Free Energy Surface
G/P	Glycol/Pyrrole
GTO	Gaussian Type Orbital
HA	Humic Acid
HB	Hydrogen Bond
HLLW	High Level Liquid Waste
HLW	High Level Waste
HN	Hydration Number
HSs	Humic Substances
MD	Molecular Dynamics
MM	Molecular Mechanics

List of Abbreviations

MPA	Mülliken Population Analysis
MtD	Metadynamics
NBO	Natural Bond Order
N-M	Nalewajski-Mrozek
P/P	Pyrrole/Pyrrole
PES	Potential Energy Surface
PME	particle-mesh Ewald
PMF	Potential Mean Force
QM	Quantum Mechanism
QTAIM	Quantum Theory in Atoms in Molecule
RCP	Ring Critical Point
RDF	Radial Distribution Function
RI	Resolution of Identity
SF	Selectivity Filter
SOM	Soil Organic Matter
STO	Slater Type Orbital
TM	Truncated Model
US	Umbrella Sampling
WBI	Wiberg Bond Indices
WT	Wild Type
WtD-MtD	Well-tempered Metadynamics

List of Tables

List of Figures

CHAPTER –1

Introduction to Natural and Synthetic receptors/binders and Computational Methodology

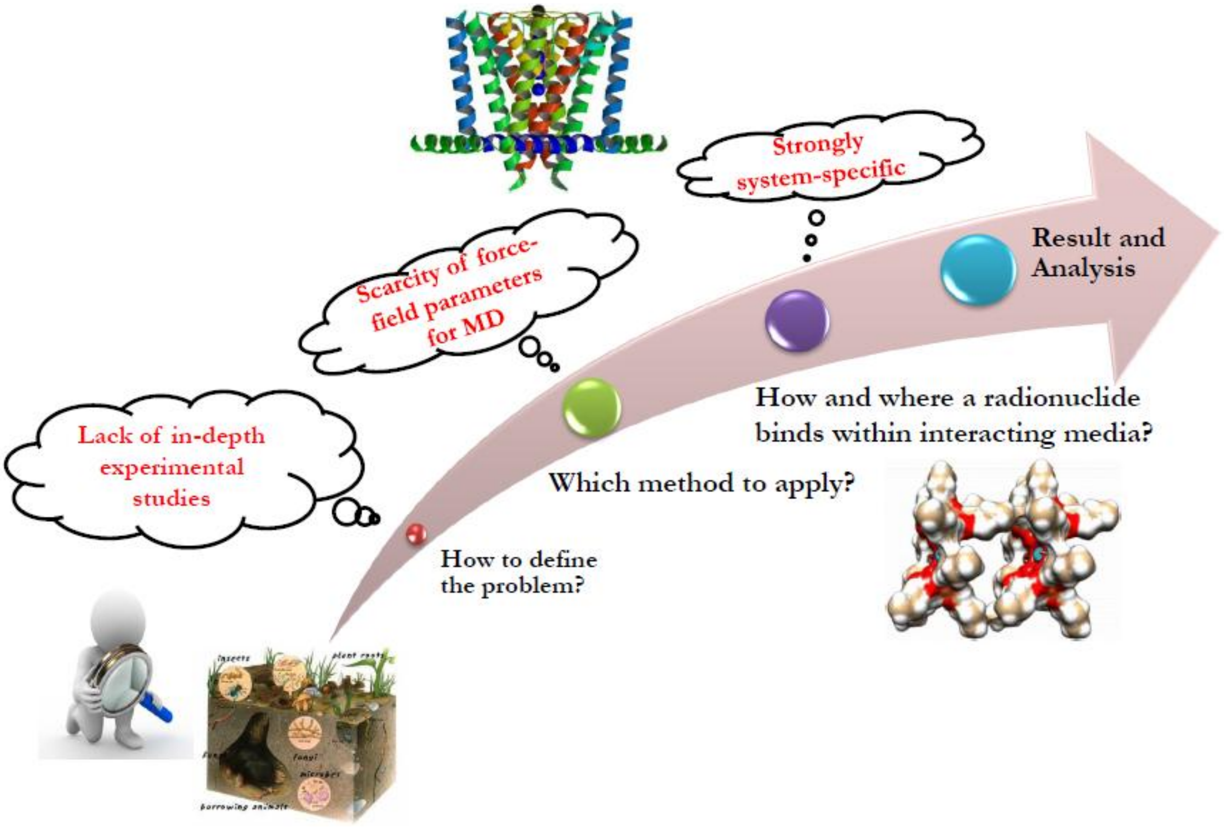

1. Introduction

To meet the energy requirement per capita, the world has opted for several energy sources. The presently limited reservoir of coal and the alarming effect of greenhouse gases led us to look for better alternative energy resource options. In 1938, arguably the first nuclear fission was carried by Hahn and coworkers, which later infused the possibility of using the nuclear energy as one of the best thought clean energy resources for electricity generation (Figure 1.1). However, first successful electricity generation using nuclear power was carried out more than a decade later at near Arco, Idaho. Since then growing number of nuclear power plants throughout the world is reiterating people's confidence on the usage of nuclear energy. A single nuclear fission event can generate a gigantic 200 MeV of energy. However, nuclear energy production comes with some penalty.

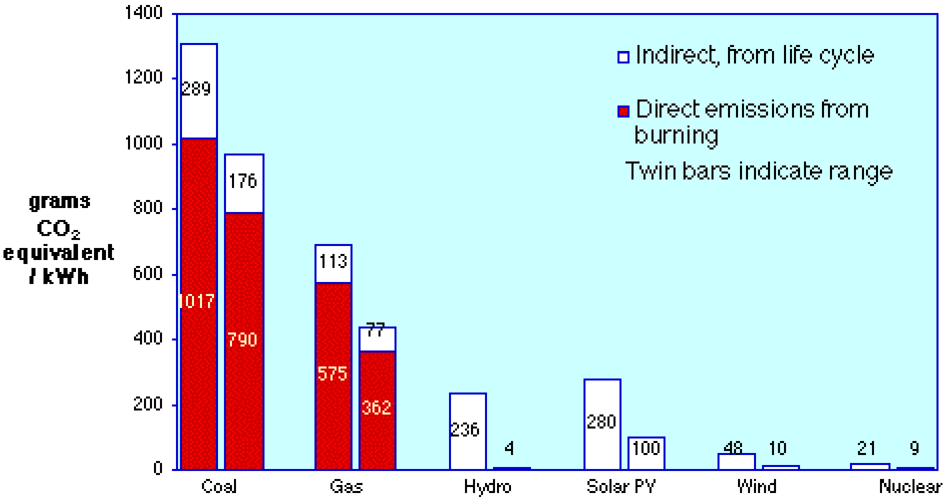

Figure 1.1: Greenhouse Gas Emissions from Electricity Productions.
(Source: IAEA Bulletin 42,2; 2000)

Nuclear fission process generates highly radioactive fission products and actinides. Presence of numerous engineering safety features in nuclear power plant (NPP) ensures the safety of NPP leading the probability of a NPP accident to significantly small. However, in past few decades we have witnessed few NPP accident namely, Three Mile Island (TMI, 1979), Chernobyl

(1986) and most recently Fukushima daiichi NPP accident. Due to such type of events, inadvertent release of radionuclides such as ^{137}Cs and ^{90}Sr might occur into the environment which can present a potential biological/radiological threat to human health and can subsequently generate significant amount of radioactive environmental waste.[1] In this context, understanding the migration of these radionuclides *via* environmental sub-systems is utmost essential to mitigate/regulate their translocation in the chemosphere. Other dominant sources for these releases are from nuclear weapon tests,[2] and fuel reprocessing plants.[3-4]

On the other hand, the events involved in closed nuclear fuel cycle (Figure 1.2) also led to generation of nuclear wastes which are categorized into various groups based on the specific activity level.

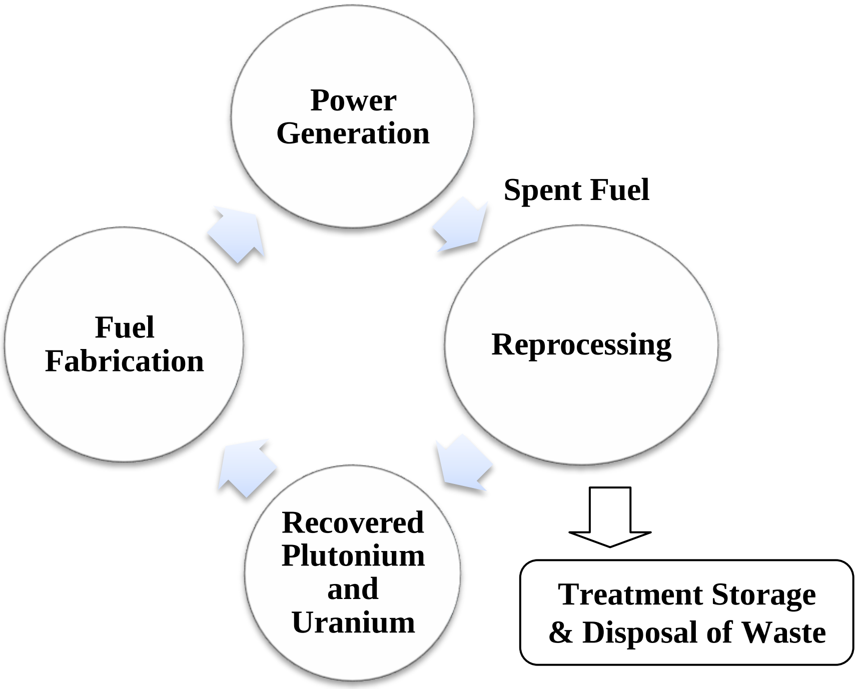

Figure 1.2: Nuclear Fuel Cycle.

Processing of the high level nuclear waste (HLW), which in general contains unextracted uranium (^{235}U, ^{238}U), plutonium (^{239}Pu) along with many other fission products like cesium (^{137}Cs), strontium (^{89}Sr, ^{90}Sr) and lanthanides (^{155}Eu), requires lot of attention in order to reduce the activity level before it can be safely disposed off. In particular, the presence of minor actinides (MAs) such as americium (^{241}Am, ^{243}Am) and curium (^{245}Cm) in high level liquid waste (HLLW) causes problems due to the significant heat generation. MAs are alpha emitters with long half-lives in the order of several hundred years.

Regardless of how nuclear waste gets generated, their post processing requires in-depth knowledge of involved radionuclide's behavioral aspects and chemical properties in various chemical environments that exist either in natural environment or in synthetic media. In nature, regulation/mitigation of the radionuclide's migration is achieved by the constituent chemical entities which are commonly known as binder or receptor. For instance, naturally occurring various components of soil organic matter (SOM) or else the ion-transporting systems of soil dwelling bacteria can act as binder to the radionuclides either in specific or non-specific way. On the other hand, the synthetic binders or receptors, which are laboratory-synthesized to achieve a specific binding feature, designed to recognize, control and capture the radionuclide of interest for efficient separation. The major challenges of waste reprocessing reside in separation of fission products and in effective separation of MAs from their chemically similar congeners (Ln^{3+}).[5] The investigations to elucidate the acting binding mechanisms of these vital processes have been a topic of many interests.[6-11] However, concurrence is yet to achieve and many issues still remain unaddressed.

Being radioactive and toxic in nature, any experimental studies directed towards deciphering the structure and dynamics of radionuclides' interactions with natural/synthetic media poses a formidable challenge. Thus, use of advanced computational modeling techniques (In Silico studies) have become an alternative lucrative option towards understanding the molecular mechanisms on how such regulation and capture occurs.[12-19] The gathered knowledge from the computational studies can be further useful to design the ion-selective probes and also to implement better bioremediation methodology. The works carried out in the present thesis primarily aims at providing microscopic insight on the structure, binding and capture mechanism of radionuclides to the different chemical entities of two distinct environments viz. natural and synthetic. We have used multiscale modeling approaches involving first principle based quantum mechanics (QM) calculations, all atom molecular dynamics (MD) and non-equilibrium metadynamics (MtD) simulations in an attempt to unravel the static as well as dynamic picture of radionuclide migration and recognition process. The choice and combination of methods have been based on the nature of studied problems. The following section provides a detail background on the various types of receptor/binders along with a basic overview on the principle of applied computational techniques.

1.1. Natural Binder/Receptor

In environmental condition, soil acts as the most important and major sink for all essential as well as toxic elements. It is also known as "nature's garbage heap".[20] SOM and soil micro-organisms are the most important components of soil which determines the fate of deposited elements before it enters into the biological life cycle. The present section provides the general background on the origin and nature of these components and their influences on metal transportations.

1.1.1. Soil Organic Matter

A fertile soil contains different layers or horizons (Figure 1.3). The upper layer of soil is basically composed of SOM. The percentage of SOM in soil depends on soil nature and various environmental factors (such as rain, humidity and temperature). In general, soil contains 2-8 percent of organic matter. In acid, leached soils, which are often sandy, substantial portions of the organic matter, remain present in the form of plant debris and reactive humic substances (HSs). SOM has three components namely,humic acid (HA), fulvic acid (FA) and humin.

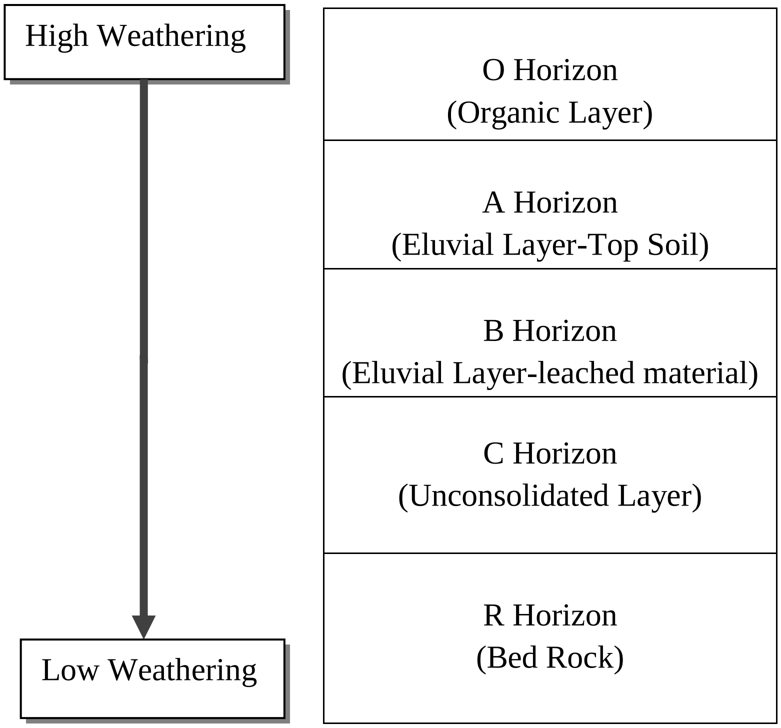

Figure 1.3: Soil Horizon.

1.1.1.1. Humic Acid

The principal component of Humic substances (HSs) is HA. It is produced by bio-degradation of dead organic matter and remain as the major organic constituents of peat, coal many upland streams, dystrophic lakes, and ocean water.

The proper structure of HA is still unknown and varied widely depending of soil nature. Several studies such as chemical pyrolysis, spectroscopic analyses were carried out to determine the functional groups of HA.[21-22] For instance, Haworth et al. studied the structural component of HA using UV and mass spectroscopy.[23] Few nuclear magnetic resonance (NMR) studies are also available in the literature about the HA and FA.[24-25] Although the components of soil HA are well identified, conformation of these acids are not known with certainty. By combining the derived data from many experimental investigations, various structural formula for HA and FA have been proposed.[26-30]

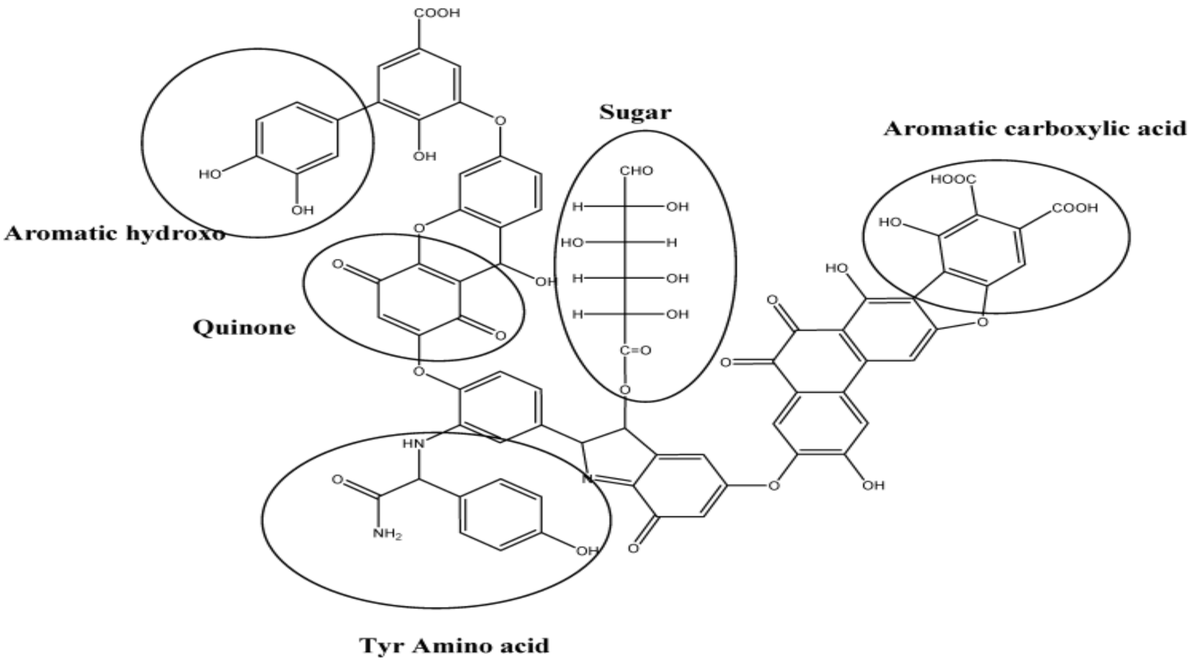

Figure 1.4: Model Structure of Humic acid by Stevenson**.**

In 1989, Leenheer proposed the structure of HA which described it as a complex mixture of many different acids containing carboxyl and phenolate groups as primary functional groups.[31] Presence of these functional groups makes it chemically active towards metals. Although it contains high oxygen concentration in its structure but a good percentage of the oxygen atoms remain in the interior as ether linkages (Figure 1.4). Along with these functional groups, HA may also have amino acid residues (for ex. Tyrosine).[13] HAs may also contain nitrogen, sulfur and phosphorous depending on the soil nature. It is the fraction of Humic substances that is not soluble in water under acidic conditions ($pH < 2$) but is soluble at higher pH values. It can be extracted from soil by various reagents and which is insoluble in dilute acid. HA is the major extractable component of HSs and of dark brown in color.[21]

HA can form complexes with ions that are commonly found in the environment. This metal complexation properties of HA[32] control the bio-availability of metals in environment. HA is also known to play vital role in living organism. It mainly transfers nutrients to living organism.

1.1.1.2. Fulvic Acid

This fraction of HSs is soluble in water under all pH conditions. It remains in solution after removal of HA by acidification. By chemical nature, FA is more reactive than HA as most of the oxygen atoms in FA structure remain as reactive carboxylate and phenolate functional groups. FA has light yellow to yellow brown color.

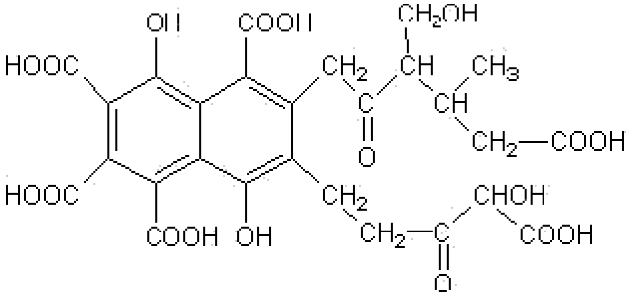

Figure 1.5: Model Structure of Fulvic acid by Buffle.

Difference between HA and FA can be explained by variations in molecular weight, numbers of functional groups (carboxyl, phenolic OH) and their extent of polymerization. The low molecular weight FA[33] have higher oxygen contents and lower carbon content than the high molecular weight HA. Due to the presence of many carboxylate groups (-COOH) in FA, it is acidic in nature. The total acidity of FA (900-1400 meq/100g) is considerably higher than for HA (400—700 meq/100g). The ratio of HA and FA varies from soil to soil. It usually decreases with increase in soil depth. Generally the forest soil contains more amount of FA as compare to HA whereas in case of grassland soils the situation is reported to be reverse.

1.1.1.3. Humin

This fraction of HSs is not soluble in water and alkali at any pH value. Humins are black in color. Humin is very stable and not as active as HA and FA. It is reported to have aliphatic nature and generally contains major portion of aliphatic, carbohydrate and aromatic carbon.[34]

1.1.2. Popular Mode of Investigations for Metal-SOM binding

The binding of metal ions with SOM have been extensively studied by various research groups. The motivation behind these investigations was to determine the availability of bare metal ions (such as Cu^{2+} ,Cd^{2+}) in soil solution in the presence of SOM which provides information on soil to plant transfer factor for the metal of interest. Apart from this, one of the aim has been the assessment of the metal toxicity level of soil solution (correspond to the concentration ratio of free hydrated ion and total metal concentration). Potentiometric and titrimetric techniques always remain popular method for metal concentration determination. However, the chemical heterogeneity of SOM, its variable binding sites and the effects of several environmental parameters (pH) have always made the study on these complexation processes more complicated.

In order to incorporate these several influencing and crucial factors into the final results, use of several analytical models such as Model V of Tipping and Hurley,[35] Model VI[36] and non-ideal competitive absorption (NICA)-Donnan model[37] are quiet popular till date. However, the conclusions derived from these models are strongly dependent on the used equations, assumptions, analytical data set and often remain specific for a particular metal ion. For example, the accuracy of Model V was earlier questioned by Kinniburgh et al.[38] on the basis of its "inconsistency in the development of the electrostatic model".

Although computational investigation can provide additional support such as possible structure and binding affinities to experimental observations, due to the structural uncertainty of FA, only a handful studies have been carried out. Trout et al.[39] have used semi-empirical methods and estimated the deprotonation energies of Leenheer FA model.[7, 40] Further they also investigated the interaction of aluminium cation (Al^{3+}), benzene and pyridine with this FA model.[41] The studies of Rösch and his co-workers[42] should be noted here where the binding affinities of a number of functional groups to uranyl was reported using density functional theory (DFT) based calculations.

However, due to simpler model, effect of the neighboring groups to the metal binding affinities was not accounted, which might not truly reflect the metal binding free energies. Due to the increasing power of computer hardware, it is now possible to carry out DFT calculation of medium size system (100-200 atoms). In this regard very recently, Sundararajan et al.[13] have carried out the structure and possible binding motifs of uranyl ion to HA and FA model structures proposed by Stevenson and Wang et al[43] using a combined density functional theory (DFT) and Molecular Dynamics (MD) simulations. In this study, they have identified a number of aspects such as conformational flexibility and role of neighboring residues which influences the binding affinities of uranyl to HA.

1.1.3. Soil microorganisms and Bioremediation

Soil microorganisms are known to play distinct and unique role as a binder/receptor to detoxify the contaminated soil. In bioremediation technique, often microorganisms remain a popular candidate to restore the natural characteristics of soil *via* mineralizing wastes.[44] Commonly two methods are applied for these procedures. In first option, removal of contaminated soil is done before treating it in a bio-reactor (extraction-treatment technique). In second option, *in situ* treatment of the field is carried out by culturing of microorganisms. Compare to extraction-treatment technique, *in situ* treatment does not require bio-reactor and added systems while appropriate nutrition, mineral and environment are needed in *in situ* technique to increase the microbial activity. Thus engineering difficulties are quiet less for *in situ* treatment.[45]

Often microbial reduction of toxic metals processes led to changes in its chemical properties which further causes change in mobility of the metal in the contaminated field. For instance, sulfur reducing bacteria are commonly used to reduce Cr^{6+} to immobile Cr^{3+} oxidation state.[46] These techniques are not limited to main group elements. Presently, similar strategies can also be adopted for different radionuclides. For instance, uranium in VI oxidation state remain highly soluble in aquatic media. Reduction to IV oxidation state *via* microorganisms decrease the solubility to reduce the migration ability.[47] Various organisms such as *Anaeromyxobacter dehalogenans*,[48] *Desulfitobacterium Species*[49] are rigorously tested to serve this purpose.

Thus, the choices of microorganisms are not simple and require extensive in-depth knowledge on the acting microbial processes in the field. The adequate understanding on the metal translocation pathway and its interactions with living organisms are crucial to engineer the microorganism with proper characteristics. Apart from these experiments, computational modeling involving state-of-the-art QM calculations are popularly being used to address the aforementioned issues.[50] Further, radionuclides like Cs^+ and Sr^{2+}, due to their chemical similarities with Na^+, K^+ and Ca^{2+}, can enter the biological life cycle or food chain following the ion-transporting route.[51] The underlying binding and translocation mechanism of these radionuclides *via* ion-channel route is still remain elusive and require significant investigations.

1.2. Synthetic Receptors

As evident from its name, these classes of receptors are laboratory synthesized to serve a specific purpose of recognition. Most of these receptors are designed/fine tuned and synthesized upon consideration of the user's interest and its applicability. In the context of this thesis, this section is devoted to provide a brief introduction on the well known Macrocyclic host molecules.

1.2.1. Macrocycles

It can be defined as cyclic macromolecule having three or more donor atom to coordinate to metal ions. In general, the cyclic structure which contains nine or ten donor atoms in the cavity to form a ring is coined as Macrocycle. There are many biological macrocyclic receptors available in nature. For example, chlorophyll, vitamin B12 and heme. The most intriguing property of macrocycle is its selectivity towards a particular metal ion due to the acting macrocyclic effect. In order to selectively remove natural contaminants as well as radionuclides from waste, researchers in last few decades paid considerable attention on the synthesis of various macrocycles. Most common synthetic receptors are Calixarene, Calixcrown, and Cucurbituril.

1.2.1.1. Crown ethers

Crown ethers are cyclic chemical compounds that consist of a ring containing several ether groups (Fig 1.6). It interacts with the alkali cations strongly. It chooses metal cations on the basis of size fit criteria to fit in the interior of the macrocycle. Metal ions form complexes with crown ether *via* strong ion-dipole electrostatic interactions. Among all the alkali metal cations, K^+ bounds most strongly with crown-6 ether.

In the crown ether, the interaction between ligand and the metal ion is considered to be more electrostatic in nature, rather than the usual covalent binding as observed for the transition metal complexes of the aza, thia, and phospha macrocycles. 1:1metal-ligands are quite common for crown ethers.

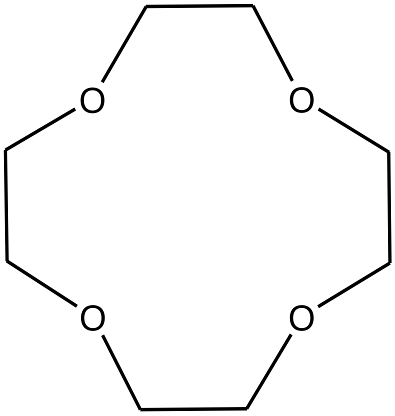

Figure 1.6: Structure of Crown-[4]-ether.

However, for very large metal ions which are incapable of fitting into smaller macrocyclic cavities, sandwich-type structures can also occur. Although crown ethers provide strongly metal specific binding sites, the reorganization of the ligand upon complexation can induce the negative entropy factor to decrease the favorability of the reactions.

1.2.1.2. Calixarenes and Calixcrowns

They are bucket shaped macrocycles made from condensation of para-substituted phenols with formaldehyde (Fig 1.7). They can be functionalized at the upper and lower 'rim'. This can give a hydrophobic pocket and a spherand like '*highly preorganised*' cation binding site.

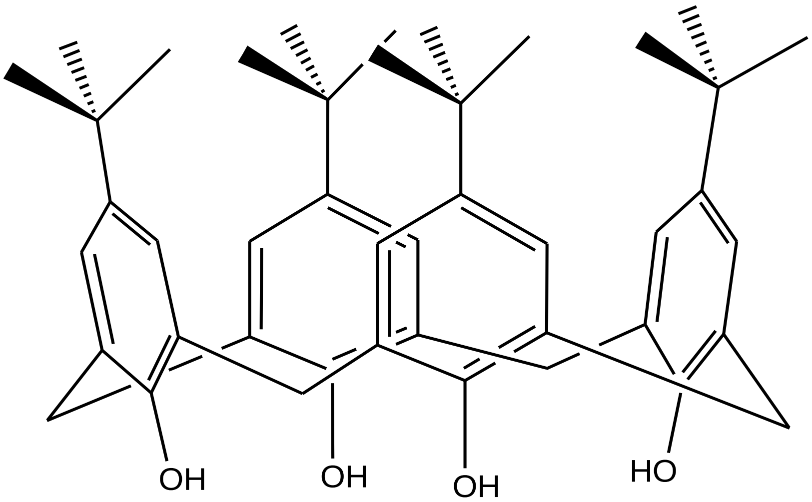

Figure 1.7: Structure of Calixarene.

A modified variant, calixcrown is an important member of the macro polycyclic or cage-molecule's family. In this receptor, the monocyclic structures of calixarenes and crown-ethers are combined through the bridging of phenolic oxygens of a calixerene by a polyether chains to produce metal binding cavities. Presence of crown ring provides the strong electrostatic interaction while aromatic moieties of calixarene contribute *via* cation-π interaction to favorably binding the ion of interest.

For nuclear waste management program, use of crown based ligands for ^{137}Cs and ^{90}Sr extraction are very popular. For instance, in Caustic-Side Solvent Extraction (CSSX) process, calix[4]arene-crown-6 extractant is used for cesium removal.[52] In widely used Stronium Extraction process (SREX), Sr^{2+} is removed using di-t-butylcyclohexano-18-crown-6 in 1-octanol medium.[53-54] Due to absence of any anion binding site, the involvement of counter ions in these radionuclide extraction processes is not specific in nature. However, it is perceived that counter ions plays critical role to modulate the extraction efficiently. To utilize the favorable influence of counter ion, Sessler and coworkers synthesized unique variants of receptors namely, synthetic ion-pair, which contain both cation and anion binding site in the same molecule to synergistically help the binding of each other.[8-10, 55-56]

1.2.1.3. Cucurbit-[n]-uril

Cucurbit-[n]-urils (or CBn) is macrocyclic molecules consisting of glycoluril repeat units. These compounds are particularly interesting to chemists because they are molecular containers that are capable of binding other molecules within their cavity. The name is actually derived from the resemblance of this molecule with a pumpkin of the family of *Cucurbitaceae*.

Based on the number of carbonyls (n) in each of the carbonyl portal, many variants are named. For example, cucurbit[6]uril has six carbonyl at the open portal. The cavity of cucurbit[6]uril has nanoscale dimensions with an approximate height of 9.1 Å, outer diameter 5.8 Å and inner diameter 3.9 Å. Cucurbiturils are efficient host molecules in molecular recognition and have high affinity for positively charged or cationic compounds. High association constants with positively charged molecules are attributed to the carbonyl groups that line each end of the cavity and can interact with cations in a similar fashion to crown ethers.

Host-guest interactions also significantly influence solubility behavior of cucurbiturils. Cucurbit[6]uril dissolves poorly in most of the solvents but solubility can be improved in an acidic solution. The cavitand forms a positively charged inclusion compound with a potassium ion or a hydronium ion respectively which have much greater solubility than the uncomplexed neutral molecule. The hydrophobic cavity of Cucurbit-[n]-urils can accommodate few number of water molecules. For examplex, CB[5] and CB[6] can have two and four water molecules inside the cavity. These kinetically trapped water molecules are reported to be of higher energy and release of these water molecules are thermodynamically favorable process.[57] Thus the encapsulations of dye molecules inside the cavity require removal of these water molecules. The favorable inclusion of several dye molecules inside CB also made the host molecule a potent candidate for drug delivery.[58]

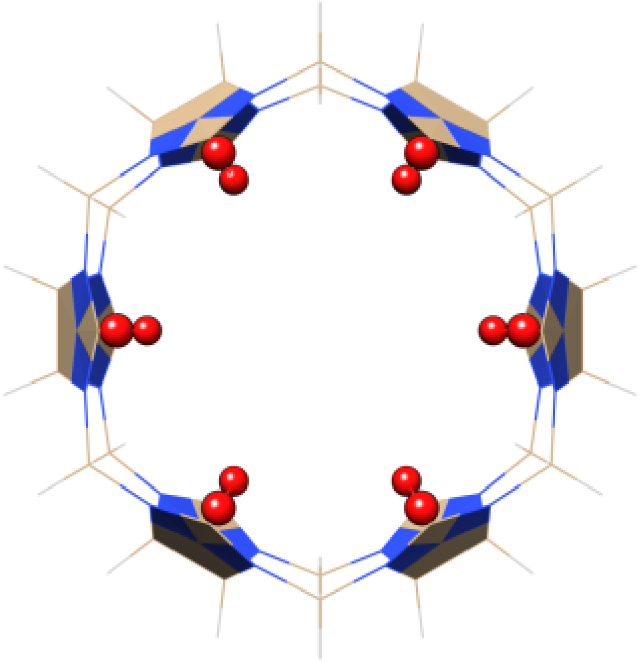

Figure 1.8: Structure of Cucurbit-[6]-uril.

Recent experimental[59-60] and theoretical studies[61] with several crystallographic investigations[62-64] also projected that CB analogues can also be used as probable candidate for radionuclide removal process. Radionuclide metals can possibly bind at the carbonyl portal to interact with hard oxygen donors of the site. Interestingly, it is also reported that the intrinsic binding property of metal at the electron rich carbonyl portal is perturbed/enhanced by the presence of third species in the hydrophobic cavity. How such modulation occurs at the molecular level is still under microscopic investigations and further studies indeed required to reach a concurrence.

1.3. Introduction to Computational Chemistry

Computational chemistry has become an indispensible tool for the investigations of complex molecular systems which are very difficult to handle experimentally for their associated costs or involved risk factors. The computational chemistry gives prediction about the system by providing relevant information which helps chemist in decision making process before going for the actual experiment. In last few years, we have observed a tremendous development in this area. There exist a wide variant of computational technique which has their own merits and demerits. The popular branches are quantum mechanism (QM), molecular mechanics (MM), molecular dynamics (MD) and most recently the metadynamics (MtD) methods. The choice of the proper method for computation is strongly dependent on the problem of interest and also on the system size. This section briefly discusses the background of aforementioned techniques.

1.3.1. Quantum Mechanics

QM is the basis of applied quantum chemistry. Computational quantum chemistry is primarily used to do numerical computation of molecular electronic structures by *ab initio* and semi-empirical techniques.

Availability of highly advanced super computer facility has given a new wing to these computationally expensive techniques. These techniques can be used to understand the chemical structure and calculate many chemical parameters like vibrational frequency, nmr shift, thermodynamic properties of metal complexation process. The main purpose of these techniques can be summarized in these points:

- To know the bonding and structures in the molecular systems.
- To calculate the electron and charge distribution in a system.
- To calculate potential energy surface (PES).
- To provide information about probable transition state of a reaction.

- To calculate the electronic, magnetic and optical properties of materials.
- To study the effect of various parameters on chemical reactions or living biological systems and evaluate binding mechanisms.
- To estimate the energetic parameters (entropy, enthalpy, free energy) of chemical reactions.
- To calculate rate constants of elementary reactions.

1.3.1.1. ab initio

The term "*ab Initio*" is latin for "from the beginning". This name is given to computations which are derived directly from theoretical principles. It uses Schrödinger equation with electron correlation function for calculation of relevant parameters using experimental data. Most of the time, this refers to an approximate quantum mechanical calculation. The approximations made are usually mathematical approximations, such as using a simpler functional form for a function or getting an approximate solution to a differential equation. *ab initio* Hartree Fock theory (HF) cannot predict the exact energy of a system due to the missing contribution of correlation energy of electrons due to coulomb repulsion.

1.3.1.2. Semi-empirical Techniques

This technique is used for large systems where it is not feasible to use HF formalism without any approximations. This empirical method does not include two- electron part of the Hamiltonian explicitly. It is faster than *ab initio* technique. The use of empirical parameters allows some inclusion of correlation effects into the methods. Only valence shell electrons are considered in this technique. Core electrons are taken care by introducing empirical functions to model the interactions between atom (nuclei + core electrons) and the other particles. This technique cannot properly take care of non bonding interactions. Minimal basis set is used for the computations.

1.3.1.3. Density Functional Theory

Density Functional Theory (DFT) is the most reliable technique for the determination of the molecular property accurately. It takes care of correlation energy (particularly coulomb correlation which is not included in HF theory) to give a more accurate prediction on the exact energy of the system. To know the molecular properties of a system, the first thing one must evaluate is the energy of the system and more importantly how the energy is changing when atoms are moving around. The positions of nucleus and electrons have to be defined in the system to know the position of atom. One can simplify the problem by taking consideration of nucleus and electrons separately. The electrons respond to the changes in environment rapidly than the nucleus due to higher mass of the later.

For given set of coordinates of electrons which are moving around the nucleus, we can solve the equation of Schrodinger to get the lowest energy configuration known as ground state. The most simplified Schrodinger equation can be expressed as:

$$H\psi = E\psi \tag{1}$$

In this equation, H is the Hamiltonian operator and ψ is a set of eigen states of the Hamiltonian. Each of the solution ψ_n has eigen values which are E_n, a real number which satisfies the eigen value equation. For more complex systems, the interactions between the electrons also need to be considered for estimation of energy. For many electron systems, the Schrodinger equation can be expressed as:

$$\left[\frac{\hbar^2}{2m}\sum_{i=1}^{N}\nabla_i^2 + \sum_{i=1}^{N} V(r_i) + \sum_{i=1}^{N}\sum_{j<i} U(r_i, r_j)\right]\psi = E\psi \tag{2}$$

The first two terms of the left side of the equation (2) implies the kinetic energy of the system, the interaction of the electrons and the nuclei, respectively. While third term defines the interaction between electrons where 'm' denotes the mass of the electron and ψ is electronic wave function.

It is the function of spatial coordinates of the electrons. E provides the ground state energy of the system. However, the wave function is not physical in nature to find the probability of finding electrons in configuration space.

In place of wave function, electron density is the more adoptable term for estimation of molecular properties. The density functional theory deals with this electron density $n(r)$ at a particular position in space. It can be defined by this equation:

$$n(r) = 2\sum_i \psi_i^* (r)\psi_i(r) \tag{3}$$

factor two appears because the electrons are having spin and Pauli Exclusion Principle states that individual wave functions can be occupied by two electrons provided they have different spins. The density functional theory stands on two fundamental mathematical theorems of Kohn and Hohenberg.

The first theorem can be stated as "The ground state energy of Schrodinger's equation is a unique functional of electron density." The term functional can be defined as function of functions. In their next theorem, they stated the need of true functional to get the final solution of Schrodinger equation, which may be stated as "The electron density that minimizes the energy of the overall functional is the true electron density corresponding to the full solution of the Schrodinger equation."

The energy functional can be defined as:

$$E[\{\psi_i\}] = E_{known}\,[\{\psi_i\}] + E_{XC}\,[\{\psi_i\}] \tag{4}$$

In this equation, ψ_i is the single electron wave function.

$$E_{known}\,[\{\psi_i\}] = \frac{h^2}{m}\sum_i \int \psi_i^* \nabla^2\psi_i d^3r + \int V(r)n(r)d^3r + \frac{e^2}{2}\iint \frac{n(r)n(r')}{|r-r'|} d^3r d^3r' + E_{ion} \tag{5}$$

The terms, in order, defines the kinetic energy of the system, the interaction of nuclei and electrons and coulomb interaction between of electrons, while the last term denotes the coulomb interaction between a pair of nuclei.

The second term in equation (4) is known as exchange correlation functional which accounts all quantum chemical effects which are not included in the known term. In this context, we can compare the Kohn sham equation which is similar to equation (2) except the last extra term is missing in the later.

$$\left[\frac{h^2}{2m}\nabla^2 + V(r) + V_H(r) + V_{XC}(r)\right]\psi_i(r) = \varepsilon_i\psi_i(r) \qquad (6)$$

The third term is known as Hartree potential and expressed as:

$$V_H(r) = e^2 \int \frac{n(r')}{|r-r'|} d^3r' \qquad (7)$$

The exchange correlation potential $V_{XC}(r)$ in the equation can be defined as the functional derivative of exchange correlation energy with respect to electron density.

$$V_{XC}(r) = \frac{\delta E_{XC}(r)}{\delta n(r)} \qquad (8)$$

Finding the true form of this term can provide the true solution of equation (6). So it is evident that to get the ground state energy of the system, one must have to define hartree potential and exchange correlation potential which in turn needs the electron density function *n(r)*. Equation (3) suggests the importance to define single electron wave function for the system properly. This can only be known by solving final Kohn-Sham equation [eq. no. (6)].

Hence, all the equations are correlated to each other to make a circle. To find the solution, an iterative way is applied in DFT by providing trial electron density which in turn gives another better approximate for electron density and the process goes on until we find the electron density which satisfies our applied condition. Thus Kohn-Sham equation is self-consistent.

The electron density can be obtained only by defining spin orbitals [$\chi_j(X)$] which is the finite combination of set of functions.

$$\chi_j(X) = \sum_{i=1}^{k} \alpha_{j,i} \varphi_i(X) \tag{9}$$

X is the vector of coordinates which defines the position of the electron. In the above equation, i and j implies the spin state of the electron. $\alpha_{j,i}$is the expansion coefficient and φ_i(X) is the set of functions known as basis function. Larger basis set provides higher accuracy in calculation. Thus selection of basis set is very important for proper description of the system.

1.3.1.4. Basis Sets

A basis set is a set of mathematical functions that used to describe molecular orbitals, which are expanded as a linear combination with coefficients to be determined. It is a collection of vectors that defines the space. Quantum chemical calculations are typically performed within a finite set of basis functions. When finite basis set is expand towards infinite complete set of functions then it approaches to the basis set limit. Many types of basis sets are being used now-a-days. Although these are not exact atomic orbitals due to the approximations and simplifications inherent in their analytical formula. The types of different basis sets can be summarized as follows:

Slater-Type Orbitals (STOs):

In early years, the STOs are used to define MOs. It is naturally a good basis set and provide direct physical interpretation of the molecular orbitals. Use of this basis function is computationally expensive because most of the integrals required during SCF calculation are calculated numerically. It explains long range and short range interaction in the molecule accurately.

Its definition can be represented as follows:

$$\emptyset_{abc}^{STO} = N x^a y^b z^c e^{-\zeta r} \tag{10}$$

Where, N is normalization constant

Total angular momentum (L) = $(a + b + c)$.

ζ= width of the orbital (larger ζ gives tight function, while smaller ζ gives diffuse function).

Gaussian Type Orbitals (GTOs):

GTOs can be expressed using the following equation,

$$\emptyset_{abc}^{GTO} = Nx^a y^b z^c e^{-\zeta r^2} \tag{11}$$

Here, the terms have the same meaning like STOs. The main difference between STOs and GTOs is that the variable function in the equation is Gaussian. Using the Gaussian product theory, it is much easier to compute and computationally less expensive. This basis function is widely used for calculation by quantum chemists.

Choice of basis set:

It is always better to take the largest basis set available because larger the basis set smaller will be the inaccuracy. Computational time is highly dependent on the size of the system. Thus it is always a compromise to choose the proper basis set for computation. The applied basis function should have polarization and diffuse function to properly describe the molecular system but as the number of basis function increases, the computational time increases in the fourth power of number of basis functions.

Few things which are important for choosing of basis set may be noted below:

a) It depends on the Z value of atom. Larger basis set can be used for low Z atoms.

b) For larger anions, the outer electron will be in diffused form. So consideration of diffuse function and polarization function can better explain the behavior of that kind of anions. The presence of diffuse function in basis set is symbolized by adding ‘+’ sign to the basis set designator. For example, 6-31+G. Addition of another ‘+’ sign signifies that diffuse function added to the hydrogen atom also.

c) For transition elements, polarization function can be added to the basis set by adding ‘d’ orbital to all heavy atoms. Addition of ‘*’ sign in the basis set designator implies the use of polarization function during computation. For ex. 3-21G*.

d) Split valence basis set (def2-SV(P)) is now becoming a good choice for explaining valence and core separately by splitting them in two parts. The first part is inner core while second part is the valence orbitals. Similarly double zeta or triple zeta basis set like TZVP can split the core electrons.

1.3.1.5. Pseudo-potential

For low Z atom, accurate wave function can be constructed but for high Z element like actinides, consideration of all electrons can become computationally expensive that can make the convergence process slow. To look at this problem another way, we can think of all electrons outside the nuclei as of two parts. One is valence electrons which are influenced by the external potentials and mainly involved in chemical reaction while another is core electrons which are not involved in chemical bonding and remain unchanged under structural modification of the complex. If we consider all electron wave function in DFT, then rapid oscillations of valence orbital’s wave functions is observed at the core region to satisfy the orthogonality constraint. It is impractical to represent such functions using plane waves as the size of the basis set would be prohibitive. Thus pseudo-potential concept is developed where the core electrons are replaced by effective core potential (ECP) that act as a set of pseudo functions. The combination of plane wave function and the pseudo potentials can describe successfully the chemical bonding phenomena. ECP reduces the number of basis function during calculation and also takes care of relativistic effects for heavy atom like Cs and I.

Small core *vs.* large core ECP:

Pseudo-potentials are typically characterized by core radius (r_c). The potential for distances smaller than r_c is described by suitable analytical function typically a polynomial or spherical Bessel function. “Hard” pseudo-potential (small r_c) i.e. small core ECP requires more plane wave basis functions for describing the region beyond r_c than for “Soft” pseudo-potential but too large r_c will deteriorate the quality of calculated result and also make the pseudo-potential less transferable while for heavy atom, calculation with small core ECP is computationally expensive.

1.3.1.6. Need of Dispersion and Solvation effects

Incorporation of solvation effect and dispersion in the system helps to build environmental condition. Solvation may be of two types:

a) ***Implicit Solvation:*** here, the respective system is thought to be in known dielectric media where the system forms a cavity within the dielectric continuum of permittivity ε which represents the solvent. For our model, a continuum model having dielectric constant of water $(\varepsilon = 80)$ has been assumed to represent explicit solvation.

b) ***Explicit Solvation*****:** The solvent molecule can be also added explicitly to the system to provide proper solvation to the system.

It has now become a common practice to incorporate the primary hydration shell properties of metal *via* explicit solvation scheme. Later, the hydrated metal is considered to be emerged in a dielectric media of solvent which mimic the metal solvation property in infinite continuum.

1.3.2. Molecular Mechanics (MM)

In MM, no electrons are considered to describe the molecular system in atomic level. It is an application of Newtonian mechanics at molecular level. It considers atoms as point charge. They interacts each other using parametrized force field. It takes into account both nonbonded and bonded interaction for estimating molecular energy of the system. Compare to MM techniques, *ab initio* is most accurate as it directly solves the Schrödinger equation but it is slow and computationally expensive compared to others.

For small system (up to 250 atoms) one can successfully use *ab initio* method but for larger organic systems, MM calculations and semi-empirical techniques becomes a good choice.

1.3.3. Classical Molecular Dynamics (MD)

It is one of the principal tools in the theoretical study which provides dynamic feature of a chemical phenomenon. This tool is frequently used for studying biological molecules and it provides valuable information on the time dependent fluctuation of various chemical properties and conformational changes. In classical MD, trajectories of atoms are generated by solving Newton's equation of motion. Thus MD by virtue is deterministic in nature. Quantum effects are not considered in classical MD. The accuracy of the results are strongly dependent on the applied force field in the simulations. Hence, parameterizations of forcefield with respect to the available experimental data is crucial to bring the accuracy of the results to the acceptable level. By definition, force field is a functional form of parameter which is used to calculate the potential energy of the system of atoms. The potential energy function, V(r) of a common force field can be defined as the sum of internal, or bonded (E_{bonded}) and external, or non-bonded ($E_{nonbonded}$) terms.

$$V(r) = E_{bonded}\,(r) + E_{nonbonded}\,(r) \tag{12}$$

Here r defines the position vector of each atom. E_{bonded} considers interaction occurring within the molecule and comprises of many terms such as bond stretching, $E_{bond-stretch}(r)$, bending, $E_{bond-angles}\,(r)$ and improper dihedral angle distortion, $E_{improper\ \ angles}\,(r)$.

$$E_{bonded}\,(r) = E_{bond-stretch}(r) + E_{bond-angles}\,(r) + E_{improper}\,(r) \tag{13}$$

First term of the equation (13) is defined as the harmonic potential for an atom pair connected *via* covalent bond.

$$E_{bond-stretch}(r) = \sum_{bonds} \frac{1}{2} k_b (b - b_0)^2 \tag{14}$$

Here, k_b correspond to force constant and determines the strength of bond.

Second and third term denote the potential energy change associated with the angle and improper dihedral angle distortion, respectively.

$$E_{bond-angles}(r) = \sum\nolimits_{bond-angles} \frac{1}{2} k_\theta (\theta - \theta_0)^2 \tag{15}$$

$$E_{improper}(r) = \sum\nolimits_{improper} \frac{1}{2} k_\emptyset (1 + \cos(m\emptyset - \delta)) \tag{16}$$

k_θ and $k_\emptyset$ are the corresponding force constants.$E_{nonbonded}(r)$ term is calculated as the sum of vander Waals interaction and coulombic interaction.

$$E_{nonbonded}(r) = V_{LJ} + V_{Coulombic} \tag{17}$$

van der Waals interaction is often computed using Lennard Jones equation, which computes the approximated inter-atomic interaction between atom-pair. This interaction includes weak London dispersion force, and forces acting between permanent and/or instantaneous dipole moments. It can be expressed using following simple equation,

$$V_{LJ} = 4\varepsilon \left[\left(\frac{\sigma}{r}\right)^{12} - \left(\frac{\sigma}{r}\right)^{6} \right] \tag{18}$$

Here, σ denote the finite distance at which the inter-particle potential become zero and ε corresponds to the depth of the potential well.

On the other hand, Columbic interaction takes into account of electrostatic interaction acting between an atom pair at a distance r.

$$V_{Coulombic} = \sum\nolimits_{atom-pairs} \frac{q_i q_j}{4\pi\varepsilon_0\varepsilon_1 r} \tag{19}$$

1.3.3.1. Steps involved in Molecular Dynamics

A simple MD simulation is consist of several steps. Based on initial positions of atoms, at first potential energy is calculated. Later structural minimization is carried out to release the strain in the conformation/systems.

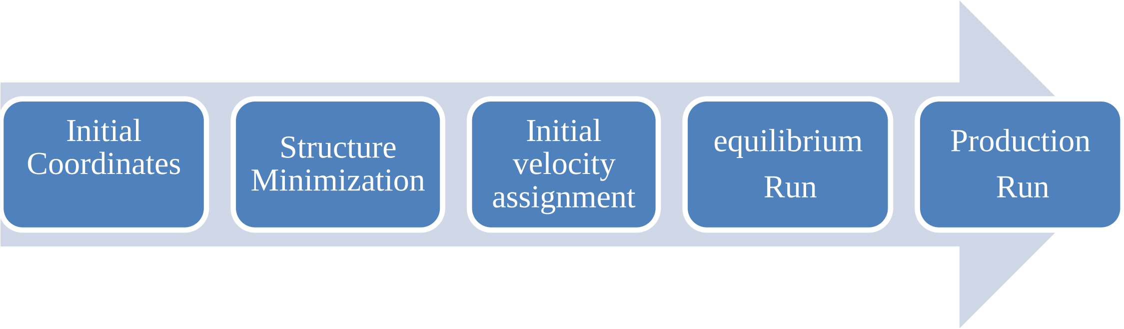

Figure 1.9: Simple Flow-chart of MD simulation

If explicit solvation used, solvent molecules are added to the simulation box to fill the void. Later initial velocities are assigned in order to increase the temperature to the desired value. In next step, temperature and pressure are controlled using appropriate thermostat and borostat. Finally, production run is performed to analysis the property of interest.

1.3.4. Metadynamics (MtD)

Often physical reactions occur at microsecond time scale. Following the course of such reactions with classical MD simulations are highly time consuming and quite impractical to perform as it requires huge number of MD steps. At present, most MD simulations are performed to explore chemical information from nano second to hundreds of nano seconds. However, most of the biophysical events occurs in microsecond to millisecond region. For instance, folding phenomena of a denatured protein may take 10^{-4} s which requires 10^{11} MD steps to perform before protein attains the folded configuration. Similarly, ion permeation through the biological ion-channel also requires time in micro second time scale. The energy barrier of such reactions can be of several order of kT.[65]

Coarse-grained simulation can provide a solution to this problem, which simplify the system description during simulation by considering less number of degrees of freedom and eliminating the fine interaction details. However, often information about the right choice of degrees of freedom on studied system remains unavailable. Another solution to the aforementioned problem is to use Metadynamics which *accelerates the rare events* to overcome the energy barrier.

The method of Metadynamics is pioneered by Prof. Parrinello.[65] Metadynamics focuses on overcoming the energy barrier by filling the potential well with history dependent biased potential. It is a powerful simulation technique which reconstructs the free energy surface as a function of selected degrees of freedom. These degrees of freedom are more commonly known as "Collective Variables (CV; $S(x)$)".

1.3.4.1. Collective Variable (CV)

As explained by Laio et al.[65] the chosen CV in metadynamics simulation should have following properties:

a) The used CV should completely follow the actual course of reaction.

b) Gaussian deposition along the axis of chosen CV should cover all the slow events which are relevant to the process of interest.

c) It is important to use optimum number of CV so that computational time should not become too large.

1.3.4.2. Types of CV

Here we have used following CVs in MtD simulations in the present thesis.

a) Distance: the distance between a pair of atoms/groups

b) Coordination Number: coordination number of a selected atom/ion.

1.3.4.3. Free energy surface (FES)

The MtD method progressively build-up a memory-based biasing potential energy term, $V_{MtD}(t)$ by adding Gaussian "hills" in order to restrict the system revisiting the same region of the space, and is aimed at reconstructing the free energy surface (FES) of a given process much earlier than equilibrium MD could achieve. The FES along chosen CV is given as,

$$V(S(x),t) = w\sum_{t'=\tau_G,2\tau_G,..,t'<t} \exp\left(-\frac{(S(x)-s(t'))^2}{2\delta s^2}\right) \tag{20}$$

As evident from the above equation, the biased potential is dependent on the choice of CV, δs (Gaussian width) and w (Gaussian height). At τ_G interval Gaussians are deposited into the potential well. The optimum choice of δs and w determines the accuracy of reconstructed FES and also influences the simulation time. Prior knowledge about the probable free energy barrier often helps to determine the optimum values of Gaussian width and height. For instance, for small energy barrier, use of large height and width can produce erroneous results and again, too small value of height and width can increase the simulation time significantly.

The enhanced bias explores the rare events along a chosen time dependent collective variable (CV), $S\ (x,t)$ and reconstructs the approximate potential of mean force (PMF) by the equality,

$$F_{MtD}\,(S(x),t) = -V_{MtD}\,(S(x),t) \tag{21}$$

in the region, $P(S)$, explored by the CV up to time t.

1.4. Challenges and Hurdles on Modeling Radionuclide Interaction

Computational modeling on the interaction of radionuclides with different interacting media is not straight forward. It requires overcoming lots of challenges and hurdles in order to correctly describe and interpret the true events involved in such interactions.

For instance, unavailability of proper crystal structure of SOM components poses confusion over acceptance of appropriate model. Although the available experimental information provides clues regarding the composition of model structure, the distribution of various functional groups in large surface area again requires adequate justifications. Additionally, due to large size and conformational flexibility of natural interacting media (such as SOM and ion channel), predicting the global minima among several possible conformations is an uphill task. Often due to the unavailability of experimental investigations particularly for radionuclides, defining the binding sites for the upcoming radionuclides also becomes quite challenging. Equilibrium and non-equilibrium based simulation techniques can provide these details with accuracy.

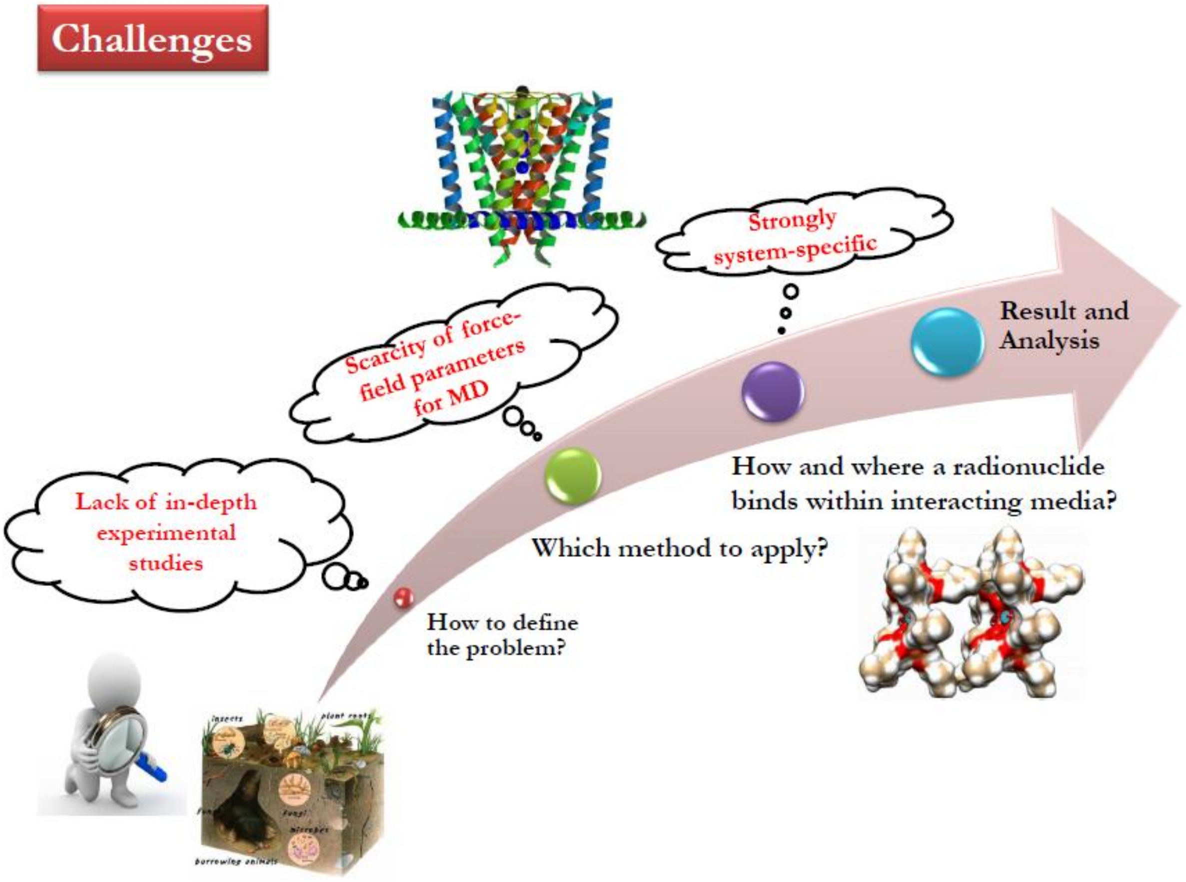

Figure 1.10: Problem solving approach

However, such simulations require proper calibrated forcefield parameters for the model structure and radionuclide. Thus, parameterization of the applied forcefield parameters with respect to available experimental results is pivotal to get the correct result. Once the radionuclide bound conformations are obtained, DFT based calculations are extremely useful to assess the electronic structure, selectivity of radionuclides in the binding site. Further, large size of bimolecular systems make the simulation highly computationally expensive while mimicking the geo-chemical environment to incorporate the effect of chemosphere into the simulations put additional burden on the computation.

On the contrary, availability of crystal structures of most of the synthetic structures partly reduces the conformation based confusions. Hence, use of state-of-the-art QM tools is reported to be adequate to calculate the binding affinities of radionuclides in the rigid receptors. However, accurate prediction of thermodynamic parameters for the binding requires benchmarked computational methodologies.

Considering the above facts, in the present thesis we adopted multiscale modeling techniques to address the radionuclide interaction in diverse interacting media.

1.5. Objective and Outline of the Present Thesis

The present thesis is aimed at understanding the binding and transport mechanism of various radionuclides in various natural and synthetic binder/receptor using multiscale modeling approach (QM, MD and MtD). The choice of the applied method is based on the type of problem of the investigations.

Soil organic matter (SOM) and soil microorganism (soil dwelling bacteria *bacillus cereous*) are taken as the representatives of natural binders/receptor. Whereas, for synthetic receptor, the newly reported calix-crown and calix-pyrrole containing multitopic ion-pair receptor and cucurbit-[5]-uril hosts are considered for computational studies. The main goals of the present thesis are:

a) To decipher the interaction and migration mechanism of harmful radionuclides ^{137}Cs and ^{90}Sr in SOM and further investigate the effects of water molecules on modulating the binding mechanism using multi-scale modeling technique (DFT, MD and MtD). (Chapter 2)

b) To explore the selectivity and permeation energetic of Cs^+ and Sr^{2+} in nonselective ion channel of a soil dwelling bacteria in the presence of interfering cations (Na^+, K^+, Ca^{2+} and Ba^{2+}) with the help of DFT, MD and MtD. (Chapter 3 and 4)

c) To elucidate the structure and cooperative binding mechanism of various cesium salts in a newly reported synthetic multi-topic ion-pair receptor using DFT based calculations. One of the important objectives of this study is to benchmark the computational methodologies by comparing with the available experimental data. (Chapter 5)

d) Predicting the binding/extraction ability of Sr^{2+} with the aforementioned ligand using the benchmarked computational methodology (DFT). (Chapter 6)

e) To investigate the direct influence of counter ion in binding of Am^{3+}/Eu^{3+} in cucurbit-[5]-uril. Further, to assess the possibility of separating Eu^{3+}/Am^{3+} pair from nuclear waste using relativistic DFT analysis. (Chapter 7)

In each of the Chapters we describe the reasoning behind the choice of problem followed by the details on the applied computational methodologies, results of the investigations and finally illustrates the inference of the chapter. In final chapter 8, summary of the present thesis are delineated with a futuristic vision.

CHAPTER –2

Differential Binding of Strontium and Cesium Cations in Fulvic Acid

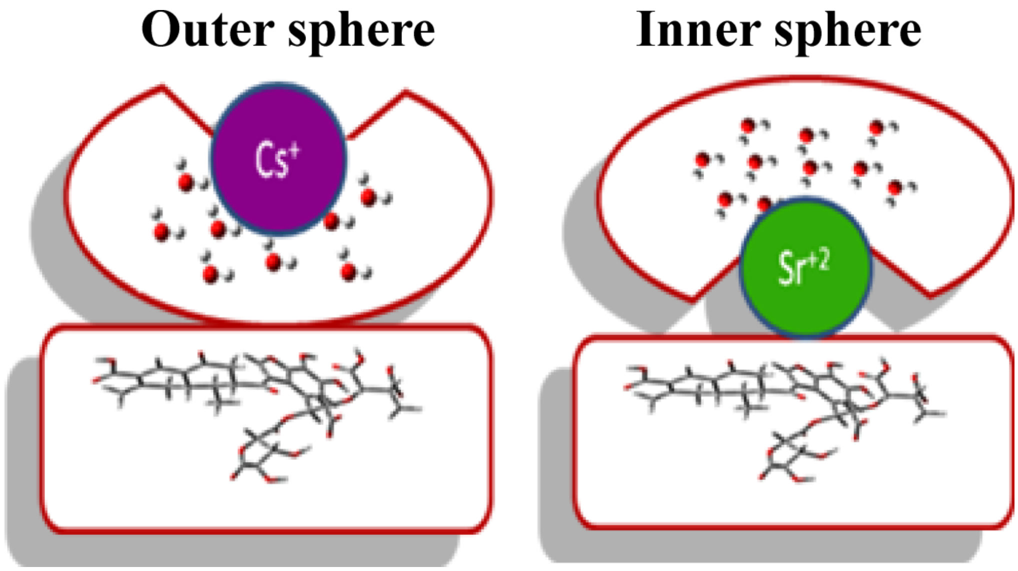

2.1. Introduction

Once get released into the environment, long lived radioactive fission products such as ^{137}Cs and ^{90}Sr can present a potential biological threat to human health.[66] The dominant sources for these releases are from nuclear reactor accidents,[1] nuclear weapon tests,[2] fuel reprocessing plants etc.[3] Being radioactive in nature, handlings of these two radionuclides requires extra safety precautions in case of experimental studies. These radionuclides once deposited onto the soil, can further react with the first layer of soil, which generally contains large amount of soil organic matter (SOM). Humic acid (HA) and fulvic acids (FA) as major components of SOM. Both HA and FA contain various functional groups such as carboxyl, quinone and phenolate, which can bind various radionuclides,[21] restricting the mobility of these ions in soil environment depending on the water content, pH and ionic strengths of the acids.[67-68]

Most of the experimental studies are focused to evaluate SOM influence on radionuclide sorption into mineral layers,[69-72] while experiments on the direct interaction of Cs^+ and Sr^{2+} with FA are limited.[73] Nevertheless, these studies perceived the vital role of SOM on radionuclide mobility. For example, Staunton et al.[74] observed enhanced absorption of cesium into montmorillonite and illite mineral surfaces in the presence of FA.[75] Furthermore, similar chemical properties of its group congeners (K^+ and Ca^{2+}) is suggestive of the fact that Cs^+ and Sr^{2+} might also be absorbed by plants and enter into the human food chains.[76-77] For instance, Sanchez et al.[78] observed a significant amount of Cs^+ is absorbed by plants in organic soil, whereas the Sr^{2+} uptake in plants was observed to be minimal.[79] Apart from this, several data fitting semi empirical models were also proposed to understand the metal-SOM interactions.[80-81] The accuracy of such modeling approach is metal specific and depends on the availability of experimentaly derived parameters.[82]

Theoretical methods such as quantum mechanics (QM) and molecular dynamics (MD) can provide valuable information on the structures, conformational flexibility and cation binding affinities of SOM at the molecular level.[83-84] However, only a few of computational studies have been carried out due to uncertainty in the structure of FA.[85] Of the various possible FA models, Leenheer model[7] is considered to be one of the realistic model, which possess essential functional groups present in FA. Trout and Kubicki[39, 41] have calculated the proton and guest affinities of carboxylate functional groups using the Leenheer model. Burk et al.[18] and Mayeux et al.[19] have calculated the Cs^+ binding affinity to several isolated functional groups of SOM in gas phase. In both studies, the effect of solvents was not considered which may not reflect the true binding affinities as in realistic SOM. The influence of water molecules on the binding affinities of several multivalent cations to SOM was investigated by Aquino et al.[86-88] using classical MD simulations. Recently, Sundararajan et al. have investigated structures and possible binding motifs of uranyl ion to HA and FA models using a combined density functional theory (DFT) and MD based calculations.[13] In line with Aquino et al., they have also emphasized the importance of incorporating solvents effects and neighboring groups, which can modulate the binding affinities of the actinide ion. A combination of different theoretical methods can be extremely useful to tackle the challenging speciation issue of radionuclides in SOM. Note that the use of QM alone can accurately describe the static picture and to some extent the structural conformations using the ab initio molecular dynamics (AIMD) simulations with limited system size and time scale. Similarly, classical MD and its non-equilibrium counterpart, metadynamics (MtD)[89-90] can provide valuable information on dynamical behavior of the system and can treat significantly bigger systems with larger time scale quiet efficiently.

In this Chapter, we present a systematic theoretical approach which applies all these three methods (MtD, MD and QM) to explore the binding mechanism of Cs^+ and Sr^{2+} to FA in presence of explicit water molecules. We choose FA model to represent SOM because of its higher reactivity as compared to HA.[21] Our strategy is as follows. We first carried out a set of DFT calculations in order to find the most probable binding site of FA, interacting with radionuclides. The resulting FA structure is then embeded in explicit water. Complexing ion (Cs^+ or Sr^{2+}) is added and the system is equilibrated through classical MD simulation. MtD is then used to find the stationary points in the free energy landscape of FA-water-ion complexes. MD simulations and QM calculations are carried out on the MtD extracted structures to understand the speciation and binding preferences of Cs^+ and Sr^{2+} to FA. Finally, we arrive at a differential binding mechanism between the two radionuclide ions with SOM, mediated by the intervening water molecules.

2.2. Computational Methods

Quantum Mechanical Study. The chosen FA model contains four carboxylic acid groups (denoted as 'A', 'B', 'C', and 'D' in Figure 2.1), quinone, phenolic hydroxo groups and heterocyclic rings which are the minimum prerequisites for an FA model. The starting structure is taken from Trout and Kubicki.[39] For geometry optimizations, we have used a dispersion corrected BP86 functional[91-92] with def2-SV(P)[93] basis set. This combination is observed to predict accurate geometries.[13, 61, 94-95] To speed up the calculation, a resolution of identity (RI) approximation is invoked for coulomb exchange integrals using a corresponding auxiliary basis set (def2-SV(P)/J). For energetics, a dispersion corrected B3LYP functional[96-97] with TZVP basis set[98-99] is used. For both Cs^+ and Sr^{2+} cations, a def2-SV(P) (for geometry optimizations) and def-TZVP basis set were used to describe the valance orbitals, whereas the core orbitals were modeled via def-ECP (contains 46 core electrons for cesium, 28 electrons for strontium) pseudo potential. The influence of larger basis set TZVP on the structures are found to be minimal (Table 2.1). Changing from double-ζ to triple-ζ basis set we find little change in the computed structures. Hence, throughout the study, medium sized basis set is used for geometry optimization. Long range electrostatic interactions are accounted by the COSMO continuum solvation model[100] for both the geometry optimizations and as well as the energy evaluations.

Table 2.1: Optimized geometric parameters (Å) of Cs^+ and Sr^{2+} binding to FA for dispersion corrected def2-SV(P) (B1) and TZVP (B2) level using BP86 functional.

Basis set	Sr^{2+}-O_{FA}	Sr^{2+}-O_{water}	Cs^+-O_{FA}	Cs^+-O_{water}
B1	2.553, 3.528	2.521, 2.543, 2.561 2.598, 2.662, 3.678	3.258, 3.330	3.134, 3.174, 3.184, 3.243, 3.267, 3.362
B2	2.565, 3.595	2.545, 2.586, 2.593, 2.646, 2.686, 3.835	3.291, 3.356	3.230, 3.233, 3.246, 3.326, 3.341, 3.445

In these calculations, the dielectric constant (ε =80) of water is used to mimic the solvent effect as implemented in TURBOMOLE (TURBOMOLE V6.3 2011).[101] Harmonic frequency calculations are performed using the AOFORCE module to identify the species at minima and for thermodynamic properties. Thermodynamic quantities such as change of enthalpy (ΔH), entropy (ΔS), and Gibbs free energies (ΔG) for the complexation are derived from FREEH module.

Proton affinities of carboxylate functional groups of FA ($FA^{-1} + H_3O^+ \rightarrow FA + H_2O$) and subsequent ion binding energies (ΔE) of FA^{-1} with [$FA^{-1} + M(H_2O)_n^{+/2+} \rightarrow FA\text{-}M\text{-}(H_2O)_m^{0/+} + (H_2O)_k$ for M=Cs^+/Sr^{2+}] are calculated using the following equations.

$$\text{Proton affinity} = [E(FA) + E(H_2O)] - [E(FA^{-1}) + E(H_3O^+)], \tag{1}$$

$$\Delta E = \left(E[FA.M(H_2O)_m]^{0/+1} + E[(H_2O)_k]\right) - \left(E[FA^{-1}) + E[M(H_2O)_m]^{+/2+}\right) \tag{2}$$

where n and m are the number of water molecules in the metal-hydrate and FA-metal-water systems, repectively. k is the number of water molecules released during binding reaction. These numbers are evaluated through MD and subsequent DFT level calculations (discussed below). Further, Natural Population Analysis[102] (NPA) scheme is used to quantify the charge transfer from metal to FA and water molecules upon complexation. The effects of other density functionals on the computed binding energetics of the radionuclides to FA are carried out using ORCA 3.0 program package.[103]

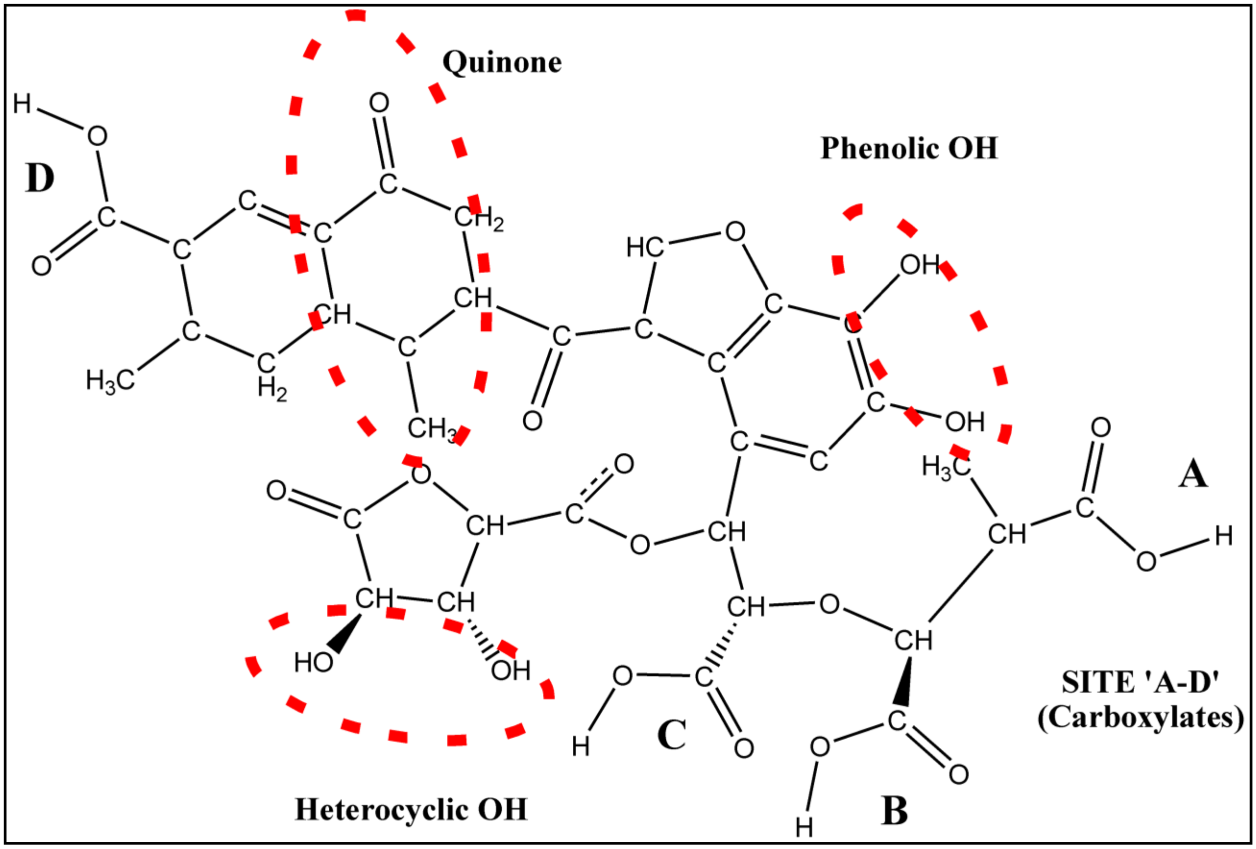

Figure 2.1: Model Structure of FA showing the presence of various functional groups.

MD Simulation. All MD simulations are carried out using GROMACS 4.5.4 package.[104] The required force field parameters of Cs$^+$ and Sr^{2+} ions are taken from Aqvist et al.[105] and Larentzos et al.,[106] respectively. Partial atomic charges are further modified using the charges derived from the NPA scheme. Force field parameters of FA are determined using ANTECHAMBER[107] module based on the General Amber Force Field (GAFF).[108] FA is solvated in a box of size $4\times4\times4$ nm^3 containing 2141 TIP3P[109] water molecules. FA is equilibrated after successive steps of energy minimization (steepest descent method) and position restrained simulations for 800 ps by allowing movement of water molecules around FA. The systems (FA, water and metal ion) are kept at a fixed temperature of 300 K via V-rescale thermostat.[110] For long range electrostatic interaction, Particle Mesh Ewald (PME)[111] sums are used, while LINCS algorithm[112] is followed to constrain bonds between hydrogen and the heavy atoms at their equilibrium lengths. For short range electrostatic and van der Waals interaction a cut off of 14 Å is applied. Finally, during 10 ns equilibration period, equation of motion is integrated with 2 fs time step. Purposefully, for the cation containing systems, cations are kept 8 Å away from the most preferable binding site of FA ensuring no interaction between them.[113] The equilibrated structures are then used as the starting configuration for MtD simulations (discussed below). Next we have carried out classical MD simulations for another 5 ns on the MtD extracted structures of the ion-FA complexes. The choice of cation bound FA structures for the final MD simulations is based on the free energy landscape obtained from MtD simulations.

In addition, conformational entropy is calculated based on well-known Schlitter's method,[114] which provides an approximate upper bound of conformational entropy S,

$$S < S_{Schlitter} = \frac{1}{2} k_B \ln det\left[1 + \frac{k_B T e^2}{\hbar^2} M\sigma\right]. \tag{3}$$

where, k_B is Bolzmann's constant, e is Euler's number, $\hbar$ is Planck's constant divided by 2π, T is absolute temperature, M is three dimensional diagonal matrix consisting of N atomic masses of solute atoms for which the entropy is calculated, σ is covariance matrix to take care of atom positional fluctuations and is represented by

$$\sigma_{ij} = \langle (x_i - \langle x_i \rangle)(x_j - \langle x_j \rangle) \rangle \tag{4}$$

where, x_i is the Cartesian coordinate of the atom i.

Metadynamics Simulation. We have employed MtD method[115] to enforce the migration of cation towards FA by adding into the potential well a time-dependent external biased potential (V_{MtD}) along a chosen set of collective variable (CV). V_{MtD} is a construct of Gaussian hills with height, H and width, w that are added at a time interval, τ_G so as to overcome the free energy barrier associated with local minima, which eventually leads to exploration of more configuration space in realtively short time. Finally, the resulted potential enables one to reconstruct the free energy landscape for the system without any prior assumption. Details of this method can be found elsewhere.[65] Two CVs, namely, hydration number of the ion and the distance of the ion with respect to the center of mass (COM) of the system are taken to construct two dimensional free energy surface (2D-FES) landscape. The rapid search of local minima in FES depends on the values of H and w. As experimental hydration energy of Sr^{2+} (-330 kcal mol^{-1}) is roughly six

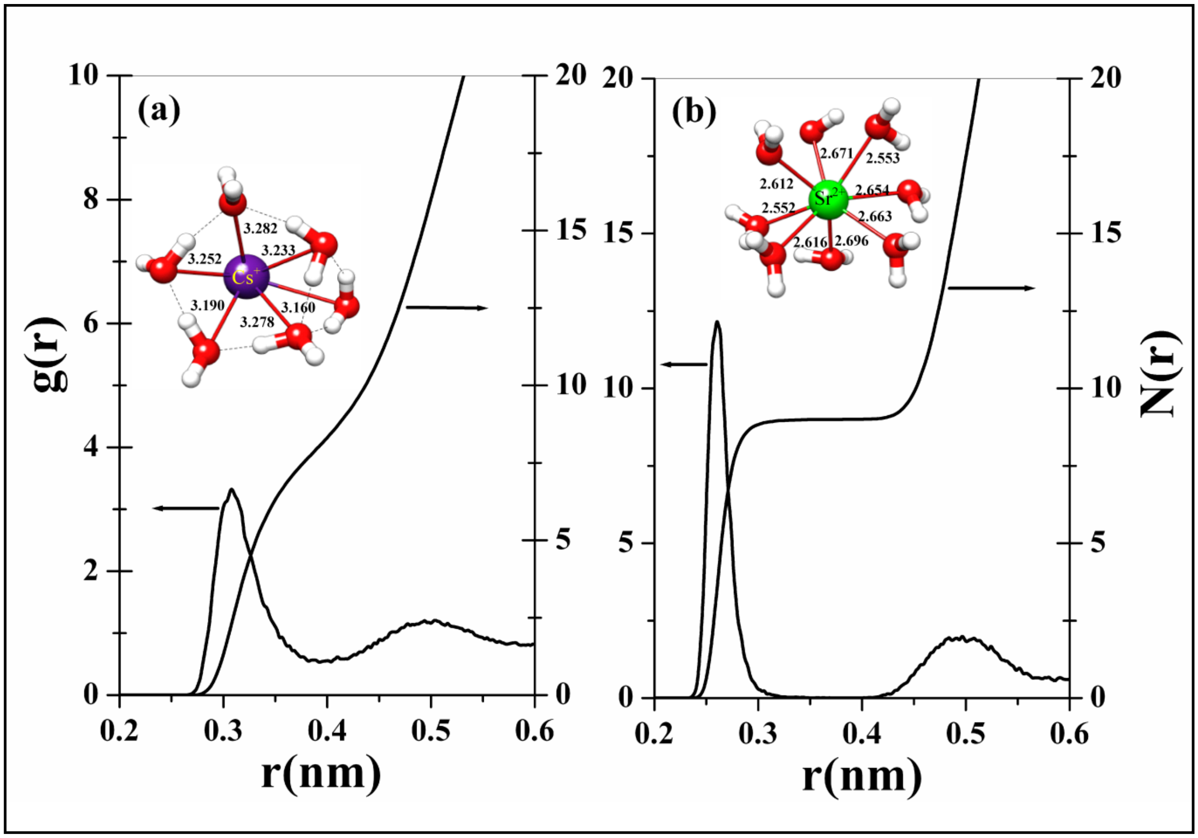

Figure 2.2: Radial distribution functions, $g(r)$ and corresponding integrals, $N(r)$ of (a) Cs^+ and (b) Sr^{2+} with respect to oxygen atom of water molecules. Structure of metal-hydrate systems as extracted from the plateau region of the $N(r)$ plots and optimized at BP86/def2-SV(P) level are shown in the inset.

times higher compare to Cs^+ (-59 kcal mol^{-1}),[116] smaller Gaussian height is applied for Cs^+ (0.05 kcal mol^{-1}) as compared to Sr^{2+} (0.1 kcal mol^{-1}), while Gaussian width (w) of 0.25 is used for both the cations. Gaussians are added after every ps. Finally, systems are subjected to production run of 100 ns with trajectories being saved every 1 ps for further analysis. FES profiles are explored from the deposited Gaussian. All MtD simulations are performed using PLUMED 1.3[117] patch to the GROMACS software package.

2.3. Results and Discussion

2.3.1. Solvation of Cs^+ and Sr^{2+} Ions

The hydration free energy of radionuclide ions plays a vital role for the effective binding of radionuclide with FA. Several experiments[118-121] and electronic structure calculations[12, 122-123] have predicted that the hydration number of Sr^{2+} and Cs^+ varies from six to eight water molecules. Particularly, Ali and co-workers[12, 123] have reported that eight water molecules can directly coordinate to Sr^{2+} , whereas partial solvation of up to six water molecules to Cs^+ is noted.

We have calculated the hydration number ($N(r)$) of both the cations using the radial distribution function (RDF) using equilibrium MD (Figure 2.2). The RDF profile for Sr^{2+} shows a sharp first peak at 2.62 Å and it is separated by depletion zone, confirming the stability of first hydration shell. In contrast to Sr^{2+} , RDF profile of Cs^+ indicates a relatively broad peak at 3.10 Å, which corresponds to closest Cs^+-O_{water} separation. Clearly, hydration shell around Cs^+ is relatively weaker. From the RDF profile we found that first hydration shell of Cs^+ and Sr^{2+} contains six and eight water molecules, respectively. Thus, while calculating ion binding free energies using Eq. (2), we took n =6 and 8 for Cs^+ and Sr^{2+} , repectively.

The hydrated metal ion structures [$Cs(H_2O)_6^+$ and $Sr(H_2O)_8^{2+}$] were extracted from the MD trajectories (after 10 nanoseconds of equilibrium period) and optimized them at the DFT level [(BP86/def2-SV(P)]. Optimized hydrated metal ions indicate that water molecules around Sr^{2+} are more rigid as compared to Cs^+ . Further, we find that water molecules around Cs^+ form an asymmetric hydrated structure[124] (Cs^+ -O_{water} - 3.160-3.282Å) whereas for Sr^{2+} , the water molecules remains strongly coordinated (Sr^{2+}-O_{water} - 2.552-2.696 Å) to ion (Figure 2.2). Our optimized radionuclide-water bond lengths are in excellent agreement with the previously reported computational study (Cs^+-O_{water} -3.25 Å,[125] Sr^{2+}-O_{water} -2.56-2.61 Å[12]) and with available XAFS data[121] (Sr^{2+} -O_{water} -2.60 Å).

Table 2.2: Computed hydration free energy (kcal mol^{-1}) of Cs^+ and Sr^{2+}.

Cation	Calculated	Exp. Value*
Cs^+	-47.1	-59.8
Sr^{2+}	-338.3	-330.1

***** Experimental values are taken from ref. no. 116

Further, the calculated hydration free energies for Cs^+ (-47.1 kcal mol^{-1}) is somewhat underestimated (by 10 kcal mol^{-1}) as compared to experimental data,[116] whereas for Sr^{2+} (-338.3 kcal mol -1), the calculated value is overestimated by 8 kcal mol^{-1} (Table 2.2). Nevertheless, our calculated hydration free energies of both the metals are observed to follow the experimental trend closely.

2.3.2. Structure and Proton Affinities of FA

As mentioned earlier, the chosen FA model has four carboxylic acid functional groups which are denoted as ‘A’, ‘B’, ‘C’ and ‘D’ (Figure 2.1). Our optimized geometric parameters for the functional groups in the FA model are closer to the experimental data.[126-127]

Table 2.3: Computed vibrational frequency (υ_{asym}) of neutral FA model.

Functional Groups of FA	Calculated Frequency (cm^{-1})	Exp^* (cm^{-1})
C=O (SITE A, SITE B, SITE C, SITE D) of COOH	1740, 1809, 1770, 1764	1718
Quinone	1716	-
Phe-OH	3146, 3461	-
Het-OH	3356, 3461	-
C-OH (SITE A, SITE B, SITE C, SITE D) of COOH	3237, 3446, 3472, 3469	3372
Carboxylic (C-O, O-H)	1372, 1378, 1392	1395

***** Experimental values are taken from ref. no. [128]

The computed asymmetric stretching frequencies (ν_{asym}) for the various functional groups present in FA are comparable to experimental IR data (Table 2.3).[128]

The pKa of the carboxylic acid functional group varies from 2-4 in FA at physiological pH.[7] Thus at neutral pH range, the carboxylic acid group is expected to deprotonate first as compared to hydroxyl functional group (pKa = 6-8).

Table 2.4: Calculated proton affinities and relative energies (kcal mol^{-1}) of FA at different deprotonated states.

FA	Proton affinity	Relative Energy
FA (A)	-34.1	+2.43
FA (B)	-36.3	+4.56
FA (C)	-31.7	0.00
FA (D)	-36.9	+5.42

Single deprotonation of carboxylic acid groups at various sites led to four anionic FA models, denoted by FA(N), where N refer to various deprotonated carboxylate site i.e. A-D in Figure 2.1. Notably, the four carboxylic groups of FA do not have the same chemical environment. Proton affinity values presented in Table 2.4 show that among the four possible deprotonated sites, we find that FA(C) is the most stable structure [by 5 kcal mol^{-1} with respect to FA(D)]. In FA (C) structure, the negative charge of carboxylate 'C' group is delocalized due to the presence of electronegative ether group near to it. It is evident from the structure in Figure 2.1 that the nearby heterocyclic OH group interacts strongly *via* hydrogen bonding (1.49 Å) with the deprotonated carboxylate group. The negative charges created by deprotonating at sites 'B' or 'D' sites is not stabilized by the neighboring groups as compared to 'C' or 'A' site. Thus, the calculated relative energies follows the order, FA(C) > FA(A) > FA(B) > FA(D), which are consistent with the experimental observation of Leenheer et al.[7] (Table 2.4). Similar to relative energetics, our calculated proton affinity of different deprotonated structures also suggest 'C' site in FA is the most stable structure having the lowest proton affinity value (-31.70 kcal mol^{-1}). Thus at physiological pH (pH=7), the FA(C) site remains deprotonated, which can bind Cs$^+$ or Sr^{2+} radionuclide. Hereafter, for simplicity, FA(C) will be represented as FA.

2.3.3. Binding of Radionuclides to FA

Below we first obtain the possible structure of FA bound radionuclide ions in explicit water solvent through the search of local minima of ion-FA interacting system using metadynamics siumulation. The structures deduced from MtD simulation is then utilized in equlibrium MD simulation and DFT calculation in order to shed light into the differential binding of the two ions with FA.

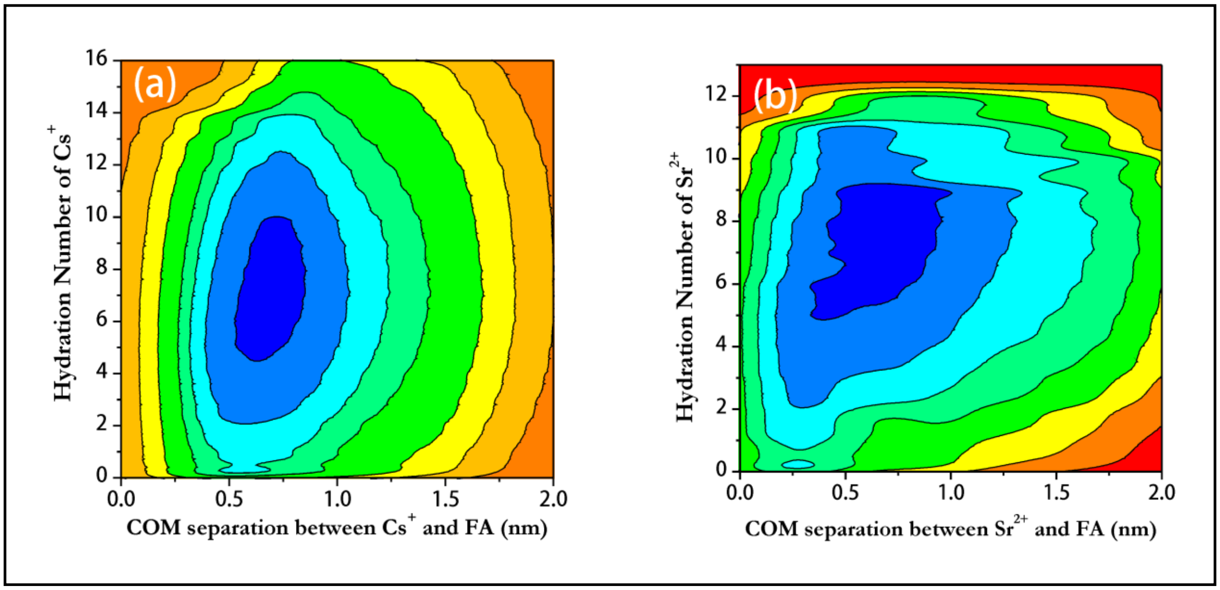

Figure 2.3: Free energy landscapes of (a) Cs-FA and (b) Sr-FA complexes obtained from MtD simulations are shown. Free energy is plotted as a function of hydration number of the ions and their separation from the centre of mass (COM) of the binding site ‘C’ of FA. Energy increases from blue to red in the free energy landscape. Cation bound FA structures are extracted from the energy minima and are further subjected to MD and QM calculations.

MtD Simulation

A 100 ns MtD simulation trajectory reveal that Cs$^+$ is dominantly found near the bulk water at a distance of 6-7 Å from the ‘C’ site of FA. However, Cs$^+$, intermittently for short duration of time is also found nearby carboxylate and heterocyclic OH binding sites of FA (Figure 2.4). In the FES plot presented in Figure 2.3, we find a broad blue region around 6 Å away from the 'C' site of FA indicating a global minima away from FA. This suggests that interaction of Cs^+ with FA is rather weak and water-FA interaction dominates over Cs^+-FA interaction. In contrary, Sr^{2+} is frequently observed to come closer and remain bound to FA for longer duration (5-10 ns, Figure 2.4) resulting in the formation of free energy minimum near to FA. For Sr^{2+} , the local minima is tilted towards the carboxylate of FA, suggesting the interaction is strong with FA.

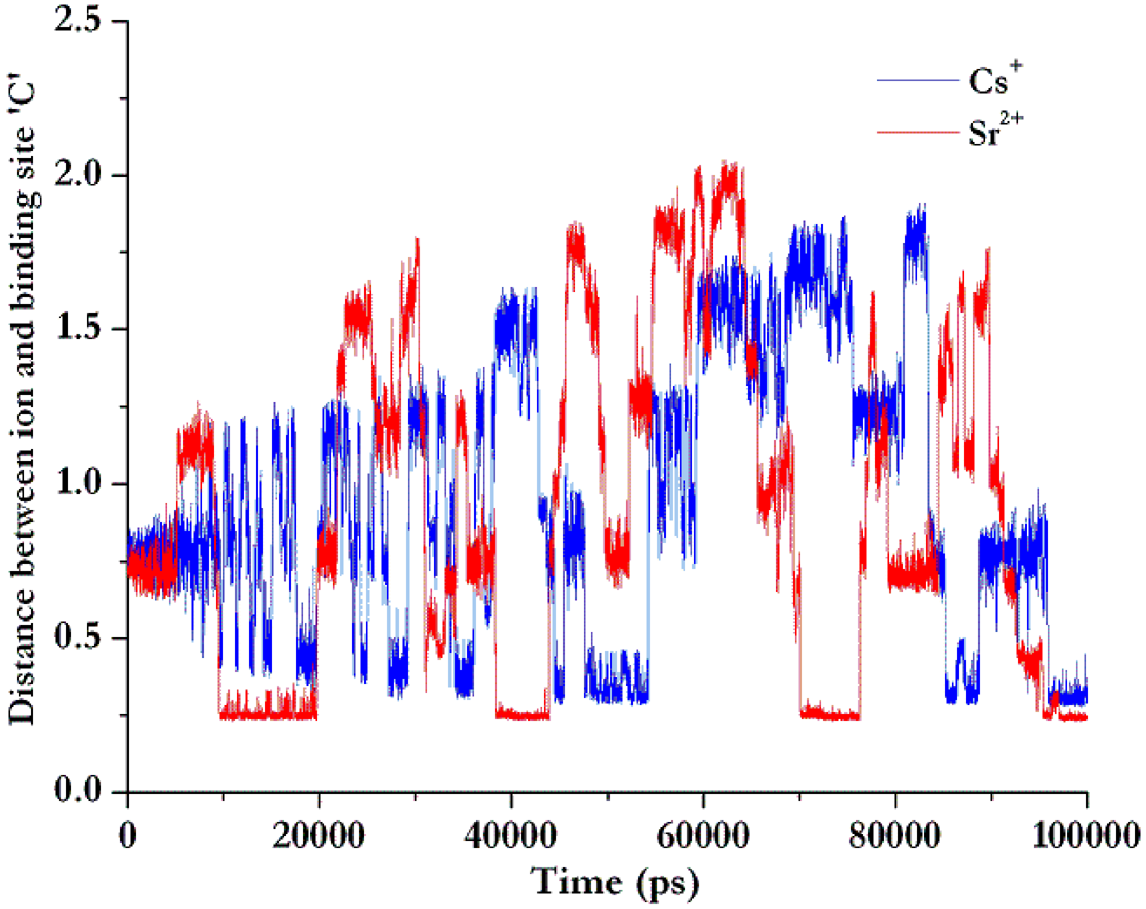

Figure 2.4: Plot of COM separation between ion and Site 'C' (nm) with respect to time (ps) for MtD simulation.

To understand the nature of binding pattern and mechanism, we have analyzed the individual interactions of the two radionuclides with FA and water. The change of average interaction energy with respect to COM separation between radionuclide ions and FA are shown in Figure 2.5. It is quite evident that all three components (ion-water, water-FA and ion-FA) contribute to the average interaction energy significantly. As Sr^{2+} approaches to the 'C' site of FA, the Sr^{2+}-water and FA-water interaction energy decreases (becomes more positive), which is compensated by the favorable interaction energy between FA-Sr^{2+} (more negative). These are largely due to the shedding of water molecules from solvation shells of ion and FA, which gives rise to less negative interaction energy for Sr^{2+} -water system.

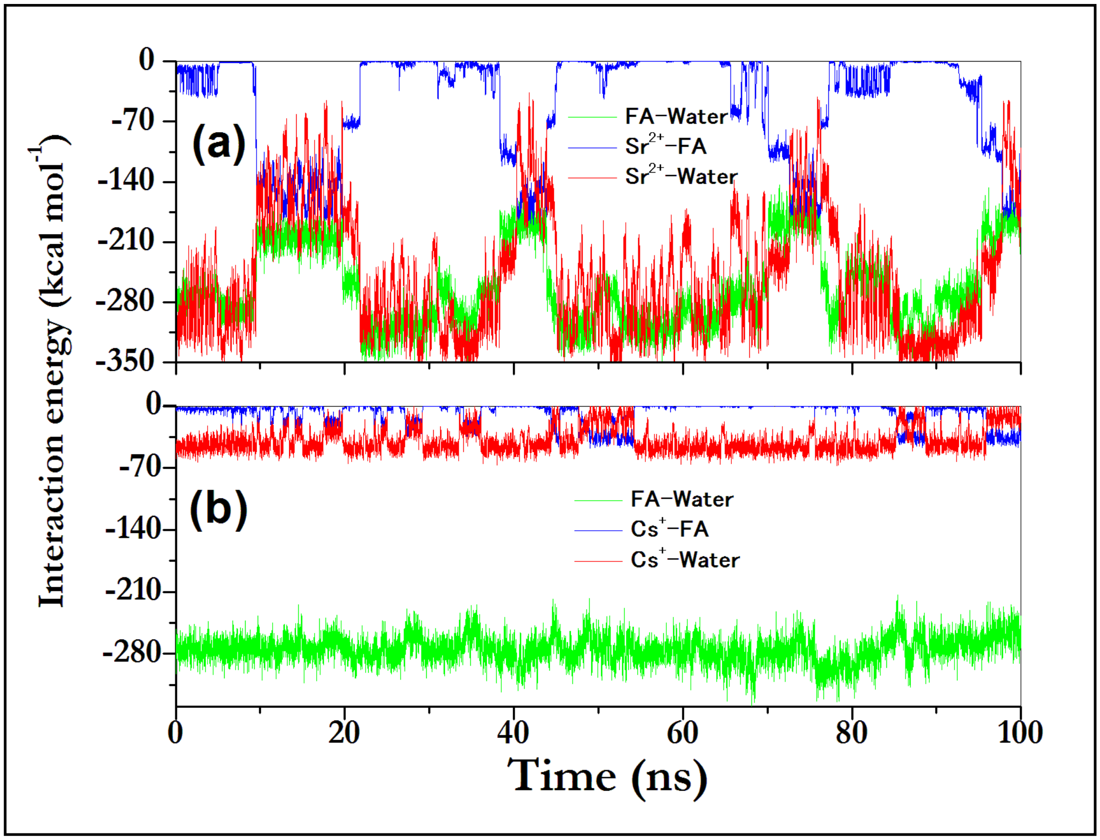

Figure 2.5: Interaction energies for (a) Sr^{2+} and (b) Cs^{+} during 100 ns MtD simulations. Ion-water, ion-FA and FA-water interaction energies are indicated in red, blue and green color respectively.

Due to the smaller hydration energy of Cs^{+} (-59 kcal mol^{-1}), the shedding of water molecules is more facile as compared to Sr^{2+}. Thus, Cs^{+} is expected to bind FA strongly. However, FA-water interaction energy (-280 kcal mol^{-1}) is much stronger as compared to Cs^{+}-FA interaction energy. This leads to weak binding of Cs^+ to FA. On the other hand, Sr^{2+}-water and FA-water interaction energies are comparable to each other. Consequently, Sr^{2+} can break the FA-water interaction in order to bind favorably with FA.

MD Simulation

Our MtD simulations suggest that Cs^+ is expected to get diffused at the bulk as compared to Sr^{2+}. In order to evaluate the binding affinities of both the radionuclides towards FA, frequently visited configurations are extracted from MtD trajectory where cations are found to be bound to FA. A 5 ns equilibrium MD simulation is carried out on these cation bound FA structures. Note that neighboring hydroxo groups also interact strongly, which influences the binding of ions to FA.

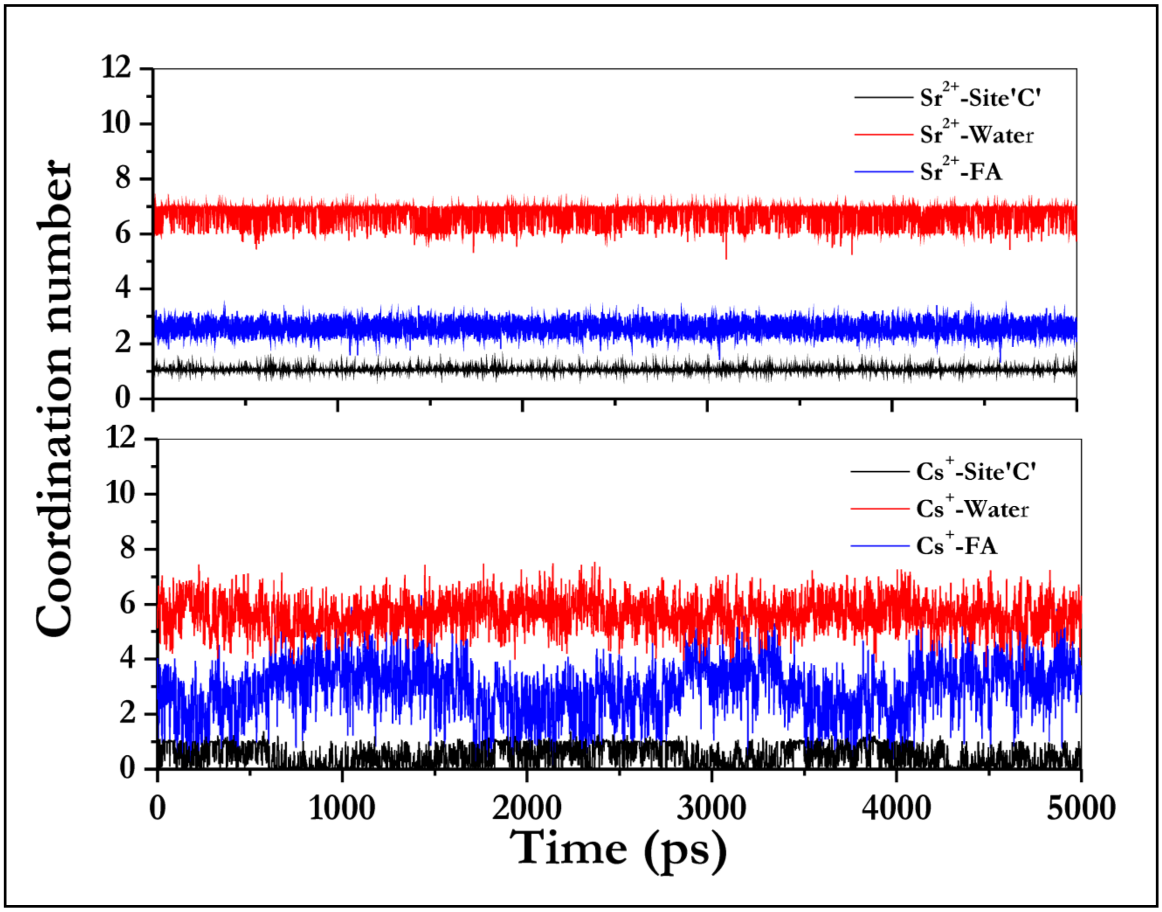

Figure 2.6: Coordination number for (a) Sr^{2+} and (b) Cs^+ as a function of time (ps) during equilibrium MD simulation of MtD extracted FA-ion-water complexes. Ion-Water, ion-FA and ion-site ‘C’ coordination numbers are shown in red, blue and black respectively.

To quantify the overall contribution of FA, water and site ‘C’ interacting with the ions, the coordination number (CN) of the ions to these chelating agents are plotted with respect to time (ps) in Figure 2.6. We have considered the primary coordination shell radius of Cs^+ to be 3.10 Å and of Sr^{2+} to be 2.62 Å for the simulation. Throughout the simulation, Sr^{2+} hydration number varies from six to seven, whereas for Cs^+ , it fluctuates between four to six (red line in Figure 2.6). Furthermore, the carboxylate at site C is mono-dentate for both Sr^{2+} and Cs^+ ion (black line in Figure 2.6). While calculating ion binding free energies using Eq. (2), however, we took m =6 for both the cations, Cs^+ and Sr^{2+} . Note that the value of k in equation (2) is now determined as 0 (for Cs^+) and 2 (for Sr^{2+}).

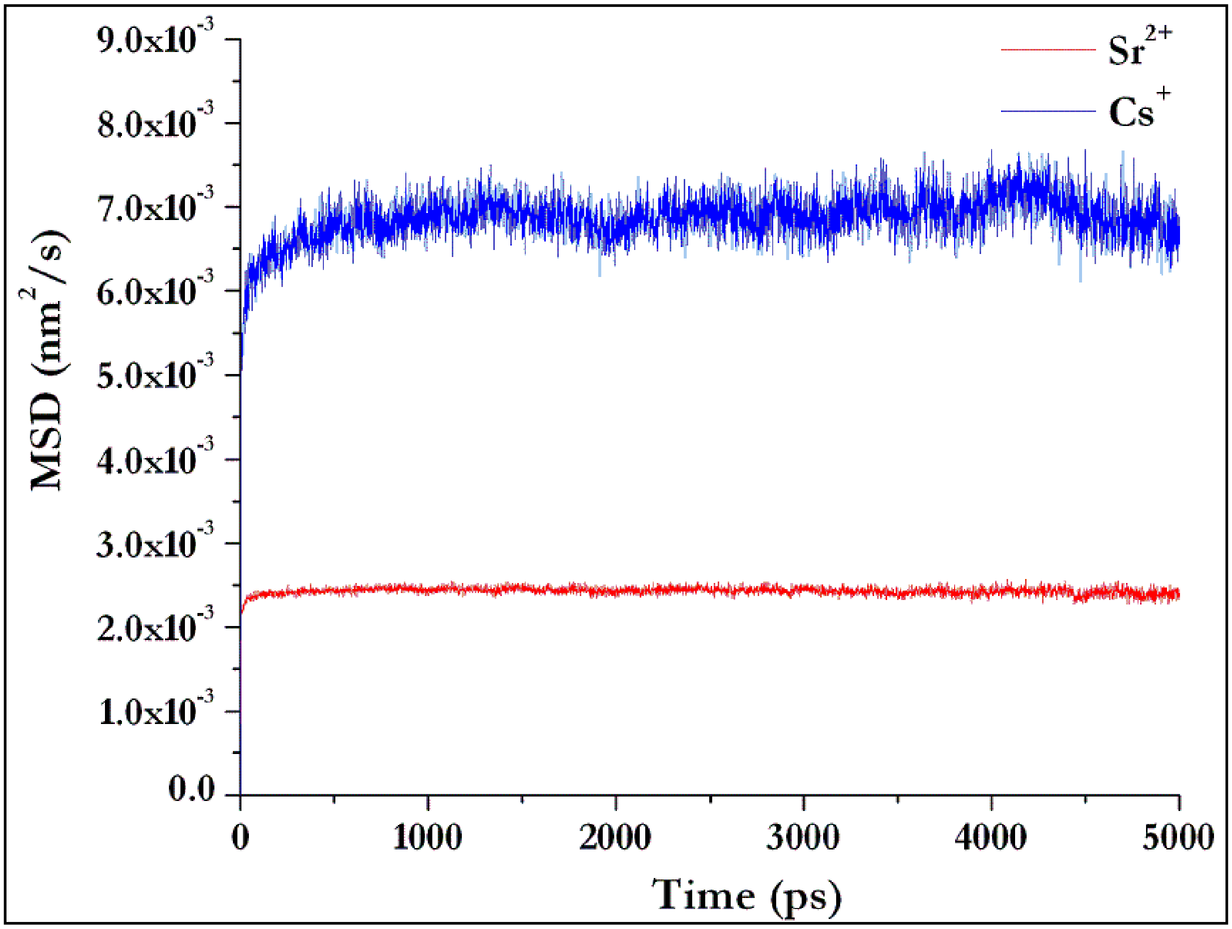

Figure 2.7: Mean square displacement (MSD) of the ions in FA-water system *vs* Time (ps) during equilibrium MD simulation.

In Figure 2.6, due to the influence of neighboring hydroxo group, the CN varies from 1 to 5 for Cs^+ whereas, it is 2-3 for Sr^{2+} (blue line). It is important to mention here that such neighboring group participation could not be observed in the "small" models[18] containing isolated functional group. Further, to assess the diffusiveness of both the metals in the FA-water system, we have calculated the mean square displacement (MSD) of the ions and found that MSD of Cs^+ is three times higher as compared to Sr^{2+} (Figure 2.7). These variations confirm the higher mobility of Cs^+ as compared to Sr^{2+}. The favorable binding of radionuclides to FA in the presence of water molecules often depend on entropic factors, where loss of conformational entropy upon interaction leads to unfavorable binding.

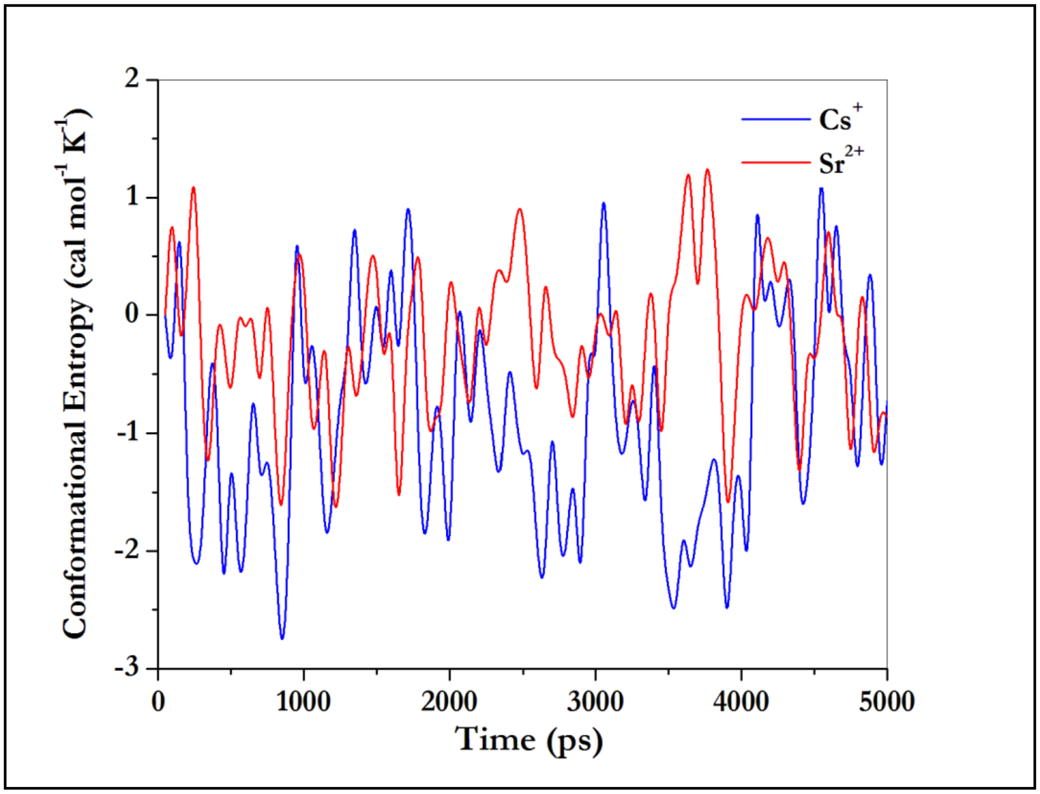

Figure 2.8: Conformational entropy *vs.* time plot from 5 ns equilibrium run of MtD extracted FA-ion complexes in the presence of water.

Figure 2.8 shows the calculated conformational entropy. Clearly, Cs-FA system exhibits relaltively larger negative entropy values. This is due to favorable FA-water interaction and weak hydration shell of Cs^+ . On the other hand, for Sr-FA system, the change of conformational entropy is minimal and fluctuates from -1 to 1 cal $mol^{-1}K^{-1}$.

DFT Calculation

Figure 2.9 represents the optimized structures extracted from the MtD trajectory at the BP86/def2-SV(P) level. In our optimized structures, we find that Cs^+ interact weakly at the deprotonated site of FA, which is consistent with our MtD and MD simulations. Furthermore, the water molecules are hydrogen bonded (1.63-1.84 Å) with each other and with FA carboxylate functional groups (1.62-1.78 Å). We also find nearby functional groups interact strongly with Cs^+ ($Cs\text{-}O_{ether}$ = 3.177 Å, $Cs\text{-}O_{Het}$ = 3.102 Å) which led to asymmetric bi-dentate binding motif for $Cs\text{-}O_{COO}$ (3.258-3.330 Å). In Cs^+-FA adduct, some of the the Cs^+ -H_2O bond length are found to be elongated as compared to the bare Cs^+ -hydrate structure.

In the case of strontium, an asymmetric monodentate binding motif is noticed for Sr^{2+} -O COO (2.533 Å, 3.528 Å) due to the strong interaction with oxygen of heterocyclic OH functional group (2.513 Å). However, in contrast to Cs^+ binding to FA, water molecules do not solvate the proximal functional groups of FA and mostly remain firmly held by the Sr^{2+} (2.521 Å). This is probably due to the strong hydration energy of Sr^{2+} as compared to Cs^+ , which restricts the mobility of water molecules.

Thermodynamic quantities for the ion-FA systems are presented in Table 2.5. Similar to MD study, binding free energy for Cs^+ with FA are found to be unfavorable (ΔG= +3.88 kcal mol^{-1}) whereas, the binding of Sr^{2+} with FA is favorable (-10.40 kcal mol^{-1}). Noticeably, similar formation enthalpies (ΔH) are obtained for both the reactions (-15 kcal mol^{-1}). However, incorporation of entropy effect leads to unfavorable binding of Cs^+ . Thus Cs-FA complexation is entropy driven while Sr-FA complexation is enthalpy driven.

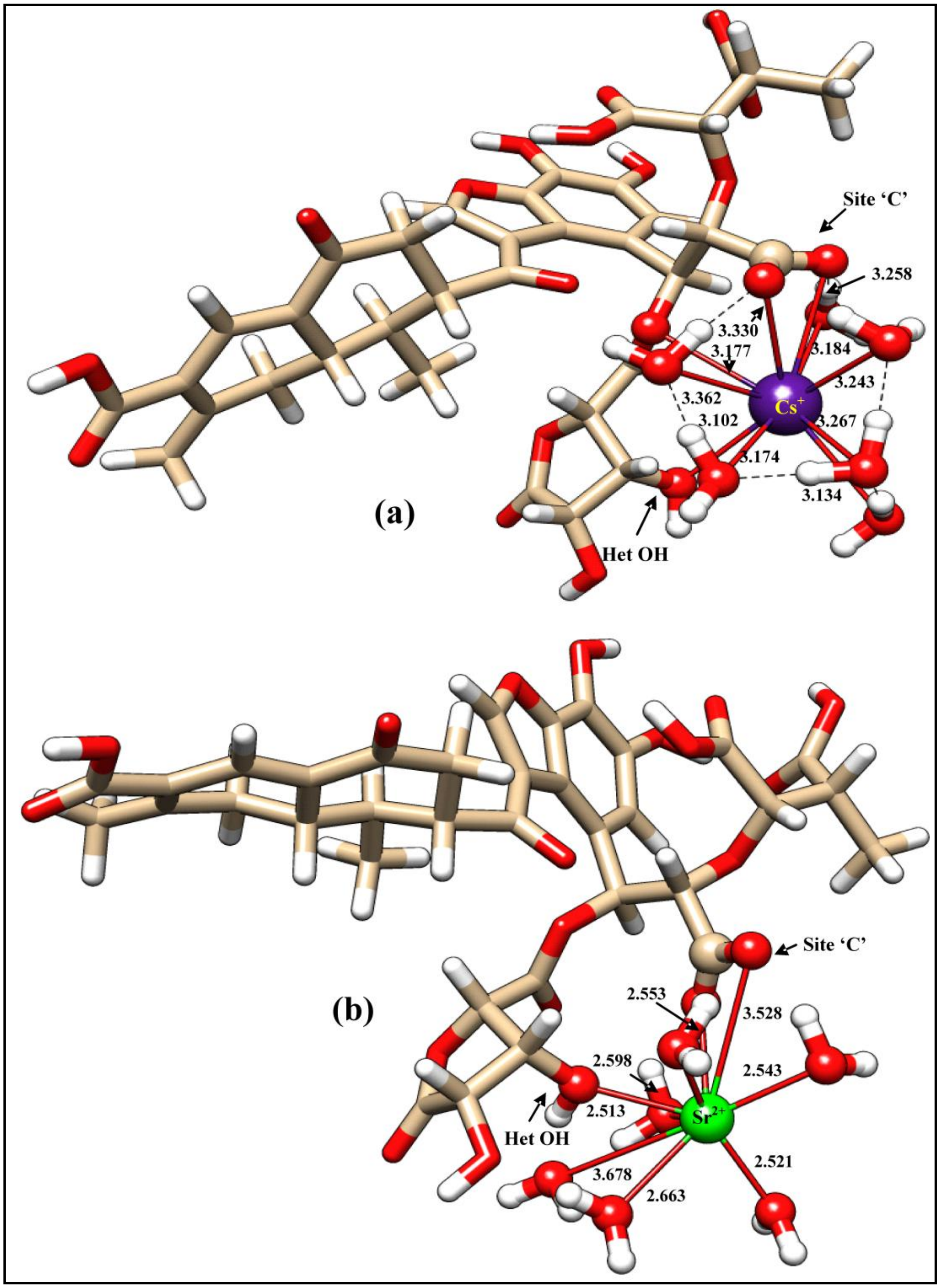

Figure 2.9: Optimized structure of (a) Cs^+ and (b) Sr^{2+} binding to FA at the ‘C’ site. Active site coordination and the secondary interactions with FA and water are shown in ball and sticks, whereas the remaining atoms are shown in ball and stick frame.

Further, the origin of differential binding affinities of the radionuclide cations to FA can be correlated to the extent of charge transfer (Table 2.6) from the radionuclides to FA. We find that the net charge transfer (derived from NPA scheme) from FA to Cs^+ is very small (by : 0.05 a.u) as compared to Sr^{2+} (by 0.13 a.u) to FA. Interestingly, coordinating water molecules of Cs^+ are found to be strongly involved in hydrogen bonding with each other and with FA that lead to significantly different charge transfer value (-0.14 a.u) as compared to water molecules around Sr^{2+} (0.02 a.u) (Figure 2.9). As mentioned earlier, this can be attributed to the smaller hydration energy of Cs^+.

Table 2.5: Thermodynamic quantities (kcal mol^{-1}) of optimized metal-FA complexes in FA(C) model.

Model	Ion	ΔH	TΔS	ΔG
FA (C)	Cs^+	-15.32	-19.20	+3.88
	Sr^{2+}	-15.50	-5.10	-10.40

Table 2.6: Natural population analysis of metal-FA complexes.

Systems	Charge transfer (Δq)		
	Cs/Sr	FA	6WAT
Cs-FA	0.050	-0.193	-0.142
Sr-FA	0.127	-0.111	0.016

Finally, we have also calculated the binding energies for both the cations with different density functional (DFs), such as, M06-2X, M06L and B97-D3, using optimized structures. Indeed, all DFs predict Cs^+ binding is unfavorable whereas Sr^{2+} binding is largely favorable (Table 2.6). These scrupulous investigations on various aspects lead us to conclude that Cs^+ interacts with FA in an outer sphere binding mechanism whereas Sr^{2+} binds with FA via outer sphere binding motif.

Table 2.7: Binding energy (kcal mol^{-1}) of Metal-FA complexes at various density functional levels.

System	Density Functional (DF)			
	M06-2X	M06-L	B97-D3	B3LYP-D3
Cs-FA	+4.64	+3.84	+5.58	+0.76
Sr-FA	-8.75	-11.47	-11.25	-12.04

2.4. Synergy with Experiments

The molecular level understanding of the speciation of radionuclide Cs^+ and Sr^{2+} cations are investigated through several experimental techniques. Our investigations have addressed various such features, which nicely correlate with the experimental results.

Helal et al.[73] reported that Cs^+ does not form any adduct with FA, whereas Xu et al.[83] reported that only minimal changes are observed in the ^{133}Cs chemical shift in the presence of natural organic matter. These studies indicate that Cs^+ interaction with FA is rather weak. In our combined QM, MD and MtD simulations, we find that the Cs^+ interaction with FA is unfavorable ($E(Cs^+)$ =4 kcal mol^{-1}), largely due to entropic reasons. Further, the FA-water interactions (-280 kcal mol^{-1}) are very strong as compared to Cs-water (-59 kcal mol^{-1}). These findings led us to conclude that Cs binds to FA through outer sphere mechanism, where the bound water molecules to Cs^+ are interacting with the FA. Thus to form the stable complex with Cs^+ , water concentration in soil plays a vital role in geochemical environment. For the case of Sr^{2+} and other alkaline earth metal ions such as Ca^{2+} , experimental studies[84, 129] predict strong binding to FA and enthalpy may be the dominant factor.[130] Indeed our calculations predict that Sr^{2+} binding to FA is very strong due to favorable enthalpy factors. Furthermore, the Sr^{2+} cation directly bind with the functional groups of FA which led us to propose an inner sphere complexation. Although the hydration energy of Sr^{2+} is very large (-330 kcal mol^{-1}), the electrostatic interaction between FA and Sr^{2+} is responsible for the favorable binding of Sr^{2+} to FA. A similar inner sphere binding is also proposed for uranyl binding to HA and FA recently by us.[13]

2.5. Conclusion

The speciation and interactions of radionuclides in SOM are important to understand their migration and transport[131-132] into various living organisms such as plants and aquatic species. We have addressed this issue using a variety of tools such as MtD, MD simulations and DFT based calculations. Our investigations predict that Cs^+ interacts with SOM through outer sphere pathway and the water molecules plays a vital role for the weak binding of Cs^+ to FA. Thus the increase of water content in soil might lead to Cs^+ being weakly coordinated to FA due to dominant water-FA interactions and form an outer sphere complex. This binding is energetically unfavorable due to negative entropic contribution, thus the complex formation is entropy driven process. For Sr^{2+} -FA complex, Sr^{2+} interaction with FA is observed to be favorable because of two contributing factors. Due to high charge by radius ratio, its interaction with functional groups such as carboxylate and hydroxyls is much stronger than that of Cs^+ . This also assists to overcome favorable water-FA interaction via an inner sphere binding motif. Secondly, contrary to Cs^+ -FA system, entropy plays a minor role, thus complex formation is enthalpy driven and hence energetically favorable. As an important conclusion, the observed binding mechanism of both the radionuclides provides probable explanations on the availability of these radionuclides in soil solutions. In presence of organic matter as the interacting media, we thus expect Cs^+ to remain more mobile and available as compared to Sr^{2+} for further plant uptake or subsequent reactions with mineral layers.[133-137] Hence, SOM can selectively bind Sr^{2+} in the presence of competing radionuclide Cs^+. Here, it is important to emphasize that our study does not deal with the effects of competitive binding of other cations like K^+ , Ca^{2+} or the binding via multiple ligands simultaneously, which will certainly complicate the binding mechanism.

CHAPTER –3

Permeation of Cesium and Other Monovalent Ions Through Non-selective NaK Ion Channel of Soil Dwelling Bacteria

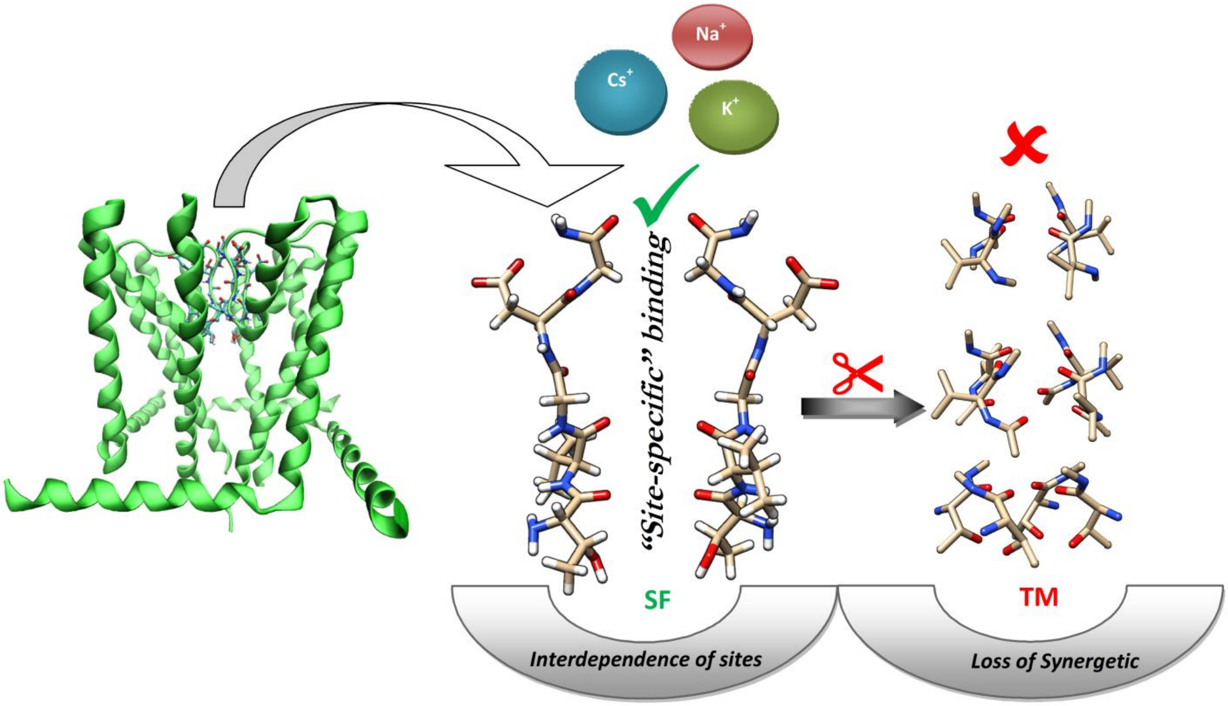

3.1. Introduction

Once deposited into soil, radionuclide such as ^{137}Cs and ^{90}Sr interacts with various soil components. As discussed in Chapter 2, SOM-water mixture present in the soil strongly modulate the migration of ^{137}Cs and ^{90}Sr. Apart from SOM, microorganisms such as bacteria are also ubiquitous to soil. In bacteria, the translocation of elements such as Na^+ and K^+ from extra cellular surface to the internal cell surface is achieved by its own ion transporting systems, like ion channels. There are reports, which suggest that several ion channels can be used as a transport route for Cs^+ to enter into the biological life cycle.[51] In this chapter, we aim to investigate the possibility/favoribility of cesium translocation in comparison to Na^+ and K^+ in a nonselective ion permeating channel using multiscale modeling techniques.

Ion permeating channels are pore forming transmembrane protein[138], which play critical roles for the transmission of nerve impulse and controls several biochemical processes such as regulating cardiac,[138] skeletal[139] and muscle contraction.[140] The salient feature of various ion channels is their striking ion selectivity. For example, potassium channel (K^+ channel) has a distinct quality of selecting K^+ in presence of Na^+ at a ratio of 1000:1,[138] in spite of their same valence and miniscule difference in ionic radii (0.36 Å). In recent years, several crystal structures of various ion channels have been reported.[141-145] All ion channels have a specific structural sequence in their selectivity filter (SF), which discriminately mediates the translocation of ions. For instance, K^+ channels are known to preserve a structural signature sequence of $_{75}TVGYG_{79}$ in their SF. The backbone carbonyl ligands of these five residues along with the hydroxyl group from T75 create four contiguous and chemically equivalent K^+ binding sites, selectively permeating K^+ over Na^+ .[146-148]

Recently, Shi et al.[149] determined the crystal structures of a new class of ion channel namely, NaK ion channel from *Bacillus cereus*. The structure of NaK channel comprises of four subunits arranged in four fold symmetric fashion to create a pore at the centre. Each subunit is composed of outer and inner transmembrane helices, namely M1 and M2, which is connected to each other by a re-entrant loop or pore helice. SF with a structural sequence $_{63}$TVGDG$_{67}$ (Figure 3.1) is a construct of the loop. Note that the functional groups (carbonyl, carboxylate and hydroxyl groups) of the five residues can possibly create five binding sites. However, out of these amino acids, carboxylate group of D66 points outside the pore axis and carbonyl group of G65 and D66 remain tangential to the pore axis.[150] Hence G65 and D66 practically do not bind to the metal center during the ion translocation, which eventually make the total number of binding sites equal to four. The amino acid sequence in the SF of NaK shows strong resemblance with that of the K^+ channel (TVG$\underline{\text{Y}}$G) except that tyrosine (Y) is now replaced by acidic aspartate (D) residue.

Ever since the nonselective nature of NaK is known, a plethora of activities began,[148, 150-159] all aimed at deciphering the root reason behind nonselectivity, because that could serve as a testbed for the different mechanisms proposed towards explaining selectivity in ion discriminating channels. While lingering over the years, our understanding on the selectivity issues of tetrameric channels has advanced and became more matured,[148, 160-161] Some debetable issues began to crop up recently to explain the “nonselectivity” occuring in NaK channel. Available experimental structures on wild type and engineered NaK channel suggest that site S3 is most nonselective[150] and three binding sites in place of four (as they are in selective K + channel)[148] causes the loss of its discriminating character. The latter observation is further substantiated by potential of mean force (PMF) calculation of the ion translocation through the SF of engineered NaK channel.[156] Computational studies on the nonselectivity of NaK channel entreat a variety of concepts: hydration number (HN), variable metal-protein ligand coordination number (CN), ratio of HN and CN of the permeating cations, water containing vestibule that disrupts the protein SF matrix causing planes of carbonyl oxygen to dislocate, flexibility of the dynamical hydration valve in the vestibular region, presence of hydrogen bond (HB) between D66 and N68.[151-155, 159, 162]

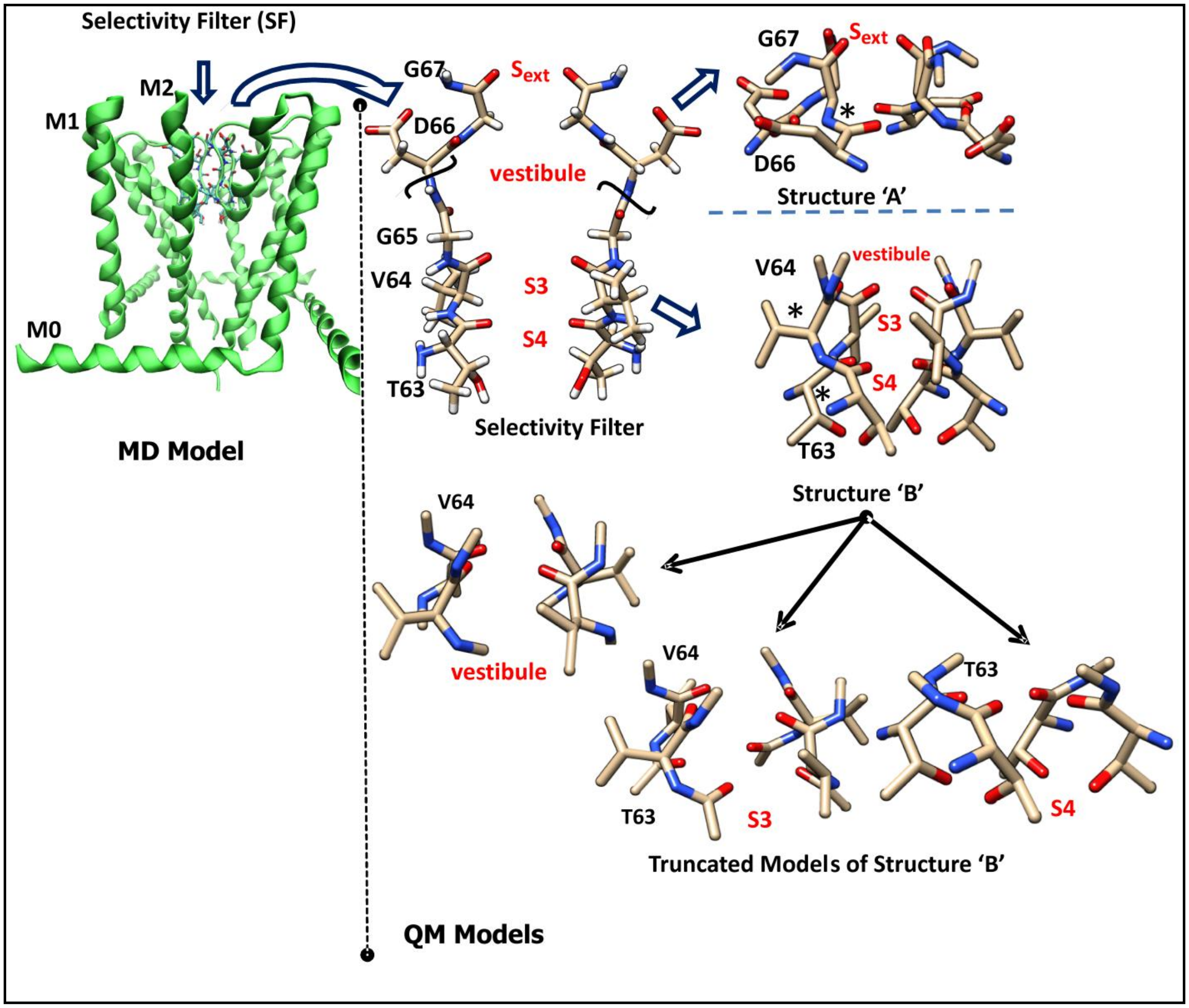

Figure 3.1: NaK ion channel and its different binding sites in the selectivity filter (SF) are shown. Color schemes used are: yellow, C; blue, N; red, O; grey, H. Left panel shows ribbon presentation of the tetrameric channel helix. The signature sequence, $_{63}$TVGDG$_{67}$ forming the SF is presented in licorice representation. During all-atom molecular dynamics (MD) simulation the entire tetraameric channel is used. Right panel shows the zoomed view of the SF and its various binding sites. Realistic models of the SF binding sites, structure 'A' and structure 'B' that has been utilized to perform DFT calculations are shown. Structure 'B' is further truncated (in the truncated model, TM) into stand-alone binding sites: vestibule, S3 and S4 in order to study the ion binding characteristic in isolation. Selected C$\boldsymbol{\alpha}$ atoms, shown with asterisk mark in the model structures, 'A' and 'B' are physically constrained in order to preserve the optimum pore radius (see methods below). For clarity reason hydrogen atoms are not shown in case of structure 'A', 'B' and truncated models of structure 'B'.

Although nonselectivity is the hallmark of NaK channel, that does not renders to same permeability of all alkali metal ions. Structural investigations led by Alam et al.[150] revealed that Na^+ , K^+ , Rb^+ ions have their affinity towards specific binding sites of SF. In line with this, several computational studies also observed significantly different free energy barrier favoring higher permeability of K^+ than Na^+.[152, 154-155]

The above background of our current understanding on monovalent ion permeation raises one intriguing conundrum: the ‘site-specific’ selectivity in the ‘nonselective’ SF of NaK channel. Herein, we address this issue by elucidating the structure, binding and translocation behavior of ions through the NaK channel, covering the utmost interesting physiological and thermodynamic aspects that influences the site specifity, through a combination of quantum mechanical and classical mechanics simulations. In the process, we also aim to address the outstanding issue of cesium migration *via* ion channel route. In this investigation we have used density functional theoretical (DFT) approach on realistic model of NaK SF to determine the origin of site-specific ion selectivity, while metadynamics (MtD) based molecular dynamics (MD) simulations were performed to construct the PMF profiles of the translocating ions in the wild NaK channel.[149] The use of synthetic toy models resembling the binding sites of ion channel often lead to valuable insights.[160-161] However, as we present in this Chapter in the case of NaK channel, use of further truncated model (TM) (considering only one binding site at a time), derived from our realistic QM model (cf. Figure 3.1), can lead to erroneous conclusion and fail to capture the the synergetics of contiguous binding sites (such as treating S3 and S4 together), in accordance with experimental observation.[148] Finally, we focus to arrive at a clearer picture on the process of site-specific binding and translocation using the combined results of DFT and MtD-MD based calculations.

3.2. Computational Details

3.2.1. Quantum Mechanical Study

Model Structures. The published crystal structure of WT NaK contains two subunits, which were duplicated to create a functional tetrameric channel and is available from the potassium channel database (KDB).[163] Before the QM calculations were intitiated, we have performed a 10ns long equilibrium MD simulation (see below). The last frame of this MD trajectory can be thought to represent an equilibrated structure of NaK channel. The starting structures for QM calculations were built from equilibrated structure of NaK ion channel by extracting the five SF residues (namely, T63, V64, G65, D66 and G67) from each of the four subunits. The resulting structure with all four probable binding sites representing the full SF, consists of more than 270 atoms. Performing QM calculations on such gigantic systems is highly expensive. Thus, to optimize the computational expensiveness, the structure was truncated in between D66 and G65 (Figure 3.1). This leads to two model structures (A and B) with different binding sites. Structure ‘A’, is composed of G67 and D66 residues, consists only one binding site for cation i.e. external entrance or S ext , whereas structure ‘B’ contains remaining sites namely vestibule, S3 and S4. Further, structure ‘A’ and ‘B’ was modified at the peptide junction by substituting the CO-NH- group with -CONH(CH_3) in order to avoid unreasonable hydrogen bond formation among the nearby subunits that could have caused filter’s structural distortion.

The truncated structures are not *adhoc* and can be justified by the following reasons. (1) Previous structural investigations[149-150, 164] predict that the binding of cation at the external entrance (S ext) is mediated only by the carbonyl group of G67 residue. Notably, presence of hydrogen bond between the negatively charged carboxylate group of D66 and the amide hydrogen of G67-N68 backbone helps to make the entrance rigid, which in turn maintains structural integrity. As our model structure for S ext contains -CONH(CH_3) (representing N68 side chain) at the terminal of G67 residue, it preserves the “through space” interaction,[150] naturally occuring inside the NaK SF. (2) The size of next possible binding site, vestibule, formed by carbonyl group of V64, is wide enough to accommodate three to four water molecules, where the permeating cation can easily get diffused away. As mentioned earlier D66 does not play any role in cation binding at vestibule region. (3) Unlike S_{ext} , carbonyl groups of V64 and T63 residues together form S3. Although, the structural consideration indicates that binding at vestibule and S4 requires involvement of only one residue (V64 for vestibule; T63 for S4), the cation binding at both the sites indirectly gets affected by other connected consecutive binding sites, either because of conformational rearrangement, or by the presence of other cations. To this end, in order to study the synergistic effects of contiguous binding sites, structure 'B' was further truncated to form small synthetic models (denoted as TM), each containing only one binding site i.e., vestibule, S3 and S4. The isolated binding sites of the TM model (Figure 3.1) are thought to be free from the effects of the presence of other nearby binding sites.

Optimization Protocol. All starting structures were optimized using pure generalised gradient approximated BP86 functional[91-92] with medium sized def2-SV(P) basis set,[93] which is earlier shown to produce good structural parameters in accord to the experiments.[61, 94-95] Nevertheless, a set of calculations are performed on TM structures using larger basis set (def2-TZVP)[99] to comment on the basis set dependency over geometry and energetics of metal-bound systems. Neither the alternation of binding affinity trend nor any significant structural changes were noticed with the use of larger basis set (Table 3.1). To speed up the calculation, a resolution of identity (RI) approximation is invoked for coulomb exchange integrals using a corresponding auxiliary basis set (def2-SV(P)/J). For energy evaluation, three-body dispersion corrected[165] hybrid B3LYP[96-97] functional (B3LYP-D3) with triple ζ TZVP basis set[98-99] was used. For heavy metal Cs^+ , the core orbitals (containing 46 core electrons) were modelled via def-ECP pseudo potential. def2-SV(P) (for geometry optimizations) and def-TZVP basis sets (for energy minimizations) were used to describe the valence orbitals. All geometry optimizations were carried out at gas phase with tight SCF convergence criteria (10^{-8} a.u on the density). The basis set superposition error (BSSE) for the metal bound complexes were found to be within the window of 1-3 kcal mol^{-1} , indicating not to incorporate counter poise corrections for subsequent energetics calculations. In the process of energy evaluation, COSMO continuum solvation model[100] was used to take care of long range electrostatic interactions as implemented in TURBOMOLE v6.3.[101]

Table 3.1: Choice of basis set:

(I) Optimized structural parameters (bond distances in Å) of metal ion-TM (synthetic truncated model) complexes at SF binding sites, S3 and S4 using two different basis set (def2-SV(P) and def2-TZVP). The lowest and the highest values of the four bond lengths (Å) for carbonyl oxygen and hydroxyl oxygen atoms, ligated with the metal ions are reported.

TM	Ion	M-(O=C)	$M\text{-}OH_{Thr63}$	M-(O=C)	$M\text{-}OH_{Thr63}$
		BP86/def2-SV(P)		BP86/def2-TZVP	
TM-S3	Na^+	2.480-6.160 (V64) 2.275-2.612 (T63)	-	2.362-6.125 (V64) 2.291-2.701 (T63)	-
	K^+	2.875-2.896 (V64) 2.973-3.118 (T63)	-	2.909-2.920 (V64) 2.999-3.140 (T63)	-
	Cs^+	3.144-3.168 (V64) 3.185-3.231 (T63)	-	3.159-3.171 (V64) 3.226-3.265 (T63)	-
TM-S4	Na^+	2.456-2.511 (T63)	3.450-3.503	2.433-2.485 (T63)	3.674-3.764
	K^+	2.751-2.795 (T63)	3.385-3.455	2.751-2.795 (T63)	3.385-3.461
	Cs^+	3.057-3.092 (T63)	3.492-3.550	3.055-3.097 (T63)	3.868-4.007

(II) Effect of basis set (def2-SV(P)/ def2-TZVP) on the binding energy (kcal mol^{-1}) of K^+-TM

K^+	Binding energy ($\Delta E(el)_{bind}$)				
	$\Delta E(el)_{bind}^{gas}$	$\Delta E(el)_{bind}^{5}$	$\Delta E(el)_{bind}^{10}$	$\Delta E(el)_{bind}^{20}$	$\Delta E(el)_{bind}^{80}$
S3	-52.1/-48.4	-42.2/-37.7	-40.6/-36.0	-39.7/-35.0	-39.1/-34.3
S4	-40.3/-39.2	-28.3/-27.0	-25.9/-24.5	-24.5/23.2	-23.4/22.1

In NaK ion channel, the secondary protein backbone attached to the SF region works as a structural constraint to maintain the vicinity of four nearby subunits. This in turn preserve optimum pore radius to form appropriate cation binding sites. Optimization of our model structures without such constraint led to significant increase of pore radius. In most occasions, maximum three out of four subunits are observed to interact with the attached cations, thus underestimating the cation binding affinities. Previous MD studies[166-167] indicated the importance of "topological" constraints on the coordination number in protein. Structural analysis of ion selectivity in NaK further emphasizes the rigidity of the SF during ion binding.[150] The presence of methylene spacer in the synthetic models used by Dudev and Lim,[160-161] served as the needed constraint during the optimization. Keeping these facts in mind, physical constraints were applied on a few selected backbone carbon atoms of model structures (for structure ‘A’, one and for structure ‘B’, two carbon atoms). In Figure 3.1, these three Cα atoms are marked by ‘*’. The coordinates of these carbon atoms are “*frozen*” in order to restrict their movements in the Cartesian space. The selection of backbone carbon atoms were made in such a way that the applied constraint should not restrict the free movement of directly coordinating protein ligands (carbonyl and hydroxyl groups).

Analytical harmonic frequency calculations were performed for all structures to characterize the stationary points. Thermodynamic quantities such as changes in Gibbs free energies (ΔG) and entropy (ΔS) were derived. Natural population analysis (NPA)[102] was performed to quantify the charge transfer among metal, SF and water molecules. We would like to point out that most of the reported optimized structures are at their potential minima, without any imaginary frequency in their respective potential energy surface. Note that only in few cases the imaginary frequencies of values ranging from 5*i*-35*i* were obtained, which corresponds to the presence of constraints in structure. Throughout only real modes are considered in order to compute the contribution of various components in the partition function calculations. We believe that the error associated with these small number of cases will have negligible effect[168] over the major conclusions drawn on overall binding energetics.

Reaction Scheme. Capture and subsequent permeation of an ion from bulk to NaK SF is an outcome of the chelating strengths of the water molecules in the bulk and the protein ligands in the SF. First, using the following reaction schemes we have calculated the binding free energies (BFE) at different ion-chelating sites of NaK for each of the three cations (M^+ , M = Na, K, and Cs), not in competition with other ions.

$$S_{ext} + \mathrm{M}^{+}(\mathrm{H_2O})_6 \rightarrow \mathrm{S_{ext}} . \mathrm{M}^{+\cdot}(\mathrm{H_2O})_{n=0,2,4} + (\mathrm{H_2O})_{n=6,4,2} \tag{1}$$

$$\mathrm{S3}/S4 + \mathrm{M}^{+}(\mathrm{H_2O})_6 \rightarrow \mathrm{S3}/S4.\mathrm{M}^{+} + (\mathrm{H_2O})_6 \tag{2}$$

Crystallographic difference map analysis of the metal-bound NaK complexes[150] indicate four water molecules are attached in the first-shell of metal ions during their capture into the S_{ext} site from the bulk. In view of this, we performed calculations with varying HN ($n = 0,2,4$) at S_{ext} . As the binding sites S3 and S4 at the SF interior are analogues to the corrosponding binding sites of K^+ channel, the available carbonyl groups at the respective site can satisfy the overall CN of metal cations. Hence, no water involvement in binding is considered at these sites. Hydrated metal structures used in the above equations are obtained using successive MD and DFT calculations on metal water systems (see below).

Site specific selectivity of a given ion in the presence of other co-permeant ions can be judged by the free energies of ion exchange reactions. Ion exchange (M1+ →M2+ ; M2 substituting M1) free energies between two metal cations, M1+ and M2+ (viz., $\Delta G(K^+ \rightarrow Na^+)$, $\Delta G(Cs^+ \rightarrow K^+)$ and $\Delta G(Cs^+ \rightarrow Na^+)$) at the binding sites are calculated using the following exchange reaction schemes,

$$\mathrm{S_{ext}} . \mathrm{M1}^{+\cdot}(\mathrm{H_2O})_{n=0,2,4} + \mathrm{M2}^{+}(\mathrm{H_2O})_6 \rightarrow \mathrm{S_{ext}} . \mathrm{M2}^{+\cdot}(\mathrm{H_2O})_{n=0,2,4} + \mathrm{M1}^{+}(\mathrm{H_2O})_6 \tag{3}$$

$$\mathrm{S3} - \mathrm{M1}^{+} + \mathrm{M2}^{+}(\mathrm{H_2O})_6 \rightarrow \mathrm{S3} - \mathrm{M2}^{+} + \mathrm{M1}^{+}(\mathrm{H_2O})_6 \tag{4}$$

$$\mathrm{S4} - \mathrm{M1}^{+} + \mathrm{M2}^{+}(\mathrm{H_2O})_6 \rightarrow \mathrm{S4} - \mathrm{M2}^{+} + \mathrm{M1}^{+}(\mathrm{H_2O})_6 \tag{5}$$

In the above equations, $M(H_2O)_6^+$ represents hydrated metal ion. The SF bound ions are represented as $S3\text{-}M^+$ and $S4\text{-}M^+$ for sites S3 and S4, respectively, and $S_{ext}\text{-}M^+(H_2O)_{n=0,2,4}$ represents partially hydrated (n=0,2,4) ion at the external site, S_{ext} . The free energy change associated with the above equations is given by

$$\Delta G_{ex}^{\varepsilon} = \Delta G_{ex}^{gas} + [\Delta G_{solv}^{\varepsilon}]_{\text{product}} - [\Delta G_{solv}^{\varepsilon}]_{\text{reactant}} \tag{6}$$

where $\Delta G_{gas}{}^{ex}$ is the free energy change associated with ion exchange reactions in the gas phase and ΔG_{solv} ε solv is the free energy change in transfering a reactant or product partner from gas phase to solution phase with dielectric constant, ε. The difference in the sum of electronic energies, thermal energies including zero point energy, work term with the entropy change between reactants and products at T=300K is used to find ΔG_{gas} . Dielectric constant of ion channel is known to vary from 5 (for deeply buried binding sites, site 3 and 4) to 30 (at the external entrance)[167, 169-170] and thus the behaviour of ion binding is expected to be different from bulk water environment (ε=80). To model the different dielectric media mimicking the channel interior, calculations were performed with three different ε values (5, 10, and 20), using gas phase optimized structures. Additionally another sets of calculations were performed at ε=80 to study and compare the fate of these reactions in the bulk.

Energy Decomposition Analysis. To determine the nature of interaction between the alkali metals and SF, energy decomposition analysis (EDA) was performed using the methods of Morokuma[171] and Ziegler[172] at GGA/B3LYP-D3/TZP level with ZORA[173], as implemented in the program package ADF 2013.[174] The total bonding energy (ΔE_{bond}) between the two fragments (metal and protein) was calculated using the following equation,

$$\Delta E_{bond} = \Delta E_{elstat} + \Delta E_{pauli} + \Delta E_{orb} + \Delta E_{disp}\,, \tag{7}$$

where, ΔE_{elstat} and ΔE_{pauli} represents the electrostatic and repulsive interaction energy contributions between the fragments, respectively. ΔE_{orb} is the stabilizing energy that arises from the orbital contributions and thus represents the strength of covalent bonding between the fragments. ΔE_{disp} accounts for the dispersion interaction in the process of binding.

3.2.2. Molecular Dynamics Study

Structure Modelling. Each subunit of tetrameric NaK protein channel contains 1-104 residues. We have simulated the full protein channel (PDB ID: 2AHY) including the M0 helix (see in contrast Vora et. al.[152]). The lipid bilayer from the initially equilibrated lipid bilayer-embeded solvated tetrameric channel[163] was removed to save computation time. In this study, presence of M0 helix was used to maintain the structural integrity of tetrameric ion channel. However, it is important to mention that although in real translocation scenario, M0 helix mediates the opening and closing of ion channel, the presence of M0 helix does not cause any structural changes at the SF.[164] Four Cα atoms from each of the subunits of M0 helix were tethered using positional constraints with a force constant of 2.4 kcal mol^{-1} Å^{-2} . The chosen Cα atoms are at the junction where two M0 helices interact with each other due to proximity of two nearby subunits. The SF region of the channel was thus allowed to reorganise in response to the ion permeation, while the tethered atoms, away from the SF region, fluctuates in a way similar to that in a lipid-embeded system.[175]

Simulation Strategy. All MD simulations are performed at 300 K in the NVT ensemble with amder99sb-ildn force field[176] using GROMACS 4.5.4 suite.[104] The TIP3P water[177] solvated ion channel with the added ions (to manitain electroneutrality) was comprised of more than 0.26 million atoms. For short range electrostatic and van der Waals interactions, a cut off of 14 Å was applied. For long range electrostatics interaction, Particle Mesh Ewald[111] method is used, while LINCS algorithm[112] is implemented to constrain bond between hydrogen and the heavy atoms at their equilibrium lengths. Finally, 10 ns equilibration run was conducted by integrating the equation of motion with 2 fs time step. RMSD of the structure was calculated with respect to initial structure considering the backbone Cα atoms. Insignificant deformations were noted upon equilibration ($<$ 1 Å), which justify that the choice of the tethering atoms was appropriate.

The equilibrated structure was further taken to prepare cation containing ion channel systems. The cations were placed in the bulk water at more than 7 Å away from the external entrance, S_{ext} of pore to ensure negligible interaction between ion and protein matrix. Appropriate number of anions were added to maintain the charge neutrality. Further, 5 ns of equilibration runs were performed on these systems before we proceed for final MtD simulations with the equilibrated structures.

3.2.3. Metadynamics Simulation

To enforce the translocation of ions through the pore, MtD methodology[115] was applied. The MtD method progressively build-up a memory-based biasing potential energy term $(VMtD(t))$ by adding Gaussian "hills", in order to restrict the system revisiting the same region of the space, and is aimed at reconstructing the free energy surface (FES) of a given process much earlier than equilibrium MD could achieve. The enhanced bias explore the rare events along a chosen time dependent collective variable (CV), $S(x,t)$ and reconstructs the approximate potential of mean force (PMF) by the equality,

$$F_{MtD}(S(x),t) = -V_{MtD}(S(x),t), \tag{8}$$

in the region, $\sum_{(S)}$, explored by the CV up to time t. We have chosen the distance of the permeating ion with respect to the center of mass (COM) of ion channel as the CV in order to generate 1D PMF. Applied MtD parameters for the calculations are as follows: the height of the Gaussian hill is 0.1 kcal mol^{-1} , and its width is 0.05. The Gaussians were added after every 1 ps. In addition, reflecting lower and upper walls at the direction of pore axis were applied at ±30 Å away from COM of the ion channel to restrict the diffusion of ion away to the bulk and to ensure the prompt entrance of ion inside the SF. Finally, systems were subjected to production run with trajectories being saved every 1 ps for further analysis. All MtD simulations were performed using GROMACS patched with PLUMED 1.3.[178]

3.2.4. Equilibrium US correction of MtD discovered free energy

Because of the inherent nonequilibrium features associated with the MtD method, the true equilirbium thermodynamic information is difficult to obtain unless hills with very small values of heights (H) and widths (w) are added at long time intervals. Thus reconstructing equilibrium free energies from nonequilibrium simulations[179] are associated with the accuracy and covergence isuues.[180] MtD is however, an elegant method for conformational search along a chosen set of CV, and unlike umbrella sampling (US) method, is free from the prior assumptions on final state. Here the MtD method is used to generate the ion permeation pathway with absolute certainty. The MtD discovered PMF is then refined with the help of US correction. The details of this corrective step can be found in Refs.[90, 181-182] In brief, in the MtD-US correction approach, first a single MtD run along the chosen CV is used to discover a pre-optimized biasing potential, $V_{MtD}(s(x), t_b)$ upto a certain build-up time, t_b. Subsequently the MtD run is stopped and a conventional equilibrium US simulation is initiated along the MtD-discovered CV path using the physical force field derived potential energy, V_{phys}, additionally incremented by the time independent biasing potential (non-negative) that was accumulated over the previous MtD run. The US step allows ergodicity to be satisfied, since the metastabilties along the permeation pathway are removed by the elevated biasing potential (obtained through MtD step) and the diffusive dynamics in the chosen CV space can be sampled with ease with a reasonable computational effort in the spirit of a equlibrium run. After the US run is completed, we have calculated the biased probability density, $\rho_{US}(s)$ of finding the system at given COM spearation, s between the permeating ion and the channel through a histogram sorting. Finally, the US corrected PMF is given by

$$F(s) = -V_{MtD}(s(x)) - k_B T ln \rho_{US}(s), \tag{9}$$

where the last term is a corrective measure to the MtD discovered PMF (compare with equation 8). With the MtD-generated hill potential, an US sampling phase of 300 ns was performed for each of the permeating ions and the values of the COM separation CV was recorded at 1 ps interval, totalling 3×10^5 samples at the end of the correction run. To evaluate $\rho_{US}(s)$, a bin size of 0.01 Å was chosen.

3.3. Results

3.3.1. Solvation of Metal Ions

It is well known that both HN and the hydration energy of ions play crucial roles during their capture from the bulk and subsequent permeation through the ion channel by partial or complete shedding of their primary hydration shell. Several experimental and computational studies have been reported on the possible HN of Na^+ and K^+ in their first solvation shell, which suggest that it can vary from four to six for Na^+ and six to eight for K^+.[183-187] In view of these diverse reports, here we have conducted MD and DFT calculations on ion-water systems. We have calculated radial distribution functions (RDF), $g(r)$ and the running integration number (represent HN) for both cations, which suggest six water molecules can directly coordinate to both the metal ions in the primary coordination shell (Figure 3.2).

RDF profiles for K^+ and Na^+ have a sharp peak at 2.72 Å and 2.36 Å distance, respectively, which correspond to metal-O_{water} distance and are indeed very close to the previously reported values of Whitfield et al.[187] (K^+-O_{water}: 2.7-2.8 Å) and to that of Carrillo-Tripp et al.[188] (Na^+ -O_{water}2.37 Å K^+-O_{water} : 2.79 Å). Similar to their observation, we also found a relatively sharp first peak is followed by a deep depletion zone which becomes shallower as we proceed towards K^+ . This implies the stronger hydration shell structure for Na^+ as compared to K^+ .

Further, the MD-discovered primary hydration shells of Na^+ and K^+ were used in DFT calculations at B3LYP-D3/TZVP//BP86/def2-SV(P) level in order to obtain hydration free energies.

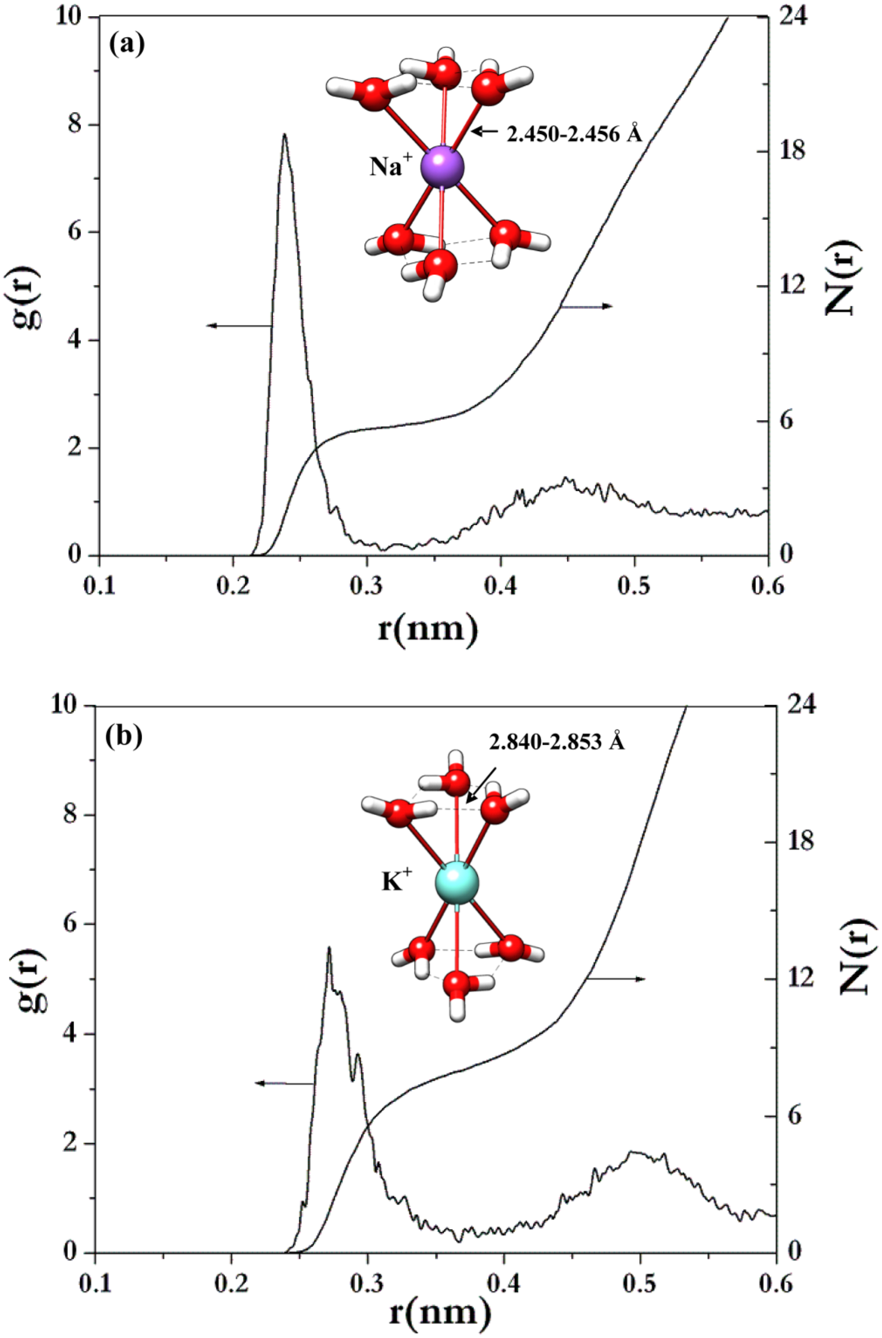

Figure 3.2: Radial distribution functions, g(r) and corresponding running integrals, N(r) of (a) Na+and (b) K+ with respect to oxygen atoms of water molecules. Structure of metal-hydrate systems as extracted from the plateau region of the N(r) plots and optimized at BP86/def2-SV(P) level are shown in the inset. The optimized structures are found to reproduce the experimentaly determined hydration free nergy trend

The optimized hydrated structures for both the metal ions are found to be of D3 symmetry. Our calculated M$^+$-O$_{water}$ bond distances from QM calculations are 2.450-2.456 Å for Na$^+$ and 2.840-2.853 Å for K$^+$ (Figure 3.2). For K$^+$, our hydrated structure is very close to the QM predicted structure of Rao et al.[184] and also like ours, recent experiments using neutron diffraction[185] and EXAFS[186] estimated an average HN of six for K$^+$. Although, we have noted an overestimation of 5 to 10 kcal mol^{-1} in the calculated values, the hydration energy order were found to follow a correct trend with respect to the reported experimental values (Table 3.2).

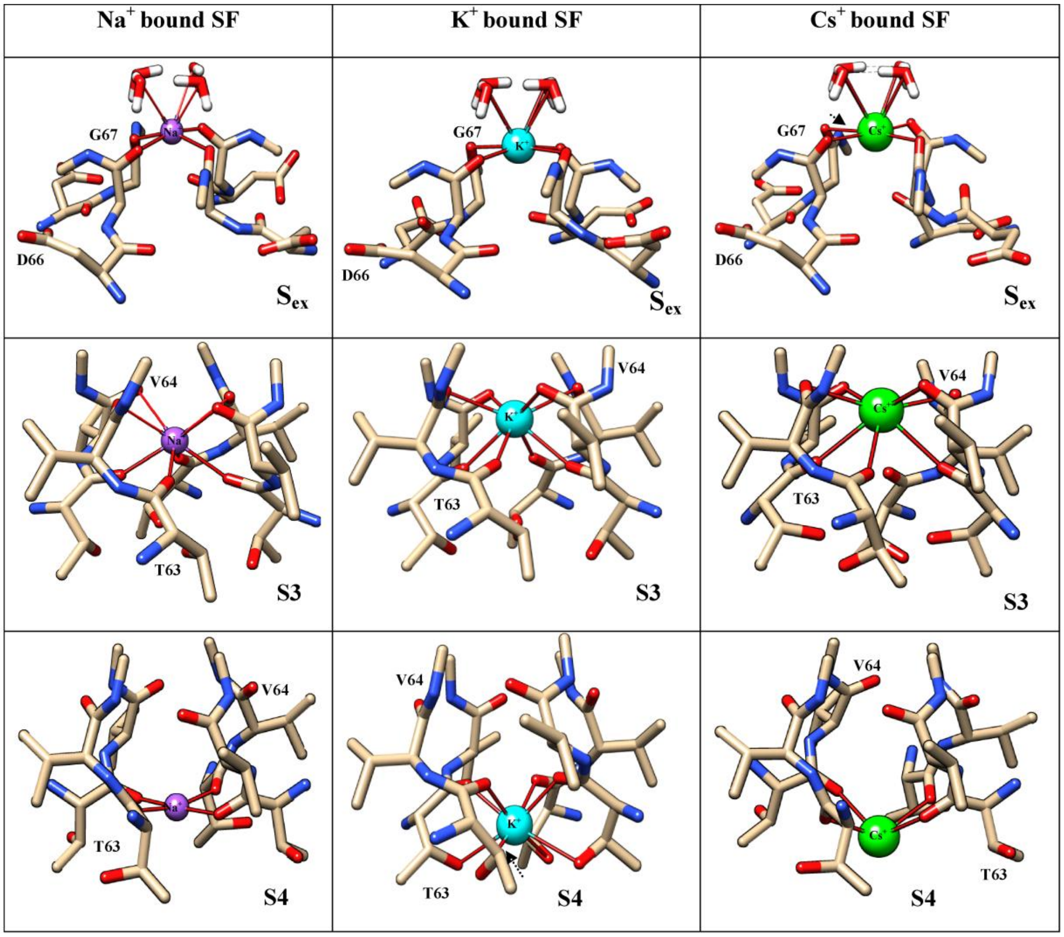

Figure 3.3: Metal ion-bound optimized structures of the selectivity filter of NaK for the three ions Na$^+$, K$^+$, and Cs$^+$ as obtained from DFT calculation of structure ‘A’ and ‘B’. Top panel: external binding site, S$_{ext}$, middle and bottom panels are for binding sites, S3 and S4, respectively. Hydrogen atoms are not shown for clarity. Color code: red = oxygen, blue = nitrogen, yellow = carbon.

Table 3.2: Calculated hydration free energy (kcal mol^{-1}) of alkali metals ions.

Hydrated Alkali metal ions	B3LYP-D3/TZVP//BP86/def2-SV(P)	Experimental[a]
	Calculated	
$[Na(H_2O)_6]^+$	-97.3	-87.3
$[K(H_2O)_6]^+$	-76.2	-70.6
$[Cs(H_2O)_6]^+$	-64.5	-59.8

[a]values taken from ref no. 116

The slight over estimation can be accredited partially to the absence of secondary shell in the metal hydrated structure, which has been accounted here using implicit solvation approach. For Cs^+, based on our results of Chapter 2, hexahydrated metal structure (Cs^+-O_{water} : 3.160-3.282 Å) was taken, which was earlier found to follow correct hydration energy trend.[189] Hence, in the bulk, metal HN was considered to be six for all the three ions.

3.3.2 Site-Specific Selectivty of Metal Ions

X-ray crystallographic data[150] of multiple-ion-bound NaK channel suggests that its SF sites chelates with the ions using three ligand types: G67-carbonyl (with water) for S_{ext} ; V64-carbonyl (with water) for vestibule; V64-carbonyl and T63-carbonyl for S3; and T63-carbonyl/hydroxyl for S4. Here we explore how these seemingly similar, chemically nonselective environment of the filter sites can exhibit preferential binding with the monovalent ions and their transport through the filter. We first plan to address these issues through DFT calculation by elucidating (1) the structures of the filter sites bound to the ions (Figure 3.3 and Table 3.3), (2) their binding energetics (Tables 3.5), and (3) the ion exchange free energy trend (Table 3.6). In each of these topics we additionally investigate the effects of the absence of HB between D66 and N68 by replacing the carboxylate group of D66 with neutral methyl group at S_{ext}.

Later we present the results of MD simulations for the PMF profile of the permeating ions, which corroborates well with DFT calculations and clearly demonstrate the site-specific selectivity in the nonselective NaK.

Table 3.3: Calculated structural parameters for alkali metal ions at different binding sites of the selectivity filter of NaK channel. The lowest and the highest values of the four bond lengths (Å) for carbonyl oxygen-, hydroxyl oxygen- and water oxygen- atoms, ligated with the metal ions are reported.

Binding Sites	Ion	Interacting Residues	M-(O=C)	M-(O=C)^{exp}	M-OH$_{T63}$	M-O$_{water}$
S$_{ext}$[b]	Na$^+$	G67	2.312-2.334 (2.379-2.407)	-	-	2.907-3.078 (2.713-2.880)
	K$^+$	G67	2.624-2.649 (2.671-3.206)	2.52[a]	-	3.053-3.175[d] (2.946-2.994)
	Cs$^+$	G67	2.954-3.025 (2.997-3.206)	-	-	3.139-3.272 (3.154-3.584)
Vestibule[c]	Na$^+$	V64	- (2.444-2.464)	-	-	- (2.917-3.029)
	K$^+$	V64	- (2.675-2.688)	-	-	- (3.048-3.111)
	Cs$^+$	V64	- (2.967-3.005)	-	-	- (3.202-3.237)
S3[c]	Na$^+$	V64	2.862-3.175 (2.480-6.160)	-	-	-
		T63	2.459-2.506 (2.275-2.612)			
	K$^+$	V64	2.899-2.932 (2.875-2.896)	-	-	-
		T63	2.807-2.816 (2.973-3.118)			
	Cs$^+$	V64	3.121-3.160 (3.144-3.168)	-	-	-
		T63	3.088-3.125 (3.185-3.231)			
S4[c]	Na$^+$	T63	2.280-2.321 (2.456-2.511)	2.38[a]	5.317-5.580 (3.450-3.503)	-
	K$^+$	T63	2.577-2.628 (2.751-2.795)	2.97[a]	3.045-3.195[d] (3.385-3.455)	-
	Cs$^+$	T63	2.934-2.998 (3.057-3.092)	-	5.678-5.799 (3.492-3.550)	-

[a] values are taken from ref no.150

[b] Values in parenthesis are for neutral methyl group substitution of negatively charged carboxylate group of D66.

[c] Values in parenthesis are for truncated model representation of structure 'B'.

[d] Reported experimental value for K$^+$-O$_{water}$ = 3.06 Å and K$^+$-OH$_{T63}$ = 2.79 Å.[150]

Finally in the Discussion section we have provided a critical overview of the results and described in detail the effects on the binding characteristics when structure ‘B’ is truncated (cf. Figure 3.1) into smaller toy models namely, vestibule, S3 and S4 . All the results presented below are for singly permeating ion, free from ‘contamination’ due to the absence any other ‘rivalry’ cations.

3.3.3. Cation binding at SF sites

Optimized structural parameters for the metal-bound binding sites are tabulated in Table 3.3. At the solvent exposed external site, S_{ext} , the ions while being coordinated with backbone carbonyl oxygen atoms of G67 can remain partially hydrated.

Table 3.4: Effect of water molecules around metal ions in the site, S_{ext}.

(I) Optimized strucural parameter (bond distances in Å. The lowest and the highest values of the four bond lengths for carbonyl oxygen atoms, ligated with the metal ions are reported).

Ion (M)	Water molecules around metal	M-(O=C) (Gly 67)	$M\text{-}(O{=}C)^{exp}$	$M\text{-}O_{Water}$	$M\text{-}O_{Water}^{exp}$
Na^+	Zero	2.255-2.277	-	-	-
	two	2.315-2.378	-	2.547, 3.244	-
	four	2.312-2.334	-	2.907, 2.947, 2.967, 3.078	-
K^+	Zero	2.582-2.596	-	-	-
	two	2.577-2.738	-	2.889-3.043	-
	four	2.624-2.649	2.52[a]	3.053, 3.106, 3.114, 3.175	3.06[a]
Cs^+	Zero	2.892-3.028	-	-	-
	two	2.898-3.069	-	3.187-3.236	-
	four	2.954-3.025	-	3.139, 3.225, 3.245, 3.272	-

[a]corresponding values are taken from ref no. 150

(II) Binding free energy (kcal mol^{-1}) of ions with varying water molecules around metal complex at ‘S_{ext}’

S_{ext}	Coordinated water molecules around metal											
	Zero				Two				Four			
	ΔG_{bind}^{5}	ΔG_{bind}^{10}	ΔG_{bind}^{20}	ΔG_{bind}^{80}	ΔG_{bind}^{5}	ΔG_{bind}^{10}	ΔG_{bind}^{20}	ΔG_{bind}^{80}	ΔG_{bind}^{5}	ΔG_{bind}^{10}	ΔG_{bind}^{20}	ΔG_{bind}^{80}
Na^+	-57.0	-32.6	-19.4	-9.2	-107.7	-81.8	-67.9	-57.0	-79.4	-53.1	-39.1	-28.1
K^+	-13.1	10.9	23.9	33.9	-108.7	-83.5	-69.9	-59.3	-75.6	-49.6	-35.7	-24.8
Cs^+	-16.9	10.6	25.4	37.0	-111.8	-82.7	-67.0	-54.8	-72.6	-42.6	-26.5	-13.9

(III) Ion exchange free energy (kcal mol^{-1})

S_{ext}	Coordinated water molecules around metal											
	Zero				Two				Four			
	ΔG_{ex}^{5}	ΔG_{ex}^{10}	ΔG_{ex}^{20}	ΔG_{ex}^{80}	ΔG_{ex}^{5}	ΔG_{ex}^{10}	ΔG_{ex}^{20}	ΔG_{ex}^{80}	ΔG_{ex}^{5}	ΔG_{ex}^{10}	ΔG_{ex}^{20}	ΔG_{ex}^{80}
Na^+/K^+	-43.9	-43.5	-43.3	-43.1	1.0	1.6	1.9	2.2	-3.7	-3.5	-3.4	3.3
K^+/Cs^+	3.8	0.4	1.5	-3.0	3.1	-0.8	-2.9	-4.5	-3.1	-7.0	-9.2	-10.9
Na^+/Cs^+	-40.1	-43.1	-44.8	-46.1	4.1	0.9	-0.9	-2.3	-6.8	-10.5	-12.6	-14.2

Increasing the HN (refer to Eq. (1); n=0, 2 and 4) progessively led to elongation of M-O_{G67} bond distances, which is quiet expected due to the greater involvement of water molecules in the metal coordination sphere (Table 3.4). For all ions, M-O_{G67} bond distances are noted to be somewhat shorter than the M-O water bonds. For tetra-coordinated water structures, the computed bond distances in K^+ -O_{G67} and K^+-O_{water} lies in the range (2.624-2.649 Å) and (3.053-3.175 Å), respectively. These values are in close agreement with the reported crystal structure (2.52 Å for K^+-O_{G67} and 3.06 Å for K^+-O_{water}) (Table 3.3 and Figure 3.3). In view of the reported HN of K^+ at S_{ext} and such close structural resemblance with our optimized four water coordinated structures (Table 3.4), hereafter we will consider n=4 for HN at this site. Significantly longer M^+-O_{water} distance ranges (2.907-3.078 Å for Na^+ ; 3.053-3.175 Å for K^+ and 3.139-3.272 Å for Cs^+) with respect to hexa hydrated metal complexes in the bulk (2.450-2.456 Å for Na^+; 2.839-2.852 Å for K^+; 3.160-3.282 Å for Cs^+) is noted, which again suggest somewhat weaker participation of water molecules at S_{ext} as compared to hydrated metal complex due to the presence of strong field carbonyl ligand of G67. We have also observed a strong HB (1.565-1.690 Å) formed between the carboxylate of D66 and G67-N68 backbone. In order to assess the effects of this HB on the structures at S_{ext} site, we have replaced the negatively charged carboxylate of G67 with neutral methyl group. This replacement in addition to switching off the HB interaction also diminishes the charge delocalisation leading to weakening of the metal-carbonyl interaction. Indeed, in replacement of carboxylate by methyl substituent, we observed an elongation of M-O_{G67} bond whereas M-O_{water} is found to be shortened (Table 3.3).

Similar to S_{ext} , ions can also remain partially hydrated at vestibule while interacting with carbonyl groups of V64. Here again, involvement of four water molecules in binding for K^+ was reported in the crystal structure.[150] To this end, structure 'B' was used to analyze the ion binding ability at vestibule site. Interestingly, upon optimization of metal-bound-vestibule, we observe translocation of all metal ions towards the S3. This corresponds to the loss of selectivity at the vestibule, which prompt the metal ions to drift to the nearest minima (*i.e.* S3). For this reason, in structure ‘B’, where the vestibule acts in unison with S3 and S4, we have not considered vestibule as a possible binding site. At S3, the specific arrangement of carbonyls of V64 and T63 provides octahedral ligand arrangement to K^+ where it can reside at the middle of two planes formed by the carbonyls of V64 and T63. The K^+-$O_{carbonyl}$ bond distances are found to be of 2.899-2.932 Å for V64 and 2.807-2.816 Å for T63, which differs only by ~0.09 Å from the observed x-ray data (2.80 Å-Val 64; 2.83 Å-T63).[150] Contrary to K^+ , both Na^+ and Cs^+ are noted to remain closer to the carbonyl plane of T63.

At S4, K^+ remains in between the planes of carbonyls and hydroxyls of T63 to maintain the octahedron coordination geometry. However, K^+ -$O_{carbonyl}$ bond distances are found to be somewhat smaller (2.577-2.628 Å) as compared to K^+ -$O_{hydroxyl}$ (3.045-3.195 Å). For Na^+ and Cs^+ , hydroxyl groups of T63 are not seen to interact effectively and get drifted 5 Å away, whereas carbonyl groups interacts strongly (2.280-2.321 Å- Na^+ ; 2.934-2.998 Å-Cs^+). Once again, Na^+ is noted to reside at the plane of carbonyl groups of T63. These imply that the stability of Na^+ lies at the junction of S3 and S4, while K^+ has unique stability at both the sites. Such observations are in accord to the previous theoretical investigations where it is noticed to have an energy barrier at the plane of carbonyls for K^+, while the same plane is selective towards Na^+.[151, 190] Due to steric reason, bigger Cs^+ ion is seen to move slightly out of the carbonyl plane towards S4. The optimized metal-bound filter structures are presented in Figure 3.3. Additionally, for each of the three ions, the Cartesian coordinates of metal-bound optimized structures of the three SF binding sites (totaling 9 structures) are provided in SI. Based on the strain energy calculations of the QM models (data not reported), we note here that no major ion-related filter deformation was observed.

Here it is important to mention that the reported X-ray crystal structures[150] suggested vestibule and S4 as one of the probable binding sites for K^+ and Na^+ , respectively. In contrary, we did not found any sort of binding selectivity for K^+ and Na^+ at the vestibule, while Na^+ did not show any significant binding interaction with the hydroxyls of T63. It is to be noted that the actual x-ray crystal structure[150] contains one Ca^{2+} and three K^+ at the SF. The ionic interaction could have facilitated the binding of K^+ at the vestibule. In order to verify the influence of inter-ionic repulsion, we have also optimized 'structure B' with two cations placed at different sites. For instance, K^+ at the vestibule, while Na^+ at S3 and vice versa. Indeed, Na^+ is observed to drift towards the junction between S3 and S4 (Na^+ -$O_{carbonyl}$ - 2.200-2.262 Å), which forces K^+ to reside at the vestibule surrounded by four water molecules (K^+ -O_{water} -2.946-2.990 Å) and carbonyl groups of V64 (2.759-2.769 Å). However in opposite scenario, Na^+ at vestibule seems to be more diffused to interact with two of the carbonyls of V64 (2.339-2.398 Å). As usual, K^+ remains at the S3 at interionic distance of 3.368 Å from Na^+ . Similarly, presence of K^+ at S3 is seen to assist Na^+ (which was initially placed at S4) to interact with the hydroxyl groups of T63 (2.434-2.584 Å). In this condition, Na^+ can afford to coordinate with one water molecule (2.249 Å) from the cavity to have favorable pyrimidal ligand environment and hence explains the experimental findings of Alam et al.[150] In the presence of K^+ at S3 site, Cs^+ is noticed to interact with the hydroxyl groups of S4 site (Cs^+ -OH_{T63} : 3.023-3.195 Å) which is otherwise (in the absence of K^+) seen to remain below the carbonyl plane of T63. When Na^+ and Cs^+ remain present at S3 and S4 site respectively, both are seen to maintain octahedron coordination geometry (Na^+-O_{V64} : 2.509-2.594 Å: Na^+-O_{T63} : 2.650-2.720 Å; Cs^+-OH_{T63} : 3.042-3.230 Å; Cs^+-O_{T63} : 2.948-3.353 Å) and hence perturbed the stable equilibrium state of single ion bound coordination environment. Therefore, the presence of competing cation at the nearest binding site can help ions to overcome the free energy barrier which in turn accelerates the translocation event. This view is in support to the arguments of

Kopfer et al.,[191] where inter-ionic repulsion is stressed to be the main reason behind the high ionic flux through K^+ channel.

3.3.4. Binding energetics of Ions inside SF

Computed binding free energies (BFE) pertaining to reaction equations (1) and (2) at the SF binding sites are tabulated (Table 3.5). Noticeably, initial gas phase calculations predicted highest binding affinity for Cs^+ , irrespective of binding sites. Incorporation of implicit solvation in calculation, however, is seen to alter the binding trend.

Table 3.5: Calculated thermodynamic parameters (kcal mol^{-1}) of alkali metal ions at the binding sites of NaK slectivity filter.

Binding Sites	Binding free energy (ΔG_{bind})						TΔS
	Ion	ΔG_{bind}^{gas}	ΔG_{bind}^{5}	ΔG_{bind}^{10}	ΔG_{bind}^{20}	ΔG_{bind}^{80}	
S_{ext}[a]	Na^+	-226.8 (-423.0)	-79.4 (-133.9)	-53.2 (-75.8)	-39.1 (-40.3)	-28.1 (-9.1)	-5.4
	K^+	-221.9 (-419.9)	-75.6 (131.6)	-49.6 (-73.7)	-35.7 (-38.2)	-24.8 (-7.2)	-1.5
	Cs^+	-238.7 (-453.2)	-72.6 (-140.9)	-42.6 (-78.0)	-26.5 (-39.3)	-13.9 (6.7)	6.8
Vestibule[b]	Na^+	- (-25.2)	- (-19.2)	- (-18.4)	- (-17.9)	- (-17.6)	
	K^+	- (-32.1)	- (-27.7)	- (-27.2)	- (-26.9)	- (-26.7)	
	Cs^+	- (-52.9)	- (-28.3)	- (23.7)	- (-21.3)	- (-19.3)	
S3[b]	Na^+	-43.2 (-45.2)	-31.6 (-35.5)	-29.5 (-33.8)	-28.4 (-32.9)	-27.6 (-32.1)	-8.7
	K^+	-55.9 (-53.7)	-44.7 (-43.9)	-42.7 (-42.2)	-41.7 (-41.4)	-40.8 (-40.7)	1.2
	Cs^+	-75.0 (-78.7)	-41.9 (-47.8)	-35.6 (-42.0)	-32.1 (-38.8)	-29.3 (-36.3)	0.3
S4[b]	Na^+	-53.2 (-31.3)	-41.3 (18.9)	-38.9 (-16.4)	-37.7 (-15.0)	-36.7 (-13.9)	1.8
	K^+	-26.4 (-42.1)	-19.5 (-30.2)	-18.6 (-27.7)	-18.2 (-26.4)	-17.8 (-25.3)	12.3
	Cs^+	-73.1 (-69.3)	-41.6 (-36.9)	-35.5 (-30.4)	-32.1 (-26.8)	-29.4 (-23.9)	9

[a] Values in parentheses are for the neutral methyl group substitution of charged carboxylate group of D66. [b] Values in parenthesis are for the truncated model representation of Structure B.

Analysis of binding free energy values suggest that the variation in HN of metal at S_{ext} led to distinct effect on the binding energy values (Table 3.4). Note that without water involvement

(HN is 0), binding of cations (with the exception of Na^+) for $\varepsilon > 5$ at S ext is unfavourable. As explained earlier, in the process of single ion translocation through the SF, ions initially at vestibule is observed to drift towards the more preferable binding site at S3. Hence this supports the notion that small Na^+ can remain favourably bound at tetra coordinated protein ligand environment. Subsequent addition of water molecule led to strongly favourable binding for K^+ as compared to Cs^+ . With involvement of two or four water molecules, the binding of Na^+ and K^+ is noted to be very similar (difference of BFE is 1-4 kcal mol^{-1}) (Table 3.4).

The effect of methyl substitution at S_{ext} increases the cumulative charges over carbonyl due to lack of charge delocalisation and also somewhat enhances structural flexibility at the entrance, which eventually led to high binding energy at $\varepsilon < 80$. However, BFE was found to decrease substantially at $\varepsilon = 80$. Notably, obtained BFE does not seem to correlate well with the increase of M^+-O_{G67} bond distance. It is to be remembered that our calculated BFE at S_{ext} does not truly correspond to the protein binding but reflects the resultant binding energy of metal in a mixed ligand environment (protein and water molecules). binding energy calculations are not performed for vestibule. For all the dielectric media (ε=5 to 80), binding strength at S3 is observed to follow the order: $K^+ > Cs^+ > Na^+$. It is important to note that S3 is a deeply buried binding pocket. Hence, expected ε is well below the values of aqueous medium. Calculated BFE values suggest that the decrease of ε substantially enhances affinity towards Cs^+ as compared to Na^+ and K^+ . Contrary to S3, binding strength of K^+ at S4 is found to be the least as compared to Na^+ and Cs^+ . Binding of Na^+ and Cs^+ occurs close to the plane of carbonyls formed by T63, which might cause higher binding strength (more negative ΔG). Calculated thermodynamic parameters strongly suggest that the binding is enthalpy driven and entropy does not have significant influence on free energies (Table 3.5). Nevertheless, as compared to Na^+ , positive entropic contribution for Cs^+

seems to favour its binding at all the binding sites, which can be accredited to its low hydration free energy (-59.8 kcal mol^{-1}).

3.3.5. Ion exchange reaction at SF

To evaluate site-specific preferential binding of alkali ions, free energy change associated with the ion exchange reactions (cf. Equations 3 to 5) were calculated and the results are presented in Table 3.6. Gas -phase energies are calculated here only as a reference purpose. Based on this the implicit solvation model results are calculated at different dielectric media, mimicking the protein matrix in solution. Comparison of $\Delta G_{ex}^{\varepsilon}$ (ε=5, 10, 20, 80) values for the triad of exchange reaction at the external site shows that Na^+ has slighly more selectivity as compared to K^+ , while Cs^+ at S_{ext} is noted to have least selectivity.

Table 3.6: Calculated ion exchange free energies (kcal mol^{-1}) of alkali metal ions at the binding sites of NaK selectivity filter.

Binding Sites		Ion exchange free energy (ΔG_{ex})				
		ΔG_{ex}^{gas}	ΔG_{ex}^{5}	ΔG_{ex}^{10}	ΔG_{ex}^{20}	ΔG_{ex}^{80}
S_{ext}[a]	Na^+/K^+	-4.9 (-3.2)	-3.7 (-2.3)	-3.5 (-2.2)	-3.4 (-2.0)	-3.3 (-1.9)
	K^+/Cs^+	16.8 (33.4)	-3.1 (9.3)	-7.0 (4.4)	-9.2 (1.7)	-10.9 (-0.5)
	Na^+/Cs^+	11.8 (30.2)	-6.8 (6.9)	-10.5 (2.2)	-12.6 (-0.3)	-14.2 (-2.4)
Vestibule[b]	Na^+/K^+	- (6.9)	- (8.5)	- (8.8)	- (9.0)	- (9.1)
	K^+/Cs^+	- (20.8)	- (0.6)	- (-3.4)	- (-5.6)	- (-7.4)
	Na^+/Cs^+	- (27.7)	- (9.1)	- (5.4)	- (3.4)	- (1.8)
S3[b]	Na^+/K^+	12.7 (8.6)	13.1 (8.3)	13.2 (8.4)	13.2 (8.5)	13.3 (8.6)
	K^+/Cs^+	19.1 (24.9)	-2.8 (3.9)	-7.1 (-0.3)	-9.6 (-2.6)	-11.5 (-4.4)
	Na^+/Cs^+	31.8 (33.5)	10.3 (12.3)	6.0 (8.2)	3.6 (5.9)	1.7 (4.2)
S4[b]	Na^+/K^+	-26.8 (10.9)	-21.7 (11.2)	-20.4 (11.3)	-19.6 (11.4)	-18.9 (11.4)
	K^+/Cs^+	46.6 (27.2)	22.1 (6.7)	16.9 (2.7)	13.9 (0.4)	11.6 (-1.4)
	Na^+/Cs^+	19.8 (38.0)	0.4 (17.9)	-3.5 (13.9)	-5.5 (11.8)	-7.3 (10.0)

[a]Values in parenthesis are for the methyl group substitution of the negatively charged carboxylic group of D66. [b]Numbers in parenthesis are for the truncated model representation of Structure B.

Interestingly, at low dielectric media ($\varepsilon < 20$), in methyl substituted S_{ext} site, the preferential binding order changes with Cs^+ becoming most preferred. This is reminiscent of the fact that in the absence of this HB, the filter looses its compact structural feature, allowing larger Cs^+ to be accommodated more easily. Further, a marginal loss of selectivity is also noted for the Na^+-K^+ ion exchange couple. Akin to the BFE trend, selectivity order of ions at S3 is found to be $K^+ > Cs^+ > Na^+$. Earlier experimental studies on selectivity[150] also observed similar trend, where Cs^+ is found to have higher affinity at S3, which however can not replace K^+ at higher concentration. Contrary to S3, K^+ has the least selectivity for S4 as compared to Na^+ and Cs^+ .

3.3.6. Energy decomposition analysis (EDA)

Energy decomposition analysis was performed to distinguish the contribution of various interactions into total bonding energy (see Table 3.7). In general, favorable ion-dipole interactions (estimated a contribution of 60-85 % into the total energy) is held primarily responsible for binding at the various sites of the ion channel. Due to increase of ionic radius from Na^+ to Cs^+ , Pauli repulsion contribution (ΔE_{pauli}) into the total bonding energy is increased, whereas, lowering of charge density led to the decrease of favorable electrostatic interaction (ΔE_{elstat}) as we move down the periodic table.

Table 3.7: Energy decomposition analysis (Energies are in kcal mol^{-1} unit)

Binding Site	Ion	Pauli repulsion ΔE_{pauli}	Electrostatic interaction ΔE_{elstat}	Orbital interactions ΔE_{orb}	Dispersion ΔE_{disp}	Total bonding energy
S_{ext}	Na^+	28.67	-250.87 (83.42)	-39.85 (13.25)	-10.02 (3.33)	-272.07
	K^+	46.94	-244.73 (84.30)	-33.88 (11.67)	-11.69 (4.03)	-243.36
	Cs^+	59.66	-239.1 (81.29)	-37 (12.58)	-18.05 (6.14)	-234.49
S3	Na^+	13.52	-98.59 (66.87)	-37.66 (25.54)	-11.18 (7.58)	-133.91
	K^+	27.82	-97.69 (68.71)	-32.97 (23.19)	-11.52 (8.10)	-114.36
	Cs^+	37.94	-88.88 (65.90)	-32.73 (24.27)	-13.27 (9.84)	-96.94
S4	Na^+	25.82	-94.66 (67.13)	-38.23 (27.11)	-8.11 (5.75)	-115.18
	K^+	42.9	-91.52 (65.02)	-35.93 (25.53)	-13.3 (9.45)	-97.85
	Cs^+	33.59	-69.88 (63.78)	-29.58 (27.00)	-10.11 (9.23)	-75.98

Values in parenthesis refer to percentage contribution of each attractive energy terms in the total attractive energies (sum of $\Delta E_{elstat,}$ ΔE_{orb} and ΔE_{disp})

We also note a structural change associated with S4 site after binding to Cs^+ . The hydroxyl side chain was observed to move away in order to accommodate the large cation. Here, Cs^+ interacts with the carbonyl group of T63 and lie below the carbonyl plane, resulting into lowest ΔE_{elstat} for Cs^+ . Dispersion also contributes to the total bonding energy (3.33 to 15.36 %) and the contribution increases as ion moves towards the deeply buried binding pockets. Owing to the low charge by radius ratio of Cs^+ , dispersion contributed more to the binding energy as compared to Na^+ and K^+ .Orbital interactions (ΔE_{orb}) majorly come from the metal-carbonyl binding interactions via covalent interactions. Thus, increase in the number of carbonyl ligands at the binding periphery of cation increases the orbital energy contributions, which is reflected in the higher value of ΔE_{orb} at the S3 (~23-26 %) and S4 (~25-27%) as compared to S_{ext} (~11-13 %).

3.3.7. Metal Ion Permeation Through NaK Channel

One of the intriguing observation made by Alam and Jiang[150] while analysing the structural detail of ion-occupied NaK channel is that its SF hardly rearranges in response to the ions. In view of this, we first investigate the filter's structural 'integrity' during single ion permeation through it, while the channel is embedded in explicit solvent environment. After the completion of a MtD event i.e. complete permeation of ions through the filter, we utlized the channel trajectories for this purpose. MtD generated atom trajectories are then subjected to Monte Carlo simulated annealing treatment[192] in order to find the best possible route for a size-adjustable sphere to swim through the channel. Graphical presentation of the annealed data is shown in Figure 3.4. The average channel pore radius is obtained from simulation trajectory. Upon careful inspection of the ion-permeation trajectories, we have sometimes observed carbonyl flipping at the SF (in the absence of cation). However, frequencies of such events are indeed very low. In the presence of ion, like in experiments,[150] here we did not observe any major changes in SF. Clearly no significant deviations in the pore radius (see Figure 3.4b) are observed with respect to the size of the permeating ions. This observation further adds to the gross nonselective feature of NaK, although, as presented above, the filter possess the site-specific selectivity characteristics at the "*microscopic*" level. Further, we analyzed the MtD trajectories for the calculation of van der Waals and electrostatic interaction energy of the system during the ion translocation process. Favourable ion permeation in the channel depends on the interaction energy contributions from various sub groups (ion-SF, SF-water and ion-water) involved in the process. We found that at the bulk, ion-water interaction persists. As the ion enters the SF, favourable ion-SF interaction tends to increase (more negative) while partial dehydrating of ion reduces ion-water interaction (more positive).

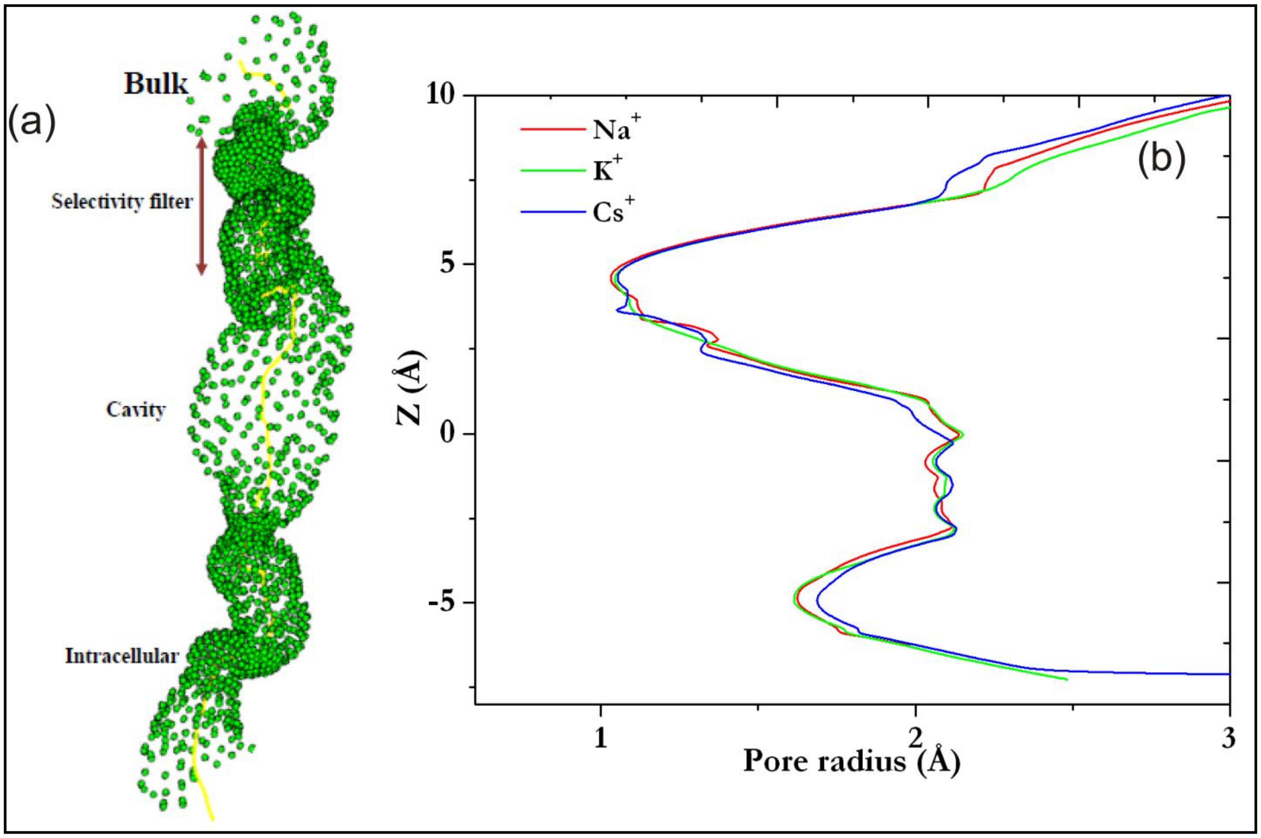

Figure 3.4: (a) Pore internal surface profile of NaK ion channel. The dots show the locus of the outer sphere of a flexible sphere with variable radius, squeezing through the pore, which finally sketches the central line of the pore (shown in yellow). (b) Plot of distance along channel axial position (Z) vs. pore radius as obtained from the average structure of the ion-SF trajectories for the three ions using HOLE suite of programs.[192] Axial position is measured from the average center of the SF.

The average of interaction energy of all the components showed a linear time dependent variation, with little change between the permeating ions, indicating the nonselective nature of ion channel. However, changes in the variation of the individual components (such as, ion-SF) of these interaction energies drastically differ from one ion to the other. This result is again a manifestation of site-specific ion-filter interactions, which can be further substantiated by an analysis of the coordination number of the permeating metal ions.

For the calculation of coordination numbers, distance of 3.2 Å was taken as the radius of first coordination shell for all metal ions. A plot of the total coordination number (with water and protein ligands) of the ions (Figure 3.5) reveals that all ions maintain a coordination number of 6-8 at the bulk. During translocation, a coordination number drop of up to four was noticed for all the three ions.

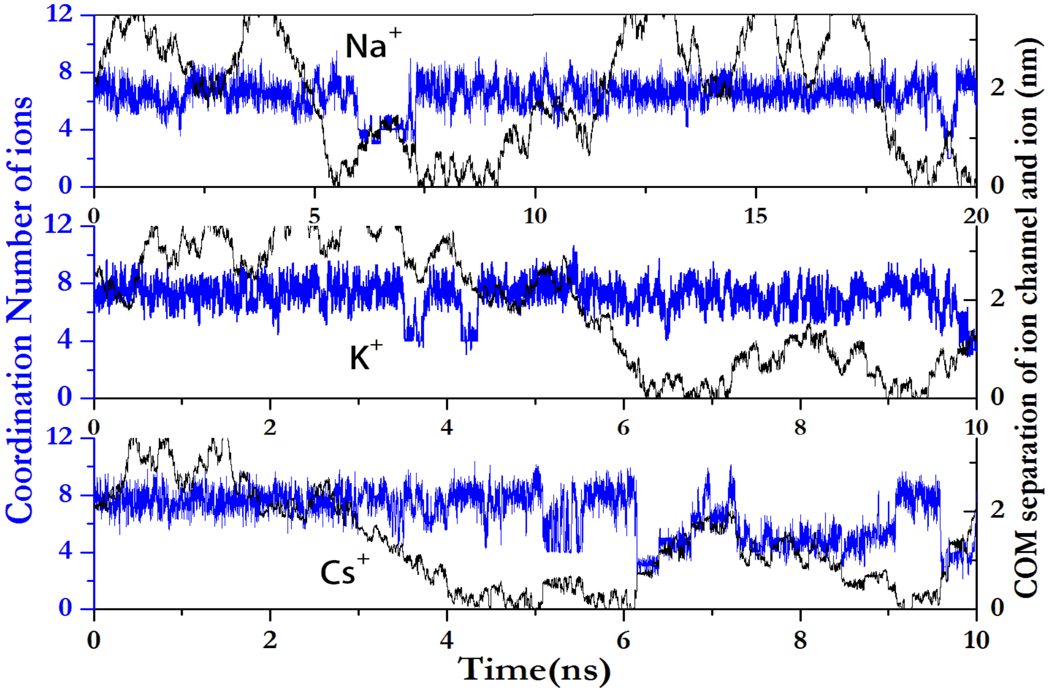

Figure 3.5: Change of total coordination number (water and protein ligand) of alkali metal ions (top panel: Na^+ , middle panel: K^+ and bottom panel: Cs^+) during their translocation through selectivity filter as obtained from MtD simulations. Axis on the right side of plot correspond the COM separation of ion channel and ion. Change of total coordination number of ions is indicated in blue whereas corresponding COM separation is shown in black colour.

In Figure 3.6, the results of the ion coordination numbers with the SF residues are presented in order to depict their participation and involvement during ion translocation. In this figure, the MtD CV (COM separation between NaK channel and the ions) is also plotted alongside as a function of MtD time.

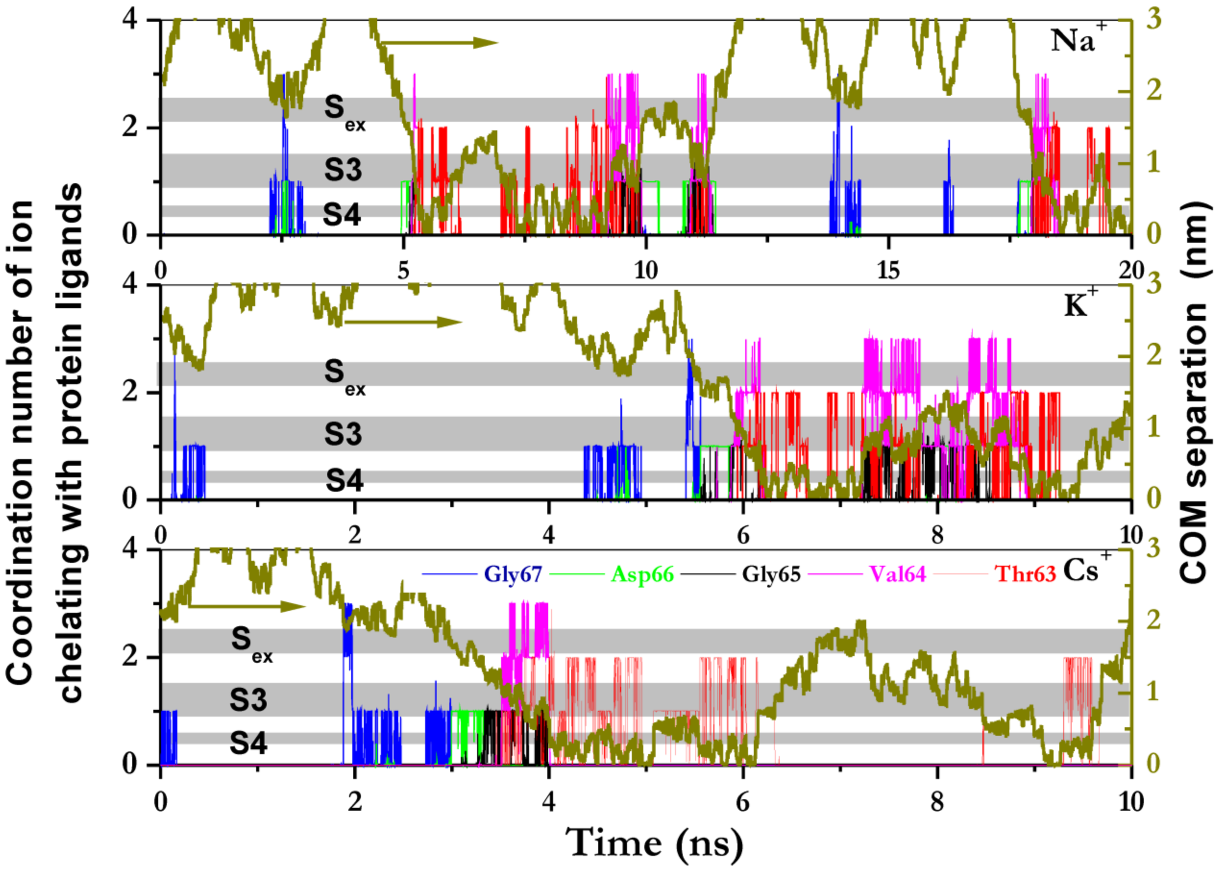

Figure 3.6: Change of coordination number of the ions (top: Na$^+$, middle: K$^+$ and bottom: Cs$^+$) with the protein ligand residues of the selectivity filter during their permeation. The different colours repsenting the ligands are: G67, blue; D66, green; G65, black; V64, violet; and T63, red. Axis on the left and right side of plots indicate contribution of different residues of the filter to coordination number, and COM separation of NaK channel and the permeating ions, respectively. Shaded horizontal strips in each of the plots indicate binding sites of the filter with respect to the COM separation, as indicated.

This CV, along with the participation of various residues in the SF, further helps delineating the locations of the binding sites of the filter. Among the five residues, major contributions from V64 (pink lines) and T63 (red lines) are evident in Figure 3.6, which is quiet expected due to the small pore size at sites S3 and S4.Importantly, due to the tangential alignment of G65 (black) and D66 (green) carbonyls with respect to pore axis in vestibular region, no significant contributions due to these residues onto total coordination are observed inside the pore. Expectedly, G67 (blue) is seen to contribute at the entrance quiet efficiently for all the ions, and specially for the bigger sized Cs^+ . Note that Cs^+ during 6-9 ns of the MtD result in Figure 3.5 does not coordinate with the protein ligands. Rather, during this time this has been found to coordinate with the channel water. The ion-channel COM separation data shows that ions starting from the bulk repeatedly enters and exits the channel during the MtD runs. Alongside these repeated events, the chealting ligands also respond in a systematic fashion. For example, G67 coordinates with Na^+ at ~ 2.5, 14, and 16 ns during the ions repeated trial to re-enter the filter. As told earlier, the accuracy and convergence[180] of MtD method is an outstanding issue and sufficient sampling that would guarantee a converged PMF profile is difficult to predict a priori. As a result, in the present Chapter, instead of generating the PMF directly from MtD, we use the method to explore the ion permeation pathway. Note that even though the reaction coordinate is defined exactly as a normal to the lipid bilayer, a straight line is usually not a proper reaction coordinate for complicated ion transport mechanism through confined space such as ion channels.[175] This is evidenced from Figure 3.5 where the time-dependent COM separation between the translocating ions and the channel can be seen to follow a path far from being a straight line. Once the pathway is detected, we use it to discover the converged results by US correction technique (see Computational Details for the method) using Equation 9. The use of MtD-US approach is an improvement over techniques of either of MtD or the US. MtD improves the possibility of exploring the low probability regions, leading to a more reliable description of the underlying free energy landscape, which is free from the ad hoc choice of a straight path as is often assumed by the users of the US method. On the other hand, US allows circumventing the convergence problem associated with the

MtD method. Thus the convergence problem in the MtD method can be avoided and the resulting PMFs are shown in Figure 3.7. We have ensured that the external area of the pore is sufficiently filled with the MtD hills bias such that the ions at the maximum distance from S_{ext} are well solvated, like the free ion in dilute solution. This also provided us a reference unbound state for subsequent estimates of PMF, which is equivalent to having the unbound ion and the channel in water medium.

The PMF results in Figure 3.7 suggest that the permeation of the three ions through the SF are a multistep process with free energy barriers and basins along the pathways. It is highly encouraging to note the resemblence of the selectivity order in each of the binding sites as obtained by the MtD-US method with those of the DFT results pertaining to ion exchange reactions. Moreover, the MtD simulations snapshots of the ion-ligand coordination structures pertaining to the S_{ext} and S3 sites are found to be similar to those obatined by DFT calculations (shown in Figure 3.3). Entry from bulk to the filter is manifested with a high energy barrier caused by the shading of water molecules of the hydrated ions. Contrary to earlier structural investigation[150], our calculations involving single ion permeation show that Na + binds preferentially at S_{ext} over the other two monovalent ions. At the vestibule the ions remian mainly diffused in the absence of a definite chelating ligand (no minimum is seen in the PMF profile). Note that the DFT results on the TM model representing the vestibule is at a variance with this finding pointing towards the weakness of the model. At the site S3, all the three ions exhibits free energy minima, *albeit* shallow. This indicates that S3 is mostly nonselective, however, as can be inferred from Figure 3.7 that K^+ preferentially binds at S3, corroborating well with the DFT results (Table 3.5). Na^+ is seen to be selective in between S3 and S4 regions. The selectivity of the ions at S4 remained unresolved (when compared with DFT calculations) in the MtD-US results probably because of the participation of water molecules residing in the immediate cavity of the filter that restores the hydration sphere of ions showing minima in the cavity region.

3. 4. DISCUSSION

3.4.1. Selectivity in nonselective NaK channel

Does NaK channel have selectivity? Ever since the SF structure of K^+ channel, responsible for selective mediation of ions has been known, the means by which selectivity is achieved raises several useful debates that have enriched the literature.

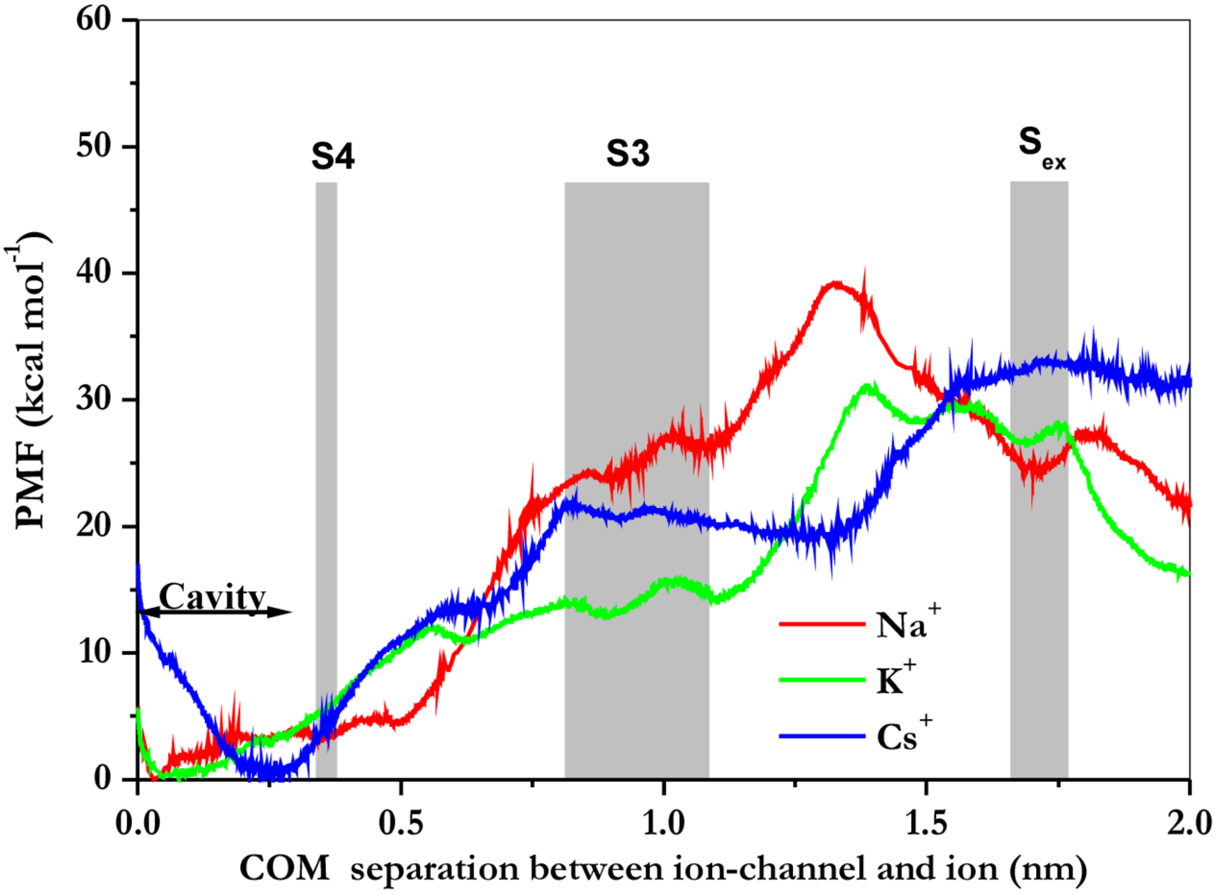

Figure 3.7:.The PMF profiles of alkali metal ions (Na^+ , K^+ and Cs^+) permeation as a function of COM separation between the NaK channel and the permeating ions (nm) are shown. The profiles are obtained after equilibrium US corrections of MtD generated free energy lanscapes. The minimum of the unbinding free energy for each of the ions is used as reference point to arrive at this plot. Shaded vertical strips indicate binding sites of NaK. Approaching towards the origin of the plot correspond to translocation of ions towards the central cavity.

The NaK channel having a similar overall structure as K^+, however, has been largely regarded as nonselective; equally permeable to Na^+ and K^+ . A few noteworthy contributions[151-158], in the field of nonselectivity in NaK focuses on the multiple ion occupancy of the channel. Whereas our molecular level knowledge of single ion permeation through NaK, free from all competing effects of 'rivalry' cations, remains incomplete. Present combined investigations using quantum and classical mechanics is an effort towards this direction with an aim to provide a greater insight to it.

Conclusively, in line with several other studies, we find that NaK is permeable to monovalent metal cations. Nevertheless, strongly 'site specific' selectivity does exist inside the pore (Table 3.5 & 3.6 and Figure 3.7). For instance, K^+ is found to have higher binding strength at the site S3, whereas Na^+ is seen to be selective at the boundary of S3 and S4. However, at least for single ion translocation, no ionic selectivity was observed at the vestibule site. As can be seen in Figure 3.7, the wide variations in the PMF profiles of the three individual ions, depth of the free energy wells and the height of the barriers, will certainly lead to variations in the conduction of the ions as one would infer from Kramer's rate.[159]

But question remains on the fact that what attributes selectivity to the specific binding sites in an otherwise nonselective channel? Like in K^+ channel,[166, 193-197] the combination of many interdependent factors, such as, coordinating environment, conformational constraints, and type of interacting ligands induce the site specificity. Our computed results suggest that even without the coordinated water molecules, smaller Na^+ can favourably occupy the plane of coordination centre formed by the four carbonyls at S_{ext} , while coordinated water molecules are needed for relatively larger K^+ and Cs^+ ion to make the favourable coordination (Table 3.4). This finding correlates well with several other studies,[167, 170, 198-200] where octahedron arrangement was found to be an important governing factor for favourable K^+ coordination. Stating this, we further emphasize that only a marginal selectivity difference at the S_{ext} between Na^+ and K^+ was observed (BFE differs only by ~4 kcal mol^{-1} , Table 3.6). This is not surprising as the solvent exposed face of S_{ext}

provides enough opportunity for both the ions to procure the suitable coordinating environment. This also stands true for other two sites (S3 and S4), where K^+ is observed to maintain the octahedron coordination arrangement, while Na^+ is too small to interact with all of the carbonyls and thus prefer to stay at the junction of two sites with total coordination number of four. Preservation of such necessary coordination numbers, particularly for Na^+ (total coordination number drops to four during translocation) and K^+ (maintains overall coordination number of eight), is largely maintained during the MtD analysis (Figure 3.5). Higher selectivity of K^+ at S3 as compared to S4 can be understood by the close inspection of optimized structures (Table 3.3). At S3, The comparable bond distances of K^+-$O_{V64(C=O)}$ (2.899-2.932 Å) and K^+-$O_{T63(C=O)}$ (2.807-2.816 Å) implies that K^+ can occupy the centre formed by eight carbonyls, which is certainly not the case at ‘site 4‘ where K^+-$O_{T63(OH)}$ bond length (3.045-3.195 Å) is noted to be significantly longer as compared to K^+ -$O_{T63(C=O)}$ (2.577-2.628 Å). NPA analysis at these sites suggest net charge transfer values of metals are in correlation with the charge density trend of alkali metals (Table 3.8). However, the computed trend does not harmonize well with the obtained BFE values. This again emphasize the importance of proper ligand orientations and other physico-mechanical factors for the site-specific selectivity at the binding pockets.

Table 3.8. Charge transfer from ligand (carboxyl, hydroxyl) to metal cations (Δq, a.u).

Binding Site	Na^+	K^+	Cs^+
S_{ext}	0.468592	0.308678	0.144325
S3	0.211734	0.088168	0.057804
S4	0.137355	0.108231	0.065678

In summary, like in the K^+ channel,[141, 143] the binding sites of NaK channel are also ion-specific. In the K^+ channel, however, all the four binding sites selectively binds to only K^+ ion. Whereas, here we have found that the binding sites of NaK possesses varying selectivity towards Na^+ , K^+ , and Cs^+ ions. For example, Na^+ favorably binds at S_{ext} (by ~ 2 kcal mol^{-1}) when compared with K^+ . Similarly, sites S3 and S4 preferably bind K^+ and Na^+ ions, respectively. All the binding sites are not selective towards Cs^+ (in comaprison to other two ions) and vestibule is the most non-specific towards any of the three binding ions. This renders overall nonspecificity in an otherwise ion-specific NaK channel.

3.4.2. Importance of Physico-mechanical constraints

Our present investigations also shed lights on the requirement of constraint for site selectivity. In NaK channel, presence of constraints due to the hydrogen bonding interactions between the carboxylate of D66 and G67-N68 peptide linkage restrict the movement of free moving G67. Important observations were reported in previous experimental studies[201] on the mutation of D66 with alanine residue, where such changes led to significantly higher flow rate for Na^+ and K^+ inside the pore. Our QM study predicts that substitution of the carboxylate group of D66 at S_{ext} by neutral methyl led to elongation of metal-ligand bond distance and shortening of metal-O_{water} bond distance (Table 3.3). For $K^+ \rightarrow Na^+$, the calculated $\Delta G_{ex}(\varepsilon)$ value is seen to reduce by 1-2 kcal mol^{-1} . Although this is not significant, allows us to infer that the presence of aspartate residue has indirect influence over the selectivity. This finding is reminiscent to the findings of Eisenman[202] that anionic field strength of the coordinating ligands can impel the selectivity and supports the claim of Thomas et al.[200] that "*slight constraints*" are indeed necessary to induce appreciable selectivity in binding sites of ion channel.

3.4.3. Interdependency of consecutive binding sites over ion selectivity

Previous experimental observations[148] indicated that the presence of contiguous binding sites could act as a decisive factor behind ionic selectivity. In view of this, we have also extended our study to find out the direct infleunce of consecutive binding sites upon selectivity trend. In this regard, we have compared the changes of structural parameters, alteration of the binding free energies of ions and subsequent modulation of ion exchange free energies in the truncated models (TM: contains stand-alone binding sites, Figure 3.1) with respect to the structure ‘B’ (contains more than one binding sites) (Tables 3.3, 3.5 and 3.6).

In contrary to Structure ’B’, vestibule at the TM model is free from the closest S3 site. Such miniature model now showed a preference order for the exchange reactions among the alkali metals : $K^+ > Cs^+ > Na^+$ at $\varepsilon \geq 10$, which otherwise doesn’t act as a favourable binding site in structure ’B’ (Table 3.3 & 3.5). For metal-bound S3 truncated model, upon optimization only marginal structural changes (except for Na^+) were noted (by $\sim$0.15 Å) with respect to metal-bound structure ‘B’ (Table 3.3). This led to similar binding (Table 3.5) and ion exchange energies (Table 3.6) as compared to structure ‘B’, and thus retains the same selectivity trend. In contrary, significant geometric changes were observed at S4 truncated model, where lengthening of M^+-O_{T63} bond length is noticed with respect to the metal-bound structure ‘B’ (by $\sim$0.25 Å). Except for K^+ , significant shortening were visible in M-$O_{T63(OH)}$ bond distances (by more than 2 Å) for Na^+ and Cs^+ . Owing to the absence of S3 in the truncated model of S4, Na^+ and Cs^+ ions are enforced to occupy unfavourable octahedron coordination geometry. These have rendered significant changes in ΔG values and altered the observed selectivity order with respect to structure ‘B’, making Cs^+ at $\varepsilon \leq 20$ to be the most selective ion, while Na^+ has the least binding preference. These observations are analogues with the previous findings on K^+ channel,[160, 166, 170] where greater possibility of attaining suitable coordination geometry was shown to be the determining factor to arrive at a K^+ selectivity over Na^+ . These results further allow us to infer that consecutive binding sites may have their influence over each other during metal binding. Thus over simplified model with stand-alone binding sites may not truly reflect the actual binding and selectivity trend of ions when compared with the more realsitic model, where all the binding sites act in unison inside the permeating SF.

3.4. Inference on Cesium Migration *via* Ion Channel Route

Our results on structural and binding aspects of Cs^+ indicate that in all the binding sites inside the SF, Cs^+ has moderate selectivity. In all occasions, obtained negative BFE values (Table 3.5) iterate that Cs^+ can favorably bind inside SF. Moreover, resultant PMF *via* MtD simulations (Figure 3.7) shows that Cs^+ permeation through the SF of ion channel is feasible, however, rate of permeation is expected to be slower than K^+. Furthermore, Cs^+ translocation through the filter does not change the pore radius profile. All these results and observations suggest that cesium can indeed use ion-channel route for possible migration to enter into the biological life cycle.

3.5. Conclusion

In this Chapter, we elucidate and rationalize the structure, binding and translocation of cesium along with other alkali metal ions through NaK ion channel in a counter ion-free non-competitive environment. Due to the absence of any inter-ionic electrostatic repulsion, the binding and permeation of a single ion can be imagined to depict a clear picture of the microscopic selectivity in an otherwise nonselective NaK channel. Our combined studies on such system using both density functional theory and molecular dynamics simulations in explicit water medium led us to summarize the following conclusions.

(a) Similar to earlier findings, we also found that the channel is permeable to all the three monovalent cations studied here. However, the filter is shown to possess strong site-specific selectivity. Channel forming proteins are relatively flexible structures, more so in the presence of water, that undergo rapid thermal atomic fluctuations often larger than the small difference in ionic radius between the three ions. The signature of site-specific selectivity is however found to be so pronounced that even with the inclusion of explicit water in the MtD calculaton, the selectivity trend of the permeating ions remained intact throught out the filter that corroborates well with the implicit solvent model results of DFT calculations. As explained, conformational arrangement, type of coordinating ligand and constraints present in the system are found to be the main governing factor to fine tune the selectivity.

(b) We found S3 and S4 are more selective towards K^+ and Na^+ , respectively. K^+ is observed to prefer octahedron coordination environment whereas Na^+ is found to remain favorably bound at carbonyl plane formed at the junction of S3 and S4 . However, presence of cation at S3 can force Na^+ towards S4 site to attain pyramidal conformation involving water from the cavity. Further, a marginal selectivity is noted for Na^+ over K^+ at S_{ext}. The vestibule region is completely nonselective in nature and the presence of inter-ionic repulsion is essential to prompt ion binding at the vestibule. The optimized structural coordinates and selectivity orders are found to be in excellent agreement with the available crystal structures.

(c) we find that the use of over simplified synthetic models without the presence of consecutive binding sites may lead to wrong estimation of the selectivity trend. This explains the indirect influences of nearby binding sites over ionic selectivity of a particular site. Our EDA analysis suggests that the metal binding is dominated by electrostatic interaction. Nevertheless, orbital interactions may also contribute significantly at the deeply buried sites (S3 and S4).

(d) As an important conclusion, we found Cs^+ can favorably bind at S3 binding site and its permeation through the SF of ion channel is energetically feasible. Moreover, such permeation does not led to structural deformation at the SF. Hence, ion channel route can be considered as as one of the transport pathway for Cs^+.

Finally, it is important to emphasize that, unlike QM methods the MtD-MD methodology is devoid of several electronic effects such as polarization, charge transfer phenomena, which has been known to affect metal binding. These aspects are incorporated and addressed in Chapter 4. Nevertheless, present combined investigations using QM and MtD-US-MD methods have provided very useful insights over the bottleneck of ion translocation phenomenon.

CHAPTER –4

Permeation of Strontium and Other Divalent Ions through Non-selective NaK Ion Channel

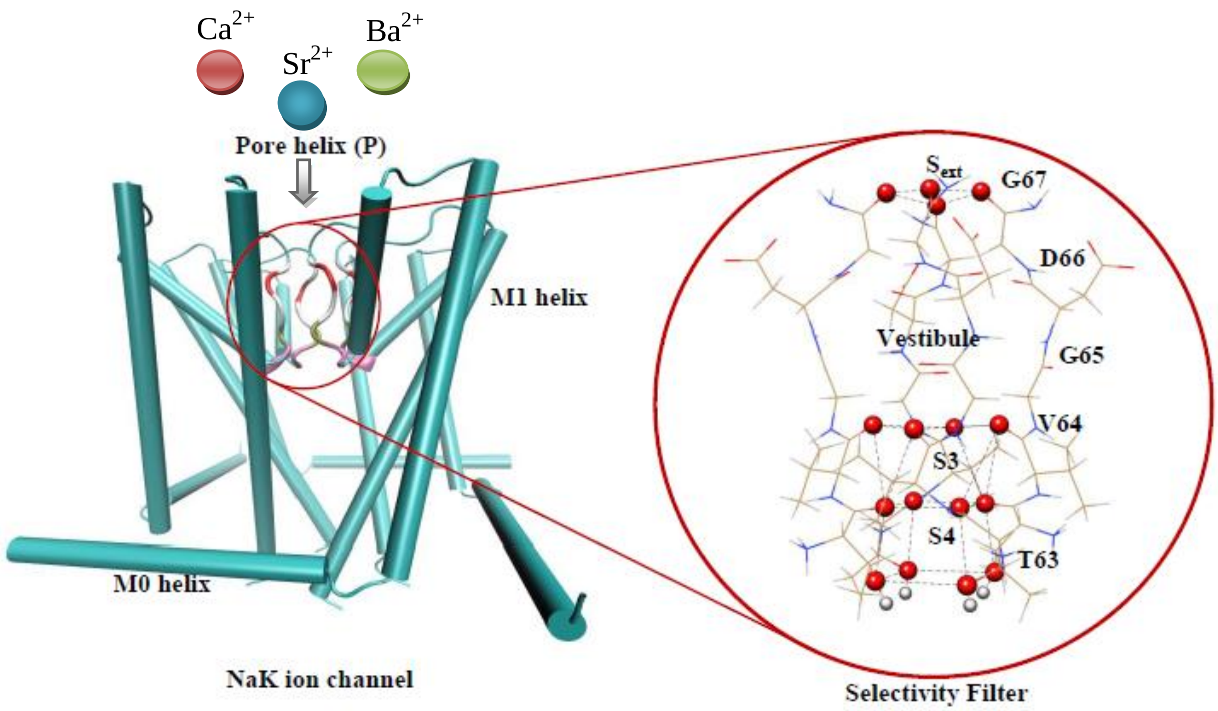

4.1. Introduction

The ionic balance inside the intracellular medium is maintained by the presence of pore forming transmembrane protein like Na^+ and K^+ ion channel.[203] These ion channels possesses particular amino acid sequence at the selectivity filter (SF) to selectively mediate the translocation of a particular ion. For instance, K^+ ion channel with SF sequence of **TVGYG** only permits the permeation of K^+ through the pore.[203] Recently reported, NaK ion channel from *Bacillus cereus*, is an exception as it allows permeation of all alkali metals and mostly remain non-selective.[149, 164] In comparison to SF of K^+ ion channel, only one change at the amino acid sequence in SF of NaK ion channel (**D** in place of **Y**; **TVGDG**) led to its intrinsic non-selective feature. In Chapter 3, we have found that the non-selectivity in NaK ion channel does not necessarily correspond to complete annihilation of selectivity at the specific binding sites of SF (Figure 4.1: S_{ext}, vestibule, S3 and S4). Instead, site-specific selectivity do exist inside SF but no monovalent ion has supreme selectivity at all sites, which eventually give rise to the overall non-selective characteristic.[204]

One of the unexplored and rather interesting features of the NaK ion channel is its ability to permeate divalent ions as well such as, Ca^{2+} and Ba^{2+}. In this regard, Jiang and co-workers[201] investigated the Ca^{2+} specificity inside SF and pinpointed the unique chelation mode on Ca^{2+} binding in two distinct binding sites based on crystal soaking experiment. Reported experiment revealed that Ca^{2+} can possibly permeate as well as block the SF to act as a "*permeant blocker*". Further, crystallographic presence of Ca^{2+} at the S_{ext} site suggested the external entrance as other possible binding site for Ca^{2+}. However, presence of interfering multiple ions (other than divalent ion) inside the SF serves as a bottleneck to conclusively comment on the equilibrium site-selectivity and stability of divalent ions in all these binding sites. Among other divalent metals Sr^{2+} requires a special mention due to its several radioactive isotopes. Keeping in mind the similar size of Sr^{2+} and K^+, question also remains whether Sr^{2+} can use NaK ion channel as a transport route in natural environment. Energetics of such permeation events along with structural aspects of divalent metal binding is still largely unknown. Question remains on what makes Ca^{2+} a "*permeant blocker*" ion; secondly, how and at what energetic cost, chemical congener Sr^{2+} as well as Ba^{2+}, a potent blocker of K^+ ion channel, permeate the SF of NaK ion channel. How their translocation energetics differ from the monovalent ion, such as, K^+?

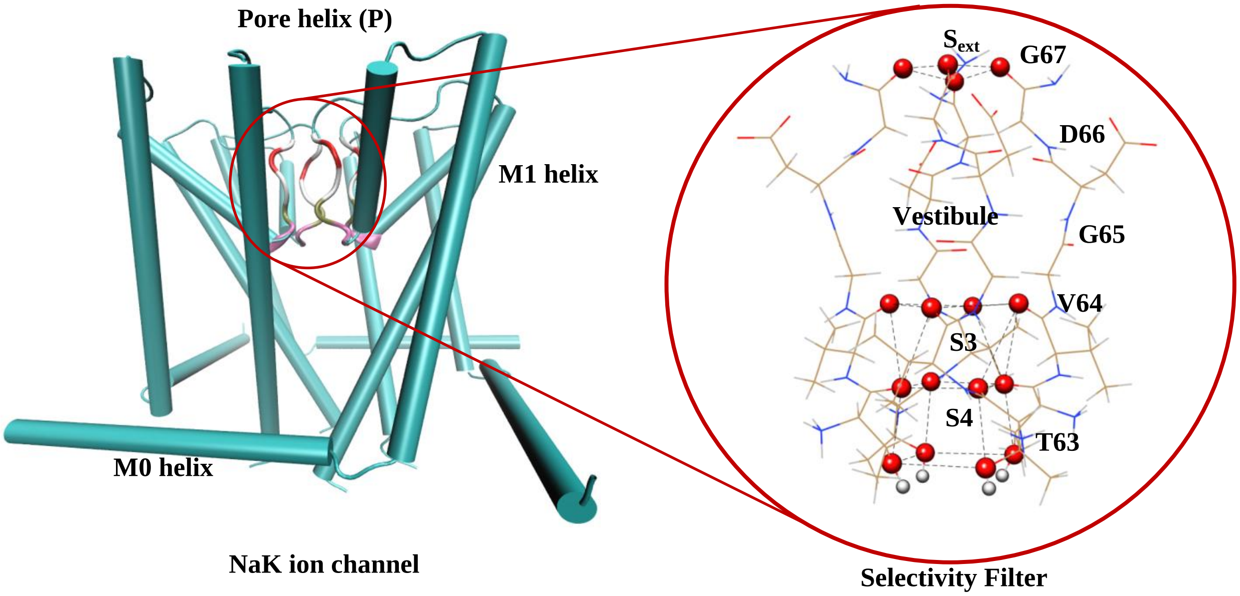

Figure 4.1: Equilibrated Structure of NaK ion channel is shown at the left side. Selectivity Filter (SF) is shown in licorice presentation. Zoomed view of SF is shown at the right side of the figure with the following color schemes: Tan, C; blue, N; red, O; and gray, H.

Use of highly accurate first principle based quantum mechanical methods such as density functional theory (DFT) are limited for investigations of ion channel associated problem due to their prohibitively large system size. In Chapter 3, we have found that proper modelling of ion-channel in combination with appropriate computational technique can accurately predict/determine the structure and binding free energies of ions in the specific binding pockets of ion-channel.[160-161, 204] Due to the static nature, DFT results are meant to provide equilibrium selectivity at the binding sites. On the other hand, computational methodologies such as biased/unbiased molecular dynamics (MD) simulations are now widely used to explain the ion-permeation events.[155-156, 197] One of the classical problems one faces while working with standard forcefield based method is the absence of polarization effect (for water as well as ions), which often turn out to be the crucial factor in depicting true picture of ion's minimum energy permeation pathway through SF.[205] Even though polarizable water models are available, incompatibility of using fully polarisable forcefield model for water with non-polarizable protein model is evidently a bottleneck, which deprives the direct inclusion of the polarizability factor into the results. One way to circumvent this problem and incorporate polarizable environment (implicitly) is to use mean-field polarizable model of water. In this regard, scrupulous investigations[206] provided information on what conditions polarizable Hamiltonians are transformed to non-polarizable ones. In the mean field polarizable water model (MFP), charges on atoms of water molecule is locally adjusted, on-the-fly, self-consistently to reflect the local environment (e.g., the protein interior). In effect, the resulting effective polarizable model implicitly includes the electronic screening effects into an otherwise non-polarizable model system and, hence, remains computationally as efficient as the standard non-polarizable force field calculations which scales the atomic charge by the inverse of electronic part of dielectric constant of water.[207] Similarly, scaling the ionic charge based on the dielectric constant of the dissolved medium (for water, the scaling factor is 0.75) to incorporate electronic continuum correction is also proven to improve the agreement between simulation and experimental observations.[208] Thus, combination of both methods (QM and MD) with appropriate computational technique is expected to give wealth of information on the structure, binding, selectivity and energetics of ion permeation though the SF. In this Chapter, we use aforementioned methods with the aim of deciphering the permeation events of divalent ions (Ca^{2+}, Sr^{2+} and Ba^{2+}) through NaK ion channel. The structure, binding and site-specific selectivity of divalent metals ions are calculated using density functional theory (DFT) based calculations, while well tempered metadynamics simulations (Wt-MtD) in a polarizable environment are applied to understand the energetics of such ionic translocation. Detail account on the computational protocol used in this work is elaborated next in the computational methods section. Finally, we compare the site specificity and permeation energetics of divalent ions with that of K^+ to comment on the differences between divalent *vs.* monovalent ion translocation.

4.2. Computational Methods

4.2.1. Quantum Mechanical Study

In Chapter 3, using Density functional theory (DFT), we elucidated the structure and binding of monovalent ions (Na^+, K^+ and Cs^+) to all binding sites inside selectivity filter (SF) of NaK ion channel.[204] The applied methodology, structure model and optimization protocols were reported to produce excellent correlation with the available experimental information. Hence, here we have adopted same methodology for divalent ions and details of the methodology can be found in Chapter 3. Below provides a brief description on the applied computational level.

(I) Choice of Model Structure: The SF of wild type NaK ion channel possess amino acid signature $_{63}$TVGDG$_{67}$.[209] Two different structure models (**A** and **B**), which were built from truncated SF of NaK ion channel, are chosen to investigate the site-specific binding of divalent ions (Figure 4.2). Peptide junction of both the structures with -CO-NH- group are replaced with -CO-NH(CH_3) to prevent the hydrogen bonding formation between the sub units. Structure **A** contains $\mathbf{S_{ext}}$ binding site and composed of G67 and D66 residues. Although D66 residue does not directly participate in metal binding, presence of hydrogen bonding between its carboxylate group and peptide linkage of G67-N68 residue is reported to have unique indirect influence over $\mathbf{S_{ext}}$ binding site. Thus, inclusion of D66 in Structure **A** is important to depict the accurate structural aspect and true metal binding free energies. Structure **B** consists of two amino acids (V64 and T63) to contain three binding sites namely vestibule (coordinate metal *via* carbonyl of V64 and water molecules), S3 (coordinate metal *via* carbonyl groups of V64 and T63) and S4 (coordinate metal *via* carbonyl and hydroxyl groups of T63). Among these binding sites, vestibule is not considered in this study due to its non-specific character as observed in experiments[210-211] and inferred from our computational investigations in Chapter 3.[204]

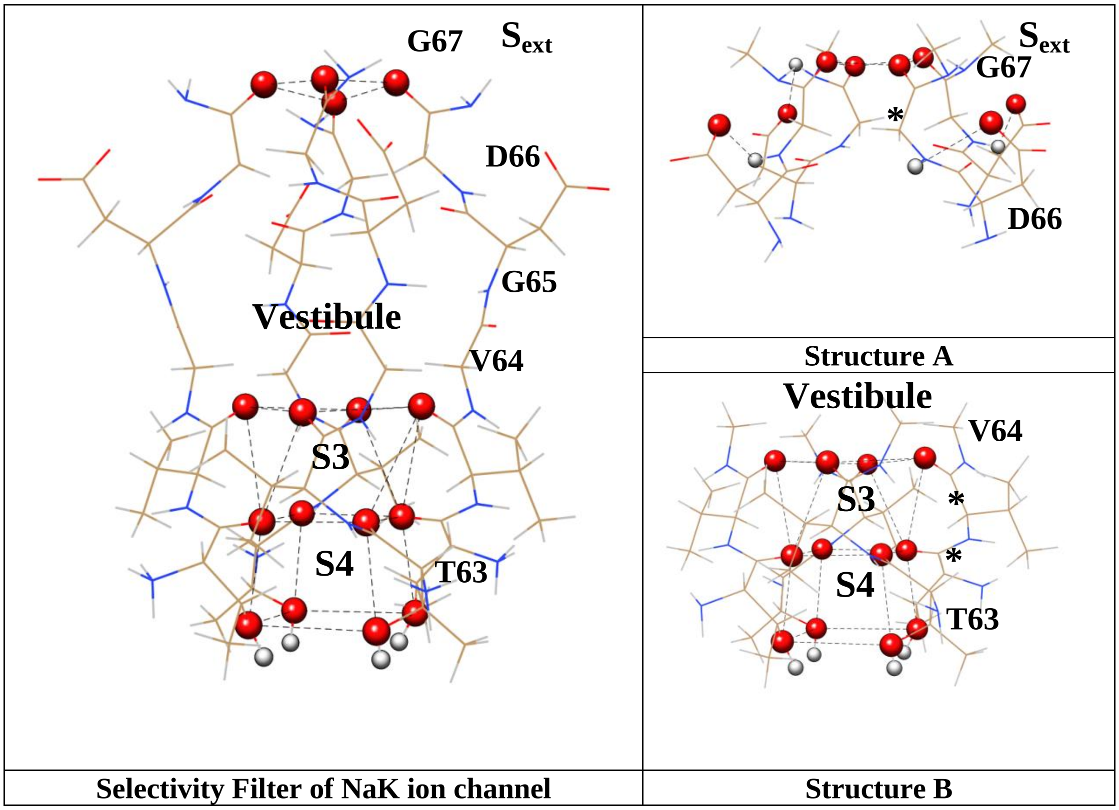

Figure 4.2: Left panel is the entire SF of NaK channel with amino acid sequence $_{63}$TVGDG$_{67}$. Structure A and B are truncated model from SF which have been utilized to perform DFT calculations. Color schemes used are yellow, C; blue, N; red, O; and gray, H. Realistic models of the SF binding sites, structure A, and structure B that are shown. Coordinates of selected Cα atoms of structures, A and B, shown with an asterisk in the model, are frozen in order to preserve the optimum pore radius.

(II) <u>Optimization protocols</u>: Geometry optimizations of all structures are carried out using TURBOMOLE 6.6 package[212] in gas phase with pure GGA density functional BP86[91, 213] and medium sized def2-SV(P) basis set.[93] Notably, the usage of large basis set are previously reported to have negligible effect on the optimized structures and energetics. Tighter convergence criteria

(10^{-8} eV) are applied for all calculations. As justified in Chapter 3,[204] few selected Cα atoms of the structure A and B are kept frozen during DFT optimization in order to preserve the optimum pore radius of binding sites. Further, analytical frequency calculations are performed using AOFORCE module to verify the structure as the minima in potential energy surface. Most of the structures are found to have no imaginary frequencies with the exception of a few, ranging between 5-30i, which can be attributed to the frozen coordinates. We believe that the presence of such small imaginary frequency is expected to have negligible effect[168] on the structure and energetics trend. In all calculations, only real modes are considered for free energy calculations. Single point calculations on the optimized structures are performed at B3LYP[96-97]/TZVP[98-99] level with the incorporation of Grimme's three body dispersion correction[165] (D3) using ORCA 3.0.3 program package.[214] In all calculations, coulombs integrals are computed using corresponding auxiliary basis set (def2-SV(P)/J for optimizations; TZVP/J for single points) by invoking Resolution of Indentity (RIJ/RIJCOSX) approximations. Counterpoise corrections are previously[204] seen to have only small effect (in the range of 1-3 kcal mol^{-1}) on energetics, hence not incorporated in the final results.   The effect of different dielectric media (ε= 5, 10 and 20) into the single point calculations are modelled using COSMO continuum solvation model.[215]

(III) <u>Reaction Schemes</u>: Binding free energies (ΔG_{bind}) of all divalent metal ions are calculated at temperature 300 K using following reaction schemes

$$S_{ext} + M(H_2O)_n{}^{2+} = S_{ext}\,.M^{2+}(H_2O)_m + (H_2O)_{n-m} \qquad (1)$$

$$S3/S4 + M(H_2O)_n{}^{2+} = S3/S4.M^{2+} + (H_2O)_n \qquad (2)$$

Apparently, in ion permeation events, hydration energy of metal plays crucial role in binding free energy calculations. Choice of hydrated metal structure is based on the earlier reported studies by us and other.[216-219] For Ca^{2+}, hexa hydrated structure is taken for the study while hydration number of eight is considered for the primary hydration shell of Sr^{2+} and Ba^{2+}. Further, in order to validate the applied solvation model, hydration energies are calculated which are noted to follow the experimental trend (Table 4.1).[116]

Table 4.1. Calculated structural parameters and hydration energies of divalent metal ions

Hydrated Metal	Used equation	M-O (Å)	Calculated	Experimental[a]
$Ca(H_2O)_6^{2+}$	$M^{2+}(g) + (H_2O)_n(aq) = M^{2+}(H_2O)_n$ (aq)	2.328-2.337	-357.5	-360.0
$Sr(H_2O)_8^{2+}$		2.528-2.766	-346.3	-330.1
$Ba(H_2O)_8^{2+}$		2.678-2.995	-320.4	-302.9

[a] values are taken from Ref no. 116

Ion exchange free energies are calculated for divalent ions, using following equations, with respect to K^+ to gain comparative insight on divalent vs. monovalent ion binding at the binding sites of SF.

$$S_{ext}\,.K^{+}(H_2O)_4 + M(H_2O)_n^{2+} = S_{ext}\,.M^{2+}(H_2O)_4 + K(H_2O)_6^{+} + (H_2O)_{n-6} \qquad (3)$$

$$S3/S4.K^{+} + M(H_2O)_n^{2+} = S3/S4.M^{2+} + K(H_2O)_6^{+} + (H_2O)_{n-6} \qquad (4)$$

4.2.2. Molecular Dynamics Study

Equilibrated structure of NaK ion channel (PDB ID: 2AHY) is taken from our earlier investigations[204] described in Chapter 3. Four transmembrane helix (M1), each containing 104 residues, form a tetrameric scaffold to create a pore helix (P), which in turn possess the SF (Figure 1). The presence of interfacial helix (M0) maintain the structural integrity of the ion channel and mediates the opening and closing of ion channel, however that does not cause any structural change in the ion translocation scenario.[211] To save computational time, lipid membranes are not used, instead, similar to our previous study, four selected Cα atoms of M0 helix are tethered with position constraint of 2.4 kcal mol^{-1} Å^{-2}. Such tethering technique ensures the close proximity of M1 helices that maintains the structural integrity of the ion channel without affecting the overall structure of SF. In effect, the applied strategy mimics the presence of lipid membrane without adding further computational burden.[175]

(I) Simulation protocol: Molecular Dynamics (MD) simulations on NaK ion channel are performed in GROMACS 4.0.7[104] platform using amder99 force field. Prior to simulation, ion channel is solvated in a box of size 9×9×9 nm^3 containing 22017 water molecules. Divalent ion is placed around 3 Å away from S_{ext} in the extracellular medium. Electro-neutrality of simulated system is maintained by adding 14 Chloride ions. The complete solvated system is comprised of 72910 atoms. Before equilibration, energy minimization steps and successive positional restraint simulation of 800 ps are performed on the system in non-polarizable TIP3P water model.[177] Unless mentioned otherwise, final equilibrium simulation on the resultant structure are performed for 10 ns using MFP/TIP3P water model.[207] In MFP/TIP3P water model, electronic screening effects are treated by adjusting the atomic charges of the water molecule based on the local atmosphere in a self consistent manner. Thus, it implicitly incorporates the electronic polarizibility factor at the same non-polarizable model framework. In this way the existing issue of incompatibility of polarizable water model with standard non-polarizable force field of protein is overcome in a computational efficient manner.[207] Similarly, ionic charge (M^{2+}: effective charge: 1.5e) of divalent metals (M^{2+}=Ca^{2+}, Sr^{2+} and Ba^{2+}) are also rescaled by a factor of 0.75 (derived by the inverse of electronic part of aqueous phase dielectric constant, ε_{el}=1.78) to introduce electronic continuum correction into the calculation.[208] Introduction of above correction is expected to deal with local environment changes during ion permeation from bulk to interior of the protein. In all simulation, Nose-Hover thermostat with coupling constant 0.1 ps is used to maintain the temperature of the simulation box at 300 K. Particle-mesh Ewald (PME)[111] is invoked to take care of long range electrostatics, while for short range electrostatic and van der Waals interaction a cut off of 14 Å is applied. LINCS algorithm[220] is introduced to constrain bond between hydrogen and the heavy atoms at their equilibrium lengths. The resulted equilibrated structures are further used for subsequent well-tempered metadynamics (WtD-MtD) simulations.

4.2.3. Well-tempered Metadynamics Simulation Study

Ion translocation through ion channel happens in microsecond time scale. Hence, use of standard equilibrium simulations are not an option to investigate this phenomena. One way to circumvent the problem is to use biased non-equilibrium simulation technique such as metadynamics (MtD) simulations, which accelerate the rare event by depositing Gaussian shaped history dependent biased potential. The measure of applied biased potential is determined by the height (H) and width (σ) of the deposited Gaussian and act as a function of reaction controlling collective variables (CV). However, the obtained potential mean force (PMF) of the reaction using standard MtD simulations often has to deal with convergence related issues. Continuing the simulations in order to achieve the required convergence, might further led to unphysical configurational space exploration. WtD-MtD, a variant of MtD technique, provide solution to this problem by progressively scaling the height of deposited Gaussian bias to achieve at a fictitious higher temperature (T+ΔT).[221] The right choice of 'H', 'σ' of Gaussian with appropriate BIASFACTOR ((T+ΔT)/T) helps exploration of relevant configurational space in limited time.

In this Chapter, we have used WtD-MtD method to enforce the ion translocation from the extracellular surface towards the intercellular cavity. Following parameters are chosen for the simulation: H= 1 kcal mol^{-1}; σ= 0.15 nm; BIASFACTOR = 25. Convergence of the resulted free energy surface (FES) plot is tested by observing the decrease of added hill with respect of time. Finally, PMF is generated considering the minimum of ion binding free energy as the reference point. All WtD-MtD simulations are performed using PLUMED 1.3[178] plug-in patched in GROMACS 4.0.7 platform.

4.3. Results and Discussion

4.3.1. Analysis of optimized Structures

For DFT calculations, all other binding sites (S_{ext}, S3 and S4) except vestibule are considered for binding and ion-exchange free energy analysis since vestibule site is highly non-specific in nature.[164, 201, 204] Optimized structures and their structural parameters are depicted in Figure 4.3 and Table 4.2. At $\mathbf{S_{ext}}$, ions can interact with four carbonyl groups of G67 residues while two to four water molecules remain bound to the metal centre to maintain favourable coordination environment.

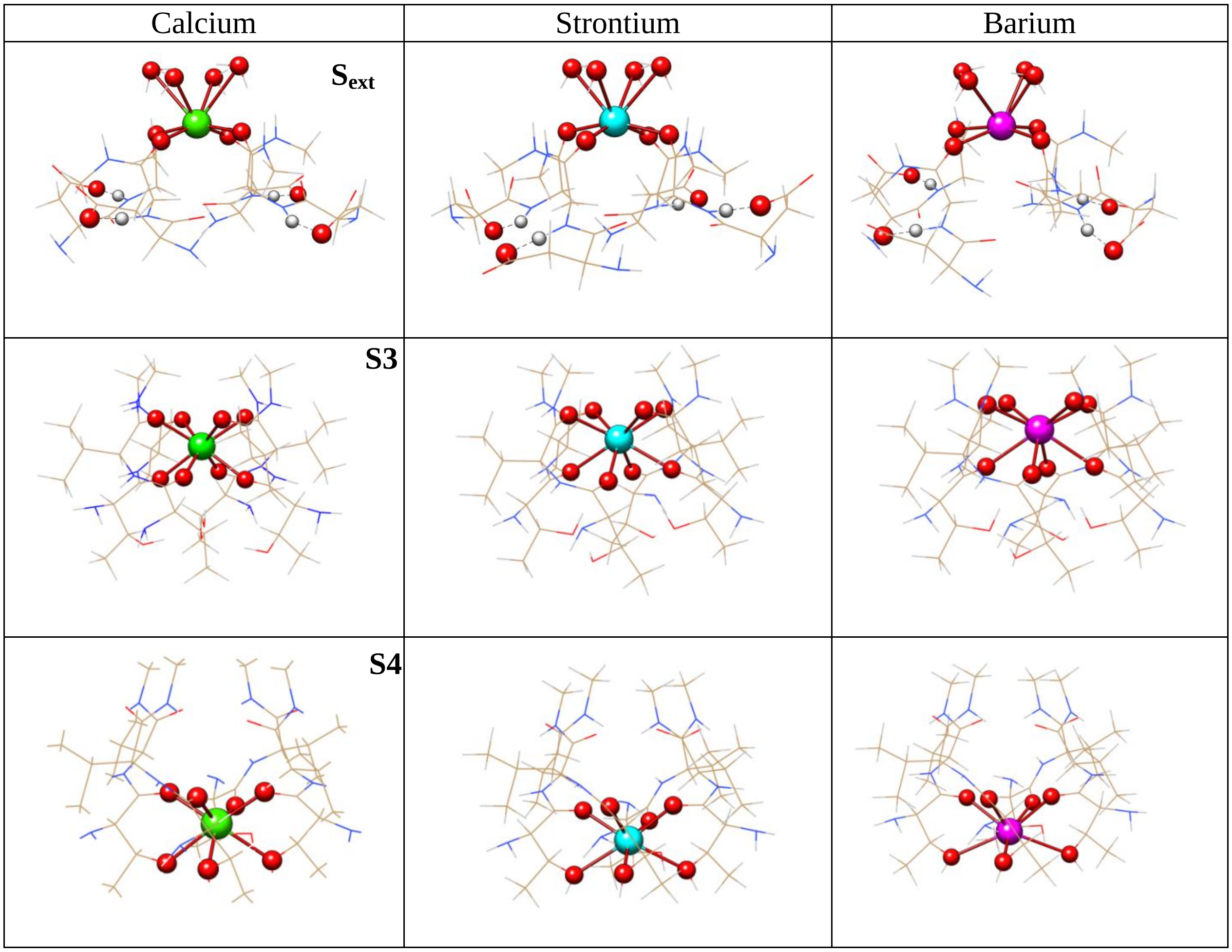

Figure 4.3: Divalent metal ion-bound optimized structures of the selectivity filter of NaK for the three ions Ca^{2+}, Sr^{2+} and Ba^{2+} as obtained from the DFT calculation. Top panel: external binding site, Sext; middle and bottom panels are for binding sites S3 and S4, respectively. Color code: red = oxygen, blue = nitrogen, and yellow = carbon, light grey = hydrogen.

Although D66 does not participate directly in metal binding, we have noticed presence of strong hydrogen bonding interaction ($O_{COO(D66)}$-$H_{NH(G67)}$: 1.504-1.637 Å for Ca^{2+}; 1.446-1.625 Å for Sr^{2+}; 1.431-1.594 Å for Ba^{2+}) between carboxylate of D66 and -NH group G67 residue which is in line with the previous experimental investigations.[201] For all metal ions, M-O_{wat} bond distances are seen to be longer than M-O(=C)$_{G67}$ bond length suggesting comparatively weaker involvement of water molecules in binding. In close match with reported x-ray structure (PDB ID = 2AHY), Ca^{2+}-O(=C)$_{G67}$ bond distances are noted to be of 2.295-2.344 Å.

Table 4.2: Calculated Structural Parameters (bond length, Å) for Metal Ions at Different Binding Sites of the Selectivity Filter of the NaK Channel.[a]

Binding Site	Ion	M-(O=C)	M-OH_{Thr63}	M-O_{water}
S_{ext}	Ca	2.295-2.344 (2.20, 2.24)[b] (G67)	-	2.506, 2.537, 3.148, 3.203 (2.43)[c]
	Sr	2.456-2.514 (G67)	-	2.734, 2.786, 2.802, 2.946
	Ba	2.619-2.679 (2.73)[c] (G67)	-	2.870, 2.896, 2.930, 3.008 (2.94)[c]
	K	2.624-2.649 (G67)	-	3.053, 3.106, 3.114, 3.175
S3	Ca	2.457-2.480 (V64) 2.476-2.505 (T63)	-	-
	Sr	2.586-2.604 (V64) 2.587-2.609 (T63)	-	-
	Ba	2.729-2.737 (V64) 2.738-2.762 (T64)	-	-
	K	2.899-2.932 (V64) 2.807-2.816 (T63)	-	-
S4	Ca	2.245-2.583 (T63)	2.543-2.680, 5.444	-
	Sr	2.432-2.515 (T63)	2.786-2.834	-
	Ba	2.574-2.683 (T63)	2.932-2.971	-
	K	2.577-2.628 (T63)	3.045-3.195	-

[a] values for K^+ are taken from Chapter 3. [b] values in bracket correspond to x-ray data from crystal structure (PDB ID: 2AHY). [c] values obtained from ref no. 164.

Further, out of four only two water molecules are seen to interact strongly (M-O_{wat}: 2.507-2.537 Å) to maintain overall coordination number to six, similar to hexa-hydrated Ca^{2+} model. On the contrary, similar to K^+ binding at the S_{ext} site octahedron coordination environment for Sr^{2+} and Ba^{2+} is attained by the four water molecules. Compared to K^+, Ca^{2+}-O(=C)$_{G67}$ bond distances are shorter by 0.3 Å. However, with the increase of ionic size from Ca^{2+} to Ba^{2+}, metal-carbonyl bond length become comparable with K^{+}. Optimized average bond lengths for Ba^{2+}-$O_{water/G67}$ are noted to be within ~0.1 Å from experimental data.[164]

At **S3**, divalent metals interact with eight carbonyls of V64 and T63 residues. Noticeably, calculated M^{2+}-$O(=C)_{V64}$ bond length are noted to be comparable with M^{2+}-$O(=C)_{T63}$ bond, which indicate irrespective of size, metal fits at the middle of the cavity. The chelation mode of Ca^{2+} at this site is unique considering the largely known binding motif at EF hand proteins. Perhaps, the presence of topological constraint enforce Ca^{2+} to interact with all carbonyl groups to maintain K^{+} like similar geometry at **S3**. Similar to S_{ext}, M^{2+}-$O(=C)_{V64/T63}$ bond distances get shorter from Ba^{2+} to Ca^{2+}. At **S4**, carbonyl and hydroxyl groups of T63 interact with metal ions. Notably, at **S4** binding site, computed M^{2+}-$O(=C)_{T63}$ bond distances are found to be significantly shorter (by ~0.2 Å) than at **S3** binding site, resulting in elongation of metal-hydroxyl bond distances. Interestingly, at **S4** site, Ca^{2+} interact only with three hydroxyl groups of four T63 residues (Ca^{2+}-OH_{Thr63} : 2.543-2.680 Å, 5.444 Å) hence favours to interact with overall coordination number of seven, similar to known binding motif of classical EF hand (a helix-loop-helix structural domain or motif found in a large family of calcium-binding proteins).[222] On the other hand, Sr^{2+} and Ba^{2+} prefers to remain octa-coordinated at both **S3** and **S4** site, this helps to maintain overall coordination number of eight, akin to their octa-hydrated solvation shell.

4.3.2. Binding and ion exchange energetics of divalent ions at different binding sites

The dielectric medium of deeply buried binding pockets remain significantly less polar as compared to bulk water and corresponding dielectric constant (ε) can vary between 5 to 30. In view of this, we have calculated metal binding free energies (ΔG_{bind}) at the aforementioned sites with varying dielectric medium (ε=5, 10 and 20) (Table 4.3). At ε=5, all metals are seen to have highest binding affinity at **S_{ext}** followed by **S3** and **S4,** whereas with the increase in ε value, metals gain strong preference at **S3** binding site.

Table 4.3: Calculated binding free energies ΔG_{bind} (kcal mol^{-1}) of metal ions and ion selectivity free energies (ΔG_{ex}, kcal mol^{-1}) of divalent ions with respect to K^+ at different binding sites of Ion channel.[a]

Binding site	**Ion**	**ΔG_{bind} (ΔG_{ex})**		
		ε=5	ε=10	ε=20
S_{ext}	Ca	-119.1 (-43.5)	-62.7 (-13.1)	-32.5 (3.2)
	Sr	-110.4 (-41.8)	-56.0 (-15.2)	-26.9 (-0.9)
	Ba	-105.7 (-37.1)	-51.7 (-10.8)	-22.7 (3.2)
	K	-75.6	-49.6	-35.7
S3	Ca	-71.6 (-26.9)	-61.4 (-18.7)	-56.0 (-14.3)
	Sr	-66.2 (-30.8)	-57.5 (-26.4)	-52.9 (-24.1)
	Ba	-64.8 (-29.5)	-56.6 (-25.5)	-52.2 (-23.4)
	K	-44.7	-42.7	-41.7
S4	Ca	-43.8 (-24.2)	-34.6 (-15.9)	-29.6 (-11.4)
	Sr	-42.2 (-31.9)	-34.5 (-27.4)	-30.4 (-25.0)
	Ba	-36.8 (-26.6)	-29.4 (-22.3)	-16.1 (-10.7)
	K	-19.5	-18.6	-18.2

[a]values for K^+ are taken from Chapter 3

In all occasions, least preferences for **S4** site is noted which can be explained by the close inspection of optimized structures. At **S3** site, metal-carbonyl bond distances suggest metal reside at the middle of binding site to interact well with all eight carbonyls. On the contrary, metals at **S4** site does not remain at the middle of binding pocket but reside slightly closer to the plane of carbonyls formed by T63, which resulted in weaker interaction with the hydroxyl functional groups and eventually led to lower binding free energies.

Particularly for Ca^{2+}, **S4** site does not provide proper coordination environment as it deviates from usual octahedron environment. The greater preference of divalent ions at **S3** and **S_{ext}** site are in excellent agreement with the reported experimental results.[201] To provide comparative view on K^+ vs divalent metal binding, we further compared ΔG_{bind} values for divalent ions with K^+. In addition, ion exchange free energies (ΔG_{ex}) with respect to K^+ are also calculated to comment on the feasibility of such ion exchange process (Table 4.3). It is important to note that ΔG_{ex} values for divalent metals at **S3** and **S4** binding sites are seen to be negative, reiterating the experimental fact that K^{+} can be favourably replaced by divalent ions such Ca^{2+} or Ba^{2+} at **S3** and **S4** site,. However, at **S$_{ext}$** site, selectivity for divalent ions over K^{+} are noted to alter with the increase in ε value.

4.3.3. Ion permeation energetics *via* WtD-MtD simulation

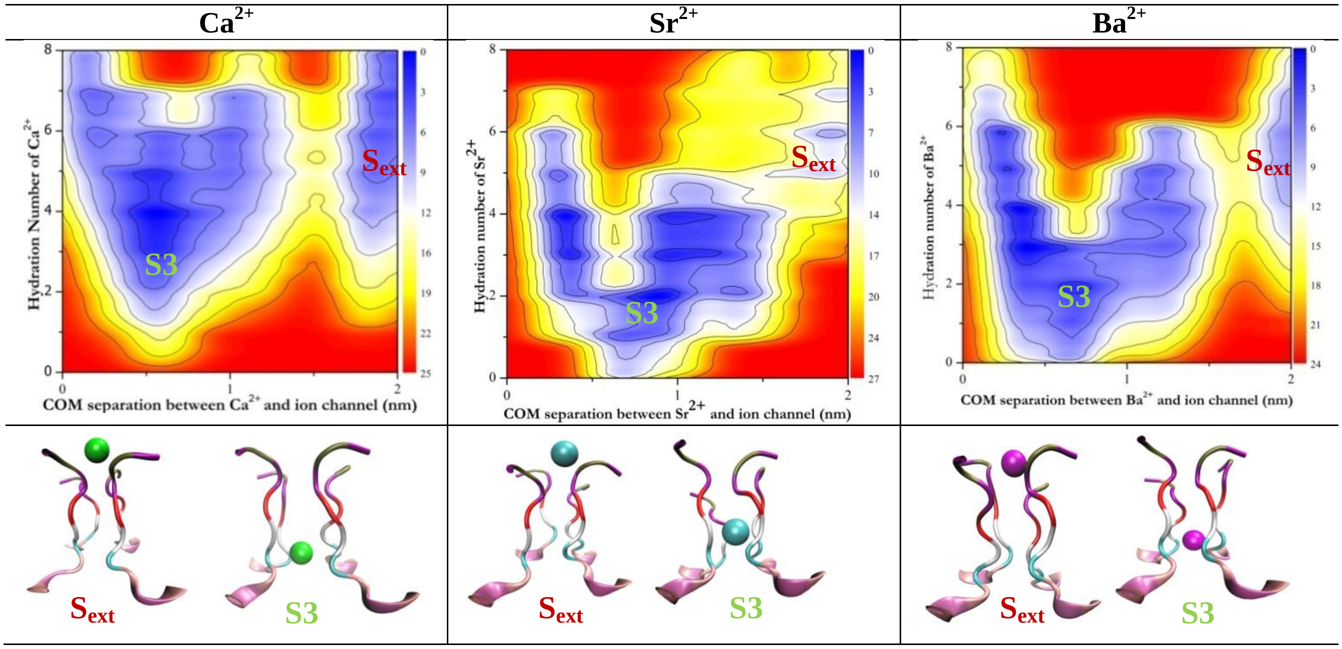

Figure 4.4: 2D-PMF profiles of divalent ions (Ca^{2+}, Sr^{2+}, and Ba^{2+}) permeation as a function of hydration number of metal ion and COM separation between the NaK channel and the permeating ions (nm) are shown in upper panel. The profiles are obtained from well-tempered metadynamics in polarizable water medium. The minimum of the unbinding free energy for each of the ions is used as a reference point to arrive at this plot. Plots of upper panel shares free energy scale of 0-24 kcal mol^{-1} (Ca^{2+}), 0-27 kcal mol^{-1} (Sr^{2+}) and 0-24 kcal mol^{-1} (Ba^{2+}) with energy gap of 3 kcal mol^{-1}.from Approaching toward the origin of the plot corresponds to the translocation of ions toward the central cavity. In lower panel, corresponding snapshots of most stable metal-binding sites (S$_{ext}$ and S3) are depicted with following colour code; Ca^{2+}: Green, Sr^{2+} : Cyan and Ba^{2+}: Magenta**.**

Further, to gain insight to ion-permeation energetics, well tempered version of metadynamics simulation was employed to study the translocation energetics of the ions through the NaK ion channel. At the start of the simulation, ions are placed at the extracellular entrance around 3 Å away from **S$_{ext}$**. As the ion permeation event involves water removal/association processes, hydration number of ion is chosen as the collective variable (CV) along with distance separation between centre of mass (COM) of ion and ion channel.

Figure 4.4 depicts 2D potential of mean force (PMF) plots for all divalent ions and seen to consist of many common features. For instance, the minima at the external entrance (1.8-2 nm from origin), for all divalent metals, suggest that $\mathbf{S_{ext}}$ (with participation of carbonyl groups of G67 and water) acts as one of the possible binding site. From $\mathbf{S_{ext}}$, further entry into SF requires shedding of water molecules from the primary coordination shell of ion. Hence, ions are required to overcome the crucial hydration energy barrier while passing through narrow pore of $\mathbf{S_{ext}}$. This energetic barrier is distinctly evident in the PMF plot and its value varies in the range of 12-15 kcal mol^{-1} (at 1.5 nm from origin) for the divalent ions. At vestibule, water molecule present there can further coordinate metal to satisfy its overall coordination number. However, we find ions to get diffuse at this site during simulation and often come out of the channel which is attributed to the non-specificity of the site. From vestibule to deeply buried **S3** site, metal coordinated water molecules are replaced by carbonyls of V64 and T63 residues resulting into decrease of hydration number. The corresponding feature is quiet evident from the 'V' shaped blue region (between 0 to 1.5 nm) of the free energy landscape. Furthermore, presence of deep minima at **S3** (at 0.5 nm from origin) indicates that divalent metals bind at **S3** most strongly. Finally, these ions pass through **S4** binding site, formed by carbonyl and hydroxyl groups of T63 residue, to enter into the intracellular cavity and become hydrated once again. In Figure 4.5, we have presented coordination number *vs*. COM separation plot (Figure 4.5), which suggests that during ion permeation, G67 (for $\mathbf{S_{ext}}$), V64 and T63 (for **S3** and **S4** binding sites) actively participate in metal binding, which is similar to monovalent ion permeation discussed in Chapter 3.

In order to provide a comparative view on energetics of divalent vs. monovalent ion permeation, we further obtained 1D-PMF for Ca^{2+} and K^{+} translocation as a function of COM separation. The resultant plot (Figure 4.6) is found to be markedly different in two aspects. Firstly, contrary to Ca^{2+}, In addition to **S3**, **S4** site also acts as probable binding site for K^+, which is in excellent correlation with experiments.[164, 201] Secondly, the energetic barrier between $\mathbf{S_{ext}}$ and vestibule is substantially lower for K^+ (by more than two times) than Ca^{2+}. This can be accredited to the lower hydration energy of K^+ as compared to Ca^{2+} (Table 4.1). Notably, our DFT results and as well as earlier experiments suggested that Ca^{2+} has superior equilibrium site-selectivity at **S3** and $\mathbf{S_{ext}}$ than K^+. However, presence of aforementioned higher hydration energy barrier for Ca^{2+} results into its partial blocking feature and reduce its rate of permeation as compared to K^+.

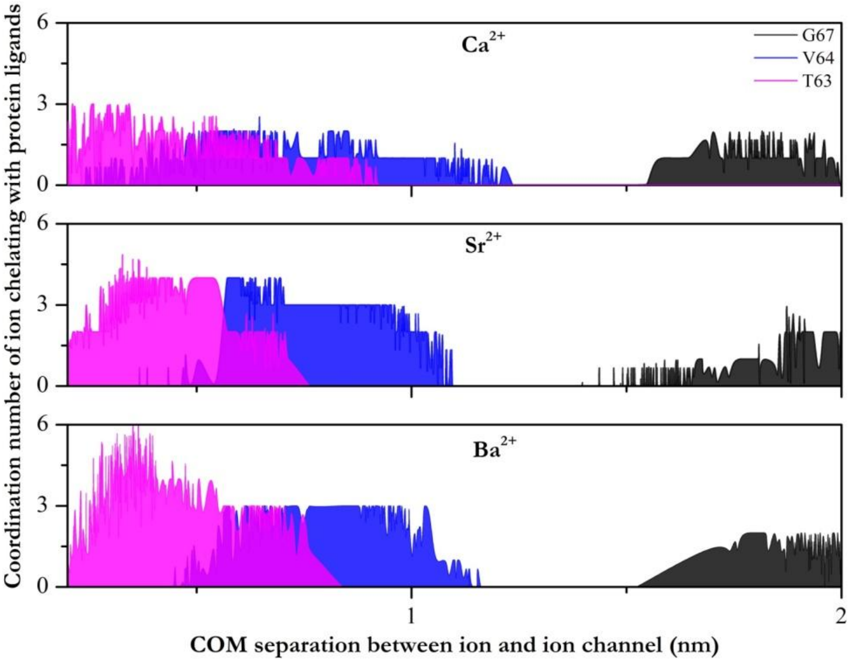

Figure 4.5: Contribution of different residues in coordination number during translocation.

Finally, to assess the effect of the polarizability on ion translocation energetics, we have performed a standard well-tempered metadynamics simulation with primitive non-polarisable TIP3P water model in the absence of electronic continuum correction for ion. Interestingly, the obtained PMF plot (red line; Figure 4.7) in non-polarizable medium underrate the ionic stability at **S3** site and even suggest a possible minima at vestibule.

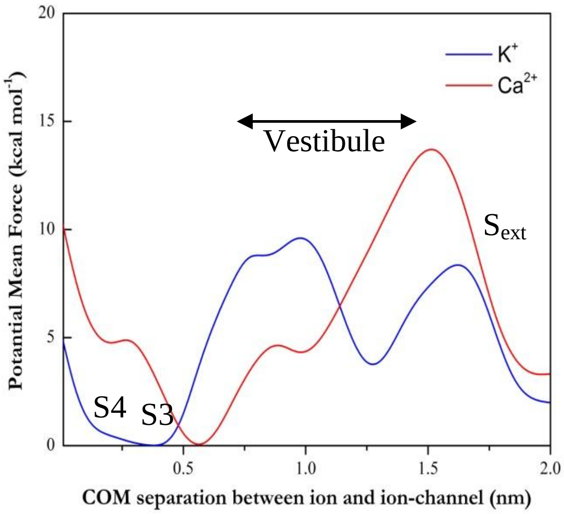

Figure 4.6: 1D-FES of K$^+$ *vs.* Ca^{2+} translocation inside SF of ion-channel in polarizable medium.

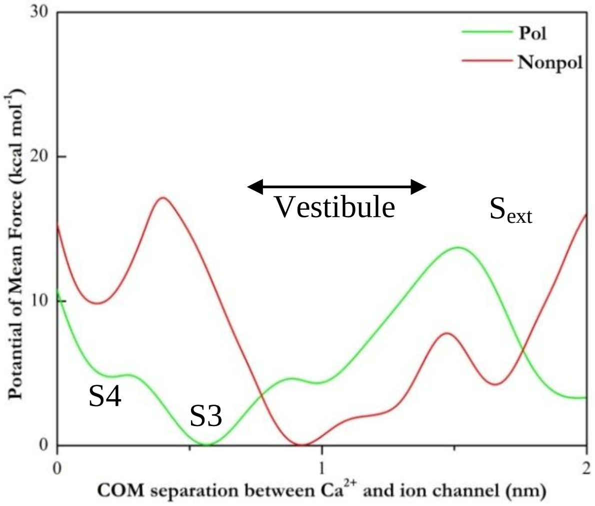

Figure 4.7: 1D-FES of Ca^{2+} translocation inside ion channel in polarizable (denoted as Pol) and non-polarizable (denoted as Nonpol) water.

Further, the predicted energetic barrier near vestibule is noted to be significantly lower when compared with polarizable model (green line). At the interior binding sites of the protein the water molecule is expected to have lower dipole moment than bulk due to the added polarization factor. In non-polarizable model, such effects remain absent, which resulted in underestimation of the metal-protein interaction and overestimation of the metal-water interaction. Consequently the non-polarizable model fails to capture the experimentally obtained trend.

4.4. Conclusion

In conclusion, we have investigated the structure, binding and energetics of divalent ion permeation through non-selective NaK ion channel using DFT and WtD-MtD simulation studies with effective polarization in polarizable water medium and ion. Our results demonstrate that the permeation energetics of divalent metals (Ca^{2+}, Sr^{2+} and Ba^{2+}) are similar in many ways and all metal ions bind strongly at **S$_{ext}$** and **S3** binding site which is in excellent agreement with the earlier experiment.[164] However, all the divalent ions including Sr^{2+} faces high energetic barrier near S$_{ext}$ to vestibule region, which is attributed to their high hydration energy. Notably, the permeation of K$^+$

through the NaK ion channel faces low energy barrier at this region as compared to Ca^{2+}, which explains the higher rate of permeation for K^+. Conclusively, the presence of higher hydration energy barrier as well as better site-selectivity for divalent ions results into its partial blocking feature inside ion channel. The inclusion of polarizability correction is also noted to be crucial for depicting true picture of translocation energetics.

CHAPTER –5

Structure and Cooperative Binding Mechanism of Cesium Salts with Multitopic Ion-pair Receptor

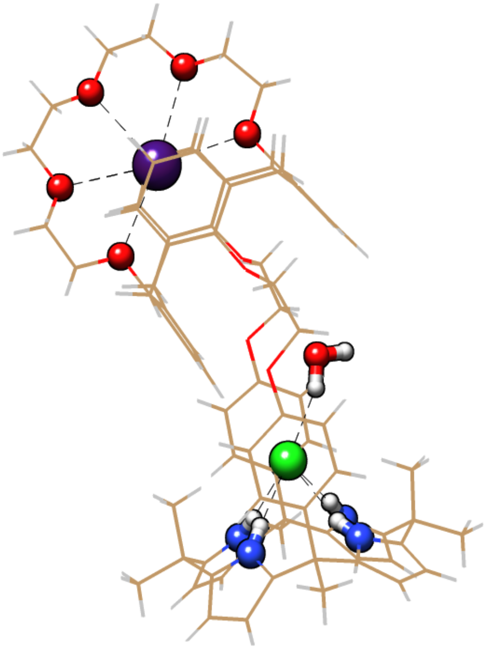

5.1. Introduction

Previous chapters (2 and 3) demonstrated that in natural environement, chemical entities like SOM and microorganism regulate the radionuclide's migration. SOM binds the radionuclides in non-specific way due to its random arrangement of diverse functional groups. Whereas, ion channel of microorganisms achives the regulation *via* specific site selectivity. The participation of counter ion in these binding mechanisms is minimal and not expected to change the course of the reaction. Synthetic receptor on the other hand are designed to capture the radionuclides *via* specific recognation motif. In this chapter we investigate the binding mechanism of cesium salts with a newly synthetized ion-pair receptor. Further, we aim to underpin the influence of counter ion in the metal binding affinity to the receptor.

Designing new ligands for the selective separation of harmful and toxic radionuclides such as cesium[3] (Cs^{137}), strontium[223] (Sr^{89}, Sr^{90}) and iodine[224-225] (I^{129}, I^{131}) have gained significant interest to reduce the volume of generating nuclear fission products from nuclear power production and from nuclear reactor accidents like Chernobyl[2] and Fukushima Diichi[1]. Post processing of these nuclear wastes using a selective ion probe remains to be the most challenging aspects of on-going nuclear strategies in the back-end of the fuel cycle. To this end, numerous experimental studies have been carried out to identify ligands suitable for selective extraction of radionuclide ions.

Some notable host molecules include crown ether,[226] calix[4]arene-crown-[6][227-228] and calix crown receptors,[229-231] which are found to bind cesium cation (Cs^+) with high selectivity. On the other hand, pyridyl terminated tripodal amide receptor[232-233] and calix-pyrrole[234-237] are promising ligands to selectively bind various halide anions (F^-, Cl^- and I^-).

Further, in solvent extraction processes, the influence of counter ions is recognized to be an important and decisive factor to achieve better separation factor.[238-239] In this direction, several multi-topic ion-pair receptors have been synthesized. Particularly Sessler and co-workers[8, 55, 240-241] have pioneered in synthesizing many ion-pair receptors, which tend to enhance the binding through favourable cooperative effects. Interestingly, within the various ion-pair binding receptors, the binding mechanism of each ion-pair are unique from one receptor to another. For example, in the crown-6-calix[4]arene-capped calix[4]pyrrole, both cations and anions are observed to bind simultaneously to the host,[8] whereas in another one (calix[4]pyrrole-calix[4]arene), the ions bind through the sequential mechanism.[55]

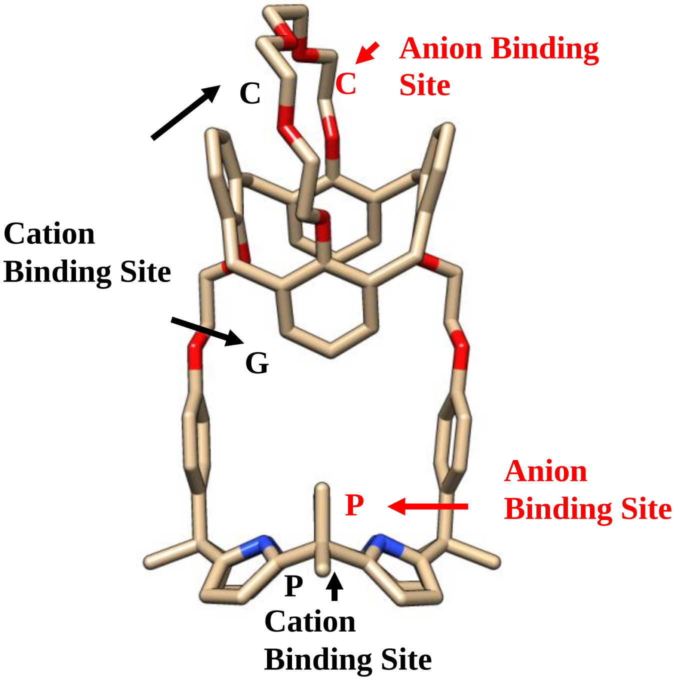

Figure 5.1: Structure of ion-pair receptor.

Very recently, Kim et al.[9-10] reported yet another ion-pair receptor (calix[4]arene crown-[5] strapped with calix[4]pyrrole moiety via glycol and aromatic linker) for the efficient extraction of Cs^+ via cation metathesis. This receptor is composed of three main cation binding sites, namely calix[4]arene-crown-5 (C), glycol site (G), the concave site of calix[4]pyrrole (P) and, two probable anion (X^-) binding sites namely convex side of calix[4]pyrrole (P) and outer sphere of the crown site (C) (Figure 5.1). This resulted in four distinguishable binding modes for the Cs salts in the receptor, namely C/P, G/P, P/P and C/C where first letter stands for cation binding site and later is for anion binding site (Scheme 1). In conjunction with experimental data, theoretical gas phase calculations using molecular mechanics (MM) force fields were also carried out to gain more insights on the preferable binding mode.

Scheme 1: Possible binding modes of Cs^+X^- in Receptor.

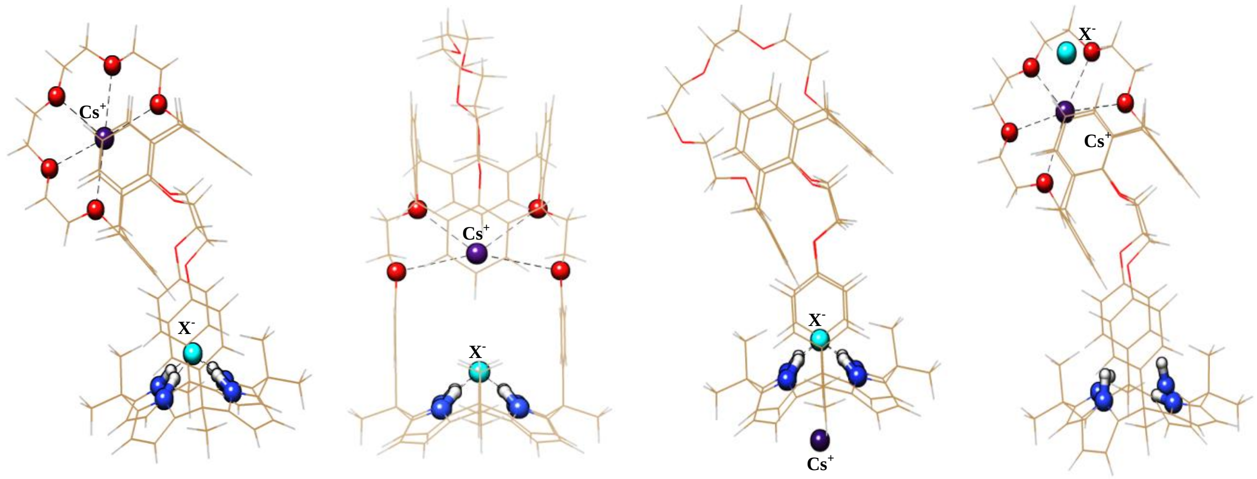

Crown/Pyrrole (C/P) **Glycol/Pyrrole (G/P)** **Pyrrole/Pyrrole (P/P)** **Crown/Crown (C/C)**

Noticeably, MM calculations carried out in the gas phase for the above mentioned ion-pair receptor[9-10] failed to follow the experimental binding trends. For example, although the experimental data suggest the C/P binding mode is to be thermodynamically favourable for CsF and CsCl, MM calculations predict C/C and G/P binding modes. Further, the computational results do not shed light over the existence of positive allosteric effects in the ion-pair binding mechanism. An elucidation of such acting cooperative effects in the receptor at the molecular level is indeed very essential and can act as a test bed for synthesizing more efficient ion binding probe.

Quantum chemical calculations at the density functional theory (DFT) level are very popular and powerful method to investigate the binding preferences of various radionuclides to different hosts.[242-244] For instance, Boda et al investigated the selective binding of Cs^+ over Na^+ with macro cyclic calix-bis-crown ether.[242] Hill et al. studied the binding of various alkali metal cations to crown ether and its analogues.[243] However, apart from the aforementioned experimental investigations, owing to the large system size, quantum chemical calculations on these reported ion-pair receptors are very rare.[245]

Here, we have carried out DFT calculations on the ion-pair receptor of Kim. et al.[9-10] to unravel the structures and binding mechanism of Cs salts. Our present study focused to address the following intriguing questions,

(i) What are the binding affinities of anions and Cs^+ in the absence of their counterparts?

(ii) Which is the most preferable binding mode for cesium salts at this receptor and why?

(iii) To what extent, cation or anions assist each other in binding?

and, (iv) To what extent solvent molecules alter the binding affinity trend?

In addition to this, we have also carried out energy decomposition analysis (EDA) to determine the various contributions of interaction energy components into the total interaction energy. Besides, topological analysis using atoms in molecule (AIM) approach is performed to decipher the nature of inter-molecular interactions existing in the ion-pair complexes. These two tools have gained considerable attention to understand the nature of bonding present between the ions and the extractants.[246-247]

5.2. Computational Details

The starting structures of the ion-pair receptor are taken from the reported X-ray structure of Kim et al.[9-10] We have considered various cesium-halide salts, viz. CsF (CCDC code: 826578), CsCl (CCDC code: 826574), CsBr and CsI along with CsNO3 (CCDC code: 826577) for complexation with the receptor. For CsBr and CsI, we have used the CsCl X-ray structure. All

X-ray derived structures are further optimized using BP86 functional[91-92] in conjunction with the def2-SV(P) basis set (denoted as B1 basis set).[93] Notably, this functional/basis set (BP86/de2-SV(P) was previously observed to produce accurate structural parameters.[61, 248-250] The effect of long range electrostatic effects are taken into account by using the implicit COSMO solvation model (water as solvent; ε= 80).[100] The size of the system is very large (173-187 atoms), such that even with double ζ-basis set (1572 basis functions), the computation is very demanding. Thus, geometry optimizations with the larger basis sets are prohibitive. Nevertheless, to comment on the basis set dependency of the structure and energetics, a set of calculations are performed for [Receptor.CsCl] complex at the C/P binding mode using a basis set of triple ζ-quality(TZVP[98-99], 2404 basis functions, denoted as B2 basis set) (Table 5.1 & 5.2).

Table 5.1: Optimized geometric parameters (Å) of Receptor-Cs^+Cl^-complex in C/P binding mode at various levels.

Optimization Level	Medium	Cs-O_C	Cs-C_A	Cl-N_P	RMSD[a]
BP86/B1	ε=80	2.94-3.12	3.44-3.45	3.21-3.23	0.26
BP86-D3/B1	ε=80	2.96-3.17	3.42-3.56	3.19-3.23	0.39
BP86/B2	ε=80	2.93-3.13	3.48-3.53	3.25-3.27	0.26
BP86/B1	ε=1	2.88-3.15	3.45-3.50	3.23-3.25	0.34
BP86-D3/B1	ε=1	2.89-3.19	3.44-3.52	3.21-3.27	0.56
X-ray	-	2.84-3.10	3.29-3.40	3.22-3.30	-

[a]RMSD values are calculated with respect to X-ray structures.

Table 5.2: Computed binding affinities (kcal mol^{-1}) of CsCl in Receptor at C/P binding mode.

DFT level for energetics	Medium	Binding affinity
B3LYP-D3/B2//BP86/B1	ε=80	-28.67
B3LYP-D3/B2//BP86/B2	ε=80	-32.28

The obtained structural changes between def2-SV(P) and TZVP basis set are found to be negligible. Further, binding affinities are also observed to deviate only by 4 kcal mol^{-1} (Table 5.2). Moreover, the above complex is also optimized at gas phase as well as at ε=80 with and without

Grimme's three-body dispersion correction term (denoted as D3 correction).[165] Noticeably, the optimized structural parameters with D3 corrections are observed to deviate more with respect to X-ray structure (Table 5.1). The same is noted for the gas phase optimized structure at BP86/B1 level. Such alteration in geometry is found to be minimal in case of COSMO optimized structure at BP86/B1 level. The above results thus justify our applied DFT level (BP86/B1 using implicit solvation scheme (ε=80)) for geometry optimization.

Compared to BP86, hybrid B3LYP[96-97] performs better in energetics calculations.[251-252] Hence, Binding affinities are computed using dispersion corrected B3LYP(D3) functional with a B2 basis set on BP86/B1 pre-optimized structuresat ε=80. For Cs^+ and I^- ions, a def-TZVP basis set was used to describe the valance orbitals, whereas the core electrons were modelled via SD-ECP (replacing 46 electrons in the core)[253] pseudo potential. To speed up the calculations, a resolution of identity (RI or RIJCOSX) approximation[254-258] was applied by using corresponding auxiliary basis sets. Similar computational methodology was successfully used by us to benchmark the alkane binding to cucurbiturils with the experimental binding free energies[95] and also to describe binding mechanism of Cs^+ in fulvic acid.[189]

Due to large system size the harmonic frequency calculations on ion-pair receptor adducts are computationally very expensive. Further, the experimentally determined thermodynamic quantities suggests the binding of ion-pair to the receptor is enthalpy driven,[9-10] hence our derived electronic binding affinities can be expected to correlate well with the experimental binding trend. All structural optimizations are performed using TURBOMOLE v 6.3.1[212] while energetics are computed using ORCA v 3.0 software.[103]

The nature of interactions present between Cs^+/X^- and the receptor have been analysed using BP86/B1 (ε=80) optimized structures by means of EDA as implemented in the ADF program package[259] based on the methods pioneered by Morokuma[171] and Ziegler[172] at a level of

BLYP/TZ2P with ZORA. It should be noted that Pardue et al.[260] reported that both BLYP and B3LYP functional predict similar EDA parameters. Thus for computational efficiency we chose BLYP/TZ2P method for the present study. The total interaction energy (ΔE_{int})between the two fragments is calculated using the following equation,

$$\Delta E_{int}(\zeta) = \Delta E_{elstat}(\zeta) + \Delta E_{pauli}(\zeta) + \Delta E_{orb}(\zeta) \qquad (1)$$

and, the percentage covalency have been calculated using the equation 2,

$$[\Delta E_{orb}(\zeta)/(\Delta E_{elstat}(\zeta) + \Delta E_{orb}(\zeta))] \text{ X } 100 \qquad (2)$$

where, ΔE_{elstat} (ζ) and ΔE_{pauli} (ζ) represents the electrostatic and repulsive interaction energy contributions between the fragments respectively. ΔE_{orb} (ζ) is the stabilizing energy arises from the orbital contributions and thus represents the strength of covalent bonding between the fragments.

Further, the quantum theory of atoms in molecule (QTAIM) was applied to depict the topological properties of the most favourable [Receptor-Cs^+X^-] complexes. QTAIM analysis, pioneered by Bader and co-workers characterizes bonding and non-bonding interactions of atoms in terms of the electron density ρ(r), Laplacian of the electron density L(r), kinetic energy density H(r) and a potential energy to the Lagrangian kinetic energy ratio (|V(r)/G(r))|.[261] For instance, the presence of a (3, -1) critical point in QTAIM topography represents a chemical bond between two atoms and are called as the bond critical points (BCPs) where the shared electron density reaches a minimum, whereas a critical point with (3, +1) and (3, +3) signatures identify a ring structure (RCP) and cage critical point (CCP) in the molecular system. The ρ(r) values at the BCPs is related to the strength of the bonds.[262] In this study, QTAIM calculations are performed at BP86/B2 level[263].

5.3. Results and Discussion

5.3.1. Solvation of Ions:

The preferential binding of ions to the receptor is known to be modulated by dehydration penalty of ions. From the earlier studies,[123, 242, 244, 264-265] it is apparent that a primary hydration number of six can be considered for the halide ions and for Cs cation. Topol et al.[264] demonstrated that the primary hydration shell of F^-, Cl^- and Br^- contains six water molecules. DFT studies by both Dang et al.[265] and Ali et al.[123] predicteda partially solvated structures for I^- and Cs^+ to be the most stable species. Recently, we have also used hexa-hydrated halide ions towards understanding the ion-host interaction at the molecular level.[244] Similarly, for nitrate, Boda et al.[242] used hexa hydrated structure in their previous quantum chemical calculation. The same solvated models have been used here in our study. To validate the solvation model, we have calculated the hydration free energies of all ions which are indeed found to be close with the experimentally derived values of Marcus et al. (Figure 5.2 and Table 5.3),[116] and in particular the trends are excellently reproduced. Thus the chosen methods BP86/B1 for geometry optimizations within the implicit COSMO solvation model and B3LYP-D3/B2 for energetics are accurate enough for the present study.

Table 5.3: Hydration free energy (kcal mol^{-1})of ions calculated at B3LYP-D3/B2//BP86/B1 level

Hydrated ion	Hydration free energy	
	Calculated	Experimental[a]
$Cs(H_2O)_6^+$	-71.43	-59.80
$F^-(H_2O)_6^-$	-120.55	-111.24
$Cl.(H_2O)_6^-$	-79.79	-81.34
$Br.(H_2O)_6^-$	-69.88	-75.36
$I(H_2O)_6^-$	-66.63	-65.79
$NO_3(H_2O)_6^-$	-70.36	-71.77

[a] experimental values are taken from ref no. 116

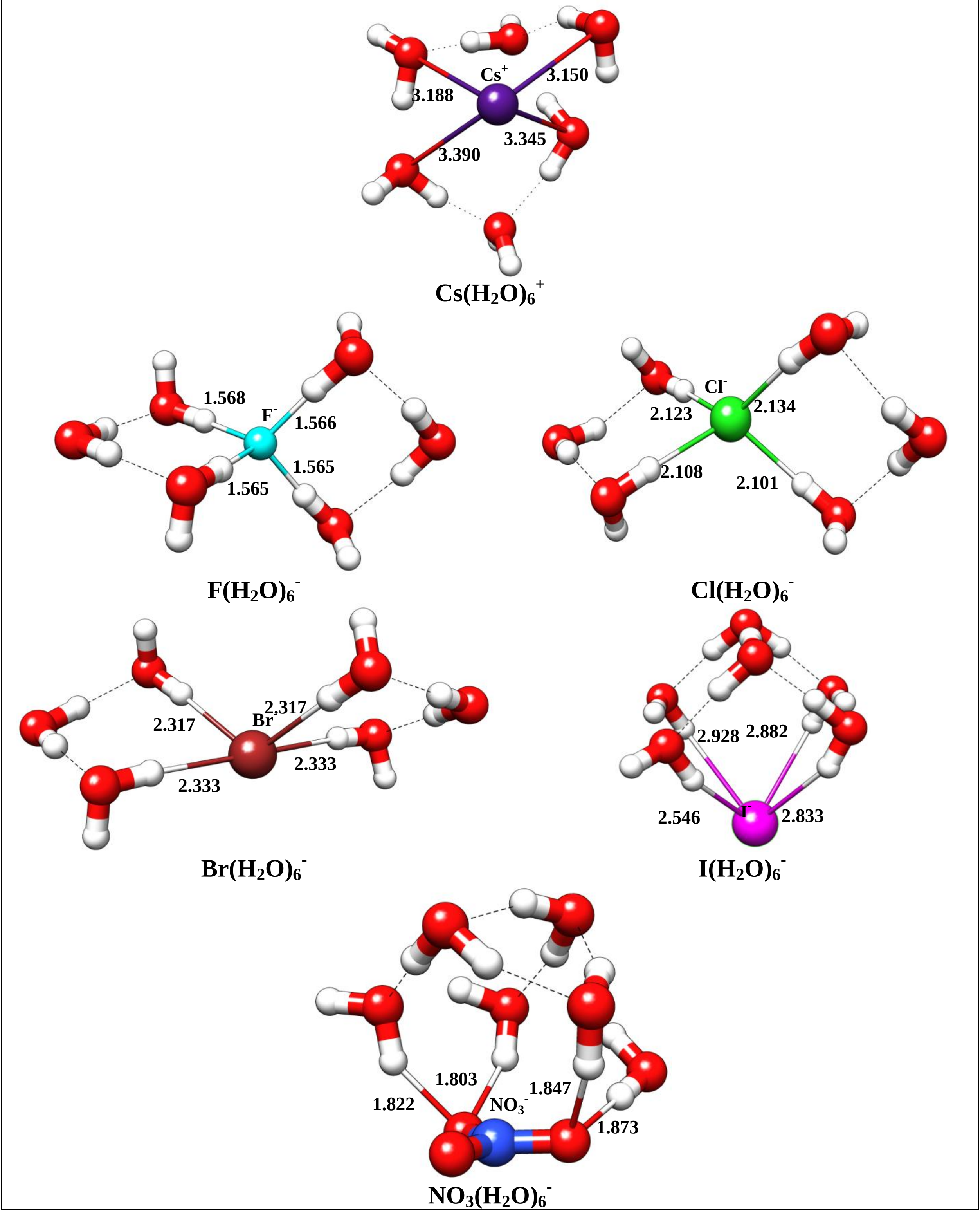

Figure 5.2: Optimized structures of hydrated ion systems.

5.3.2. Binding of Cesium to Receptor

The receptor bears three binding sites for Cs^+ namely, 'C', 'G' and 'P' site (Figure 5.1). Cs^+ cation binding affinity to the receptor have been calculated using the following equation:

$$E(Receptor) + E[Cs^+.(H_2O)_6] \rightarrow E(Receptor.Cs^+) + E[(H_2O)_6] \quad (3)$$

For the 'C' and 'G' sites, the calculated binding affinities are -15 kcal mol^{-1} and -13 kcal mol^{-1} respectively.Among the three binding sites, Cs^+ binding to the 'P'-site is least favourable (B.E ~-7 kcal mol^{-1}) (Table 5.4). Hence, 'C' and 'G' sites act as the primary binding site for Cs^+ in absence of anion.

Cs^+ at the 'C' site interacts with crown-5 oxygen atoms through strong electrostatic interaction ($Cs\text{-}O_{crown}$: 2.93-3.10 Å). Aromatic moieties of calix-[4]-arene are also found to interact with Cs^+ through cation-π interaction in the C site (Cs-Arene : 3.45-3.51 Å). However, in 'G' site, in addition to cation-π interaction with the calix[4]arene moiety(Cs-Arene : 3.54-3.74 Å), two ethylene glycol spacers ($Cs\text{-}O_G$: 3.06-3.56 Å) further provide favourable electrostatic interaction whereas larger space of the cavity reduces steric hindrance.

Finally, for the 'P' site, pyrrole rings of calix[4]pyrrole unit interacts weakly with Cs^+ via cation-π interaction ($Cs\text{-}N_P$: 3.66-3.73 Å) and thus lead to minimal binding affinity (only 7 kcal mol^{-1}) and energetically less favorable as compared to 'C' and 'G' site.

Table 5.4. Calculated Cs^+ binding and relative affinities (B.E and R.E, in kcal mol^{-1}) to the receptor.

Cation	Binding site	R.E	B. E
Cs^+	Crown 'C'	0	-15.11
	Glycol 'G'	+2.06	-13.05
	Pyrrole 'P'	+8.35	-6.76

5.3.3. Binding of Anions to Receptor

The chosen anions (X= F^-, Cl^-, Br^-, I^- and NO_3^-) can bind either at ‘P’ or at the outer sphere of ‘C’ site of the receptor through hydrogen bonding (Table 5.5). Anion (X^-) binding affinities to the receptor have been calculated using the following equation,

$$E(Receptor) + E[X^-.(H_2O)_6] \rightarrow E(Receptor.X^-) + E[(H_2O)_6] \tag{4}$$

In site ‘C’, anions can only interact with the methylene hydrogen atoms through weak hydrogen bonding (F^--H > 2 Å), whereas at the ‘P’ site, a strong hydrogen bonding (F^-...H-$N_{pyrrole}$: 1.68-1.70 Å, I^-...H-$N_{pyrrole}$: 2.58-2.63 Å) is noted. These variations in the geometry lead to favorable binding affinity at the ‘P’ site (~-5 kcal mol^{-1} for F^-) but unfavorable binding is noted for the ‘C’ site (> +5 kcal mol^{-1}). For large I^- anion, both the sites are found to be unfavorable. The computed bond lengths are consistent with the structural parameters of previously reported computational study for calix[4]pyrrole-halide system[266-267] and with reported experimental data (F^-...H-N : 1.64 Å, I^-...H-N : 2.69 Å).[268]

Table 5.5. Calculated anion binding affinities (B.E units in kcal mol^{-1}) to the receptor.

Anions	‘P’ site	‘C’ site
F^-	-5.64	+30.96
Cl^-	-8.44	+11.36
Br^-	-8.21	+5.52
I^-	+1.72	+7.96
NO_3^-	-7.57	+6.06

Evidently, electronegativity and hydration energy of anions play an important role in their selective binding at the‘P’ site. Interestingly, despite having highest electronegativity, F^- is noted to have a lower binding affinity than Cl^- and Br^-. This can be attributed to the strong solvation nature of the F^- at water medium which increases the desolvation energy barrier for F^-. Notably, earlier experiments by Kim et al.[10] also observed no complexation of F^- with the receptor in the more polar medium. For the ‘P’ site, the strength of anion binding decreases as follows,

$Cl^- > Br^- \sim NO_3^- > F^- >> I^-$

5.3.4. Cesium assisted Anion binding

Experimental studies on various ion-pair receptors[55-56] suggest that binding of anions are largely influenced by the presence of the cation. From table 5.4 and 5.5, it is evident that anion binding to the receptor is comparatively weaker as compared to Cs^+.

Table 5.6: Optimized structural parameters (Å) of Receptor-Cs^+X^- complex.[a]

Binding Mode	$Cs\text{-}O_{C/G}$	$Cs\text{-}C_A$[b]	$Cs\text{-}N_P$	$X\text{-}N_P$
Receptor-$Cs^+.F^-$				
G/P	3.15-3.99	3.48-3.55	-	2.72-2.73
C/P	2.90-3.10 (2.84-3.03)	3.40-3.43(3.40-3.46)	-	2.72-2.73 (2.76-2.81)
C/C	2.97-3.19	3.41-3.62	-	-
P/P	-	-	3.47-3.52	2.72-2.73
Receptor-$Cs^+.Cl^-$				
G/P	3.34-4.08	3.44-3.67	-	3.29-3.30
C/P	2.94-3.12(2.84-3.10)	3.44-3.45 (3.29-3.40)	-	3.21-3.23 (3.23-3.31)
C/C	2.98-3.10	3.39-3.83	-	-
P/P	-	-	3.53-3.55	3.21-3.22
Receptor-$Cs^+.Br^-$				
G/P	3.30-4.13	3.45-3.61	-	3.48-3.51
C/P	2.92-3.10	3.45-3.46	-	3.40-4.42
C/C	2.99-3.13	3.41-3.73	-	-
P/P	-	-	3.55-3.57	3.38-3.40
Receptor-$Cs^+.I^-$				
G/P	3.17-4.21	3.49-3.58	-	3.71-3.76
C/P	2.92-3.11	3.45-3.52	-	3.60-3.66
C/C	2.92-3.10	3.45-3.52	-	-
P/P	-	-	3.56-3.57	3.61-3.66
Receptor-$Cs^+.NO_3^-$				
G/P	3.23-3.62 (3.01-3.63)	3.48-3.67 (3.48-3.76)	-	2.93-2.97 (2.92-3.00)
C/P	2.93-3.11	3.38-3.51	-	2.79-2.85
C/C	2.94-3.15	3.42.3.43	-	-
P/P	-	-	3.56-3.59	2.83-2.89

[a] Values in parenthesis are the corresponding experimental values (ref no.9-10).

[b] Cs^+-C_A refer to the distance between Cs^+ and ortho and meta carbon atoms of Calix[4]arene moiety with respect to the phenoxy groups.

Thus, cation is expected to bind first to the receptor, which can subsequently enhance the binding affinity of anion to the receptor. Here, we have considered all possible four binding modes which are earlier denoted as C/P, G/P, P/P and C/C (Scheme 1). The cation assisted anion binding affinitiesare calculated using the following expression,

$$E[Receptor.Cs^{+}] + E[X^{-}.(H_2O)_6] \rightarrow E(Receptor.Cs^{+}.X^{-}) + E[(H_2O)_6] \tag{5}$$

For all the three available X-ray structures (CsCl, CsF and $CsNO_3$), our optimized structures are very close to the experimental data (Table 5.6).[9-10] For instance, the average Cs^+-O_C bond distances are within 0.1Å deviation with respect to corresponding three X-ray structures. Notably, for $CsNO_3$ at G/P mode, in contrary to experimental observation of asymmetric binding of Cs^+ and nitrate (3.19-3.50 Å), Cs^+ is noted to interact with nitrate symmetrically (Cs^+-$O_{nitrate}$: 3.26-3.28 Å). Such structural change can be attributed to the presence of crystallographic solvent molecule (ethanol) in the X-ray structure (see below).The Cs^+-O bond lengths at the 'C' site is comparatively shorter as compared to Cs^+-O_{Arene} due to strong electrostatic interactions. As expected, the X-N_P bond lengths are elongated as we go from F^- to I^- due to decreasing electronegativity which leads to weakening of hydrogen bonding down the group. Notably, Cs-O_G bond distances (G/P mode) in the complexes are found to be somewhat elongated (>0.4 Å) as compared to Cs-bound-receptor in the absence of anions. Such elongation is found to be larger as we move down the group from CsF to CsI complexes. The presence of anion at 'P' site also resulted in shortening of Cs-N_P bond distance (by ~0.1 Å in P/P mode). In contrary, the computed Cs-O_C bond distances in C/P and C/C modes remain almost unchanged with respect to [Receptor-Cs^+]. In the presence of Cs^+ at 'G' site, X-N_P bond lengths are elongated significantly (by ~0.09 Å for CsCl,~0.10 Å for CsBr, ~0.11 Å for CsI) from CsCl to CsI as compared to bare anion binding to the receptor [Receptor-X^-]. Such elongation even becomes more prominent

(>0.15 Å) for the G/P mode of $CsNO_3$ complex. However, in case of CsF, X-N_P distance remain unaltered even in presence of Cs^+ at 'G' site probably due to the large inter-ionic distance between the ion-pair (~5 Å). For all salts, presence of cation at 'C' or 'P' site does not change in anion-pyrrole bond length. These observations are further suggested that the close proximity of anion near cation can induce such structural changes (specifically for G/P binding mode). Due to the favorable columbic interaction, the presence of Cs^+ in close proximity to anions at C/C, P/P and G/P mode enhances the binding affinities of anions (Table 5.7).

Table 5.7: Cs^+ assisted anion (X^-) (a) and anion (X^-) assisted Cs^+ binding (b) affinity (B. E, units in kcal mol^{-1}) to receptor.

(a)

Binding Mode	Cs^+ assisted X^- binding[a]				
	F^-	Cl^-	Br^-	I^-	NO_3^-
G/P	-4.27 (-5.64)	-14.76 (-8.44)	-15.81 (-8.21)	-6.24 (+1.72)	-21.63 (-7.57)
C/P	-7.61 (-5.64)	-13.55 (-8.44)	-12.71 (-8.21)	-2.25 (+1.72)	-12.63 (-7.57)
C/C	+23.45 (+30.96)	+3.12 (+11.36)	-2.85 (+5.52)	-2.58 (+7.96)	+1.08 (+6.06)
P/P	-11.64 (-5.64)	-16.83 (-8.44)	-16.04 (-8.21)	-5.13 (+1.72)	-13.82 (-7.57)

(b)

Binding Mode	X^- assisted Cs^+ binding[b]				
	F^-	Cl^-	Br^-	I^-	NO_3^-
G/P	-11.69 (-13.05)	-19.37 (-13.05)	-20.65 (-13.05)	-21.02 (-13.05)	-27.11 (-13.05)
C/P	-17.08 (-15.11)	-20.23 (-15.11)	-19.62 (-15.11)	-19.09 (-15.11)	-20.17 (-15.11)
C/C	-	-	-	-	-
P/P	-12.77 (-6.76)	-15.15 (-6.76)	-14.59 (-6.76)	-13.61 (-6.76)	-13.01 (-6.76)

Although, CsF has highest lattice energy among the Cs halides,[269] we find that the presence of Cs^+ does not appreciably enhance the binding affinity of small and high electronegative anion such as

F^- at G/P mode due to larger inter ionic distance between the Cs^+ and F^-. However, for larger Br- and I- ion, the inter ion-pair distance decreases (~3 Å) for G/P mode which leads to significant enhancement of the binding affinity of Br^- and I^- in the presence of Cs^+ (Table 5.7). Even in the presence of Cs^+, the anion binding affinities at the C/C binding mode are noted to be weak for all Cs-salts. However, with the increasing size of halide, we find an increase in the extent of favorability for 'C' site. particularly for I^-, owing to the close inter-ionic separation at C/C binding mode (5.97 Å) and proper size compatibility between the opposite ions. Thus 'C' site is now noted to be more favorable than 'P' site in the presence Cs^+ at 'C' site (Table 5.7). Similarly the presence of Cs^+ at ‘P’ site also enhances the anion binding affinities (P/P mode) by almost 6 kcal mol^{-1}.

5.3.5. Anion assisted Cesium binding

Until now, we have shown that cation does assist the anion binding to the receptor. Taking consideration of binding affinity (Table 5.4 & 5.5), we can expect anion to bind the receptor later to Cs^+. Nevertheless, the presence of anion can also regulate cation binding ability due to the acting cooperative effect. As all the anions are noted to have unfavorable binding affinity at the outer sphere of ‘C’ site, hence anions are not expected to bind at the ‘C’ site prior to cation binding. Thus, C/C binding mode is not considered here. Anion assisted cation binding affinity is calculated using the following expression,

$$E[Receptor.X^-] + E[Cs^+.(H_2O)_6] \rightarrow E(Receptor.Cs^+.X^-) + E[(H_2O)_6] \qquad (6)$$

We indeed find a significant enhancement (by ~5-10 kcal mol^{-1}) of binding strength for Cs^+ in the presence of anions for all modes except for CsF in G/P binding mode. As mentioned in the earlier section, particularly for the G/P mode of CsF, the larger inter ionic distance between the Cs^+ and F^- diminishes the effect of positive allosteric effect. Similar to cesium assisted anion binding, we find that proximal presence of anion in close proximity with Cs^+ (for P/P and G/P mode) assist the binding of cation most (Table 5.7).

5.3.6. Overall binding affinity of ion-pairs to receptor

We have also calculated the overall binding affinity for cesium salts to receptor using the following expression,

$$E[Receptor] + E[Cs^{+}.(H_2O)_6] + E[X^{-}.(H_2O)_6] \rightarrow E(Receptor.Cs^{+}.X^{-}) + 2E[(H_2O)_6] \quad (7)$$

As expected, the C/C binding mode is noted to be less preferable for all cesium salts except for CsI (Table 5.8). In the presence of I^-, the considerable preference of Cs^+ to bind at 'C' site over 'P' site in the contact ion-pair complexes of CsI (C/C and P/P) (Table 5.7) seems to originate slightly higher preference of C/C mode for CsI than the P/P mode. Relative binding strength of CsF in receptor is predicted to be less as compared to CsCl and CsBr. The computed binding affinity trends suggest that C/P mode to be the most favorable for CsF and CsCl, whereas $CsNO_3$ ion-pair complex prefers G/P mode which are in good correlation with experimental data.[9-10]

Table 5.8: Net Cs^+X^- binding affinity (B. E, units in kcal mol^{-1}) to the receptor

Binding Mode	Cs^+F^-	Cs^+Cl^-	Cs^+Br^-	Cs^+I^-	$Cs^+NO_3^-$
G/P	-17.32	-27.82	-28.86	-19.30	-34.68
C/P	-22.72	-28.67	-27.83	-17.37	-27.74
C/C	+8.34	-11.99	-17.96	-12.54	-14.03
P/P	-18.40	-23.59	-22.80	-11.89	-20.59

We find that the calculated binding affinity trend for $CsNO_3$ in close agreement with experimentally observed G/P binding mode. It should be noted that with pure calix-pyrrole system which is only capable to bind ion-pair via P/P binding mode, Wintergerst et al.[270] reported binding of $CsNO_3$ to the host molecule is weakest (or unbound) among the three Cs salts (CsCl, CsBr and $CsNO_3$). Although our used host molecule is markedly different (as it contains 'C' site for cation) in comparison to the aforementioned calix-pyrrole system, we can qualitatively compare the performance of these two host molecules at the P/P binding site. We do predict a similar trend, where within the three salts (CsCl, CsBr and $CsNO_3$), binding affinities for $CsNO_3$ is least for the P/P binding mode (-23.59 kcal mol^{-1}- CsCl; -22.80 kcal mol^{-1}- CsBr; -20.59 kcal mol^{-1}- $CsNO_3$). Notably, for $CsNO_3$, the preference of G/P over the C/P binding site is due to the presence of favorable bi-dentate coordination between the ion pairs in the former binding motif.Particularly for large anions like Br- and I-, a slight preference for G/P mode over C/P mode is observed. This can be ascribed to the favorable electrostatic interactions present between the oppositely charged ions of large ionic radii at short distances which indeed help to stabilize the contact ion-pair complex formation.

5.3.7. Role of Crystallographic solvent molecule

In the X-ray crystal structures of CsF, CsCl and $CsNO_3$ bound receptor, a crystallographic methanol molecule, a water molecule and an ethanol molecule are found (Figure 5.3). In order to quantitatively describe the influence of these explicit solvent molecules on the structures and relative binding affinities, we further calculated the binding affinity using following expression,

$$E[Receptor] + E[Cs^{+}.(H_2O)_6] + E[X^{-}.(H_2O)_6] + E[sol] \rightarrow E(Receptor.Cs^{+}.X^{-}.sol) + 2E[(H_2O)_6] \quad (8)$$

where, X= F^-, Cl^-, NO_3^- and Sol denotes CH_3OH, H_2O and C_2H_5OH

We have also calculated the relative energies (R.E in kcal mol^{-1}) for all binding modes with respect to the most stable species of all three Cs salts (Table 5.9).

Table 5.9: Calculated binding affinities (B. E, units in kcal mol^{-1}) and relative energies (R. E, units in kcal mol^{-1}) of [Receptor.CsX] (X= F^-, Cl^-, NO_3^-) complex in the presence of crystallographic solvent molecule.[a]

Binding Mode	Net BE for CsF	MM prediction[26]	R.E	Net BE for CsCl	MM prediction[25]	R.E	Net BE for $CsNO_3^-$	MM prediction[25]	R.E
G/P	-32.26 (-17.32)	-193.1	+1.1	-29.45 (-27.82)	-135.5	+3.2	-44.46 (-34.68)	-135.8	-
C/P	-33.32 (-22.72)	-165.6	-	-32.62 (-28.67)	-115.8	-	-35.47 (-14.03)	-116.7	+9.0
P/P	-18.08 (-18.40)	-182.5	+15.2	-29.57 (-23.59)	-117.6	+3.0	-26.88 (-20.59)	-103.5	+17.6

[a] Values in parenthesis denote for B.E without the influence of crystallographic solvent molecule

(a)

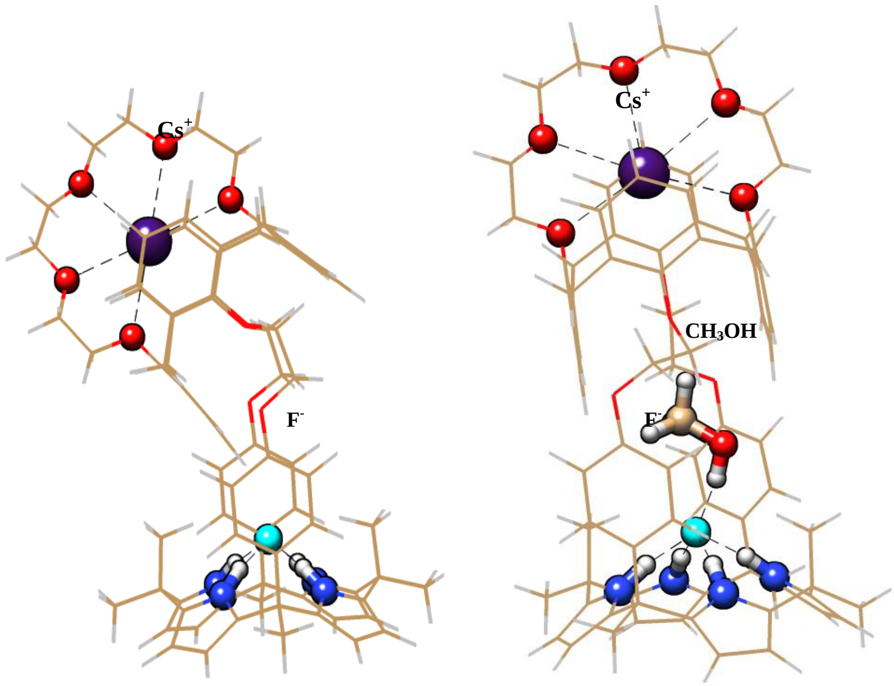

Receptor-Cs^+F^- Receptor-$Cs^+F^-.CH_3OH$

(b)

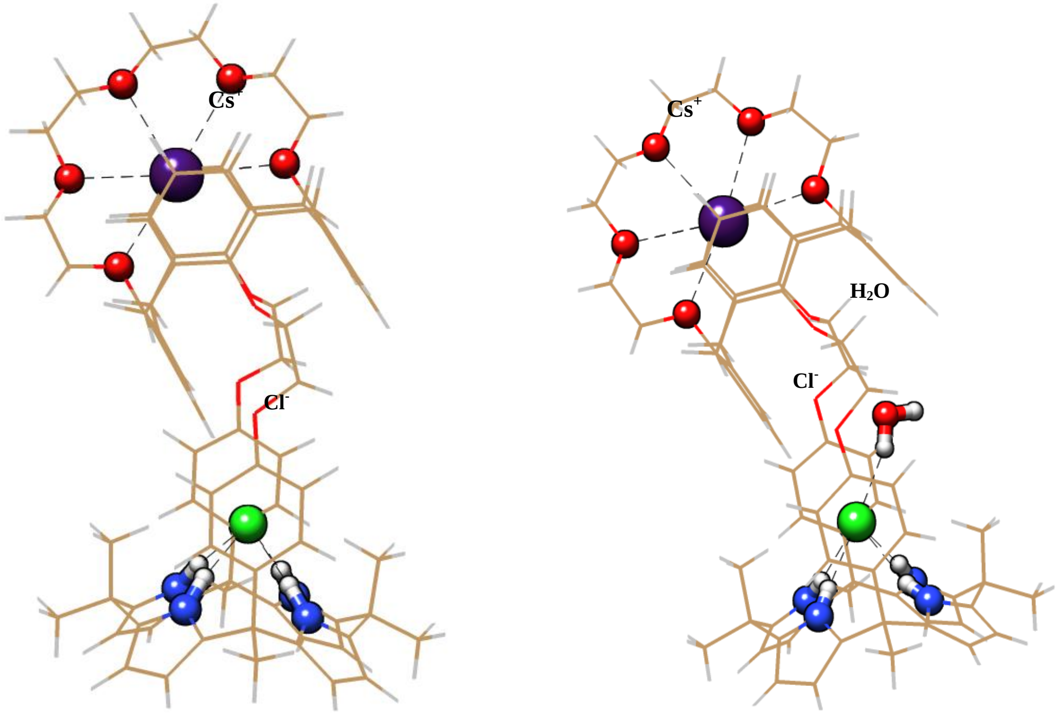

Receptor-Cs^+Cl^- Receptor-$Cs^+Cl^-.H_2O$

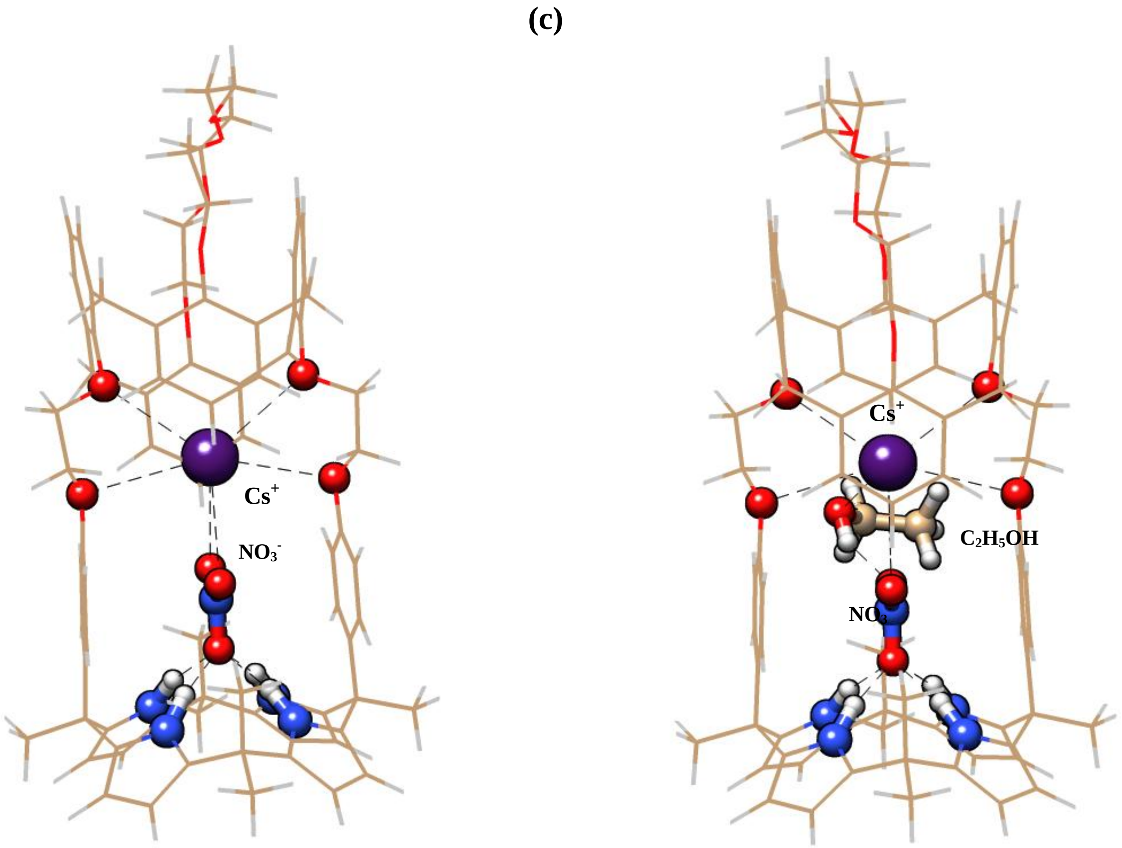

Receptor-Cs$^+$NO$_3^-$ Receptor-Cs$^+$NO$_3^-$.C$_2$H$_5$OH

Figure 5.3: Optimized structures of (a) Receptor-Cs$^+$F$^-$complex (C/P binding mode),(b) Receptor-Cs$^+$Cl$^-$ complex (C/P binding mode)and (c) Receptor-Cs$^+$NO$_3^-$ complex (G/P binding mode)in the absence and presence of solvent molecule. Primary interactions are shown using ball and stick model.

Here, we have not considered C/C binding mode as we noted this binding mode to be least favorable in previous calculations. The optimized structures (Table 5.10) showed very small displacement from the reported X-ray structure [RMSD: 0.357 Å (CsF), 0.309 Å (CsCl) and 0.478 Å (CsNO$_3$): Figure 5.4]. Although the structures are perturbed very little due to the presence of solvent molecules, the overall binding affinities are modified significantly (up to 10-15 kcal mol^{-1}, Table 5.9) but importantly does not alter the overall binding trends. This indeed suggests that solvent molecules in close proximity to the ions provide charge delocalization through hydrogen bonding thus stabilizing to the solvent separated Cs salt complexes.

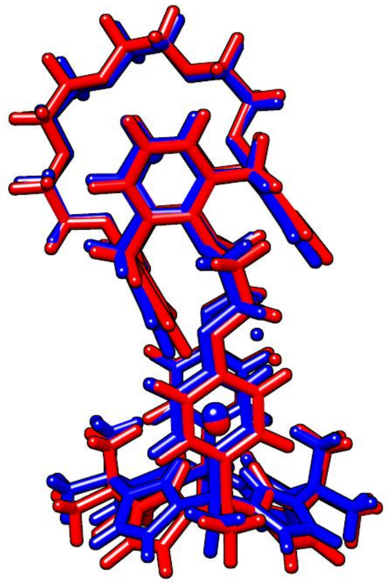

Receptor-Cs$^+$Cl$^-$.H$_2$O complex

Figure 5.4: Superimposition of optimized structures (red) and crystal structures (blue) of Receptor-Cs$^+$Cl$^-$.H$_2$O complex.

Table 5.10. Optimized structural parameters (Å) of Receptor-Cs$^+$X$^-$ complex in presence of solvent molecule[a]

	Cs-O$_{C/G}$	Cs-C$_A$[b]	Cs-N$_P$	X-N$_P$
Receptor-Cs$^+$.F$^-$.CH$_3$OH				
G/P	3.14-3.85	3.48-3.80	-	2.77-2.80
C/P	2.93-3.11 (2.84-3.03)	3.47-3.51 (3.40-3.46)	-	2.72-2.76 (2.76-2.81)
P/P	-	-	3.51-3.56	2.72-2.75
Receptor-Cs$^+$.Cl$^-$.H$_2$O				
G/P	3.10-4.47	3.39-3.55	-	3.25-3.27
C/P	2.92-3.11 (2.84-3.10)	3.45-3.51 (3.29-3.40)	-	3.23-3.26 (3.23-3.31)
P/P	-	-	3.53-3.58	3.24-3.29
Receptor-Cs$^+$.NO$_3^-$.C$_2$H$_5$OH				
G/P	3.17-3.68 (3.01-3.63)	3.53-3.93 (3.48-3.76)		2.93-2.94 (2.92-3.00)
C/P	2.93-3.11	3.46-3.54	-	2.87-2.92
P/P	-	-	3.54-3.59	2.82-2.92

[a] Values in parenthesis are the corresponding experimental values (ref no. [9-10])

[b] Cs$^+$-C$_A$ refer to the distance between Cs$^+$ and ortho and meta carbon atoms of Calix[4]arene moiety with respect to the phenoxy groups.

It should be noted that a direct comparison of solvent effect on the binding affinities cannot be made between the different cesium salts due the presence of non-identical solvent molecule at different ion-pair complexes. However, we can rationalize the observed change in binding affinity with respect to different binding modes for a particular ion-pair complex. For CsF ion-pair complex, very similar binding affinities are predicted for both C/P and G/P binding sites in the presence of a solvent methanol molecule (R.E= +1.1 kcal mol^{-1}). Here, at G/P mode, methanol acts as a bridge between the ions where hydrogen on the hydroxyl group ofthe methanol remain hydrogen bonded with F^- (1.67 Å) and oxygen of methanol coordinate to Cs^+ (2.97 Å). The inter-ionic distances are now elongated further (5.45 Å) as compared to contact ion-pair complex to form solvent bridged ion-pair complex. These subsequent changes help the ion-pair to get stabilized more inside the receptor (binding affinity increased by~15 kcal mol^{-1}). Further, we find C/P mode for CsF is slightly more favourable (by only 1 kcal mol^{-1}) as compared to G/P. This is in accord with the reported experimental observationsof Kim et al.[10] where a slow equilibrium between the G/P mode and the thermodynamically stable C/P mode was noted.However, for CsCl, the binding affinity at C/P mode still remains more preferable as compared to G/P mode but now the margin of difference is 3 kcal mol^{-1} (R.E=+3.2 kcal mol^{-1}). Similar to CsF, here also water is observed to remain hydrogen bonded albeit weakly with Cl^- (2.21 Å). Hence, an enhanced binding affinity is smaller for CsCl as compared to CsF. In case of $CsNO_3$ the G/P ion-pair complexis found to be largely preferable (by 9 kcal mol^{-1}) as compared to C/P mode (R.E=+9.0 kcal mol^{-1}). Here, Cs^+ interacts strongly with the oxygens of the 'G'site (Figure 5.3). As mentioned earlier, an asymmetric strong bi-dentate interaction of NO_3^- with Cs^+ (3.34-3.59 Å) is also noticed resulting in a strongly favourable binding as compared to P/P and C/P modes. For $CsNO_3$ binding at G/P site, Cs^+ interact with an oxygen atom of an ethanol molecule (3.19 Å) while a strong hydrogen bonding interaction with ethanol and NO_3^- (1.92 Å) further stabilize the structure leading to very strong binding affinity through a solvent bridged ion pair complex thus the overall binding affinity is stabilized by ~10 kcal mol^{-1}.

5.3.8. Comparison with reported MM calculations

Contrary to previously reported gas phase MM calculations[9-10] (Table 5.9), our calculations predict favourable binding modes more accurately. Although the experimental X-ray and NMR data favor C/P binding mode for CsF, CsCl and G/P mode for $CsNO_3$, the MM calculations conclude favorability of G/P binding motif for both CsF, CsCl. However, for $CsNO_3$ the MM calculations do predict the correct G/P binding mode to be most preferable. Notably, unlike MM calculations, the present computational methodology incorporates the implicit solvent effect through the COSMO solvation model. To understand whether the incorrect trend predicted by MM calculations originates due to solvation, we further calculated the binding affinities of CsCl with the receptor in the gas phase (Table 5.11). We note that absolute binding affinities are larger as compared to the solvated systems. More importantly, here also gas phase calculations failed to follow the experimental trend. Hence, owing to the lack of solvation effects, incorrect binding affinity trends were predicted.

Table 5.11. Gas phase binding affinities (B. E, units in kcal mol^{-1}) of CsCl in receptor at B3LYP-D3/B2//BP86/B1 level

Binding Mode	Binding energy
G/P	-105.04
C/P	-90.22
C/C	-80.88
P/P	-105.04

Finally, to gauge the influence of different solvent media to the binding affinities, calculations with [Receptor.CsCl] were performed with chloroform as solvent (ε=5.5). The net binding affinity of all the complexes increases by almost 8-15 kcal mol-1but overall the favourability towards C/P binding mode remain unchanged at both solvent environments (Table 12). This provides further support to the notion that solvent media of low polarity can modulate the extraction efficiency of Cs salts to the receptor.

Table 5.12: Optimized geometric parameters (Å) and binding affinities (kcal mol^{-1}) of Receptor-$Cs^+Cl^-.H_2O$ complexes.

Receptor.$Cs^+Cl^-.H_2O$	Epsilon (ε)	Cs-$O_{C/G}$	Cs-C_A	Cs-N_P	Cl-N_P	Binding energy
		BP86/B1				B3LYP-D3/B2//BP86/B1
G/P	80	3.10-4.47	3.39-3.55	-	3.25-3.27	-29.45
	5.5	3.10-4.57	3.38-3.57	-	3.26-3.30	-44.95
C/P	80	2.92-3.11	3.45-3.51	-	3.23-3.26	-32.62
	5.5	2.91-3.12	3.45-3.52	-	3.24-3.27	-45.28
	Exp[a]	2.84-3.10	3.29-3.40	-	3.23-3.31	-
P/P	80	-	-	3.53-3.58	3.24-3.29	-29.57
	5.5	-	-	3.46-3.51	3.24-3.28	-37.91

[a] Experimental values are taken from ref. no 9

5.3.9. Energy Decomposition Analysis (EDA)

The nature of the interactions present between the radionuclides and the receptor has been further analysed through EDA (Table 5.13). It is well known that the total interaction energy of a complex strongly varies with the use of different fragment systems. With view of this, here we have considered two different fragment pairs viz. FP_A and FP_B. FP_A investigates the interactions between cesium bound receptor with anions, whereas fragment FP_B deals with the interaction between anion bound receptor with cesiumcation. EDA calculations have been performed for the most preferred binding mode of CsX complexes (i.e. C/P mode for CsF,CsCl and G/P mode for CsBr, CsI and $CsNO_3$).

For both the fragment pairs i.e. FP_A and FP_B, we find the contribution of electrostatic interaction (ΔE_{elstat}) is considerably higher (>70 %) as compared to orbital interaction (ΔE_{orb}) (~20-30 %) in the overall interaction energy. This is suggestive of the fact that the electrostatic interaction of cesium and anion at their corresponding binding site plays a dominant role in stability of the complex. This is also revealed in the QTAIM study (see below). Further, for all complexes, negative value of total interaction energy points towards the well stabilization of cesium and anion inside the complex.

Table 5.13: Energy decomposition analysis (energies in kcal mol^{-1}) on complexes of Cesium Salts with Receptor at BLYP/TZ2P level. The values in the parentheses give the percentage contribution to the total attractive interactions ($\Delta E_{\mathrm{Elstat}} + \Delta E_{\mathrm{Orb}}$).

Fragment Pair	Complex	Binding Mode	Pauli repulsion $\Delta E_{\mathrm{pauli}}$	Electrostatic interaction $\Delta E_{\mathrm{elstat}}$	Total steric interaction	Orbital interactions ΔE_{orb}	Total interaction energy ΔE_{int}
FP$_A$	Receptor-Cs^{+}····F^{-}	C/P	81.04	-142.31 (70.78)	-61.27	-58.73 (29.22)	-120.00
	Receptor-Cs^{+}····Cl^{-}	C/P	68.68	-105.93 (74.54)	-37.25	-36.18 (25.46)	-73.43
	Receptor-Cs^{+}····Br^{-}	G/P	56.42	-115.25 (81.69)	-58.83	-25.84 (18.31)	-84.67
	Receptor-Cs^{+}·····I^{-}	G/P	64.34	-112.90 (83.06)	-48.52	-23.03 (16.94)	-71.59
	Receptor-Cs^{+}····NO$_3^{-}$	G/P	55.51	-117.50 (80.46)	-62.00	-28.54 (19.54)	-90.53
FP$_B$	Receptor-F^{-}·····Cs^{+}	C/P	55.28	-87.81 (72.03)	-32.52	-34.09 (27.97)	-66.62
	Receptor-Cl^{-}····Cs^{+}	C/P	51.58	-84.86 (71.85)	-33.27	-33.24 (28.15)	-66.52
	Receptor-Br^{-}····Cs^{+}	G/P	20.13	-74.46 (74.33)	-54.33	-25.71 (25.67)	-80.04
	Receptor-I^{-}·····Cs^{+}	G/P	25.58	-77.94 (73.20)	-52.36	-28.54 (26.80)	-80.90
	Receptor-NO$_3^{-}$····Cs^{+}	G/P	25.66	-85.50 (74.22)	-59.83	-29.70 (25.78)	-89.54

In case of FP$_A$, The bonding energy is noted to be more negative for the [Receptor.Cs^{+}]....[F^{-}] than the other anions. The ΔE_{orb} is significantly more negative for the [Receptor.Cs^{+}].....[F^{-}] than [Receptor.Cs^{+}].....[Cl^{-}], resulting in the greater stability of the former by 22 kcal mol^{-1}. In addition, the total steric interaction is less attractive in [Receptor.Cs^{+}].....[Cl^{-}] than the others due to the lesser contribution from electrostatic interaction term to this pair. The Pauli repulsion for the cesium bound receptor and anion is lower for all other anions as compared to F^{-}. For FP$_B$, The total steric interaction is estimated to be more negative for Br^{-}, I^{-} and NO$_3^{-}$ bound receptor due to the lesser contribution of Pauli repulsion term.

5.3.10. QTAIM Analysis

We have investigated the topological properties at the BCPs forthe most favourable receptor-$Cs^{+}X^{-}$.complexes (Table 5.14-5.18). All the systems analyzed here clearly display BCPs indicating the non-bonded interactions that exist between the Cs^{+}/X^{-} and receptor molecule. In the molecular graph, the big circles correspond to attractors attributed to positions of atoms and critical points such as (3, -1) BCP (red), (3, +1) RCP (yellow) and (3, +3) CCP (green) indicated by small circles (Figure 5.6).

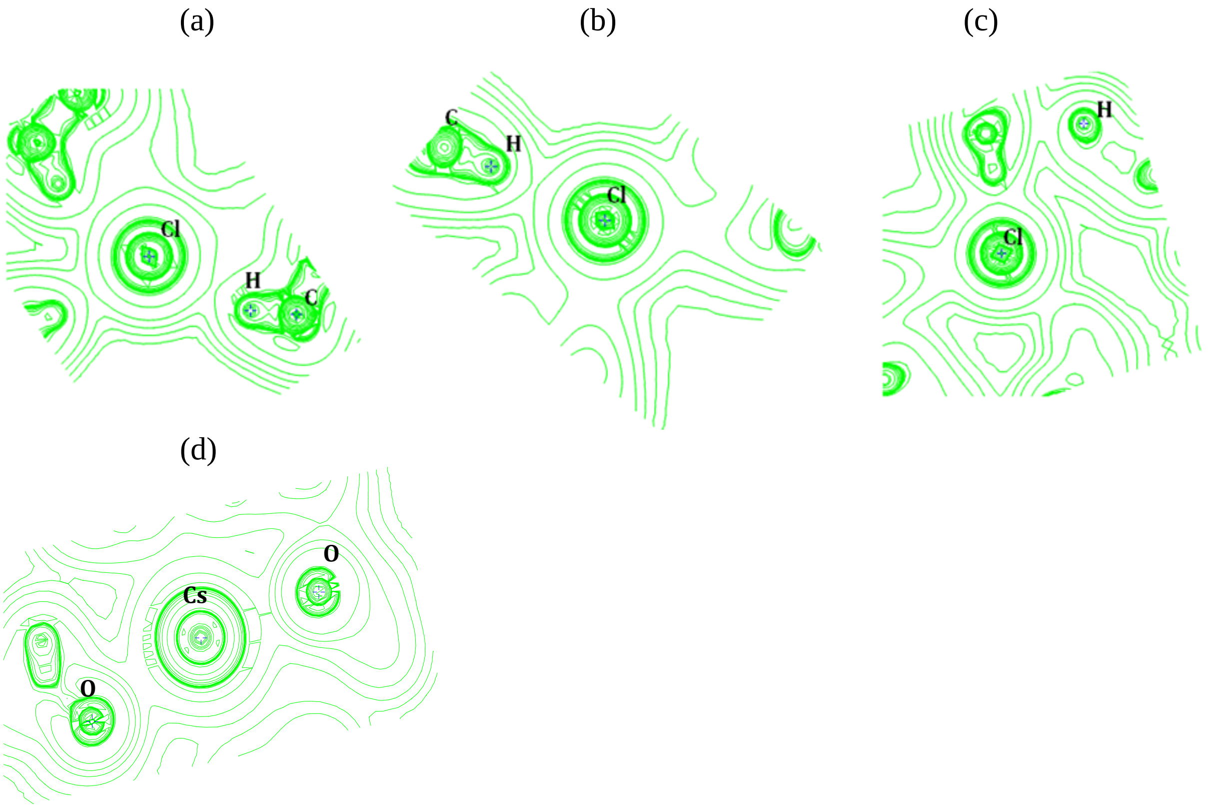
(a) (b) (c)

(d)

Figure 5.5: The Laplacian of electron density describing the (a) C-H···Cl interaction (calix[4]pyrrole) (b) C-H···Cl interaction (calix[4]arene) (c) C-H···Cl interaction (π-spacer) (d) (a) $Cs^{\cdot\cdot}O_C$ interaction of Receptor-$Cs^{+}Cl^{-}$ complex (C/P).

In the C/P-CsF complex, seven different bond paths have been observed between F^{-} and 'P' site. Of the seven bond paths, four are N-H...F type and remaining three are C-H...F type interactions (Figure 5.5). Of the three C-H...F interactions, two corresponds to the hydrogen bonding between the methine hydrogens of the 'P' site and the anions, whereas the last one is attributed to the hydrogen bonding of anions with nearby hydrogen of calix[4]arene moiety.

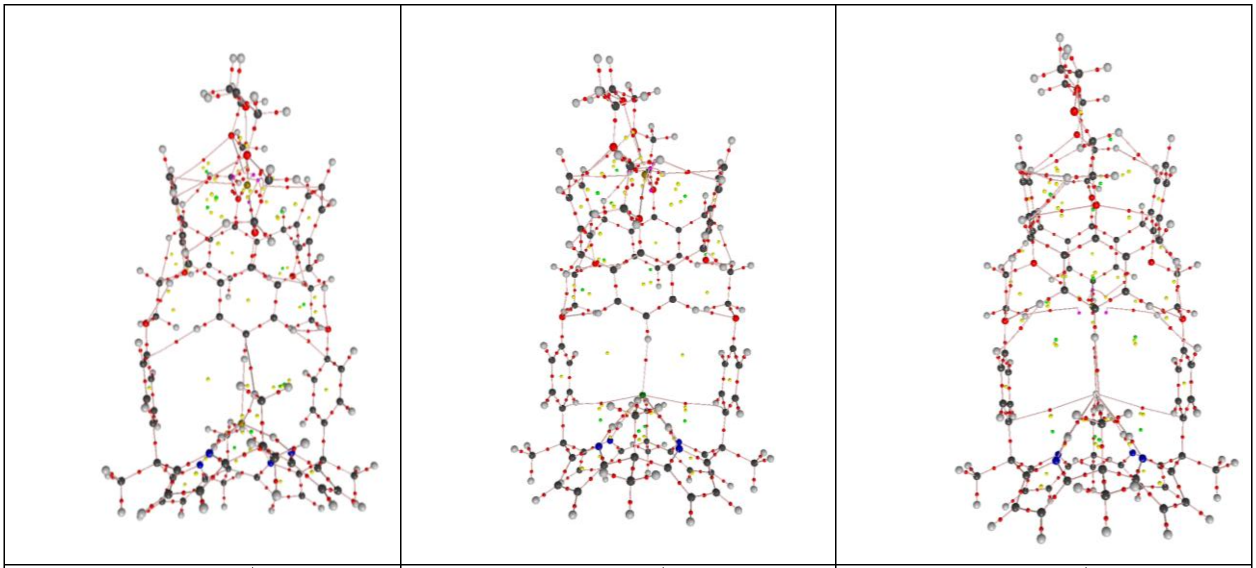

(a) Receptor-Cs$^+$F$^-$ (C/P) | (b) Receptor-Cs$^+$Cl$^-$ (C/P) | (c) Receptor-Cs$^+$Br$^-$ (G/P)

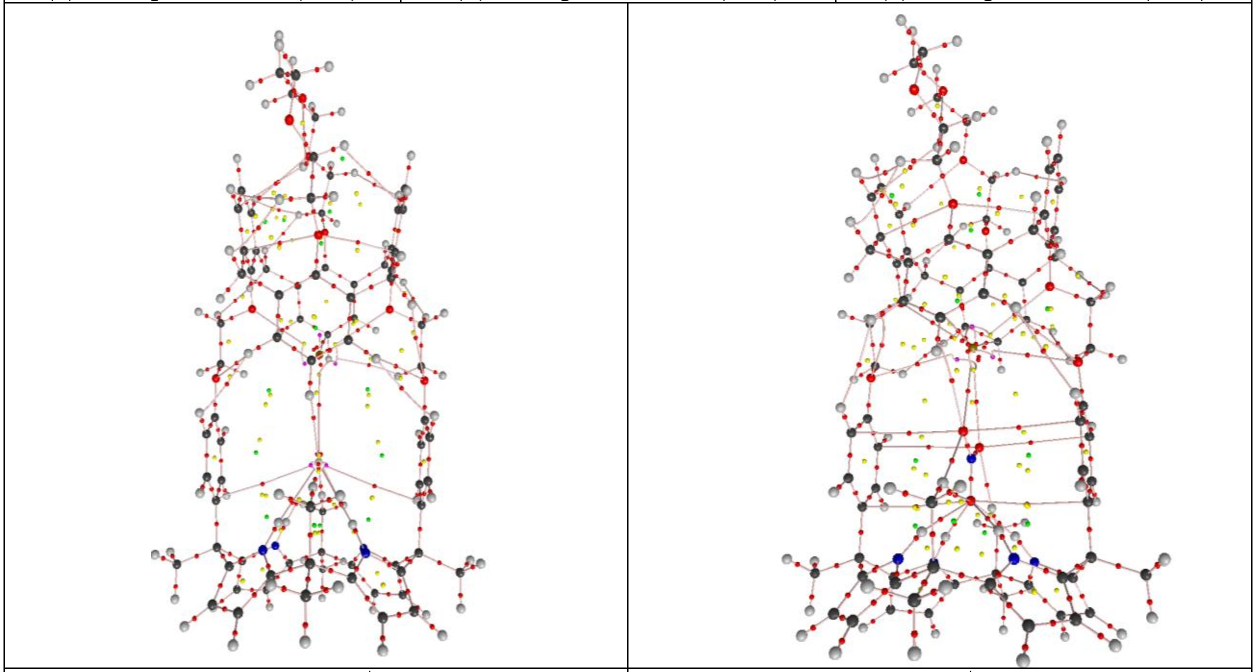

(d) Receptor-Cs$^+$I$^-$ (G/P) | (d) Receptor-Cs$^+$NO$_3^-$ (G/P)

Figure 5.6: Molecular graphs of the titled cases computed at BP86/B2 showing bond paths, bond critical points in red (BCPs) and ring critical points (RCPs) in yellow.

C/P-CsCl system also noted to have these seven different bond paths and additionally two C_π...Cl interactions are also observed (Figure 5.5). The calculated topological properties at the BCP between the interacting atoms with the corresponding anions suggest that as the size of the anions increases, the charge density at BCP decreases. For a typical hydrogen bond, the values of the electron density at the BCP should be within 0.002–0.035 a.u.[271] Our calculated value for the anions bound in 'P' site falls in this range (Table 5.14-5.18). It is interesting to note that, mainly H…X bonding interactions stabilize the incoming anions. The ρ values at the H…X BCPs suggest that there are seven such hydrogen bonding interactions that fall into two distinct sets.

Among the seven hydrogen bonds, four are comparatively stronger whose ρ values lie at ~ 0.0165 a.u. whereas for the remaining three weak hydrogen bonds, this value lies at ~0.003 a.u. These varying degrees are consistent with the geometric parameters (Table 5.6). It is clear that the hydrogen bonding between the methine hydrogens of the 'P' site and the anions ions are not symmetric and the strength of the hydrogen bonds is distinguished using the properties of the electron density at BCP. It is interesting to find that the four strong hydrogen bonds (N-H...X) get weakened and other three weak hydrogen bonds (C-H...X) are strengthened gradually as we move from the fluoride to iodide. Interestingly, in the $CsNO_3$ ion-pair complex, NO_3^- shows different bond paths between the NO_3^- anion and 'P' site and with the aromatic linker.

Cremer and Karaka[272] have developed a scale to determine the nature of bonds based on these topological properties. Accordingly, in all the cases the BCPs between C-H...X bonds have negative Laplacian, a positive kinetic energy density H(r) and a potential energy to the lagrangian kinetic energy ratio (|V(r)/G(r))| of less than 1. Critical points with such characteristics have been identified by Cremer as constituted by atoms that share a shared interaction (ionic, van der Waals, or hydrogen bonds). While the negative L(r) values and small negative H(r) values along with a –|V(r) /G(r)| values at the BCPs between N-H...X bonds are indicative of a weak non-bonding interactions.

Table 5.14: Topological properties of Receptor-Cs$^+$F$^-$ (C/P) computed at BP86/B2 level. ρ(r) in units of eÅ^{-3}, L(r) in units of eÅ^{-3}, G(r), V(r), H(r) in units of a.u. Å^{-3}.

Receptor-Cs$^+$F$^-$ (C/P)							
BCP	ρ(r)	L(r)	G(r)	H(r)	ε	V(r)	-V(r)/G(r)
N-H···F	0.0461	-0.0353	0.0403	-0.0050	0.0204	0.0453	-1.1241
N-H···F	0.0465	-0.0357	0.0408	-0.0050	0.0199	0.0458	-1.1225
N-H···F	0.0443	-0.0338	0.0386	-0.0048	0.0207	0.0435	-1.1269
N-H···F	0.0442	-0.0337	0.0385	-0.0048	0.0215	0.0433	-1.1247
C-H···F	0.0058	-0.0062	0.0048	0.0014	0.1974	0.0034	-0.7083
C-H···F	0.0073	-0.0076	0.0062	0.0014	0.0939	0.0048	-0.7742
C-H···F	0.0054	-0.0056	0.0042	0.0013	0.0625	0.0029	-0.6905
O···Cs	0.0199	-0.0172	0.0160	0.0011	0.1329	0.0149	-0.9313
O···Cs	0.0149	-0.1219	0.0114	0.0008	0.0795	0.0106	-0.9298
O···Cs	0.0163	-0.0136	0.0126	0.0009	0.0847	0.0117	-0.9286
O···Cs	0.0149	-0.0122	0.0114	0.0008	0.0789	0.0106	-0.9298
O···Cs	0.0201	-0.0175	0.0163	0.0011	0.1338	0.0152	-0.9325
C_π···Cs	0.0094	-0.0075	0.0062	0.0013	3.1113	0.0049	-0.7903
C_π···Cs	0.0093	-0.0076	0.0062	0.0013	2.8472	0.0049	-0.7903

Table 5.15: Topological properties of Receptor-Cs$^+$Cl$^-$ (C/P) computed at BP86/B2 level. ρ(r) in units of eÅ^{-3}, L(r) in units of eÅ^{-3}, G(r), V(r), H(r) in units of a.u. Å^{-3}.

Receptor-Cs$^+$Cl$^-$ (C/P)							
BCP	ρ(r)	L(r)	G(r)	H(r)	ε	V(r)	-V(r)/G(r)
N-H···Cl	0.0277	-0.0189	0.0202	-0.0014	0.0129	0.0216	-1.0693
N-H···Cl	0.0282	-0.0191	0.0206	-0.0015	0.0135	0.0221	-1.0728
N-H···Cl	0.0269	-0.0184	0.0194	-0.0011	0.0142	0.0206	-1.0619
N-H···Cl	0.0269	-0.0185	0.0197	-0.0012	0.0149	0.0209	-1.0609
C-H···Cl	0.0094	-0.0076	0.0062	0.0013	0.0081	0.0049	-0.7903
C-H···Cl	0.0090	-0.0072	0.0059	0.0013	0.0135	0.0046	-0.7797
C-H···Cl	0.0095	-0.0077	0.0064	0.0013	0.0137	0.0050	-0.7813
C_π···Cl	0.0039	-0.0028	0.0023	0.0005	0.8139	0.0018	-0.7826
C_π···Cl	0.0042	-0.0030	0.0025	0.0005	0.1235	0.0019	-0.7600
O···Cs	0.0189	-0.0164	0.0152	0.0011	0.1349	0.0141	-0.9276
O···Cs	0.0141	-0.0115	0.0107	0.0008	0.0713	0.0099	-0.9252
O···Cs	0.0154	-0.0128	0.0118	0.0009	0.0904	0.0109	-0.9237
O···Cs	0.0141	-0.0115	0.0107	0.0008	0.0724	0.0099	-0.9252
O···Cs	0.0191	-0.0163	0.0152	0.0011	0.1329	0.0141	-0.9276
C_π···Cs	0.0093	-0.0076	0.0062	0.0013	5.4798	0.0049	-0.7903
C_π···Cs	0.0091	-0.0074	0.0061	0.0013	2.2582	0.0047	-0.7705

Table 5.16: Topological properties of Receptor-Cs$^+$Br$^-$ (G/P) computed at BP86/B2 level. ρ(r) in units of eÅ^{-3}, L(r) in units of eÅ^{-3}, G(r), V(r), H(r) in units of a.u. Å^{-3}.

Receptor-Cs$^+$Br$^-$ (G/P)							
BCP	ρ(r)	L(r)	G(r)	H(r)	ε	V(r)	-V(r)/G(r)
N-H···Br	0.0190	-0.0127	0.0124	0.0003	0.0275	0.0120	-0.9677
N-H···Br	0.0192	-0.0128	0.0125	0.0003	0.0269	0.0122	-0.9760
N-H···Br	0.0182	-0.0123	0.0119	0.0004	0.0302	0.0114	-0.9580
N-H···Br	0.0180	-0.0121	0.0117	0.0004	0.0310	0.0112	-0.9573
C-H···Br	0.0095	-0.0067	0.0056	0.0010	0.0211	0.0046	-0.8214
C-H···Br	0.0091	-0.0064	0.0054	0.0010	0.0234	0.0043	-0.7963
C-H···Br	0.0033	-0.0023	0.0018	0.0005	0.6375	0.0013	-0.7222
C_π···Br	0.0043	-0.0029	0.0024	0.0005	1.3654	0.0019	-0.7917
C_π···Br	0.0042	-0.0028	0.0023	0.0005	1.3723	0.0019	-0.8261
Cs···Br	0.0060	-0.0040	0.0033	0.0007	0.0015	0.0025	-0.7576
C-H···Cs	0.0032	-0.0029	0.0021	0.0008	0.2691	0.0014	-0.6667
C-H···Cs	0.0032	-0.0029	0.0021	0.0008	0.3960	0.0014	-0.6667
O···Cs	0.0079	-0.0071	0.0061	0.0010	0.1100	0.0051	-0.8361
O···Cs	0.0089	-0.0079	0.0069	0.0010	0.1152	0.0059	-0.8551
C_π···Cs	0.0067	-0.0049	0.0040	0.0009	0.6206	0.0030	-0.7500
C_π···Cs	0.0089	-0.0071	0.0058	0.0013	2.4049	0.0045	-0.7759

Table 5.17: Topological properties of Receptor-Cs$^+$I$^-$ (G/P) computed at BP86/B2 level. ρ(r) in units of eÅ^{-3}, L(r) in units of eÅ^{-3}, G(r), V(r), H(r) in units of a.u. Å^{-3}.

Receptor-Cs$^+$I$^-$ (G/P)							
BCP	ρ(r)	L(r)	G(r)	H(r)	ε	V(r)	-V(r)/G(r)
N-H···I	0.0162	-0.0094	0.0095	-0.0001	0.0149	0.0095	-1.0000
N-H···I	0.0162	-0.0095	0.0095	-0.0001	0.0152	0.0095	-1.0000
N-H···I	0.0148	-0.0089	0.0087	0.0002	0.0197	0.0085	-0.9770
N-H···I	0.0147	-0.0089	0.0086	0.0002	0.0188	0.0084	-0.9767
C-H···I	0.0087	-0.0057	0.0048	0.0009	0.0220	0.0039	-0.8125
C-H···I	0.0093	-0.0061	0.0052	0.0009	0.0199	0.0043	-0.8269
C-H···I	0.0050	-0.0034	0.0026	0.0007	0.4325	0.0019	-0.7308
C_π···I	0.0051	-0.0031	0.0026	0.0005	2.1084	0.0021	-0.8077
C_π···I	0.0050	-0.0030	0.0025	0.0005	1.8963	0.0020	-0.8000
Cs···I	0.0073	-0.0047	0.0039	0.0008	0.0038	0.0030	-0.7692
C-H···Cs	0.0031	-0.0029	0.0021	0.0008	0.7412	0.0013	-0.6190
O···Cs	0.0022	-0.0023	0.0017	0.0006	0.3557	0.0011	-0.6471
O···Cs	0.0109	-0.0094	0.0084	0.0010	0.1234	0.0074	-0.8810
O···Cs	0.0118	-0.0101	0.0091	0.0010	0.1270	0.0081	-0.8901
C_π···Cs	0.0076	-0.0057	0.0047	0.0011	1.0105	0.0036	-0.7660
C_π···Cs	0.0082	-0.0067	0.0054	0.0013	8.2469	0.0042	-0.7778

Table 5.18: Topological propertiesofReceptor-Cs$^+$NO$_3^-$ (G/P) computed at BP86/B2 level. ρ(r) in units of eÅ^{-3}, L(r) in units of eÅ^{-3}, G(r), V(r), H(r) in units of a.u. Å^{-3}.

Receptor-Cs$^+$NO$_3^-$ (G/P)							
BCP	ρ(r)	L(r)	G(r)	H(r)	ε	V(r)	-V(r)/G(r)
N-H···O	0.0282	-0.0217	0.0227	-0.0009	0.0592	0.0237	-1.0441
N-H···O	0.0283	-0.0219	0.0229	-0.0009	0.0604	0.0238	-1.0393
N-H···O	0.0258	-0.0199	0.0208	-0.0009	0.0631	0.0216	-1.0385
N-H···O	0.0259	-0.0200	0.0209	-0.0009	0.0639	0.0217	-1.0383
C-H···O	0.0041	-0.0041	0.0031	0.0009	1.3171	0.0021	-0.6774
C_{π}···O	0.0036	-0.0034	0.0027	0.0007	4.3269	0.0019	-0.7037
C_{π}···O	0.0036	-0.0034	0.0027	0.0007	4.2951	0.0019	-0.7037
C-H···O	0.0086	-0.0070	0.0063	0.0008	0.0047	0.0055	-0.8730
C_{π}···O	0.0029	-0.0027	0.0021	0.0006	0.3554	0.0016	-0.7619
C_{π}···O	0.0029	-0.0028	0.0022	0.0006	0.4010	0.0016	-0.7273
Cs···O	0.0101	-0.0084	0.0075	0.0009	0.0105	0.0065	-0.8667
C-H···O	0.0066	-0.0057	0.0048	0.0009	0.0224	0.0039	-0.8125
C-H···O	0.0029	-0.0028	0.0022	0.0006	1.2024	0.0016	-0.7273
C_{π}···O	0.0033	-0.0030	0.0024	0.0006	0.5377	0.0018	-0.7500
C_{π}···O	0.0032	-0.0029	0.0024	0.0006	0.4289	0.0018	-0.7500
Cs···O	0.0102	-0.0086	0.0076	0.0009	0.0219	0.0066	-0.8684
O···Cs	0.0047	-0.0047	0.0038	0.0009	0.0936	0.0028	-0.7368
O···Cs	0.0096	-0.0085	0.0074	0.0009	0.1138	0.0065	-0.8784
O···Cs	0.0102	-0.0089	0.0079	0.0009	0.1169	0.0069	-0.8734
O···Cs	0.0050	-0.0049	0.0040	0.0009	0.0662	0.0031	-0.7750
C_{π}···Cs	0.0059	-0.0044	0.0036	0.0009	0.7242	0.0027	-0.7500
C_{π}···Cs	0.0084	-0.0068	0.0055	0.0013	3.0972	0.0042	-0.7636

As it is obvious from Table 5.14-5.18, the ellipticity values (ε) for the N–H•••X and C-H...X interactions are nearly small and close to zero, indicating that the hydrogen bonds are conserved in all the complexes. For Cs$^+$ at the 'C' site the small values of ρ, the high values of ε and the nearly zero values of H(r) suggest, according to the Rozas[273] criterion, that all Cs···O intermolecular interactions, are basically electrostatic in nature (Figure 5.5). More specifically, it can be seen that the values of ellipticity obtained for the Cs···O interactions are within the range of 0.072–1.133. The existence of C_{π}···Cs$^+$ interactions is also revealed by the presence of corresponding BCPs in the molecular graphs (Figure 5.6). In 'G' site, bond paths have been observed between the Cs^+ and aromatic moieties of calix[4]arene along with the ethylene glycol spacer interactions.

5.4. Conclusions

Over the years, an increasing interest and urgency is devoted to improve the nuclear waste management processes through the design of new receptor macrocycles. Sessler and co-workers have designed a series of macrocycles for the selective extraction of Cs^+. Various mechanisms for the binding of Cs salt to the receptor have been suggested. In this Chapter, we have carried out a systematic study to understand the structure, binding and selectivity of various Cs salts to a recently synthesized receptor[9-10] using electronic structure calculations. To our knowledge, the electronic structure calculations reported here are the first to be carried out on such gigantic receptor without truncations. The major findings from our study are summarized as follows:

(i) We find that Cs^+ alone can favorably bind to ‘C’ and ‘G’ site of the receptor. The binding of anions occurs at the ‘P’ site, preferably due to the strong hydrogen bonding between the protons of the pyrrole ring and the anions.

(ii) Computed binding affinities further indicate that the ion-pair binding to the receptor occurs majorly via cooperative binding mechanism. Both Cs^+ and anion assist each other to provide excess stability to the ion-pair receptor complex.

(iii) In accord to experiments, we find C/P mode to be most preferable for CsF and CsCl while G/P for CsNO3. The presence of a crystallographic solvent molecule is also observed to enhance the overall binding affinity of the Cs salt to the receptor by 1-15 kcal mol^{-1}.

(iv) Irrespective of fragment pair (A and B), electrostatic contribution (ΔE_{elstat}) to the total interaction energy is estimated to be higher than the orbital interaction (ΔE_{orb}). QTAIM calculations clearly bring out the importance of strong hydrogen bonding interactionswhich stabilizes the anions at the 'P' site. In line with our EDA results, QTAIM also reveals the bonding of Cs^+ at 'C' and 'G' site is dominantly ionic in nature. Further, our results demonstrate the bulk solvent effects are crucial for the correct binding trends of Cs salts to the receptor. Thus, the applied theoretical tools in the present Chapter can be regarded to set a benchmark and can be used to predict and design new receptor molecules for the complexation of various other radionuclides such as Sr^{2+}, which is the subject matter of Chapter 6.

CHAPTER –6

Selective Separation of Strontium with multitopic ion-pair receptor: A DFT exploration

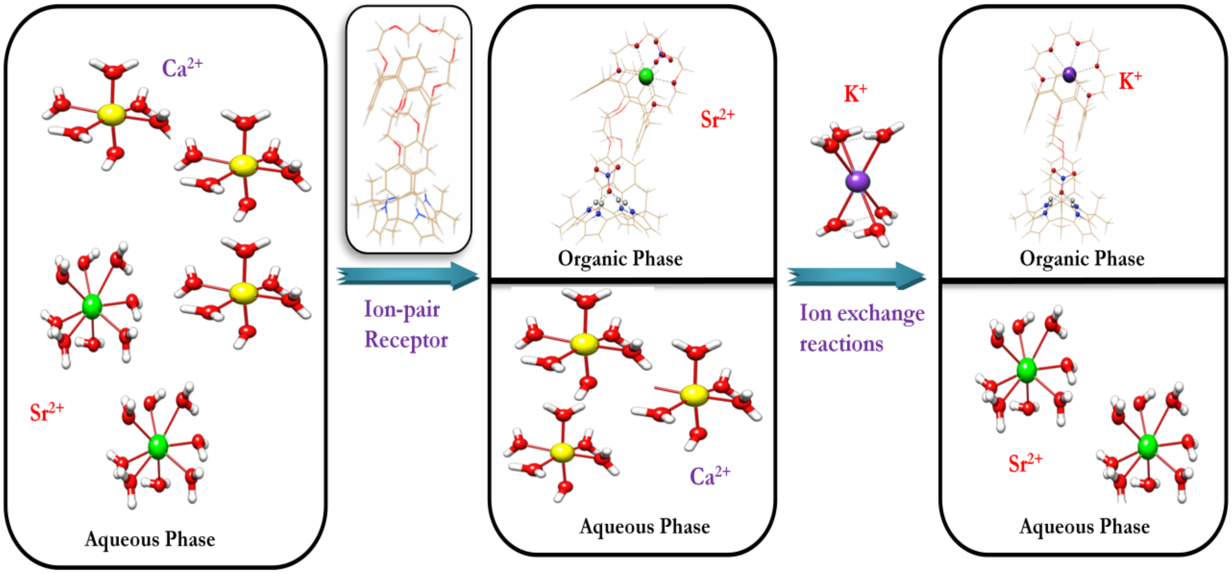

6.1. Introduction:

Selective separation of fission products like radiostrontium ($Sr^{89/90}$) from the nuclear waste is a challenging and important task, which is central to the nuclear waste management program. The prime aim behind extraction of ^{90}Sr from the nuclear waste is to reduce the volume of high level waste (HLW), which is required to minimize the undesirable decay heat production in the waste. Similarly, waste generated due to the inadvertent release of ^{90}Sr into the atmosphere also requires significant chemical treatment to reduce the radionuclide associated long term hazards and restricts its migration in the environment.

Significant research is devoted to find suitable separation techniques for Sr^{2+} extraction and recovery.[274] The major difficulty in such separation processes is the presence of interfering cations such as Ca^{2+} (particularly for environmental waste). Apart from this, strong hydration energy barrier of Sr^{2+} (-330 kcal mol^{-1}) creates difficulty to extract it into the organic phase and thus signifies the need of proper extractant with available diluents. Chemical treatments like nitrate precipitation, ion exchange methods for Sr^{2+} recovery from environmental waste are well known methods in this field. However, involvement of multiple steps and usage of too many chemical agents makes the separation procedure time consuming and reduces the recovery factor for Sr^{2+}. Keeping in mind the ionic size differences between Ca^{2+} (1.14 Å) with Sr^{2+} (1.32 Å), size based separation using crown based macrocyclic ligands is always thought to be the viable solution for the problem, particularly for liquid-liquid extraction methodology. These ligands contain convergent binding site with appropriate cavities to selectively trap Sr^{2+} *via* strong electrostatic interaction. For instance, using 4,4'(5')-bis(t-butyl- cyclohexo)- 18-crown-6 (DtBuCH18C6) in 1-octanol solvent, Horwitz et.al[53] reported selective Sr^{2+} extraction in presence of other alkali and alkaline earth metals. Further, they proposed new extraction methodology[54], SREX where they efficiently extracted Sr^{2+} from aqueous to organic medium in nitrate media.

Zhang and co workers[275] also came up with new methodology for partitioning of Sr^{2+} from nuclear waste by using two macroporous silica-based polymeric composites. Calix arenes[276-278] are also tested by many researchers as a possible extractant for Sr^{2+}.

In addition to experimental studies, use of computational methods like density functional theory (DFT)[12, 248, 279] or molecular dynamics (MD)[280-281] are very popular to address and understand the selectivity of various ligands towards radionuclide of interest at molecular level. This further helps to design[14-15] host molecules and predict their behavior prior to experimentation.

Selective capturing of Sr^{2+} and transfer it into the organic phase is the first step of the recovery process. Later, Sr^{2+} at organic phase also needs to be stripped back into the aqueous phase for efficient strontium extraction. Thus, ligands with very high binding affinities for Sr^{2+} may further create hurdles in the stripping process. It is now perceived from several studies that the concentration and involvement of counter-ions, such as nitrate also plays key-role in these processes and often increase the metal binding affinity. However, in host molecules with no anion specific binding site, the counter-ion interaction with metal become non-specific in nature and anion participation in binding become ill defined.

In this regard, Sessler and coworker reported a series of multitopic ion-pair receptors[8-10, 55] which contains both cation and anion binding sites and utilizes the cation-anion cooperative assistance to enhance the metal binding efficiency. For instance, 15-crown-5 strapped calix[4]arene-calix pyrrole receptor (Rec) is reported to selectively extract cesium *via* controlled binding and release mechanism.[9] The binding preference for Cs^{+} is achieved at the binding site by size-specificity. Whereas, higher affinity of K^{+} (than Cs^{+}) in the receptor is strategically used to ease the stripping of Cs^{+} by adding potassium salt into the organic phase. In Chapter 4, we have found that counter ions in the receptor increase the binding affinity of Cs^{+} to facilitate the Cs^{+} capture process.

Taking consideration of miniscule size differences between K^+ and Sr^{2+} (by 0.06 Å), the primary aim of the present investigation is to evaluate the possibility of using the same receptor for Sr^{2+} extraction. Here, we have opted for similar DFT methodology[279] as used in Chapter 3, which was shown to be in excellent agreement with the experimentally obtained trend for the system studied therein.[9-10] Further, we like to address following questions in relation to Sr^{2+} extraction methodology.

a) How divalent metals (Ca^{2+} and Sr^{2+}) bind to the receptor in nitrate media in comparison to K^+?

b) Whether any selectivity exists for Sr^{2+}? If yes, how such selectivity arises at the molecular level.

c) Whether choice of solvent influence the extraction process.

Finally, based on the calculations, we proposed a possible extraction methodology for Sr^{2+}.

6.2. Computational Details

Structure of the receptor is depicted in Figure 6.1. As described in Chapter 3, the following receptor contains a calix-[4]-arene-crown-5 cavity (**C**) and a calix-[4]-pyrrole (**P**) site linked *via* ethylene glycol linkages (**G**). In the receptor, site **C**, **G** and Lower rim of **P** can act as probable cation binding site, whereas site **P** and outer sphere of site **C** can possibly bind anion. Due to the presence of these multiple cation-anion binding sites, metal salts can bind to the receptor *via* different binding modes namely **C/P**, **P/P**, **G/P** and **C/C**, where initial and final letter stands for cation and anion binding site, respectively. For the sake of comparison, here we used the same nomenclature with respect to the corresponding experimental article. In the present investigation, we have considered nitrate salt of Ca^{2+} and Sr^{2+} for investigations. In addition to the aforementioned binding modes, taking consideration of divalent nature of Sr^{2+} and Ca^{2+} and electro neutrality of the metal complex, we have also considered one more binding mode **C/CP** (cation at **C** site while two nitrate molecules reside at **C** and **P** site).

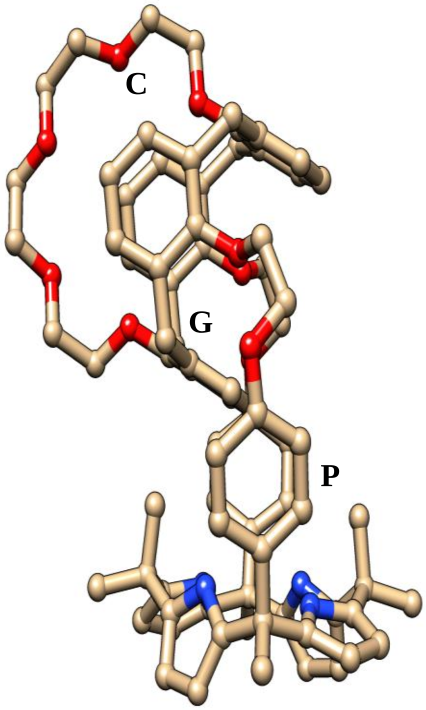

Figure 6.1: Optimized Structure of Multi-topic ion-pair receptor

Starting structure of [Rec.$K^+NO_3^-$] at **C/P** mode is taken from reported crystal structure by Kim et al.[9] The same structure was used for $Ca^{2+}$and Sr^{2+} by replacing the respective cation. Other structures with different binding modes are built accordingly. All geometrical optimizations are carried out in gas phase using dispersion corrected BP86 functional[91-92] (BP86-2D) functional with medium sized basis set def2-SV(P)[93] using TURBOMOLE v6.6 program suite.[282] Further, AOFORCE module is used to calculate the analytical frequencies for metal-receptor complexes at their most preferable binding mode in order to verify the structure as potential minima. Most of the structures are found to be free from any imaginary frequencies. Otherwise, SCREWER utility is used to distort the structure for further optimizations until minimum energy conformations are achieved. Single point calculations on the optimized structures are performed at

TZVP[98-99]/B3LYP[96-97] level with Grimme's three body dispersion correction (D3BJ)[165] using ORCA 3.0.3 package.[103] Resolution of identity approximations (RI-J/RIJCOSX) are invoked for all calculations to evaluate the Coulomb integrals and speed up the computations. Solvent effects are incorporated during energy minimization using COSMO continuum solvation model[215] for three solvents [water (ε=80; η=1.33), acetonitrile (ε=36.3; η=1.34) and ether (ε=5; η=1.45)]. The choice of two solvents are based on common organic solvent used in liquid-liquid extraction strategy and expected to provide valuable information on varying the dielectric constant of media. Finally, free energy parameters for the metal-ligand binding reactions are calculated to understand the feasibility of separation processes.

6.3. Results and Discussions

6.3.1. Hydration models for metals and nitrate

Adequate metal transfer from aqueous to organic phase using a ligand is strongly influenced by the hydration energy of metals as well as of counter ions. Thus, incorporation of hydration sphere for the metals and nitrate anion hold the key for accurate prediction of extraction energy. Previously reported experimental and computational studies on hydrated structure of K^+ and Na^+ suggest that maximum of six water molecule[184, 187-188] can be accommodated in its first solvation sphere. Our MD investigations[204] in Chapter 3 also predicted that the presence of six water molecules in the primary solvation shell of these cations whereas, in Chapter 2, we have found that Sr^{2+} can accommodate eight water molecules in its primary hydration shell. These corresponding structures are used here for further optimizations at the applied computational level. For $Ca^{2+}$and NO_3^-, based on the previously reported studies,[218-219, 242, 279] hexa-hydrated system is used throughout. The calculated M-O_{wat} bond distances are found to be in excellent agreement with the earlier reported experimental and theoretical results (Table 6.1). Further, in order to validate the solvation model, we calculated hydration energy for these metals which are noted to follow correct experimental trend.[116]

Table 6.1: Hydration free energy (kcal mol^{-1}) of ions calculated at B3LYP-D3/B2//BP86/B1 level

Hydrated ion	Hydration free energy	
	Calculated	Experimental[a]
$K(H_2O)_6^+$	-77.06	-70.57
$Sr(H_2O)_8^{2+}$	-345.21	-330.14
$Ca(H_2O)_6^{2+}$	-359.7	-360.04
$NO_3(H_2O)_6^-$	-55.27	-71.77

[a] experimental values are taken from ref no. 116

6.3.2. Structure and preferable binding modes of metal-nitrate salts with receptor

As mentioned earlier, metal-nitrate salts can bind to the receptor *via* different binding modes. Optimized structural parameters and overall binding affinities in aqueous phase for all these modes are tabulated in Table 6.2 and 6.3. For KNO_3, we have noted **C/P** binding mode to be the most preferable with binding energy (ΔE_{aq}) of -36.87 kcal mol^{-1} which is in excellent agreement with the reported crystal structure (Fig. 6.2). The binding preferability at **C/P** mode is followed by **G/P** (-31.75 kcal mol^{-1}), **C/C** (-24.85 kcal mol^{-1}) and **P/P** (-8.33 kcal mol^{-1}). The reasoning behind this trend can be understood by close inspection of their corresponding optimized structures. In least preferable **P/P** mode, K^+ interacts with the pyrrole ring *via* weak cation-π interaction (K^+-N_P: 2.95-2.97 Å). On the other hand, at **G/P** mode, K^+ weakly interacts with four oxygen atoms of glycol linkages (K^+-O_G 2.91-3.08 Å). Due to the large cation-anion distance (K^+-N_{NO3-} : 3.38 Å) at this mode, presence of NO_3^- at nearest **P** site cannot satisfy the required coordination number. At **C/C** mode, K^+ resides at **C** site (K^+-O_C: 2.78-2.93 Å) whereas NO_3^- remain in weak contact with K^+ (K^+-O_{NO3}-: 2.91-2.96 Å) at the outer sphere of crown. Here, although cation occupies a stable site, anionic instability at this binding mode led to low binding energy. On the contrary, at **C/P** mode (Figure 6.3), K^+ binds tightly at the crown cavity *via* strong electrostatic interaction (K^+-O_C: 2.77-2.98 Å) whereas NO_3^- occupy **P** site to interact with four -NH groups *via* hydrogen bonding (N_P- O_{NO3}-: 2.85-2.90 Å) resulting in highest binding free energy among all other modes.

Table 6.2: Optimized structural parameters (Å) of $M^{+/2+}NO_3^-$ -receptor complex (gas phase) for most preferable binding mode.

	M-$O_{C/G}$	M-C_A	M-N_P	O(NO_3^-)-N_P
K.Rec.NO_3				
G/P	2.91-3.08	3.11-4.06	-	2.96-3.03
C/P	2.77-2.98 (2.73-2.84)	3.04-3.16 (3.07-3.31)	-	2.85-2.90 (2.93-3.01)
C/C	2.78-2.93	3.16-3.45	-	-
P/P	-	-	2.95-2.97	2.65-3.16
Sr.Rec.$(NO_3)_2$				
G/P	2.70-2.93	3.14-3.97	-	3.25-3.53
C/P	2.60-2.86	3.04-3.26	-	2.78-2.91
C/C	2.73-2.89	3.17-3.66	-	-
P/P	-	-	2.72-2.90	2.65-3.16
C/CP	2.57-2.74	3.15-4.23	-	2.81-2.88
Ca.Rec.(NO3)2				
G/P	2.53-3.02	2.94-4.24	-	3.26-3.52
C/P	2.53-2.81	2.82-3.13	-	2.77-2.91
C/C	2.45-3.05	2.97-4.07	-	-
P/P	-	-	2.55-2.77	2.68-3.23
C/CP	2.49-2.89	2.96-4.63	-	2.80-2.88

Table 6.3: Calculated binding energies (ΔE in kcal mol^{-1}) of metal-receptor complexes at different possible binding modes.

Metal	Used equations*	ΔE_{aq}				
		C/P	G/P	P/P	C/C	C/CP
K^+	Rec + $K.(H_2O)_6^+$ + $NO_3.(H_2O)_6^-$ = K.Rec.NO_3 + $2(H_2O)_6$	-36.87	-31.75	-8.33	-24.85	-
Sr^{2+}	Rec + $Sr.(H_2O)_8^{2+}$ + $xNO_3.(H_2O)_6^-$ = Sr.Rec.$(NO_3)_x$ + $x(H_2O)_6$ + $(H_2O)_8$	-24.17	-15.05	14.85	-29.77	-29.86
Ca^{2+}	Rec + $Ca.(H_2O)_6^{2+}$ + $xNO_3.(H_2O)_6^-$ = Ca.Rec.$(NO_3)_x$ + $(x+1)$ $(H_2O)_6$	-15.40	+0.68	26.48	-19.96	-20.43

*x=2 for C/CP binding mode and 1 for all other binding mode.

In contrast to monovalent metal-nitrates, we found **C/CP** binding mode is the most preferable binding mode for Ca^{2+} and Sr^{2+} (Fig. 6.2). In this mode, Ca^{2+}/ Sr^{2+} resides at the **C** site while one of the two nitrate molecules is seen to occupy the **P** site and the other one remain at the outer rim of **C** site to directly interact with the bound metal *via* monodentate motif (Ca^{2+}-O_{NO3}- : 2.16 Å; Sr^{2+}-O_{NO3}- : 2.29 Å). It is apparent from our calculated binding energy values that **C/CP** has only a marginal preference (~1 kcal mol^{-1}) than **C/C** mode. Considering the error bar associated with the calculated values, one can assume that both the modes are equally favorable and the slight preference for **C/CP** may be a resultant of electro neutrality of the complex.

K.Rec.NO_3	Sr.Rec.$(NO_3)_2$	Ca.Rec.$(NO_3)_2$
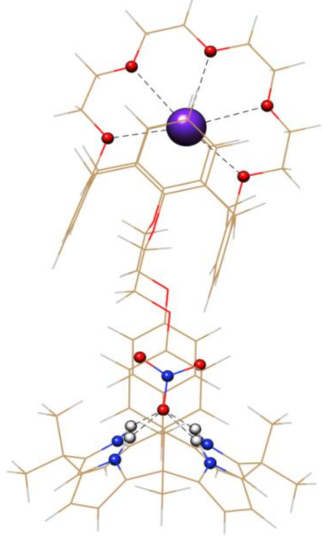	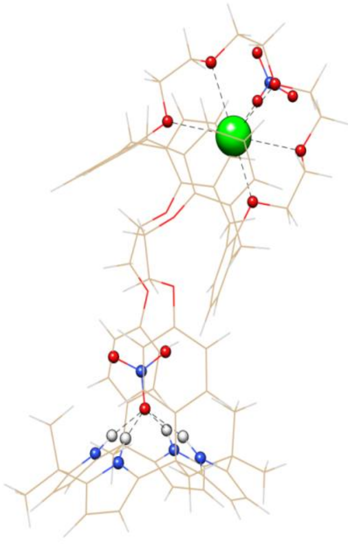	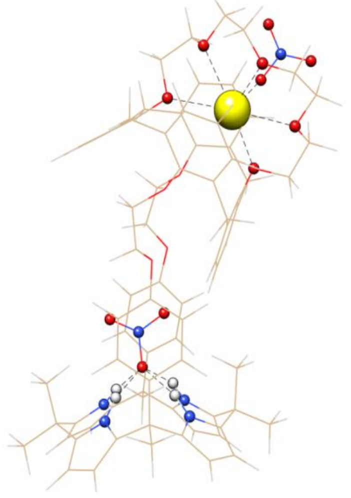

Figure 6.2: Optimized Structure of metal bound ion-pair receptor complex.

For both divalent ions, **P/P** mode is found to largely unfavorable.

6.3.3. Selectivity trend of metal ions to the receptor

Comparison of the aqueous phase metal binding energies of their most preferable binding mode indicate that nitrate salt of K^+ (-36.87 kcal mol^{-1}) has highest selectivity at the receptor which is followed by Sr^{2+} (-29.86 kcal mol^{-1}) and Ca^{2+} (-20.43 kcal mol^{-1}). To rationalize the obtained selectivity trend, we further calculated the reorganization energy (ΔG_{reorg}) of the ligand upon complexation which measures the deformation occurred in the ligand conformation in process of complexation (Table 6.4).

Table 6.4: Gas phase reorganization energy (ΔG_{reorg}, kcal mol^{-1}) of receptor upon complexation

Complex	ΔG_{reorg}
K.Rec.NO_3	17.60
Sr.Rec.$(NO_3)_2$	32.85
Ca.Rec.$(NO_3)_2$	35.84

In line with the selectivity trend, we found that binding of $Ca(NO_3)_2$ to the receptor led to maximum value of ΔG_{reorg} (+35.84 kcal mol^{-1}) which is followed by $Sr(NO_3)_2$ (32.85 kcal mol^{-1}) and KNO_3 (+17.84 kcal mol^{-1}).

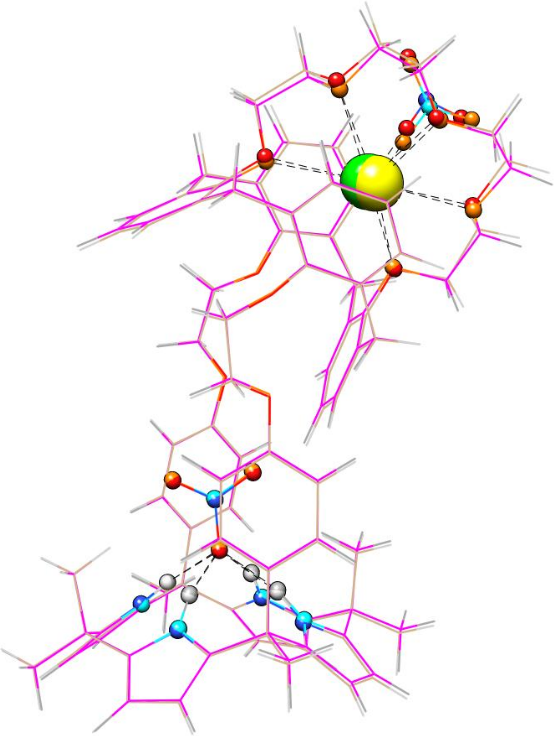

Figure 6.3: Super-imposed optimized structures of Ca^{2+} and Sr^{2+} bound receptor complexes. (Color Code: [Ca.Rec.$(NO_3)_2$] : Ca^{2+}: yellow, O: Orange, N: Cyan, C: Pink, H: deep grey; [Sr.Rec.$(NO_3)_2$] : Sr^{2+}: Green, O: Red, N: Blue, C: Tan, H: light grey;

Hence, reorganization of the conformation plays key role to define selectivity here. Superimposition of two optimized structures (Figure 6.3) for Ca^{2+} and Sr^{2+} further indicate that due to smaller size (than Sr^{2+}), Ca^{2+} does not perfectly fit at the cavity as evident from variable Ca^{2+}-O_C (2.49-2.89 Å) and Ca^{2+}-C_A bond distances (2.96-4.63 Å). This also resulted in marginal shrinkage of **C** site to coordinate with Ca^{2+}. However, Sr^{2+}-O_C (2.57-2.74 Å) and Sr^{2+}-C_A bond distances (3.15-4.23 Å) suggest that Sr^{2+} fits better at **C** than Ca^{2+}. The reason behind superior selectivity for K^+ can be explained considering its size compatibility at the site and its hydration energy value. Firstly, Calculated K^+-O_C bond distances are noted to be longer than divalent ions suggesting crown ring doesn't require to shrink in order to capture K^+. Thus, K^+ remains a better fit for the cavity. Secondly, in spite of the miniscule size difference between K^+ and Sr^{2+}, due to its high ionic potential, hydration energy of Sr^{2+} is four times more than that of K^+ (Table 6.1). This eventually poses significant energy barrier for Sr^{2+} extraction from hydrated phase than K^+. The next section describes the possible effects of different solvents in ionic selectivity and metal extraction free energies.

6.3.4. Influence of different solvents in metal extraction free energy:

Metal extraction free energies presented in Table 6.5 considers the metal separation in aqueous phase itself or *via* transfer from aqueous phase to two different organic solvents namely ether and acetonitrile.

Table 6.5: Calculated extraction free energy of metal ions (ΔG_{ext} in kcal mol^{-1}) at different solvents

Metal	Most preferable binding Mode	ΔG_{ext} (aq → ether)	ΔG_{ext} (aq → acetonitrile)	ΔG_{ext} (aq)
K^+	C/P	-31.66	-38.07	-38.74
Sr^{2+}	C/CP	-16.18	-23.38	-24.11
Ca^{2+}	C/CP	-8.31	-15.67	-16.41

It is evident that decrease in polarity of the solvent led to reduction of ΔG_{ext} but the selectivity trend ($K^+ > Sr^{2+} > Ca^{2+}$) remains unchanged. Calculated ion-exchange free energies (Table 6.6, ΔΔG) for Ca^{2+}/Sr^{2+} also predicted strong preference for Sr^{2+} and apparently the degree of its selectivity is not influenced by the choice of the solvent.

Table 6.6: Ion exchange free energies ($\Delta\Delta G_{ext}$ in kcal mol^{-1}) between Ca^{2+} and Sr^{2+}

Used equation	Solvent	Dielectric constant	ΔΔG
			Ca/Sr*
$Ca.Rec.(NO_3)_2$ (org) + $Sr(H_2O)_8^{2+}$ (aq) = $Sr.Rec.(NO_3)_2$ (org) + $Ca(H_2O)_6^{2+}$ (aq) + $(H_2O)_2$ (aq)	Ether	5	-20.57
	Acetonitrile	36.3	-20.41
	Aqueous	80	-20.39

*Sr^{2+} replacing Ca^{2+} in ion-exchange reaction

Further, similar set of calculations with two different density functionals (B97-D3 and M06-2X) are also performed using pre-optimized structures, which produced the same selectivity trend (Table 6.7). This provides confidence to our applied methodology.

Table 6.7: Calculated extraction free energies and Ion exchange free energies of metal-receptor complexes in ether medium.

Ion	Used equations	B97-D3		M062X	
		ΔG_{ext}	ΔΔG	ΔG_{ext}	ΔΔG
K^+	Rec (org) + $K.(H_2O)_6^+$ (aq) + $NO_3.(H_2O)_6^-$ (aq) = $K.Rec.NO_3$ (ether) + $2(H_2O)_6$ (aq)	-18.58	-	-36.73	-
Sr^{2+}	Rec (org) + $Sr.(H_2O)_8^{2+}$ (aq) + $2NO_3.(H_2O)_6^-$ (aq) = $Sr.Rec.(NO_3)_2$ (org) + $2(H_2O)_6$ (aq) +$(H_2O)_8$ (aq)	-9.73	-21.19	-19.53	-17.20
Ca^{2+}	Rec (org) + $Ca.(H_2O)_6^{2+}$ (aq) + $2NO_3.(H_2O)_6^-$ (aq) = $Ca.Rec.(NO_3)_2$ (org) + $3(H_2O)_6$ (aq)	-1.65	-16.92	-13.69	-23.04

Table 6.8. Ion exchange free energies of Sr^{2+} with K^+ (Organic to aqueous extraction)

Used equation	Solvent	Dielectric constant	ΔΔG
			K/Sr*
$Sr.Rec.(NO_3)_2$ (org) + $K(H_2O)_6^{2+}$ (aq) + $(H_2O)_8$ (aq) = $K.Rec.NO_3$ (org) + $Sr(H_2O)_8^{2+}$ (aq) + $NO_3.(H_2O)_6^-$ (aq)	Ether	5	-15.48
	Acetonitrile	36.3	-14.70
	Aqueous	80	-14.62

*K^+ replacing Sr^{2+} in the ion-exchange reaction

Hence, in the presence of Ca^{2+}, this receptor can potentially and efficiently act as extractant for Sr^{2+}. The considerably higher selectivity for K^+ can further be used to strip Sr^{2+} from the organic phase to aqueous phase. In order to quantitatively measure the stripping efficiency (organic to aqueous phase) of KNO_3, we further calculated ion exchange free energies (ΔΔG) for K^+/Sr^{2+} pair (Table 6.8). The calculated highly negative ΔΔG values (> -30 kcal mol^{-1}) reiterated the suitability of KNO_3 as stripping agent and hence supports the proposed Sr^{2+} recovery strategy.

6.4. Conclusions

To summarize, here we have investigated the feasibility of Sr^{2+} extraction in nitrate media using a newly reported multitopic ion pair receptor. Our results strongly predicts remarkable Sr^{2+} selectivity in the studied receptor over Ca^{2+}, a commonly inferring cation in environmental samples. In contrast to most stable C/P binding mode of KNO_3 in complex, our calculations suggest C/CP mode is the most preferable binding mode for divalent metals. The superior selectivity of Sr^{2+} over Ca^{2+} can be attributed to the best fit mechanism in the crown cavity of receptor which in turn helps to overcome its high hydration energy barrier. Hence, the receptor is predicted to selectively extract Sr^{2+} over Ca^{2+}. However, being of optimum size and having low hydration energy, K^+ showed superior selectivity over Sr^{2+}. This feature makes $K^+NO_3^-$ salt a suitable stripping agent. Hence, the captured Sr^{2+} can be stripped back into solution using KNO_3 solution. The effects of different solvents (ether or acetonitrile) during extractions suggested insignificant influence of solvents on extraction selectivity of Sr^{2+}. Our results on complexation of KNO_3 and the receptor are found to be in good agreement with the available experimental information.

CHAPTER –7

Efficient Separation of Europium over Americium using Cucurbit-[5]-uril

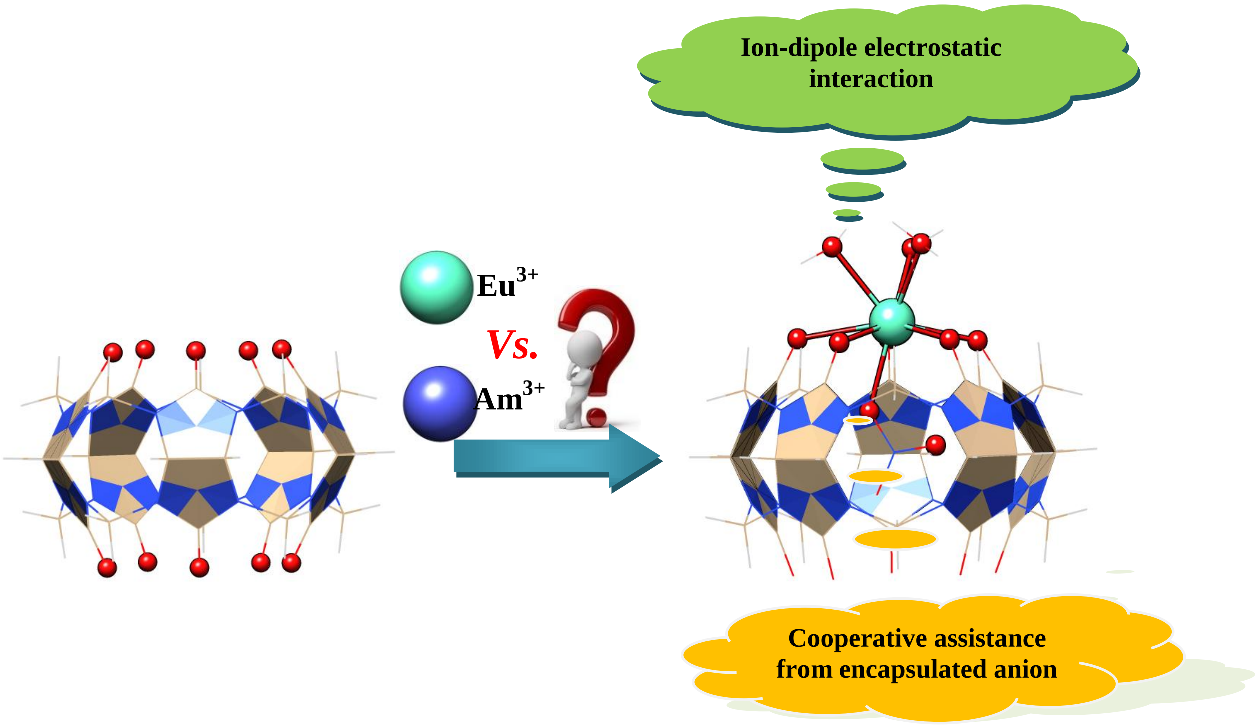

7.1. Introduction

In Synthetic media, ion-pair receptors utilize the counter ion's assistance to enhance the radionuclide's binding affinity. In Chapter 5 & 6, these receptors are projected to be useful for ^{137}Cs and ^{90}Sr separation. Beside extraction of Cs^+ and Sr^{2+}, in the back end of nuclear fuel cycle, one of the most challenging task is to separate actinides from lanthanides. In this Chapter, using relativistic DFT based investigations, we investigate the possibility of achieving such separation using a macrocyclic ligand utilizing the counter-ion assistance mechanism.

Enormous efforts are devoted in the back-end of nuclear fuel cycle to reprocess the spent fuel of high level liquid waste (HLLW) for subsequent safe disposal and for nuclear waste recycling. Along with many other fission products, the presence of minor actinides (MAs) such as americium (Am) and curium (Cm) causes problems due to the significant heat generation. MAs are long lived alpha emitters with long half-lives in the order of several hundred years. Separating the MAs from other fission products and subsequent transmutation to generate short lived radionuclides is expected to be a viable solution to long standing disposal associated problems.[5] However, the selective extraction of MAs from HLLW poses a formidable challenge due to the presence of chemically similar 4*f*-lanthanide congeners such as Eu^{3+}.[283] In this regard, significant attention was put forward to design and synthesize ion selective probes to achieve a desirable separation factor (SF) between 4*f*- and 5*f*-elements, particularly for Am^{3+}/Eu^{3+} pair.[284-286]

Owing to the very similar ionic radii (Am^{3+}: 1.115 Å *vs.* Eu^{3+}: 1.087 Å), both ions show highly comparable chemical properties. As compared to 4*f*-Eu^{3+}, the 5*f*-Am^{3+} orbital is more diffuse in nature, thus, Eu^{3+} is relatively hard acid as compared to Am^{3+}. In line with this, it was Seaborg, who first proposed that ligands, which are “Soft” (and more covalent) in nature, can be used for the selective extraction of actinides in the presence of lanthanides.[287] Of the many extractants, soft-donor ligands containing nitrogen and sulfur atoms have been reported to extract actinides in the presence of interfering lanthanides. For instance, sulfur based ligands, such as, Cyanex 301 is reported to have unique selectivity for Am^{3+} over Eu^{3+} at low pH.[288] The substantial increase in the degree of covalency between Am^{3+} and softer ligands is often suggested to be the reason for the observed selectivity. Recently, Manna and co-workers have proposed a new strategy;"*intra-ligand synergism*" in which the extractant have a mixture of hard (oxygen) and soft donor atoms (nitrogen) that tend to enhance the selectivity for Am^{3+} which was later experimentally verified.[16]

Nitrogen containing 6,6-bis-(5,6-dialkyl-1,2,4-triazin-3-yl)-2,2-bipyridines (BTBPs) are also noted to exhibit substantial Am^{3+}/Eu^{3+} separation.[289-290] Several phosphorous containing ligands were also being tested in this context.[291] However, apart from achieving desired selectivity, there remains several important concerns regarding the use of any particular ligands. Post processing of extraction-related organic waste is an important factor as the ligands should not produce toxic by-products and the generated waste volume should be as low as possible.

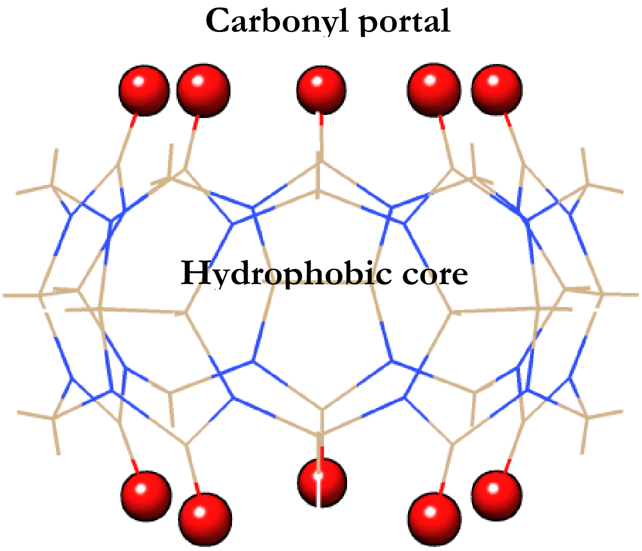

Figure 7.1: Optimized structure of CB[5] (Color code: red = oxygen, blue = nitrogen, yellow = carbon)

Thus, ligands synthesized with carbon-hydrogen-oxygen-nitrogen (C-H-O-N) principle are more preferred over ligands containing sulfur and phosphorous atoms. Beside this, the use of pre-organized chelating ligands are considered to be more advantageous[292] as it minimizes the role of negative entropy factor, which originates due to the structural reorganization of ligand upon metal complexation.[293] This in turn can increase the metal extraction efficiency and its selectivity. In view of these arguments, the use of cyclic rigid supramolecular host molecules such as cucurbit-[n]-uril could be a viable option for selective Am^{3+}/Eu^{3+} separation.

Of cucurbit-[n]-uril family with differing cavity sizes, cucurbit-[5]-uril (CB[5]) is well known to bind several metal ions including alkali, alkaline earth metals and uranyl because of its electron rich carbonyl portals (Figure 7.1).[294-296] As far as lanthanides are concerned, structures of several lanthanide-CB[5] complexes have been derived and reported so far.[60, 297-298] Recently, Chen et al. reported the complexation of Eu^{3+} with CB[5] using X-ray diffraction analysis.[297] Further, the favorable complexation of Eu^{3+} with CB[5] was recently investigated by Rawat et al.[60] using extensive experimental techniques, such as, time resolved fluorescence spectroscopy and EXAFS. Contrary to Eu^{3+}, so far there are no studies reported on Am^{3+}-CB[5] complexation processes. As observed repeatedly from the reported crystal structures,[60, 62, 295, 298-299] cation bound CB[n] complexes very often possess encapsulated anion at the hydrophobic cavity of host. This observation indicates the possible role of counter-ion on the aforementioned complexation processes. The binding mechanisms of these complexation processes are poorly understood at the molecular level and still remain elusive till date.

Presently, density functional theory (DFT) has become an obvious choice to understand the structure-function relationship of the various separation chemical processes.[300-302] At the appropriate level of theory, a strong correlation between experiments and theory is expected and have been reported recently.[61, 95, 279, 303-306] For instance, Bhattacharya et al. observed remarkable

Am^{3+}/Eu^{3+} selectivity with bis-1, 2, 4-triazinyl pyridine derivatives in an ionic liquid which was further validated using DFT studies.[305] The structures of possible binding motifs of actinyls (uranyl, neptunyl and plutonyl) with functionalized CB-[5] in VI and V oxidation states is recently reported by us.[61] Similarly, Zaiter et al. studied the selectivity of azide ligands for Am^{3+}/Eu^{3+} separations using relativistic DFT approach.[306]

In this Chapter, we have carried out an extensive relativistic DFT calculations on the complexation of Am^{3+}/Eu^{3+} pair with CB[5]. We aimed to answer the following intriguing questions,

a) How Am^{3+}/Eu^{3+} ions bind with CB[5]?

b) How encapsulated counter anions inside CB[5] influences the metal binding at the carbonyl portal?

c) Is there any considerable ionic selectivity of Eu^{3+}over Am^{3+} using CB[5] as an extractant? If any, how such selectivity arises at the molecular level?

7.2. Computational Details

All structures were optimized with BP86 functional[91-92] in conjunction with def2-SV(P)[93] basis set for all atoms except the two *f*-block ions. For both Eu^{3+} and Am^{3+}, def-SV(P) is used to describe the valence electrons. Resolution of Identity (RI) approximation[254-256, 307-308] was invoked as implemented in TURBOMOLE v 6.3.1.[212] For energetics, hybrid B3LYP functional[96-97] was used in combination with triple-ζ-TZVP basis set.[98-99] For both geometry optimization and energetics, the core electrons are modeled through small-core effective core potential (SC-ECP). The aforementioned applied computational methodology has been successfully used by us and seen to predict accurate structural and thermodynamic properties for several host-guest and metal-ligand complexes.[61, 248-250, 279] The optimized structures were further verified as minima in the potential energy surface by performing analytical frequency calculations using the AOFORCE module. All energies were corrected for thermal and non-thermal corrections at temperature 298.15 K and thus the reported energies are binding free energies. Throughout the study, a septet high spin ground state (f^6) of both metal ions is considered. Negligible spin contamination was noted while assessing the expected difference between S(S+1) of assigned state and the actual value of $<S^2>$. Further, the solvent effect was accounted through COSMO continuum solvation model using the dielectric constant of water (ε=80).[215] All solvation calculations were performed using following van der Waal radii: Am: 2.052 Å, Eu: 1.820 Å, Cl: 2.230 Å, O and N: 1.775 Å, C: 1.989 Å, H: 1.404 Å. Such values were previously reported[17, 309] to reproduce the accurate hydration free energies of metal ions and the experimental selectivity trend between Am^{3+} and Eu^{3+}.

To decipher the counter-ion effects over metal binding, three anions were considered for this study namely, chloride (Cl^-), formate ($HCOO^-$) and nitrate (NO_3^-). The binding free energies of the metal (M) cations and the anions (X^-) with the host CB-[5] were computed using following equations,

$$[M(H_2O)_9]^{3+} + CB[5] = [M.CB[5].(H_2O)_{4/5}]^{3+} + 5/4\, H_2O \quad (1)$$

$$[X(H_2O)_n]^{-} + CB[5] = [X.CB[5].(H_2O)_k]^{-} + (n-k)H_2O \quad (2)$$

Based on previous experimental and computational studies,[264, 279, 310] hexa-hydrated anionic model was considered for Cl^- and NO_3^- (n=6) while primary hydration number of four was taken for $HCOO^-$ (n=4). Anions were kept encapsulated inside CB[5] prior to optimization. Number of internal water molecules (k) inside metal bound CB[5] complexes were considered one for Cl^- and $HCOO^-$ while zero was considered for NO_3^-.

The cation (and anion) assisted anion (and cation) binding affinities with CB[5] in the case of nitrate counter-ion were computed using following equations,

$$\left[M(H_2O)_3.CB[5]\right]^{3+} + [NO_3\,.(H_2O)_6]^- = [M(H_2O)_3.CB[5].NO_3]^{2+} + 6H_2O \qquad (3)$$

$$[NO_3.CB[5]]^- + [M(H_2O)_9]^{3+} = [M(H_2O)_3.CB[5].NO_3]^{2+} + 6H_2O \qquad (4)$$

The overall binding affinities of hydrated cations and nitrate ion were calculated using the following equation:

$$CB[5] + [NO_3\,.(H_2O)_6]^- + [M(H_2O)_9]^{3+} = [M(H_2O)_3.CB[5].NO_3]^{2+} + 12H_2O \qquad (5)$$

Similar equations also hold for Cl^- and $HCOO^-$.

Actual metal extraction processes may possibly involve aqueous to organic phase metal extraction. Thus, we have further carried out calculations to understand the solvent effect on the possible extraction of Am/Eu pair in different solvent media. Two different dielectric media (ε=5 for ether/chloroform medium and ε=35 for acetonitrile/nitrobenzene medium) mimicking the organic (org) solvent were chosen for this purpose. Free energy of extraction (ΔG_{ex}) was calculated using following equations:

$$CB[5]\,(Org) + [NO_3\,.(H_2O)_6]^-(aq) + [M(H_2O)_9]^{3+}(aq) \rightarrow [M(H_2O)_3.CB[5].NO_3]^{2+}\,(Org) + 12H_2O(aq) \qquad (6)$$

Subsequently, ion-exchange free energies ($\Delta\Delta G_{Eu/Am}$) were calculated by subtracting corresponding ΔG_{ex} values of Eu^{3+} and Am^{3+}.

Evidently water molecules play a critical role over the thermodynamics of these binding processes. As it has been previously noted[311] that the use of 1 atm ideal gas pressure at 298 K for the individual water molecules (isolated water molecules at the right hand side of equations 1 to 5), which depict the standard gaseous state of water, can led to erroneous reaction free energy parameters (by roughly 4.3 kcal mol^{-1} for each individual water molecules). This is due to the significant overestimation of translational entropy of water. Here we have incorporated the well-tested standard pressure corrections[312-314] using pressure of 1354 atm (depicting the liquid water density of 997 $kg.m^{-3}$) for the individual water molecules in the aforementioned equations.

Partial atomic charges were derived for the guest and host molecules using Mülliken population analysis (MPA).[315] Molecular orbital analysis was also carried out using BP86/def2-SV(P) optimized structures of anion encapsulated M.CB[5] complexes using ORCA 3.0.3 program package.[21462] The α-spin molecular orbitals were calculated in the presence of encapsulated anion at ZORA-BP86/TZVP level.

In addition, the origin of preferential binding of ions to CB-[5] was analyzed through Nalewajski-Mrozek (N-M) bond order,[316-317] Wiberg bond indices (WBIs),[318] natural bond order analysis (NBO),[319] and energy decomposition analysis (EDA)[171-172] using TURBOMOLE generated pre-optimized structures in gas phase. Finally, in order to shed light on the topological features of binding, Bader's quantum theory of atoms in molecules (QTAIM) analysis were performed, which has been earlier reported to produce good correlation with the strength of the actinide-ligand bond.[259] All these spin-unrestricted calculations taking septet spin-multiplicity (f^6) for metal were carried out using ADF 2013.1 program package.[320-321] During calculations, 1*s* shell of Carbon, hydrogen and nitrogen were treated by frozen core approximation whereas, 1*s* to 4*d* shells for Eu^{3+} and 1*s* to 5*d* shells for Am^{3+} were kept frozen. Spin-orbit coupling effects were not incorporated into the calculations due to the large computational cost (system size > 100 atoms). In all ADF calculations, true density is used rather than the fitting value for accurate computation of Exchange-Correlation potential.

The EDA analysis was performed on the pre-optimized metal-bound complexes using polarized triple-ζ-slater type basis set, TZP with B3LYP functional at the integration level of 4.5. The scalar relativistic effects and spin orbital interactions were accounted with two body Hamiltonians in zeroth-order regular approximation (ZORA).[173, 322-325] The total bonding energy (ΔE_{bond}) between the two fragments (anion/water encapsulated CB[5] and metal-hydrate part of complex)was calculated using the following equation,

$$\Delta E_{bond}\ (\zeta) = \Delta E_{elstat}\ (\zeta) + \Delta E_{pauli}\ (\zeta) + \Delta E_{orb}\ (\zeta) \tag{7}$$

The additive sum of stabilizing electrostatic interaction energy, $\Delta E_{elstat}\ (\zeta)$ and repulsive interaction energy component, $\Delta E_{pauli}\ (\zeta)$ gives the estimate of total steric interactions. $\Delta E_{orb}\ (\zeta)$ takes account of the energy associated with orbital relaxation of fragmented molecular orbitals from excited state to ground state and thus represents the strength of covalent bonding between the fragments.

QTAIM analysis is based on the pioneering work of Bader and co-workers which provides valuable information on the bonding and non-bonding interactions of atoms inside the molecule using various descriptors such as electron density, ρ(r) and Laplacian of the electron density, L(r).[261] The possible of chemical bond formation between two nearby atoms is defined here as Bond Critical Point (BCP) where shared electron density reaches a minimum. As a well-accepted thumb rule, the values of ρ(r) > 0.2 e.bohr^{-3} indicates covalent bond while < 0.1 e.bohr^{-3} indicates ionic bond. Thus, the ρ(r) values at the BCPs are related to the strength of the bonds.[262] For covalent bond, L(r) values remain considerably negative. In this study, QTAIM calculations are performed at the ZORA-B3LYP/TZP level.

7.3. Results and Discussion

7.3.1. Hydration of metal ions

For the reliable prediction of binding free energies of Eu^{3+} and Am^{3+} with CB[5], it is essential to predict the correct hydration free energy trend of the two metal ions. Based on several experimental[116, 326-330] and computational studies,[331-338] we have considered a nine coordinated metal hydrated complexes for Am^{3+} and Eu^{3+}. However, our computed M-O$_{wat}$ bond distances are noted to be slightly elongated when compared to experimental bond length values (Table 7.1).[327-330]

Our computed average Am-O_{wat} bond length (2.53 Å) is seen to be marginally shorter (by 0.05Å) with respect to the DFT derived value (2.58 Å) of Wiebke et al.[331] while a bit longer when compared to the values obtained from MD simulations by D'Angelo et al[330] (by 0.04 Å). However, our computed average Eu-O_{wat} bond distance (2.50 Å) are noted to be very close to the previously calculated values of Dolg and coworkers[332] (2.48-2.52 Å) and that of Kuta et al. (2.51 Å).[333] In close agreement to these references, average Eu^{3+}-O_{wat} bond lengths are noted to be slightly shorter (by 0.03 Å) as compared to average Am^{3+}-O_{wat} bond lengths, which can be accredited to the ionic-radii difference of Am^{3+} and Eu^{3+} (0.03 Å). For both metal ions, our computed hydration free energies correlate nicely with the reported values (see Figure 7.2, Table 7.1).

Table 7.1: Optimized structures (in Å) and computed hydrations free energies (in kcal mol^{-1}) of Am^{3+} and Eu^{3+}

$[M(H_2O)_9]^{3+}$	M-O_{wat} bond distances			Hydration free energy		
	Computed[#]	Experimental	Calculated values from literature	Computed	Experimental	Calculated values from literature
Am^{3+}	2.510-2.591 (2.53)	2.48-2.51,[c] 2.47-2.49,[b] 2.47[e]	2.49,[e] 2.58[f]	-799.2	-	-715.6,[f] -755.0,[i] -784.9,[j]
Eu^{3+}	2.481-2.565 (2.50)	2.43-2.46,[c] 2.46[d]	2.48-2.52,[g] 2.51[h]	-805.9	-803.8[a]	-804.8,[g] -810.0,[j] -808.6,[h]-828.6,[h]

[#]values in bracket correspond to average M-O_{wat} bond distances. Literature values are from [a]Ref 116, [b]Ref 327, [c]Ref 328, [d]Ref 329,[e]Ref 330,[f]Ref 331, [g]Ref 332, [h]Ref 333,[i]Ref 335,[j] Ref 336.

For instance, the calculated hydration free energy of Eu^{3+} is within 2 kcal mol^{-1} of the experimental estimate (-803.8 kcal mol^{-1}).[116] Unfortunately, experimental data for the hydration energy of Am^{3+} is lacking,[332] thus direct comparison cannot be made. However, the DFT predicted values of Wiebke et al[331] (-715 kcal mol^{-1}) and David et al[335] (-755 kcal mol^{-1}) are underestimated by more than ~30 kcal mol^{-1} as compared to the CCSD(T) value.[336]

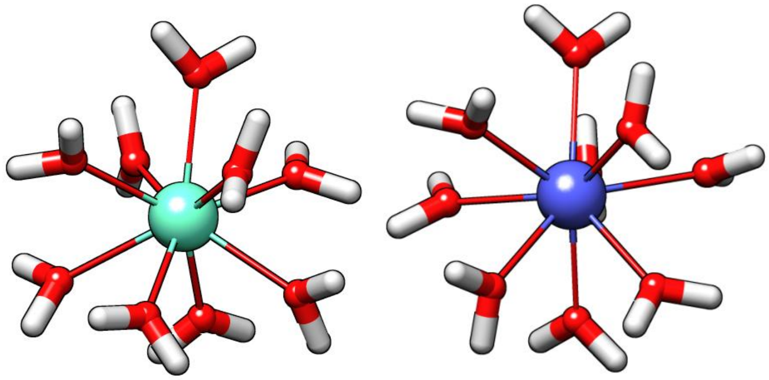

$Eu(H_2O)_9^{3+}$ **$Am(H_2O)_9^{3+}$**

Figure 7.2: Optimized structure of $M(H_2O)_9^{3+}$ complexes (Color code: green=europium, violet= americium, red = oxygen and grey=hydrogen)

On the other hand, our value is overestimated by only 15 kcal mol^{-1}. Thus, the minor error in our value when compared with the CCSD(T) value arises from the minimalist DFT method used here. Nevertheless, our aim is to compute the free energies with the supramolecule, CB[5], which cannot be studied at the CCSD(T) level due to the overall size of the system (more than 100 atoms). Thus, the computed trends in hydration free energy is reproduced well against the available experimental and CCSD(T) data, which provides confidence to our applied methodology.

7.3.2. Binding of Am^{3+} and Eu^{3+} with CB[5]

Prior experimental studies[60, 63-64, 297] on lanthanide-CB[5] complexation suggest that carbonyl portals of CB[5] are considerably smaller (portal diameter, P.D ~5.2 Å) than its higher homologue aiding the interacting metal to coordinate with all of its five carbonyl oxygen atoms. One common feature of all such reported crystal structures is that the metal center preserves an overall coordination number of nine. In particular, recent structural predictions[18] through extended X-ray absorption fine structure (EXAFS) on Eu^{3+}-CB[5] complexation further confirms such coordination number is conserved for Eu^{3+}. In view of this, we maintained the nona-coordinated metal centre in all complexes. In the absence of any counter-ions, the coordination is saturated by the addition of four water molecules. Of four water molecules, three can coordinate from the outside of carbonyl portal (denoted as H_2O^{ext}) while one water molecule (denoted as H_2O^{int}) is inside the hydrophobic cavity (i.e. 3/1 arrangement, see Figure 7.3). As reported,[57] aqueous soluble CB[5] possess two high energy water molecules which are kinetically trapped at the hydrophobic cavity. While in 3/1 arrangement, one of these water molecules remain coordinated to the bound metal ion, the other water molecule, back at the second portal, can forms a hydrogen bond with the metal bound encapsulated water molecule to attain 3/2 arrangement (i.e. three external water/two encapsulated water molecules, Figure 7.3).

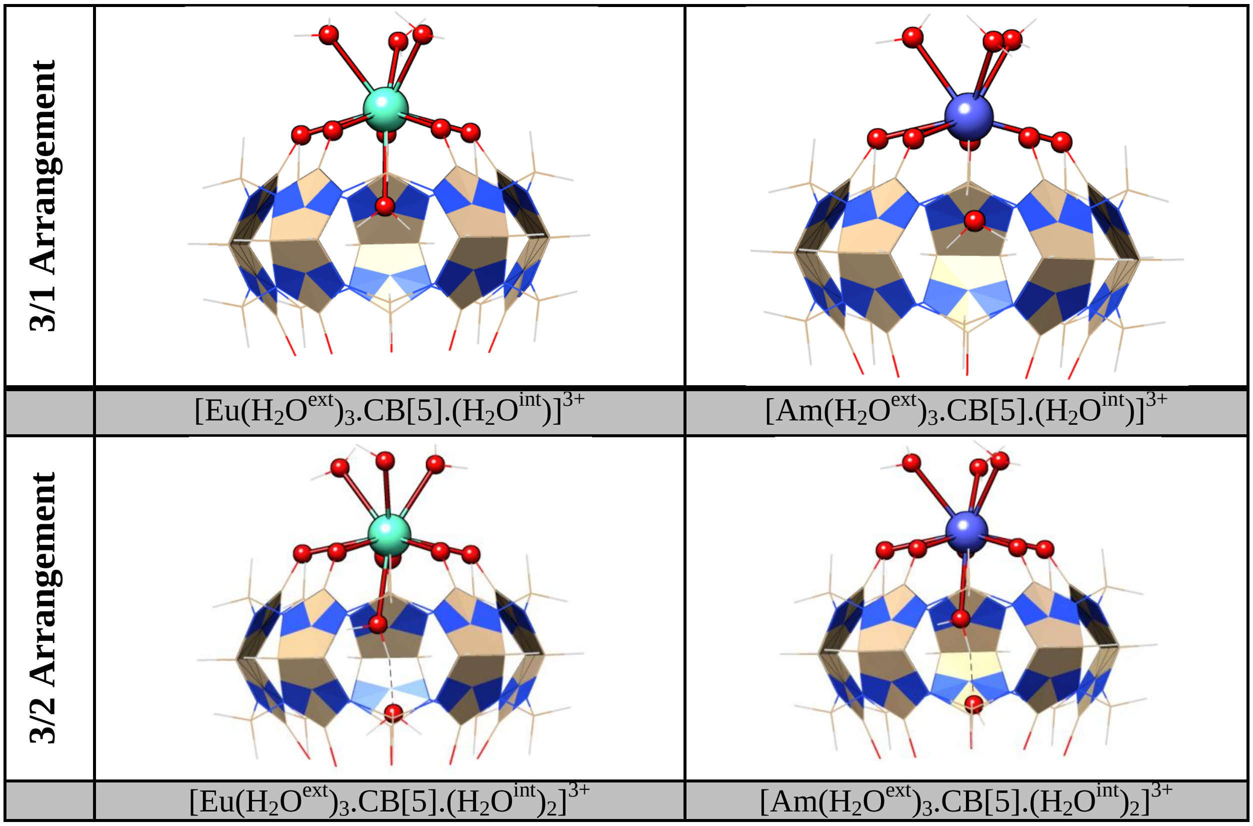

Figure 7.3: Optimized structure of M-CB[5] complexes in the absence of counter anions. Color code: green=europium, violet= americium, red = oxygen, blue = nitrogen, yellow = carbon and grey=hydrogen

Among the two optimized structures with different water coordination, we find the 3/1 and 3/2 arrangement for Eu^{3+} are equally favorable (~-4 kcal mol^{-1}), while Am^{3+} is noted to be unfavorable (by > 4 kcal mol^{-1}) in both the arrangements (Table 7.2).

Upon metal ion binding to CB-[5] portals, a significant shrinkage of portal diameter (by ~0.6 Å) is noticed as compared to bare CB[5], which is seen to be more prevailing for Am^{3+} (P.D: ~4.5 Å) than Eu^{3+}(P.D: ~4.6 Å). Due to larger ionic radii of 4*f*- and 5*f*-elements, the metal ions are somewhat displaced above the portals of CB[5] is consistent with the lanthanide bound CB-[5] X-ray data.[297-298] The optimized structural parameters for these complexes suggest that metal ions are bound to the five carbonyl oxygens of CB[5] (Table 7.2, Figure 7.3). However, the $M\text{-}O_{CB[5]}$ bond lengths are not symmetric, thus the metal ions does not reside at the middle of the portal oxygen atoms, leading some of the $M\text{-}O_{CB[5]}$ bond length relatively longer.

Table 7.2: Optimized structural parameters (in Å) and binding free energies (in kcal mol^{-1}) of $[M(H_2O^{ext})_3.CB[5].(H_2O^{int})_n]^{3+}$ (M^{3+}=Am, Eu; n=1/2) complexes.[#$]

M^{III}	External water/ encapsulated water	$M\text{-}O_{wat}^{ext}$	$M\text{-}O_{wat}^{int}$	$M\text{-}O_{CB[5]}$	Binding free energy	$\Delta\Delta G_{Eu/Am}^{a}$
					Aqueous phase	
Eu (f^6)	3/1	2.487-2.562	2.616	2.504-2.659	-3.88	-8.24
	3/2	2.506-2.589	2.550, 5.060	2.486-2.652	-4.07	
Am (f^6)	3/1	2.489-2.571	2.622	2.469-2.630	+4.17	
	3/2	2.501-2.591	2.522, 4.988	2.443-2.653	+6.81	

[#] $[M(H_2O)_9]^{3+} + CB[5] = [M.CB[5].(H_2O)_{4/5}]^{3+} + 5/4\,H_2O$. [a] $\Delta\Delta G_{Eu/Am}$ correspond to ion exchange free energy of Eu^{3+}vs Am^{3+} . [$]The standard-state pressure corrections have been incorporated in the reported Gibbs free energy values.

Further, due to the rigidity of the host, the carbonyl portals cannot move independently to interact with the bound metal. Thus, to compensate the effect, some water molecules tend to bind relatively strongly which resulted into shortening of some of the $M\text{-}O_{wat}$ bond with respect to $M\text{-}O_{CB[5]}$ bond. This observation is consistent with the available lanthanide bound CB-[5] X-ray data (Table 7.6).[297-298] The computed $M\text{-}O_{CB[5]}$ bond length for Eu^{3+} is noted to be slightly elongated (by 0.04 Å) as compared to Am^{3+}. In case of 3/1 arrangement, $M\text{-}O_{wat}^{int}$ bond distance is noticed to be somewhat longer (2.616 Å for Eu^{3+} and 2.622 Å for Am^{3+}) as compared to three bonded external water molecules (2.487-2.562Å for Eu^{3+} and 2.489-2.571 Å for Am^{3+}), suggesting weaker involvement of the former waters to the metal ions. On the contrary, for the 3/2 arrangement the $M\text{-}O_{wat}^{int}$ bond lengths are shorter ($Eu\text{-}O_{wat}^{int}$: 2.550 Å and $Am\text{-}O_{wat}^{int}$: 2.522 Å). The subsequent reduction in $M\text{-}O_{wat}^{int}$ bond distance of 3/2 as compared to 3/1 arrangement can be explained with the critical inspection of the optimized structures. Owing to the existing strong hydrogen bonding interaction between the two encapsulated water molecules (1.49 Å in Am-CB[5] complex; 1.55 Å in Eu-CB[5] complex), the metal bonded encapsulated water now behave more like hydroxide ion and resulted into strong bonding.

7.3.3. Influence of encapsulated anions over metal binding

Several experimental investigations on lanthanide-CB[5] complexation suggest that the presence of "*third species*", generally anions often modulate the overall complexation behaviour.[339] More specifically, such alteration seems to be more prominent when anions remain encapsulated inside the host.[298-299, 340-341]As metal ions form complex with neutral CB[5], it is expected that some counter-ions trapped inside might coordinate to the metal center to compensate the high charge of metal ion.

In this context, we have extended our investigations to pinpoint the influence of encapsulated counter-ions (Cl^-, NO_3^- and $HCOO^-$) into the metal ion binding processes to CB[5] (Figure 7.4). The choice of counter ions can be justified as follows: In most of the experimental studies on metal-CB[5] complexation, reported synthetic condition is acidic and often nitrate and/or chloride are used as the counter-ion. Moreover, several reported crystal structures confirmed the presence of the aforementioned ions in the hydrophobic cavity of CB[5]. For instance, studies carried by Chen et al.[297] confirmed the presence of Cl^- encapsulated inside CB-[5] in their X-ray derived crystal structures of various lanthanide-CB[5] complexes including Eu^{3+} (CCDC: 875767). Whereas, Liu et al.[63] demonstrated the encapsulation of nitrate in the lanthanide capped molecular capsule. A recent thermodynamics study[60] on complexation of Eu^{3+} to CB[5] also speculated the probable presence of encapsulated $HCOO^-$ in the metal bound host complex. In addition to this, the influences of these counter-ions on metal binding are of utmost importance from extraction point of view and thus rationalize our approach.

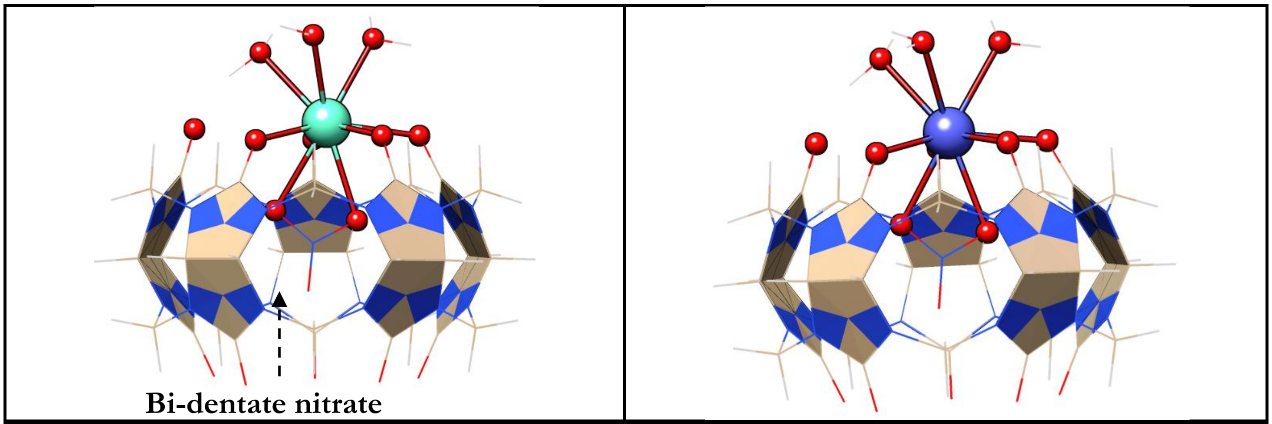

$[Eu(H_2O)_3.CB[5].NO_3]^{2+}$ $[Am(H_2O)_3.CB[5].NO_3]^{2+}$

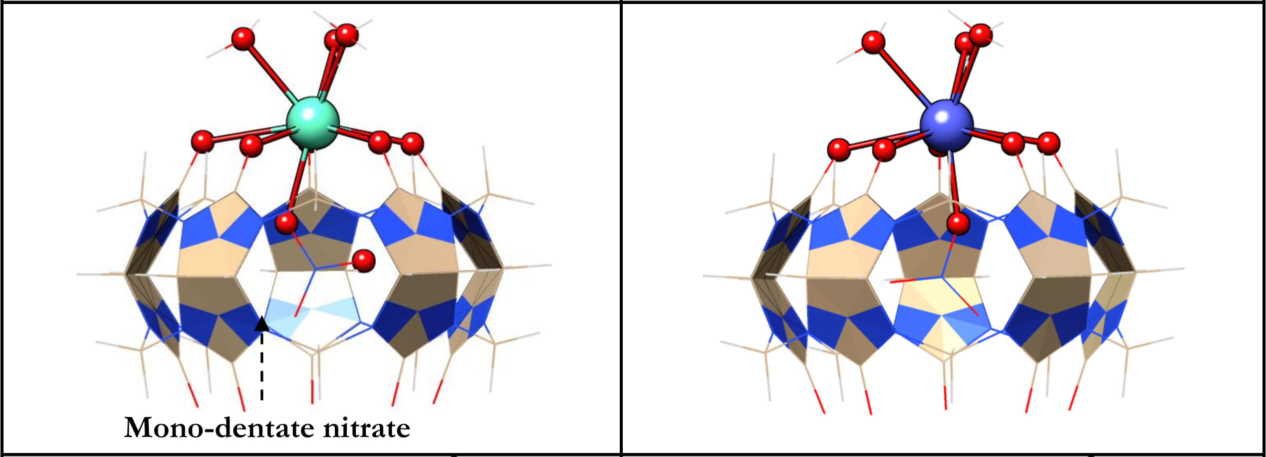

$[Eu(H_2O)_3.CB[5].NO_3]^{2+}$ $[Am(H_2O)_3.CB[5].NO_3]^{2+}$

Figure 7.4: Optimized structure of M-CB[5] complexes in the presence of encapsulated NO_3^-.Color code: green=europium, violet= americium, red = oxygen, blue = nitrogen, yellow = carbon and grey=hydrogen

To arrive at a comparative viewpoint over the metal *vs.* anion complexation with the bare host, we have computed the anion binding affinities inside the metal free CB[5] using equation 2 (Table 7.3). In the absence of metal, encapsulation of all the anions are noted to be largely unfavorable

(ΔG (Cl^-)= +31.18 kcal mol^{-1}, ΔG (NO_3^-) =+28.50 kcal mol^{-1} and ΔG ($HCOO^-$) = +45.41 kcal mol^{-1}). This can be attributed to the endothermic nature of the reactions which originates from the desolvation of anions in process of encapsulation. As evident from Table 7.2 and 7.3, metal ion binding to CB[5] is more favorable than anions (by more than 30 kcal mol^{-1}), suggesting the overall binding of metal salts with CB[5] has to be essentially a cation assisted anion binding process. Thus, we have calculated cation assisted anion binding free energies using equation 3 (Table 7.4).

Table 7.3: Calculated thermodynamic parameters (in kcal mol^{-1}) for anion (X) binding inside CB[5].$

Anion encapsulation inside CB[5]				
Encapsulated ion (X)	Used equation	ΔH	TΔS	ΔG
Cl^-	$[Cl(H_2O)_6]^- + CB[5] = [Cl.CB[5].H_2O]^- + 5H_2O$	+51.72	+20.54	+31.18
$HCOO^-$	$[HCOO(H_2O)_4]^- + CB[5] = [HCOO.CB[5].H_2O]^- + 3H_2O$	+53.43	+8.02	+45.41
NO_3^-	$[NO_3\,(H_2O)_6]^- + CB[5] = [NO_3\,.CB[5].H_2O]^- + 6H_2O$	+51.04	+22.53	+28.50

$The standard-state pressure corrections have been incorporated in the reported Gibbs free energy values.

Table 7.4: Cation assisted anion encapsulations inside CB[5]. Free energy parameters are in kcal mol^{-1}.$

M^{III}	Encapsulated ion (X)	ΔH	TΔS	ΔG[a]
Eu (f^6)	Cl^-	+13.26	+26.38	-13.11 (+31.18)
	$HCOO^-$	+12.20	+15.24	-3.04 (+45.41)
	NO_3^-	+13.32	+38.95	-25.63 (+28.50)
Am (f^6)	Cl^-	+3.90	+17.95	-14.05 (+31.18)
	$HCOO^-$	+0.12	+3.95	-3.83 (+45.41)
	NO_3^-	+3.95	+27.10	-23.15 (+28.50)

[a] Values in parenthesis correspond to anion binding free energies to CB[5] in the metal free host (cf. Table 7.3). $The standard-state pressure corrections have been incorporated in the reported Gibbs free energy values. Free energies are calculated using Eq. 3.

In the presence of cation, we note a remarkable enhancement in anion binding free energies (Table 7.4) such that all the anionic complexation processes become thermodynamically favorable with the preference order of NO_3^->Cl^-> $HCOO^-$ for both Eu^{3+} and Am^{3+} ions. It is worth noting that the chloride binding to CB[5] is indeed cation assisted which is in line with the X-ray crystal structure of chloride bound CB[5].[63] However, in contrary to Liu et al.,[64] we did not find any alteration of anion preference order upon metal ion addition as compared to the metal free host. Although cations bind first to CB[5], the presence of anion does assist the metal ion binding (Table 7.5).

Table 7.5: Anion assisted metal binding with CB[5]. Free energy parameters are in kcal **mol^{-1}.**[$]

M^{III}	Encapsulated ion (X)	ΔH	TΔS	ΔG[a]
Eu (f^6)	Cl$^-$	-43.10	+5.27	-48.37 (-4.07)
	HCOO$^-$	-28.15	+24.37	-52.52 (-4.07)
	NO$_3^-$	-42.17	+16.04	-58.21 (-4.07)
Am (f^6)	Cl$^-$	-36.17	+4.88	-41.05 (+4.17)
	HCOO$^-$	-31.47	+13.59	-45.06 (+4.17)
	NO$_3^-$	-32.82	+14.66	-47.48 (+4.17)

[a]Values in parenthesis correspond to metal binding free energies to CB[5] in the absence of encapsulated anion (cf. Table 7.2). [$]The standard-state pressure corrections have been incorporated in the reported Gibbs free energy values. Free energies are calculated using Eq. 4.

The computed binding affinities using equation 4 indicate the obtained metal binding free energies are now more favorable for both ions. Among the three anions, encapsulated nitrate enhanced the metal ion binding most (by over 53 kcal mol^{-1} for Eu^{3+}; 43 kcal mol^{-1} for Am^{3+}) followed by formate (by over 48 kcal mol^{-1} for Eu^{3+}; 40 kcal mol^{-1} for Am^{3+}) and least for chloride anion (by over 44 kcal mol^{-1} for Eu^{3+}; 36 kcal mol^{-1} for Am^{3+}). Thus, in the presence of anion, metal salts bind to CB[5] *via* cation assisted anion binding mechanism, although cooperative assistance between the ion-pairs further modulate the binding to CB[5] in a favorable way, which is somewhat similar to the previously noted cooperative binding mechanism of ion-pair inside the multi-topic ion-pair receptor.[279]

Finally, the overall complexation processes of metal salts are estimated using equation 5, which in principle considers simultaneous binding of metal and anions with CB[5] (Table 7.6). The obtained ΔG values are noted to be largest for nitrate salts as compared to the other two salts. Akin to earlier results, here also binding favorability follows the same trend i.e. NO_3^->Cl^-> $HCOO^-$. Our computed thermodynamic parameters, in particular complexation free energy (ΔG=-7.12 kcal mol^{-1}) for Eu^{3+}-CB[5] complexation in the presence of $HCOO^-$ are noted to be in excellent agreement with experimentally reported thermodynamics parameters of Rawat et al.[18] (ΔG= -6.94 kcal mol^{-1}). Further, we find the overall complexation process is largely entropy driven, which can be accredited to the subsequent removal of high energy water molecules from the host and the highly solvated metal and anions during binding.

Table 7.6: Optimized structural parameters (in Å) and thermodynamic parameters (in kcal mol^{-1})[#] for M.CB[5] complexes (M^{3+}=Am, Eu) in the presence of encapsulated anions (X).[$]

M^{III}	Encapsulated ion (X)	M-O_{wat}	M-$O_{CB[5]}$	M-X	ΔH	TΔS	ΔG	$\Delta\Delta G_{Eu/Am}$[c]
Eu (f^6)	Cl^-	2.533-2.628 [2.593][b] (2.446-2.505)[a]	2.515-2.710 [2.578][b] (2.461-2.507)[a]	2.662 (2.735)[a]	+8.63	+25.82	-17.19	-7.31
	$HCOO^-$	2.521-2.646 [2.566]	2.462-3.597 [2.724]	2.494, 2.501	+7.75[d] (+2.90)	14.87[d] (+9.83)	-7.12[d] (-6.94)	-7.47
	NO_3^-	2.510-2.629 [2.561]	2.443-3.494[2.684]	2.560-2.580	+8.87	+38.57	-29.70	-10.72
Am (f^6)	Cl^-	2.527-2.656 [2.603]	2.488-2.742[2.576]	2.618	+15.55	+25.43	-9.88	
	$HCOO^-$	2.521-2.702 [2.596]	2.475-3.517[2.701]	2.430, 2.475	+14.39	+14.04	+0.35	
	NO_3^-	2.499-2.672 [2.580]	2.461-3.347[2.653]	2.499, 2.537	+18.22	+37.20	-18.98	

$\#CB[5]+[Cl.(H_2O)_6]^- + [M(H_2O)_9]^{3+} = [M(H_2O)_4.CB[5].Cl]^{2+} + 11H_2O$

$CB[5]+[HCOO.(H_2O)_4]^- + [M(H_2O)_9]^{3+} = [M(H_2O)_4.CB[5].HCOO]^{2+} + 9H_2O$

$CB[5]+[NO_3.(H_2O)_6]^- + [M(H_2O)_9]^{3+} = [M(H_2O)_3.CB[5].NO_3]^{2+} + 12H_2O$

[a]experimental values are taken from ref. 297. [b]values in square bracket correspond to average M-$O_{CB[5]/wat}$bond distance. [c]$\Delta\Delta G_{Eu/Am}$ correspond to ion exchange free energy of Eu^{3+}vs Am^{3+} . [d]values in first bracket correspond to reported experimental values from ref. 60.[$]The standard-state pressure corrections have been incorporated in the reported Gibbs free energy values.

Our computed structural parameters for chloride encapsulated Eu^{3+}-bound complexes are found to be within ~0.2 Å with respect to the reported crystal structure.[17] The adjacent carbonyl distances at the portal (2.945-3.020 Å) are very similar to the reported values of Chen et al (2.806–2.959 Å).[17] The computed M-X bond length is always noted to be shorter for Am^{3+} than its Eu^{3+} counterpart. It is to be noted that, after encapsulation, anions like formate and nitrate can interact with the metal ions through mono-dentate and bi-dentate binding motif with their hard oxygen atoms. Based on relative energetics on the two different binding motifs, we find CB[5] has slight favorability towards bi-dentate motif of NO_3^- (by ~1 kcal mol^{-1}, Table 7.7) and mono-dentate motif for $HCOO^-$ (by ~2 kcal mol^{-1}). However, keeping in mind of the error window associated with the applied density functional, one can assume both binding motifs are equally probable and may remain in energetic equilibrium. Noticeably, for bi-dentate binding motif of anions, metal ion coordinates only with four of the five carbonyl groups such that the overall coordination number of nine is retained. Enhancement of pore radius of non-bonded portal compared (P.D~5.1Å) to the bonded one (P.D~4.5-4.6Å) is also noticed for all complexes, which is similar to the previous experimental observations.[60, 297]

Table 7.7: Relative energetics study on the preference of binding mode of encapsulated anion with CB[5].

Complex	Binding mode of encapsulated anion	Total Energy (Hartree)	Relative energy (kcal mol^{-1})
$[Eu(H_2O)_4.CB[5].HCOO]^{2+}$	Mono-dentate	-4136.928643	0
	Bi-dentate	-4136.924879	+2.36
$[Am(H_2O)_4.CB[5].HCOO]^{2+}$	Mono-dentate	-4021.972775	0
	Bi-dentate	-4021.970867	+1.20
$[Eu(H_2O)_3.CB[5].NO_3]^{2+}$	Mono-dentate	-4228.059419	+1.50
	Bi-dentate	-4228.061812	0
$[Am(H_2O)_3.CB[5].NO_3]^{2+}$	Mono-dentate	-4113.105843	+0.66
	Bi-dentate	-4113.106900	0

7.3.4. Assessment of Selectivity with CB[5]

We now assess the binding selectivity of Am^{3+} and Eu^{3+} cations to CB[5]. We find that in the absence of anion, Eu^{3+} binding is considerably more favorable than Am^{3+} by almost > 8kcal mol^{-1} ($\Delta\Delta G_{Eu/Am}$ in Table 7.2). However, in the presence of chloride and formate anions, $\Delta\Delta G_{Eu/Am}$ value reduced marginally by < 1 kcal mol^{-1}, whereas the presence of encapsulated NO_3^- enhances the $\Delta\Delta G_{Eu/Am}$ to ~11 kcal mol^{-1}. Such apparent selectivity towards Eu^{3+} also remains unaltered in different organic solvents (ε=5, 35) when compared with the aqueous media (Table 7.6 and SI, Table 7.8). Change in ion exchange free energy also remains insignificant (< 1 kcal mol^{-1}),

Table 7.8: Free energy of extraction (ΔG_{ex}) and ion exchange free energies (in kcal mol^{-1})$^{\#}$ for M.CB[5] complexes (M^{3+}=Am, Eu) in the presence of encapsulated nitrate at different dielectric media.$^{\$}$

M^{III}	Used equation	ΔG_{ex}	$\Delta\Delta G_{Eu/Am}$	ΔG_{ex}	$\Delta\Delta G_{Eu/Am}$
		ε=5		ε=35	
Eu (f^6)	$CB[5]\,(Org) + [NO_3.(H_2O)_6]^-(aq) + [M(H_2O)_9]^{3+}(aq) \rightarrow [M(H_2O)_3.CB[5].NO_3]^{2+}(Org) + 12H_2O(aq)$	-14.18	-10.45	-34.45	-10.66
Am (f^6)		-3.73		-23.79	

$^{\$}$The standard-state pressure corrections have been incorporated in the reported Gibbs free energy values.

however, the free energy of extraction is noted to increase as we approach to more polar medium. In summary, the strong selectivity for Eu^{3+} is always noticed to be prevalent, irrespective the choice of solvent or the nature of encapsulated anion. Next we embark upon several analysis tools in order to inspect the governing factors behind the preferential binding of Eu^{3+}over Am^{3+}.

7.3.4.1. Mülliken population analysis

The net Mülliken charges of both metal ions are considerably smaller as compared to formal '+3' oxidation state. This suggests strong ligand to metal charge transfer (LMCT, table 7.9). In the absence of anions, the partial charge on the metal ion is noted to be considerably larger (by upto 0.5 a.u), further supporting that anions do assist the metal ion binding through favorable electrostatic interaction. For all encapsulated anions, appreciable charge transfer to the coordinated metal center is noted, which led to highly positive overlap population in all occasions. Contrary to anions, we noted negative overlap population of M-O_{wat}^{int} bond for encapsulated water pointing out the anti-bonding character of the bond. Whereas, positive values for metal coordinated external water suggests the favorable bonding interactions. The significantly higher net charges of the external water molecules compared to the encapsulated one further reflects the higher involvement of the external water in metal binding. In all complexes, the net charge of Eu^{3+}

is smaller as compared to Am^{3+}. Moreover, partial charge on CB[5] is larger in case of Eu^{3+}-complex than Am^{3+}, which infer greater charge transfer from CB[5] to Eu^{3+} as compared to Am^{3+}. Similarly, we have also noted a significantly higher overlap population for Eu^{3+} in case of $M\text{-}O_{CB[5]}$ bond. Both attributes to stronger binding of Eu^{3+} with the carbonyl portal of CB[5] as compared to Am^{3+}.

Table 7.9: Mülliken population analysis (MPA) for M.CB[5] complexes (M^{3+}=Am, Eu) in the presence of encapsulated anions (X).

M^{III} bond order	Encapsulated species (X)	Metal spin Population (ρ_M)	Net charges (a.u)				Orbital population (d/f)	Overlap population		
			Metal	CB[5]	Water	X		$M\text{-}O_{CB[5]}$	$M\text{-}O_{wat}$	$M\text{-}X^a$
Eu (f^6)	H_2O	6.357	1.643	0.864	0.477	0.008	0.05/6.28	0.127	0.151	-0.144
	Cl^-	6.356	1.257	0.634	0.449	-0.340	0.05/6.27	0.113	0.171	0.459
	$HCOO^-$	6.311	1.249	0.672	0.433	-0.354	0.05/6.23	0.123	0.177	0.496
	NO_3^-	6.339	1.303	0.771	0.448	-0.522	0.05/6.26	0.133	0.183	0.346
Am (f^6)	H_2O	6.057	1.823	0.650	0.521	0.006	0.08/5.93	0.076	0.151	-0.251
	Cl^-	6.100	1.359	0.475	0.477	-0.311	0.09/5.99	0.073	0.137	0.532
	$HCOO^-$	6.121	1.313	0.625	0.417	-0.355	0.09/5.98	0.087	0.155	0.382
	NO_3^-	6.116	1.389	0.687	0.451	-0.527	0.09/5.97	0.093	0.163	0.367

[a] M-X denotes overlap population of $M\text{-}O_{wat}$, $M\text{-}O_{HCOO}$ and $M\text{-}O_{NO3}$ bond for H_2O, $HCOO^-$ and NO_3^- respectively.

7.3.4.2. N-M bond order analysis and WBIs

We further performed Nalewajski-Mrozek (N-M) bond order analysis from two-electron valence indices using 3-index set and also calculated Wiberg bond indices (Table 7.10).

Table 7.10: Nalewajski-Mrozek (N-M) bond order analysis and corresponding wiberg bond indices (WBIs) of M.CB[5]complexes (M^{3+}=Am, Eu) in the presence of encapsulated anions (X= Cl^-, $HCOO^-$ and NO_3^-) at ZORA-B3LYP/TZP level.

M^{III} bond order	Encapsulated species (X)	N-M Bond order			Wiberg bond indices (WBI)		
		$M\text{-}O_{CB[5]}$	$M\text{-}O_{wat}$	$M\text{-}X^a$	$M\text{-}O_{CB[5]}$	$M\text{-}O_{wat}$	$M\text{-}X^a$
Eu (f^6)	H_2O	0.177	0.141	0.171	0.149	0.131	0.122
	Cl^-	0.141	0.109	0.468	0.147	0.126	0.308
	$HCOO^-$	0.149	0.127	0.367	0.130	0.125	0.198
	NO_3^-	0.180	0.123	0.198	0.131	0.127	0.216
Am (f^6)	H_2O	0.192	0.180	0.169	0.212	0.200	0.178
	Cl^-	0.157	0.132	0.512	0.190	0.174	0.779
	$HCOO^-$	0.182	0.135	0.546	0.175	0.173	0.285
	NO_3^-	0.193	0.142	0.476	0.186	0.181	0.262

[a] Reported values of M-X denotes values for $M\text{-}O_{wat}$, $M\text{-}O_{HCOO}$ and $M\text{-}O_{NO3}$ bond for encapsulated H_2O, $HCOO^-$ and NO_3^- respectively.

The accuracy of N-M bond indices are less dependent on the basis set justifying its superiority over other well-known bond-order analysis.[342] In addition, N-M valence indices incorporate both covalent and ionic contribution between two interacting atoms to reflect the degree of covalency more efficiently.[306, 316-317] In case of M-$O_{CB[5]}$ bond, the obtained N-M and WB indices for Am-CB[5] complexes are noted to be larger as compared to Eu^{3+} , which possibly suggesting a bit higher covalent character in case of Am^{3+}. This nicely correlates with the shorter average Am-$O_{CB[5]}$ bond length than Eu^{3+} (Table 7.6). Further, in all occasions, N-M bond order values and WBIs for M-$O_{CB[5]}$ bond are greater than the M-O_{wat} bond indicating greater involvement of carbonyl portal of CB[5] than the coordinated water molecules.

7.3.4.3. Molecular orbital analysis

A careful inspection of high lying molecular orbital can reveal the vital bonding information related to the preferential stability of Eu^{3+} with CB[5] (Figure 7.5-7.8). The SOMOs of bare ions of both Eu^{3+} and Am^{3+} are dominantly *f*-based MOs. Upon complexation with CB[5] , SOMOs are modified significantly as compared to bare ions. We find that the SOMO's near valence shell of Eu-CB[5] complex are dominantly ligand-based (see Figure 7.5). *f*-orbital based MOs of Eu-CB[5] complex are noted as deeply buried beneath the valence shell and strongly stabilized with respect to SOMO (by ~0.3-1.0 eV, Figure 7.6). The bonding interaction between the encapsulated anion (NO_3^- in Figure S2) and Eu^{3+} is also seen to be visible in SOMO-14, confirming the cation-anion assistance in the Eu-CB[5] binding. On the contrary, the SOMO's of Am-CB[5] are predominantly metal-based (see Figure 7.5). Further, SOMOs and LUMO for Am^{3+} bound complexes have dominant 5*f* character (>87%), which is in line to our MPA results (Table 7.9). However, the 4*f* orbital character (~70%) of Eu^{3+} is more prominent only in case of LUMO.

Similar to MPA, these variations also indicate the extent of charge transfer from CB-[5] to Eu^{3+} is higher as compared to Am^{3+}.

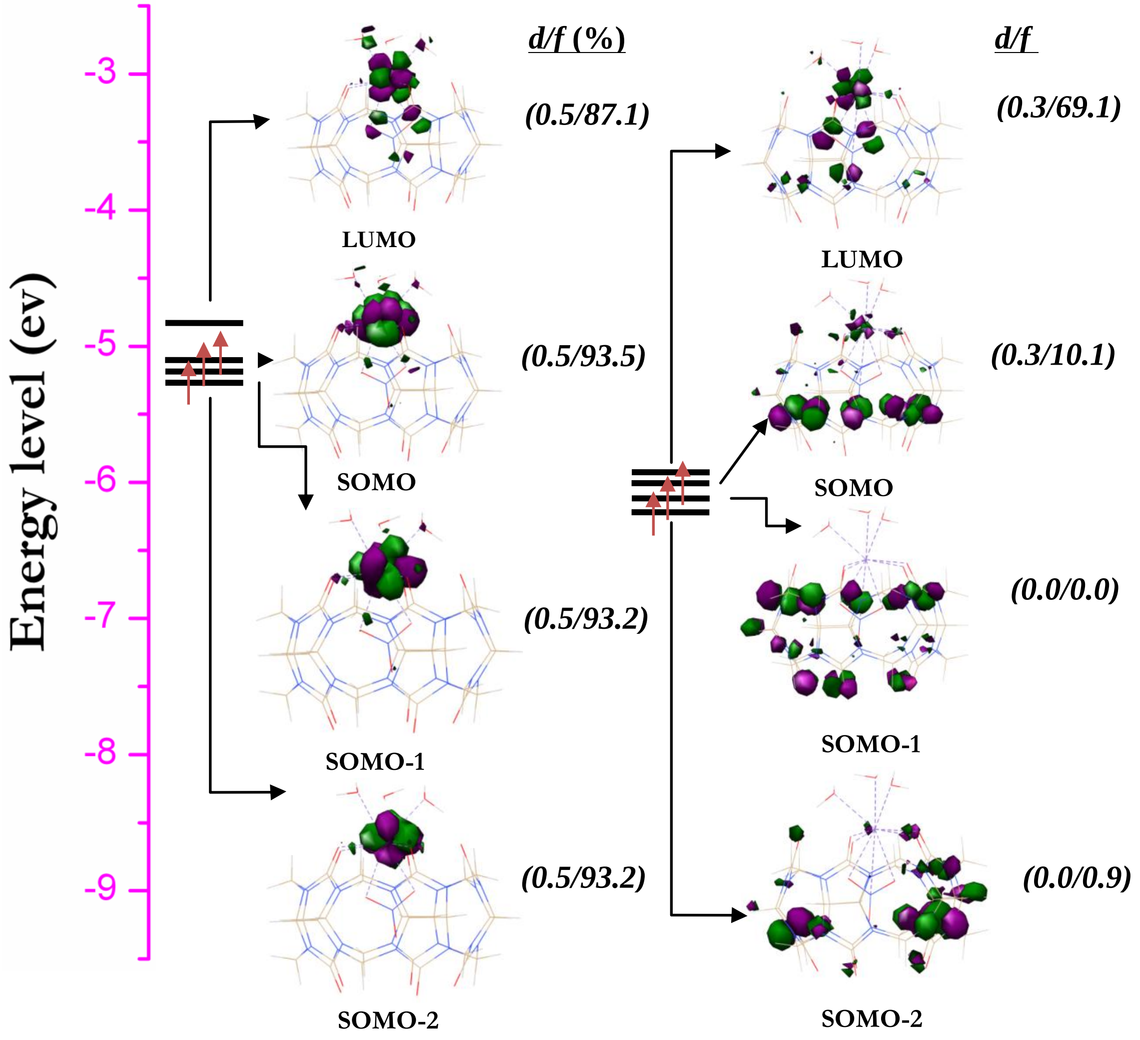

$[Am(H_2O)_3.CB[5].NO_3]^{2+}$ **$[Eu(H_2O)_3.CB[5].NO_3]^{2+}$**

Figure 7.5: α spin molecular orbitals of M.CB[5] complexes in presence of encapsulated NO_3^- ion at ZORA-BP86/TZVP level (at ε=80). The iso-surface values for the contour plots were set to 0.035e/$Bohr^3$ for all cases.

Furthermore, the energy levels of the MOs for Eu^{3+} is more stabilized than Am^{3+}, which suggests the stronger binding of the former with CB[5]. It should be noted that our Eu-CB[5] MOs are very similar to those of uranyl-CB[5] MOs, where a similar ligand based MOs are observed in the HOMO.[61]

$[Am(H_2O)_4CB[5].HCOO]^{2+}$

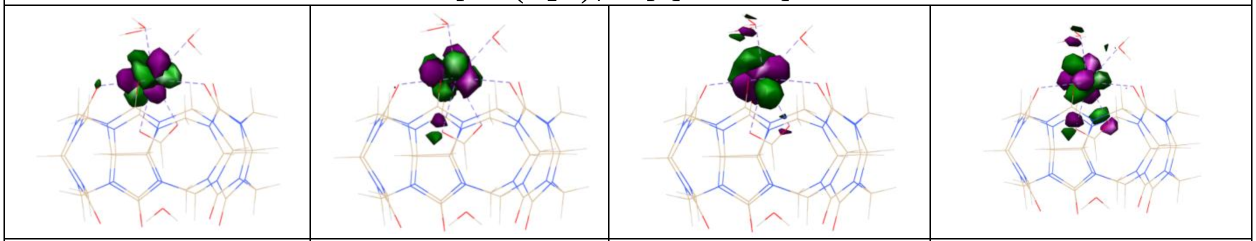

SOMO-2 SOMO-1 SOMO LUMO

$[Eu(H_2O)_4CB[5].HCOO]^{2+}$

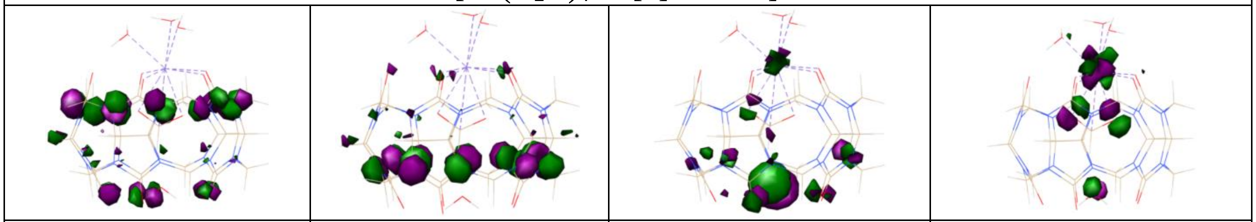

SOMO-2 SOMO-1 SOMO LUMO

$[Am(H_2O)_4CB[5].Cl]^{2+}$

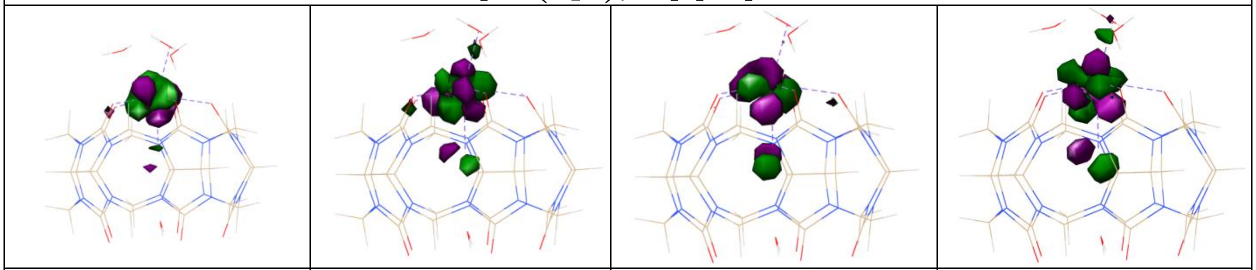

SOMO-2 SOMO-1 SOMO LUMO

$[Eu(H_2O)_4CB[5].Cl]^{2+}$

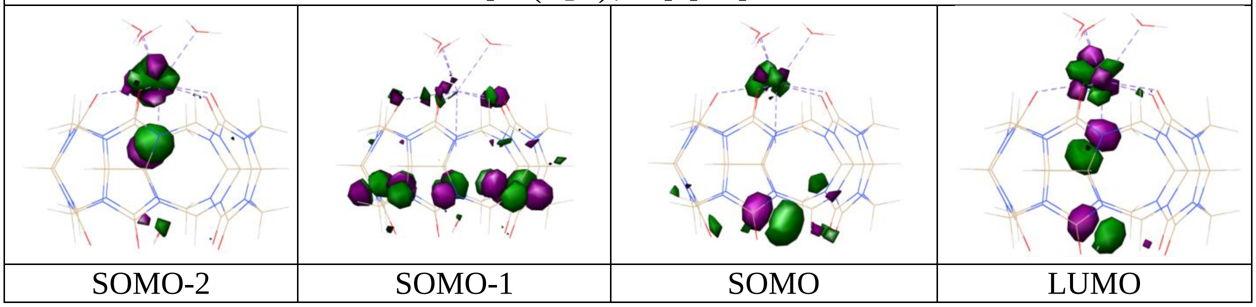

SOMO-2 SOMO-1 SOMO LUMO

Figure 7.6: α spin molecular orbitals of M.CB[5] complexes in presence of encapsulated $HCOO^-$ and Cl^- ion at ZORA-BP86/TZVP level (ε=80). The iso-surface values for the contour plots were set to 0.035e/Bohr^3 for all cases.

<table>
<tr><th colspan="3">Molecular Orbitals of [Eu(H_2O)$_3$.CB[5].NO_3]$^{2+}$</th></tr>
<tr>
<td>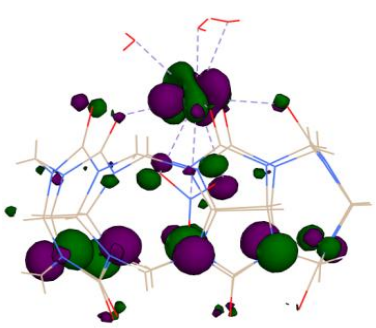
SOMO-4</td>
<td>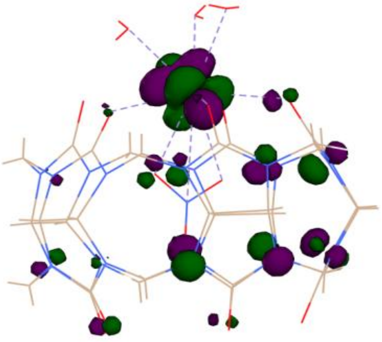
SOMO-9</td>
<td>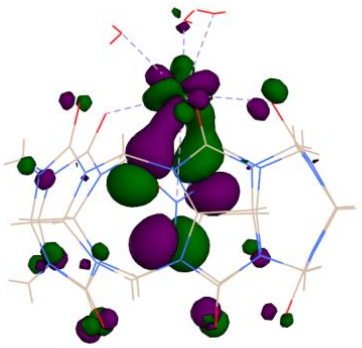
SOMO-14</td>
</tr>
<tr>
<td>d/f (%) : 0.2/53.1
Energy$^{\#}$ (ev) : -6.416 (0.339)</td>
<td>d/f (%) : 0.2/78.8
Energy$^{\#}$ (ev) : -6.504 (0.426)</td>
<td>d/f (%) : 1.1/31.6
Energy$^{\#}$ (ev) : -6.855 (0.777)</td>
</tr>
<tr>
<td>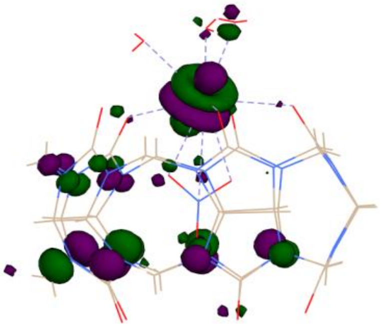
SOMO-5</td>
<td>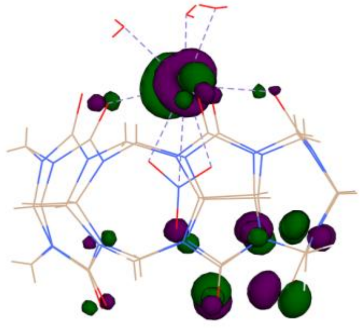
SOMO-13</td>
<td>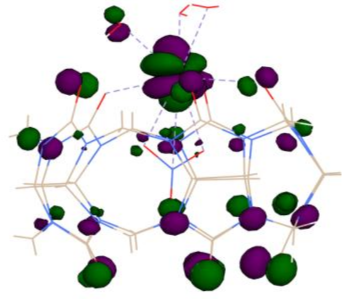
SOMO-21</td>
</tr>
<tr>
<td>d/f (%) : 0.2/61.1
Energy$^{\#}$ (ev) : -6.428 (0.351)</td>
<td>d/f (%) : 0/70.9
Energy$^{\#}$ (ev) : -6.825 (0.748)</td>
<td>d/f (%) : 0.2/57.8
Energy$^{\#}$ (ev) : -7.129 (1.052)</td>
</tr>
</table>

Values in parentheses correspond to energy difference of the orbital with respect to SOMO (in ev)

Figure 7.7: *f*-orbital based α spin molecular orbitals of [Eu(H_2O)$_3$.CB[5].NO_3]$^{2+}$ complex at ZORA-BP86/TZVP level (ε=80). The iso-surface values for the contour plots were set to 0.035e/Bohr^3 for all cases.

We also note that irrespective of the counter-ions (chloride or formate), the SOMOs remains the same for both Eu^{3+} and Am^{3+}, thus the electronic structure are mainly modulated by the metal interaction with CB[5].

Molecular Orbitals of $[Am(H_2O)_3.CB[5].NO_3]^{2+}$		
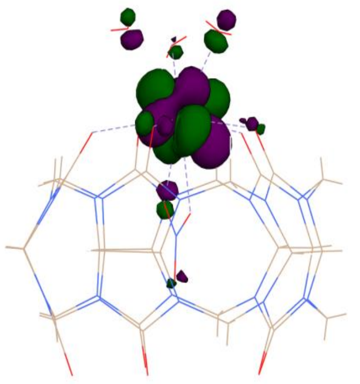 **SOMO**	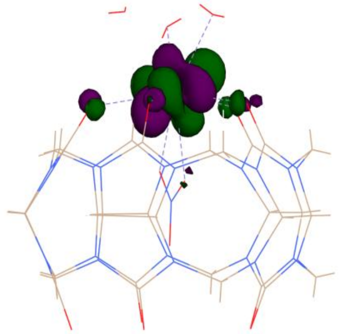 **SOMO-2**	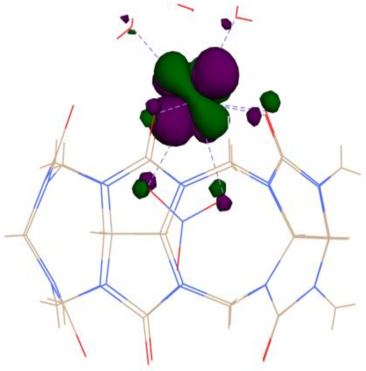 **SOMO-4**
*d/f (%):*0.5/93.5 Energy (ev)$^{\#}$: -5.235	*d/f (%):*0.5/93.2 Energy (ev)$^{\#}$: -5.270 (0.035)	*d/f (%)* : 0.3/94.6 Energy (ev)$^{\#}$: -5.744 (0.509)
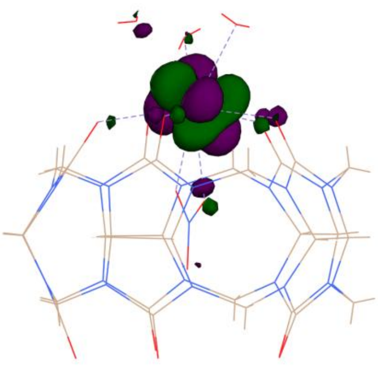 **SOMO-1**	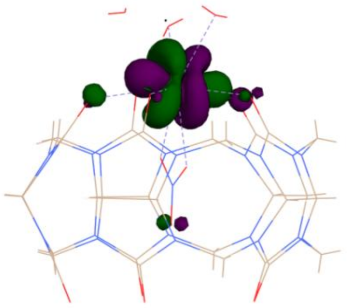 **SOMO-3**	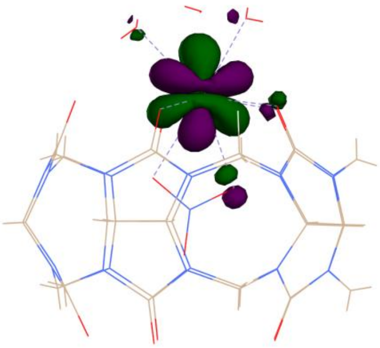 **SOMO-5**
d/f (%) : 0.5/93.2 Energy (ev)$^{\#}$: -5.258 (0.023)	*d/f (%)*: 0.3/94.1 Energy (ev)$^{\#}$: -5.527 (0.292)	*d/f (%)*:0.2/94.9 Energy (ev)$^{\#}$: -5.946 (0.711)

 # Values in parentheses correspond to energy difference of the orbital with respect to SOMO (in ev)

Figure 7.8: *f*-orbital based α spin molecular orbitals of $[Am(H_2O)_3.CB[5].NO_3]^{2+}$complex at ZORA-BP86/TZVP level (ε=80). The iso-surface values for the contour plots were set to 0.035e/Bohr^3 for all cases.

7.3.4.4. EDA and QTAIM analyses

To gain further insights on the type of interactions which contribute to the binding affinities, we have performed EDA (Table 7.11) and QTAIM analyses (Table 7.12). The total bonding energies derived from EDA is larger for Eu^{3+} as compared to Am^{3+} which is in line with our computed binding free energies (Table 7.6). The bonding energy is noted to decrease abruptly (by over 200 kcal mol^{-1}) in the absence of anion at the CB[5] cavity, which again manifests the important role of encapsulated anion in superior metal binding. In all complexes, electrostatic interaction (>54%) has the major contribution in the bonding energy with one exception. Interestingly for Eu^{3+}, in the presence of encapsulated water, orbital contributions (58%) dominated the overall bonding energy.

Table 7.11: Energy decomposition analysis[a] (energies in kcal mol^{-1}) of M.CB[5] complexes (M^{3+}=Am, Eu) in the presence of encapsulated anions (X) at ZORA-B3LYP/TZP level. The values in the parentheses give the percentage contribution to the total attractive interactions ($\Delta E_{\mathrm{Elstat}}$+$\Delta E_{\mathrm{Orb}}$).

M^{III}	Encapsulated species (X)	Pauli repulsion $\boldsymbol{\Delta E_{pauli}}$	Electrostatic Interaction $\boldsymbol{\Delta E_{elstat}}$	Total steric interaction	Orbital interactions $\boldsymbol{\Delta E_{orb}}$	Total bonding energy[b] $\boldsymbol{\Delta E_{bond}}$
Eu (f^6)	H_2O	90.35	-252.25 (41.83%)	-161.90	-350.82 (58.17%)	-512.71
	Cl^-	132.26	-486.03 (54.75%)	-353.77	-401.56 (45.24%)	-755.33
	$HCOO^-$	147.36	-502.35 (55.54%)	-354.99	-402.07 (44.46%)	-757.06
	NO_3^-	136.03	-471.25 (54.82%)	-335.22	-388.33 (45.18%)	-723.55
Am (f^6)	H_2O	138.63	-428.17 (68.20%)	-289.54	-199.59 (31.80%)	-489.13
	Cl^-	187.63	-516.11 (56.83%)	-328.48	-392.03 (43.17%)	-720.51
	$HCOO^-$	202.21	-535.26 (57.54%)	-333.05	-394.92 (42.46%)	-727.97
	NO_3^-	195.27	-505.14 (56.02%)	-309.88	-396.58 (43.98%)	-706.46

[a] anion/water encapsulated CB[5] and metal-hydrate part of complex were used as fragments

[b] $\Delta E_{bond}\,(\zeta) = \Delta E_{elstat}\,(\zeta) + \Delta E_{pauli}\,(\zeta) + \Delta E_{orb}\,(\zeta)$

Nevertheless, we find a considerable orbital contribution (>45%) for both metal ions with slightly higher value for Eu^{3+}. Importantly, the destabilizing Pauli repulsion is more dominant for Am^{3+}, which subsequently led the total steric repulsion (sum of Pauli repulsion and electrostatic contribution) somewhat less stabilizing as compared to Eu^{3+}.

Finally, we have carried out QTAIM analysis to gauge the extent of ionic/covalent interaction between two interacting atoms (Table 7.12). We find that a significantly smaller electron density (ρ<<0.1) and positive Laplacian ($\nabla^2\rho$), suggesting predominant ionic character of M-$O_{CB[5]/water}$ bond. This corroborates well with the results of MPA and N-M bond order analysis. The computed ρ and $\nabla^2\rho$ value for M-O_{wat} bond is noted to be minimum for Cl^- and maximum for NO_3^-, which is in agreement with the average M-O_{wat} bond length order (Eu^{3+}-O_{wat} -2.593Å (Cl^-), 2.566Å ($HCOO^-$), 2.561Å (NO_3^-); Am-O_{wat} -2.603Å (Cl^-), 2.596 Å ($HCOO^-$), 2.580Å (NO_3^-)) with respect to the anions. Interestingly, in spite of shorter average Eu^{3+}-O_{wat} bond length, the BCP parameters for Am^{3+}-O_{wat} bond are always found to be slightly higher. However, BCPs for M-$O_{CB[5]}$ and M-X are seen to be fairly consistent with the calculated bond distances. In the case of Cl^-, ρ is slightly higher for Am^{3+}-Cl^- when compared to Eu^{3+} as reflected from the substantially shorter Am^{3+}-Cl^- bond distance (2.618 Å vs. 2.662 Å for Eu^{3+}). In general, we always find a higher value for Am^{3+} than Eu^{3+} suggesting a better degree of covalency for the former.

Table 7.12: QTAIM analysis of electron density ρ (e/Bohr^3), Laplacian $\nabla^2\rho$ at Bond Critical Points for M.CB[5] complexes (M^{3+}=Am, Eu) in the presence of encapsulated anions (X) at ZORA-B3LYP/TZP level.

M^{III}	Encapsulated species (X)	M-O_{wat}		M-$O_{CB[5]}$		M-X[a]	
		ρ	$\nabla^2\rho$	ρ	$\nabla^2\rho$	ρ	$\nabla^2\rho$
Eu (f^6)	H_2O	0.039	0.157	0.033	0.147	0.029	0.126
	Cl^-	0.034	0.135	0.032	0.140	0.056	0.129
	$HCOO^-$	0.036	0.146	0.038	0.170	0.046	0.161
	NO_3^-	0.039	0.146	0.039	0.175	0.037	0.139
Am (f^6)	H_2O	0.045	0.193	0.043	0.195	0.034	0.151
	Cl^-	0.038	0.161	0.038	0.171	0.067	0.174
	$HCOO^-$	0.039	0.165	0.044	0.203	0.057	0.213
	NO_3^-	0.040	0.173	0.046	0.214	0.048	0.189

[a] reported values of M-X denotes values for encapsulated M-O_{wat}, M-O_{HCOO} and M-O_{NO3} bond for H_2O, $HCOO^-$ and NO_3^- respectively.

In summary, although QTAIM and N-M bond order analysis predicted slightly higher covalent character for Am^{3+}-CB[5] binding, it is the existing strong electrostatic ion-dipole interaction between Eu^{3+} and CB[5] that determines the preference of metal binding at the CB[5] portal. Similar observations were previously reported by Shi and coworkers[343] where in spite of higher covalency prevailing at Am-N bond, Eu-ligand complex was found to be more stable due to the existing ionic interactions. Here, more efficient LMCT for Eu^{3+} is noted in MPA analysis while N-M bond order, WBIs and QTAIM confirmed the strong ionic character of $M-O_{CB[5]/wat}$ bond. Furthermore, these analyses also pin-pointed the greater involvement of CB[5] than the coordinated water molecules in metal binding. Thermodynamics calculations suggested the direct assistance of encapsulated nitrate in metal binding, which is further supported by the visible bonding interaction of Eu-NO_3^- in MO analysis.

7.4. Conclusion

Designing novel ligands for the selective separation of Am^{3+}/$Eu^{3+}$is utmost essential in the back-end of the nuclear fuel cycle. However, chemically alike Am^{3+}/Eu^{3+} poses significant challenges for a specific ligand to generate significant selectivity ratio. In this Chapter, we have proposed that such supreme selectivity can be achieved using a rigid supramolecular framework, such as CB. The pre-organized platform of CB[5] and its appropriate portal diameter can selectively bind Eu^{3+} over Am^{3+}. We have carried out extensive electronic structure calculations to understand the binding and selectivity of Eu^{3+} and Am^{3+} with CB[5]. The major finding are summarized as follows,

a) Although both Eu^{3+} and Am^{3+} binds to CB[5] in similar geometric fashion with an overall coordination number of nine, CB[5] binds preferably with Eu^{3+} as compared to Am^{3+}. Both the metal ions are found to coordinate to the carbonyl portal in μ^5 coordination environment , which is consistent with the available experimental structural data. The remaining coordination is satisfied with four water molecules, of which one is encapsulated water molecule of CB[5]. The metal binding processes are noted to be largely entropy driven resembling the results obtained in the recent thermodynamic study.[60]

b) In the presence of counter-ions, thermodynamics calculations showed a significant increase in metal and anion binding in CB[5], which suggests the favorable presence of cation-anion cooperative assistance in the complexation process. Among several anions, $NO_3^-$is found to be most efficient to enhance the metal binding free energies. Note that nitric acid is the commonly used acid in the back-end of the nuclear fuel cycle. The existing bonding interaction between NO_3^- and Eu^{3+} is further confirmed by the subsequent MO analysis of the complex. The high-lying SOMO's of Eu-CB[5] complex are found to be ligand based while *f*-based orbital are seen to be highly stabilized and deeply buried beneath the valance shell. Whereas, the SOMO's of the Am-CB[5] complex are dominantly metal based.

c) *Albeit* weak, a better degree of covalency is noted for Am^{3+} than Eu^{3+} as reflected from our QTAIM and N-M bond order calculations. However, significantly higher LMCT for Eu^{3+} is noted in MPA analysis. Results obtained from MPA, N-M bond order, WBIs and QTAIM reiterated the ionic character of metal binding. These observations led us to conclude that it is the strong electrostatic interaction and efficient CB[5] to metal charge transfer in case of Eu^{3+} that directs the greater selectivity for Eu^{3+} over Am^{3+}.

Thus, the present investigation not only predicts the superior selectivity for Eu^{3+} over Am^{3+} with CB[5] but also provides mechanistic insight on the binding and explains the importance of counter-ions in such binding/extraction processes. Our calculated structural and thermodynamic parameters for Eu^{3+} are found to be in excellent correlation with the previously reported experimental information, while the calculation with Am^{3+} can be considered as a predictive tool for future experimental studies. It should be noted that most of the extractants reported are towards Am extraction from Eu, whereas our supramolecule is selective towards Eu over Am.

CHAPTER –8

Summary and Outlook

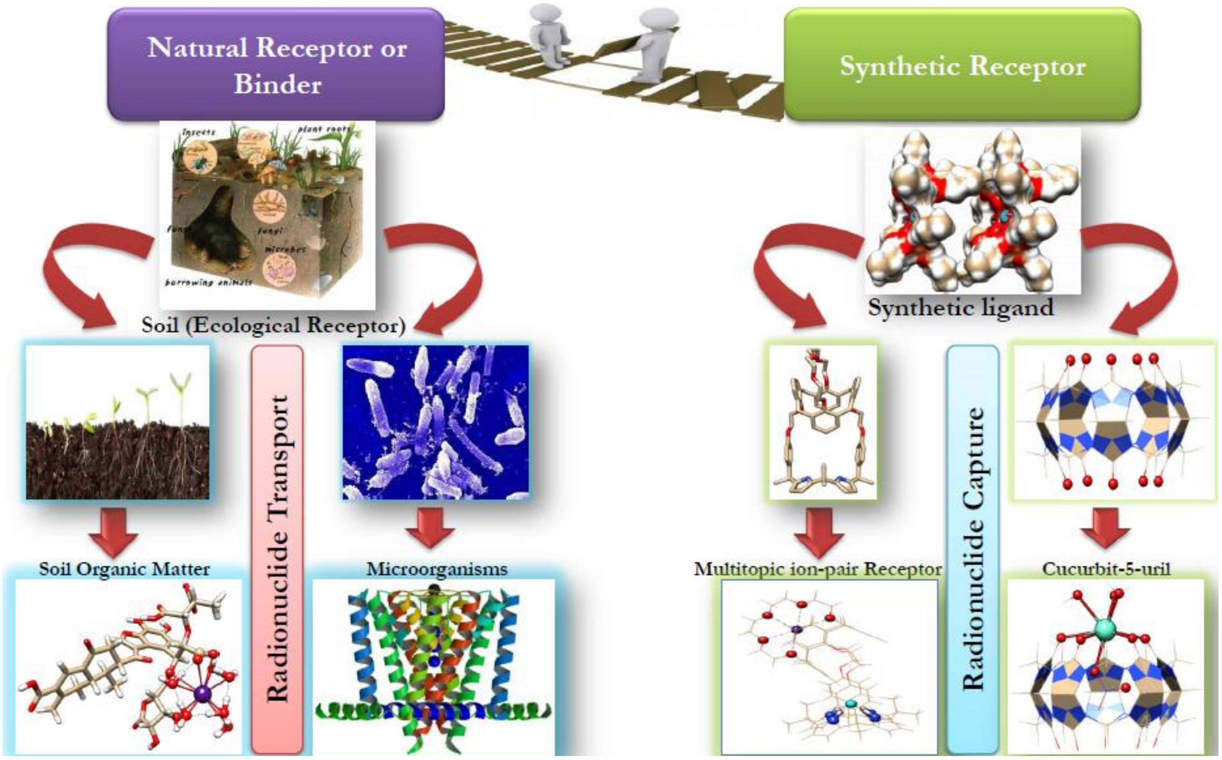

In this concluding chapter, we briefly summarize all the major findings and conclusions of the thesis. We also aim to provide a futuristic outlook and possible future extensions of the carried work. The major aim of the present thesis was to understand the binding and transport mechanism of important radionuclide cations such as Cs^+, Sr^{2+}, Eu^{3+} and Am^{3+}, in chemically diverse interacting media of different origin (*i.e* natural and synthetic binders/receptors). In this endeavor our approach has been multi-scale modeling.

In Chapter 1, we have elaborated the chemical nature of different binder/receptors and have provided bird's-eye view on all applied computational methodologies (QM, MD and MtD). Brief details on the popular mode of investigations for radionuclide binding related studies have been also addressed followed by an account on goal of the thesis.

We have considered two vital components of natural environment namely, soil organic matter (SOM) and microorganism as the interacting media for the accidently released radionuclides. Detailed results on these investigations have been discussed in Chapter 2, 3 and 4.

In Chapter 2, we have investigated the migration behavior of Cs^+ and Sr^{2+} in fulvic acid (FA) , a representative of SOM. Based on MD, MtD simulations and DFT based calculations, we predicted that Sr^{2+} interacts strongly with FA than Cs^+. FA binds with Cs^+ in non-specific manner *via* outer-sphere binding motif and neighboring functional groups are found to play a vital role in Cs^+ binding. However, due to the favorable water-FA interaction and low ionic potential value, Cs^+ failed to interact with FA efficiently, which eventually led to higher migration rate of Cs^+ in fulvic acid medium. On the other hand, we showed that owing to its high ionic potential, Sr^{2+} can surpass the existing secondary non-bonding interaction between coordinated waters and FA, which led to stronger complexation of Sr^{2+} with FA *via* inner sphere binding motif. Thus, these results demonstrated a complete picture on the migration behavior of Cs^+ and Sr^{2+} in the presence of SOM and provided the possible answer on the bioavailability of aforementioned radionuclides in soil solution for further plant uptake.

In Chapter 3 and 4, we have assessed the possibility of translocation of Cs^+ and Sr^{2+} *via* non-selective NaK ion channel of soil dwelling bacteria *bacillus cereus*. Based on the results of MtD simulations and DFT calculations, we have shown that permeation of Cs^+ through the ion channel is energetically favorable, suggesting that Cs^+ can possibly migrate *via* NaK ion channel route. However, binding free energy and ion exchange free energy trend predict that the rate of permeation is expected to be lower than K^+. To substantiate this further we have conducted a variety of calculations. DFT calculations predicted that Sr^{2+} interacts favorably at deeply buried site of selectivity filter (SF) of NaK ion channel but resultant potential mean force (PMF) profile as obtained from well tempered MtD simulations demonstrated that it faces higher energy barrier than monovalent ion (K^+) due to its higher hydration energy. This explains the lower rate of permeation of Sr^{2+} as compared to K^+.

In Chapter 5, 6 and 7, we have explored the binding and energetics of radionuclide capture *via* synthetic receptors. Here we considered synthetic ion-pair receptor and macrocyclic cucurbit-5-uril to demonstrate how these ligands achieve supreme selectivity towards specific radionuclides. The crystal structures of these synthetic receptors are known and well documented. Further, due to structural rigidity, issues on finding of most stable conformation is not problematic. Hence, Only DFT calculations are performed for these systems.

The binding mechanism of various cesium salts with calix-pyrrole strapped calix-crown based ion-pair receptor are elaborated in Chapter 5. Apart from understanding the acting binding mechanism, one of the aim of this investigation was to benchmark the applied DFT methodology based on comparison with available experimental data. By extensive electronic structure calculations, we showed that in ion-pair receptor, counter-anion plays crucial role to enhance the binding affinities of radionuclide cations. Thus, depicting the true binding energy requires incorporation of counter-ion influence into the calculations. Our obtained preferable binding modes of cesium salts with receptor are found to be in excellent agreement with the previously reported experiment.

In Chapter 6, we proposed an easy two step strontium decontamination/extraction methodology in nitrate media using the aforementioned receptor (calix-pyrrole strapped calix-crown based ligand). Using the benchmarked DFT technique, we predicted that the receptor has excellent selectivity for Sr^{2+} in the presence of commonly interfering cations such as Ca^{2+} (for environmental waste) and Na^+ (for alkaline waste). Further, ligand's supreme selectivity for K^+ over Sr^{2+} can be exploited to facilitate the stripping process of Sr^{2+} from organic to aqueous phase.

In Chapter 7, we investigated the possibility of separating Am^{3+}/Eu^{3+} pair *via* carobon-hydrogen-oxygen-nitrogen (C-H-O-N) based Cucurbit-5-uril (CB[5]) receptor. The relativistic DFT based calculations predict that CB[5] has remarkable selectivity for Eu^{3+} over Am^{3+}. The presence of encapsulated counter anion (HCOO, Cl^- and NO_3^-) inside the hydrophobic cavity of CB[5] is crucial to provide extra stability to the bound metal at the electron rich carbonyl portal. We further assessed the reasoning behind the selectivity trend performing various electronic structure calculations such as EDA and QTAIM. Strong electrostatic ion-dipole interaction along with efficient charge transfer between CB[5] and Eu^{3+} are found to be the major favorable factor to outweighs the slightly better degree of covalency between CB[5] and Am^{3+},which originated superior selectivity of Eu^{3+} over Am^{3+} in CB[5].

One key point was noted that, unlike the case of SOM, the interaction between the cations and ion channel's selectivity filter are specific in nature. Thus in spite of the non-selective feature prevalent in NaK ion channel, site-specific selectivity does exist inside SF of the channel owing to the presence of proper structural arrangement of amino acid residues. Notably, in natural media, influence of counter ion on the translocation event is expected to be negligible to change the course of the reaction. However, we have shown in Chapter 5, 6 and 7 that such anionic assistance is crucial to achieve better binding affinities for radionuclides.

To summarize, this thesis provided molecular level insights on the radionuclide binding and transport *via* natural binder/receptor and on radionuclide capture phenomena *via* synthetic receptors. The extensive computational investigations demonstrated that natural binder/receptors such as SOM, even in the absence of any specific binding site it shows distinct preference for particular radionuclide (ex. preference for Sr^{2+} in FA-water system). On the other hand, due to the presence of proper structural framework, ion channel of soil dwelling microorganisms shows site-specific selectivity towards metal cations. The synthesized ligands exhibit distinctly different behavior than the natural binder/receptor. Synthetic receptors can be designed, based on the knowledge of ion-specific interaction, with a primary goal to attain selectivity towards the metal of choice. Thus, either by specific or non-specific route, the natural binders attain control over radionuclide migration, while by virtue of specific recognition motif and strong cation-anion cooperative assistance, synthetic receptors achieves the similar goal of radionuclide capturing in synthetic media.

The present thesis can be considered as a step towards understanding how behavioral aspects of radionuclides migration and capture change with different sub-systems of natural and synthetic environment. Nature is full of surprises and consist of diverse components. Thus exhaustive studies on other integral environmental components are essential to understand how nature dictates radionuclide migration. The prime goal of these futuristic works would be implementation of these gathered knowledge to design a suitable ligand (mimicking nature!) for several societal/industrial/waste management applications.

References

1. Stohl, A.; Seibert, P.; Wotawa, G.; Arnold, D.; Burkhart, J. F.; Eckhardt, S.; Tapia, C.; Vargas, A.; Yasunari, T. J. *Atmos. Chem. Phys.* **2011,** *11*, 28319.
2. Aarkrog, A. *J. Environ. Radioact.* **1988,** *6*, 151.
3. Adriano, D. C.; Hoyt, G. D.; Pinder, J. E. *Health Phys.* **1981,** *40*, 369.
4. Carlton, H. B., L. R.; Evans, A. B.; Beary, L. A.; Murphy, C. E.; Pinder, J. E.; Strom, R. N. Cesium in the Savannah River Site Environment; WSRC-RP-92-250; Westinghouse Savannah River Company: Aiken, SC,**1992**.
5. Tsujimoto, K.; Sasa, T.; Nishihara, K.; Oigawa, H.; Takano, H. *J. Nucl. Sci. Technol.* **2004,** *41*, 21.
6. Bryan, N. D.; Abrahamsen, L.; Evans, N.; Warwick, P.; Buckau, G.; Weng, L.; Van Riemsdijk, W. H. *Applied Geochemistry* **2012,** *27* (2), 378-389.
7. Leenheer, J. A.; Wershaw, R. L.; Reddy, M. M. *Environ. Sci. Technol.* **1995,** *29*, 393.
8. Kim, S. K.; Sessler, J. L.; Gross, D. E.; Lee, C.-H.; Kim, J. S.; Lynch, V. M.; Delmau, L. H.; Hay, B. P. A *Journal of the American Chemical Society* **2010,** *132* (16), 5827-5836.
9. Kim, S. K.; Vargas-Zúñiga, G. I.; Hay, B. P.; Young, N. J.; Delmau, L. H.; Masselin, C.; Lee, C.-H.; Kim, J. S.; Lynch, V. M.; Moyer, B. A.; Sessler, J. L. *Journal of the American Chemical Society* **2012,** *134* (3), 1782-1792.
10. Kim, S. K.; Lynch, V. M.; Young, N. J.; Hay, B. P.; Lee, C.-H.; Kim, J. S.; Moyer, B. A.; Sessler, J. L. *Journal of the American Chemical Society* **2012,** *134* (51), 20837-20843.
11. Roh, C.; Kang, C.; Lloyd, J. R. *Korean Journal of Chemical Engineering* **2015,** *32* (9), 1720-1726.
12. Boda, A.; De, S.; Ali, S. M.; Tulishetti, S.; Khan, S.; Singh, J. K. *J. Mol. Liq.* **2012,** *172*, 110.
13. Sundararajan, M.; Rajaraman, G.; Ghosh, S. K. *Phys. Chem. Chem. Phys.* **2011,** *13*, 18038.
14. Sundararajan, M.; Ghosh, S. K. *The Journal of Physical Chemistry A* **2011,** *115* (24), 6732-6737.
15. Sundararajan, M. *Separation Science and Technology* **2013,** *48* (16), 2391-2396.
16. Manna, D.; Mula, S.; Bhattacharyya, A.; Chattopadhyay, S.; Ghanty, T. K. *Dalton Trans.* **2015,** *44*, 1332.
17. Manna, D.; Ghanty, T. K. *Phys. Chem. Chem. Phys.* **2012,** *14*, 11060.
18. Burk, P.; Tammiku-Taul, J.; Tamp, S.; Sikk, L.; Sillar, K.; Mayeux, C.; Gal, J. F.; Maria, P.

C. *J. Phys. Chem. A* **2009,** *113*, 10734.

19. Mayeux, C.; Gal, J. F.; Charles, L.; Massi, L.; Maria, P. C.; Tammiku-Taul, J.; Lohu, E. L.; Burk, P. *J. Mass Spectrom.* **2010,** *45*, 520.

20. Toribara, T. Y. M., M. W.; Morrow, P.E.; . Polluted Rain **1980,** *10.1007/978-1-4613-3060-8*.

21. Stevenson, F. J. *Humus Chemistry: Genesis, Composition, Reactions*. 1994.

22. Hatcher, P. G.; Clifford, D. J. *Organic Geochemistry* **1994,** *21* (10), 1081-1092.

23. Haworth, R. D. The Chemical Nature of Humic Acid. *Soil Science* **1971,** *111* (1), 71-79.

24. Hatcher, P. G.; VanderHart, D. L.; Earl, W. L. *Organic Geochemistry* **1980,** *2* (2), 87-92.

25. Mao, J.; Cory, R. M.; McKnight, D. M.; Schmidt-Rohr, K. *Organic Geochemistry* **2007,** *38* (8), 1277-1292.

26. Schulten, H.-R.; Schnitzer, M. *Soil Science* **1997,** *162* (2), 115-130.

27. Sutton, R.; Sposito, G. *Environmental Science & Technology* **2005,** *39* (23), 9009-9015.

28. Jezierski, A.; Czechowski, F.; Jerzykiewicz, M.; Drozd, J. *Applied Magnetic Resonance* **2000,** *18* (1), 127-136.

29. Perminova, I. V.; Grechishcheva, N. Y.; Petrosyan, V. S. *Environmental Science & Technology* **1999,** *33* (21), 3781-3787.

30. Piccolo, A. *Soil Science* **2001,** *166* (11), 810-832.

31. Bloom, P. R. a. L., J. A.; *Humic Substances II* **1989**, 409--446.

32. Ritchie, G. S. P.; Posner, A. M. *Journal of Soil Science* **1982,** *33* (2), 233-247.

33. Novotny, F. J.; Rice, J. A.; Weil, D. A. *Environmental Science & Technology* **1995,** *29* (9), 2464-2466.

34. Rice, J. A. HUMIN. *Soil Science* **2001,** *166* (11), 848-857.

35. Tipping, E.; Hurley, M. A. *Geochimica et Cosmochimica Acta* **1992,** *56* (10), 3627-3641.

36. Tipping, E. Humic Ion-Binding Model VI: *Aquatic Geochemistry* **1998,** *4* (1), 3-47.

37. Milne, C. J.; Kinniburgh, D. G.; van Riemsdijk, W. H.; Tipping, E. *Environmental Science & Technology* **2003,** *37* (5), 958-971.

38. Kinniburgh, D. G.; Milne, C. J.; Benedetti, M. F.; Pinheiro, J. P.; Filius, J.; Koopal, L. K.; Van Riemsdijk, W. H. *Environmental Science & Technology* **1996,** *30* (5), 1687-1698.

39. Trout, C. C.; Kubicki, J. D. *Geochim. Cosmochim. Acta* **2006,** *70*, 44.

40. Leenheer, J. A.; Wershaw, R. L.; Reddy, M. M. *Environ. Sci. Technol.* **1995,** *29*, 399.

41. Trout, C. C.; Kubicki, J. D. *Geochem. Cosmochim. Acta* **2007,** *71*, 3859.

42. Schlosser, F.; Krüger, S.; Rösch, N. A Density Functional Study of Uranyl Monocarboxylates. *Inorganic Chemistry* **2006,** *45* (4), 1480-1490.

43. Wang, J.-F.; Fang, M.-J.; Huang, H.-Q.; Li, G.-L.; Su, W.-J.; Zhao, Y.-F. *Acta Crystallographica Section E* **2003,** *59* (10), o1517-o1518.

44. Anderson, T. A.; Coats, J. R. *Bioremediation through Rhizosphere Technology*. American Chemical Society: 1994; Vol. 563, p 268.

45. Bollag, J.-M.; Mertz, T.; Otjen, L. Role of Microorganisms in Soil Bioremediation. In *Bioremediation through Rhizosphere Technology*, American Chemical Society: 1994; Vol. 563, pp 2-10.

46. Lupton, F. S.; DeFilippi, L. J.; Goodman, J. R. Bioremediation of chromium (VI) contaminated aqueous systems by sulfate reducing bacteria. Google Patents: 1991.

47. Choudhary, S.; Sar, P. *Reviews in Environmental Science and Bio/Technology* **2015,** *14* (3), 347-355.

48. Wu, Q.; Sanford, R. A.; Löffler, F. E. Uranium(VI) *Applied and Environmental Microbiology* **2006,** *72* (5), 3608-3614.

49. Fletcher, K. E.; Boyanov, M. I.; Thomas, S. H.; Wu, Q.; Kemner, K. M.; Löffler, F. E. *Environmental Science & Technology* **2010,** *44* (12), 4705-4709.

50. Sundararajan, M.; Campbell, A. J.; Hillier, I. H. *The Journal of Physical Chemistry A* **2008,** *112* (19), 4451-4457.

51. Zhu, Y. G.; Smolders, E. *J. Exp. Bot.* **2000,** *51*, 1635.

52. Walker, D. D.; Norato, M. A.; Campbell, S. G.; Crowder, M. L.; Fink, S. D.; Fondeur, F. F.; Geeting, M. W.; Kessinger, G. F.; Pierce, R. A. *Separation Science and Technology* **2005,** *40* (1-3), 297-309.

53. Horwitz, E. P.; Dietz, M. L.; Fisher, D. E. *Solvent Extraction and Ion Exchange* **1990,** *8* (4-5), 557-572.

54. Horwitz, E. P.; Dietz, M. L.; Fisher, D. E. *Solvent Extraction and Ion Exchange* **1991,** *9* (1), 1-25.

55. Sessler, J. L.; Kim, S. K.; Gross, D. E.; Lee, C.-H.; Kim, J. S.; Lynch, V. M. *Journal of the American Chemical Society* **2008,** *130* (39), 13162-13166.

56. Park, I.-W.; Yoo, J.; Kim, B.; Adhikari, S.; Kim, S. K.; Yeon, Y.; Haynes, C. J. E.; Sutton,

J. L.; Tong, C. C.; Lynch, V. M.; Sessler, J. L.; Gale, P. A.; Lee, C.-H. *Chemistry – A European Journal* **2012,** *18* (9), 2514-2523.

57. Biedermann, F.; Uzunova, V. D.; Scherman, O. A.; Nau, W. M.; De Simone, A. *J. Am. Chem. Soc.* **2012,** *134*, 15318.

58. Saleh, N. i.; Koner, A. L.; Nau, W. M. *Angewandte Chemie* **2008,** *120* (29), 5478-5481.

59. Chen, K.; Kang, Y.-S.; Zhao, Y.; Yang, J.-M.; Lu, Y.; Sun, W.-Y. *Journal of the American Chemical Society* **2014,** *136* (48), 16744-16747.

60. Rawat, N.; Kar, A.; Bhattacharyya, A.; Rao, A.; Nayak, S. K.; Nayak, C.; Jha, S. N.; Bhattacharyya, D.; Tomar, B. S. *Dalton Trans.* **2015,** *44*, 4246.

61. Sundararajan, M.; Sinha, V.; Bandyopadhyay, T.; Ghosh, S. K. *J. Phys. Chem. A* **2012,** *116*, 4388.

62. Liu, J. X.; Long, L. S.; Huang, R. B.; Zheng, L. S. *Cryst. Growth Des.* **2006,** *6*, 2611.

63. Liu, J. X.; Long, L. S.; Huang, R. B.; Zheng, L. S. *Inorg. Chem.* **2007,** *46*, 10168.

64. Liu, J.; Gu, Y.; Lin, R.; Yao, W.; Liu, X.; Zhu, J. *Supramol. Chem.* **2010,** *22*, 130.

65. Laio, A.; Gervasio, F. L. *Rep. Prog. Phys.* **2008,** *71*, 126601.

66. Zhu, Y. G.; Shaw, G. *Chemosphere* **2000,** *41*, 121.

67. Benedetti, M. F.; Riemsdijk, W. H. V.; Koopal, L. K.; Kinniburgh, D. G.; Gooddy, D. C.; Milne, C. J. *Geochim. Cosmochim. Acta* **1996,** *60*, 2503.

68. Sauve, S.; Hendershot, W.; Allen, H. E. *Environ. Sci. Technol.* **2000,** *34*, 1125.

69. Maguire, S.; Pulford, I. D.; Cook, G. T.; Mackenzie, A. B. *J. Soil Sci.* **1992,** *43*, 689.

70. Shaban, I. S.; Macasek, F. *J. Radioanal. Nucl. Chem.* **1998,** *229*, 73.

71. Hakem, N.; Apps, J. A.; Moridis, G. J.; Al Mahamid, I. *Radiochim. Acta* **2004,** *92*, 419.

72. Kumar, S.; Tomar, B. S.; Ramanathan, S.; Manchanda, V. K. *Radiochim. Acta* **2006,** *94*, 369.

73. Helal, A. A.; Arida, H. A.; Rizk, H. E.; Khalifa, S. M. *Radiokhimiya* **2007,** *49*, 458.

74. Staunton, S.; Roubaud, M. *Clays Clay Miner.* **1997,** *45*, 251.

75. Rigol, A.; Vidal, M.; Rauret, G. *J. Environ. Radioact.* **2002,** *58*, 191.

76. Zhu, Y. G.; Smolders, E. *J. Exptl. Botany* **2000,** *51*, 1635.

77. Howard, B. J.; Beresford, N. A.; Hove, K. *Health Phys.* **1991,** *61*, 715.

78. Sanchez, A. L.; Wright, S. N.; Smolders, E.; Naylor, C.; Stevens, P. A.; Kennedy, V. H.; Dodd, B. A.; Singleton, D. L.; Barnett, C. L. *Environ. Sci. Technol.* **1999,** *33*, 2752.

79. Veresoglou, D. S.; Tsialtas, J. T.; Barbayiannis, N.; Zalidis, G. C. *Agric., Ecosyst. Environ.* **1995,** *56*, 37.

80. Bryan, N. D.; Robinson, V. J.; Livens, F. R.; Hesketh, N.; Jones, M. N.; Lead, J. R. *Geochim. Cosmochim. Acta* **1997,** *61*, 805.

81. Tipping, E.; Hurley, M. A. *Geochim. Cosmochim. Acta* **1992,** *56*, 3627.

82. Bryan, N. D.; Jones, D. M.; Appleton, M.; Livens, F. R.; Jones, M. N.; Warwick, P.; Hall, A. *Phys. Chem. Chem. Phys.* **2000,** *2*, 1291.

83. Xu, X.; Kalinichev, A. G.; Kirkpatrick, J. *Geochem. Cosmochim. Acta* **2006,** *70*, 4319.

84. Kalinichev, A. G.; Kirkpatrick, J. *Eur. J. Soil. Sci.* **2007,** *58*, 909.

85. Jones, M. N.; Bryan, N. D. *Adv. Colloid Interface* **1998,** *78*, 1.

86. Aquino, A. J.; Tunega, D.; Pasalic, H.; Haberhauer, G.; Gerzabek, M. H.; Lischka, H. *Chem. Phys.* **2008,** *349*, 69.

87. Aquino, A. J.; Tunega, D.; Pasalic, H.; Schaumann, G. E.; Haberhauer, G.; Gerzabek, M. H.; Lischka, H. *Environ. Sci. Technol.* **2011,** *45*, 8411.

88. Aquino, A. J.; Tunega, D.; Schaumann, G. E.; Haberhauer, G.; Gerzabek, M. H.; Lischka, H. *Geoderma* **2014,** *213*, 115.

89. Sinha, V.; Ganguly, B.; Bandyopadhyay, T. *PLoS One* **2012,** *7*, e40188.

90. Pathak, A. K.; Bandyopadhyay, T. *Proteins: Struct., Funct., Bioinf.* **2014,** *82*, 1799.

91. Becke, A. D. *Phys. Rev. A* **1988,** *38*, 3098.

92. Perdew, J. P. *Phys. Rev. B* **1986,** *33*, 8822.

93. Schäfer, A.; Horn, H.; Ahlrichs, R. *J. Chem. Phys.* **1992,** *97*, 2571.

94. Sundararajan, M.; Ganyushin, D.; Ye, S.; Neese, F. *Dalton Trans.* **2009,** *30*, 6021.

95. Sundararajan, M. *J. Phys. Chem. B* **2013,** *117*, 13409.

96. Becke, A. D. *J. Chem. Phys.* **1993,** *98*, 5648.

97. Lee, C.; Yang, W.; Parr, R. G. *Phys. Rev. B* **1988,** *37*, 785.

98. Schäfer, A.; Huber, C.; Ahlrichs, R. *J. Chem. Phys.* **1994,** *100*, 5829.

99. Weigend, F.; Ahlrichs, R. *Phys. Chem. Chem. Phys.* **2005,** *7*, 3297.

100. Klamt, A.; Schuurmann, G. *J. Chem. Soc., Perkin Trans.* **1993,** *2*, 799.

101. Ahlrichs, R.; Bar, M.; Baron, H. P.; Bauernschmitt, R.; Bocker, S.; Ehrig, M.; Eichkorn, K.; Elliot, S.; Furche, F.; Haase, F.; Haser, M.; Horn, H. *TURBOMOLE, V6.3 2011, a development of University of Karlsruhe and Forschungszentrum Karlsruhe GmbH, 1989–2007.*

102. Reed, A. E.; Weinstock, R. B.; Weinhold, F. *J. Chem. Phys.* **1985,** *83*, 735.

103. Neese, F., Wennmohs, F., Becker, U., Bykov, D., Ganyushin, D., Hansen, A., Izsák, R., Liakos, D.G., Kollmar, C., Kossmann, S. and Pantazis, D.A. ORCA, version 3.0. *Max Planck Institute for Chemical Energy Conversion, Mülheim/Ruhr, Germany* **2014**.

104. Hess, B.; Kutzner, C.; van der Spoel, D.; Lindahl, E. *J. Chem. Theory Comput.* **2008,** *4*, 435.

105. Aqvist, J. J. *J. Phys. Chem.* **1990,** *94*, 8021.

106. Larentzos, J. P.; Criscenti, L. J. *J. Phys. Chem. B* **2008,** *112*, 14243.

107. Wang, J.; Wang, W.; Kollman, P. A.; Case, D. A. *J. Mol. Graphics Modell.* **2006,** *25*, 247.

108. Wang, J.; Wolf, R. M.; Caldwell, J. W.; Kollman, P. A.; Case, D. A. *J. Comput. Chem.* **2004,** *25*, 1157.

109. Jorgensen, W. L.; Chandrasekhar, J.; Madura, J. D.; Impey, R. W.; Klein, M. L. *J. Chem. Phys.* **1983,** *79*, 926.

110. Bussi, G.; Donadio, D.; Parrinello, M. *J. Chem. Phys.* **2007,** *126*, 014101.

111. Essmann, U.; Perera, L.; Berkowitz, M. L.; Darden, T.; Lee, H.; Pedersen, L. G. *J. Chem. Phys.* **1995,** *103*, 8577.

112. Hess, B.; Bekker, H.; Berendsen, H. J. C.; Fraaije, J. G. *J. Comput. Chem.* **1997,** *18*, 1463.

113. Doudou, S.; Vaughan, D. J.; Livens, F. R.; Burton, N. A. *Environ. Sci. Technol.* **2012,** *46*, 7587.

114. Schlitter, J. *Chem. Phys. Lett.* **1993,** *215*, 617.

115. Laio, A.; Parrinello, M. *Proc. Natl. Acad. Sci. U. S. A.* **2002,** *99*, 12562.

116. Marcus, Y. *J. Chem. Soc., Faraday Trans.* **1991,** *87*, 2995.

117. Bonomi, M.; Barducci, A.; Parrinello, M. *J. Comput. Chem.* **2009,** *30*, 1615.

118. Caminiti, R.; Musinu, A.; Paschina, G.; Pinna, G. *J. Appl. Crystallogr.* **1982,** *15*, 482.

119. Neilson, G. W.; Broadbent, R. D. *Chem. Phys.Lett.* **1990,** *167*, 429.

120. Ohtaki, H.; Radnai, T. *Chem. Rev.* **1993,** *93*, 1157.

121. Moreau, G.; Helm, L.; Purans, J.; Merbach, A. E. *J. Phys. Chem. A* **2002,** *106*, 3034.

122. Kerridge, A.; Kaltsoyannis, N. *Chem.—Eur. J.* **2011,** *17*, 5060.

123. Ali, S. M.; De, S.; Maity, D. K. *J. Chem. Phys.* **2007,** *127*, 044303.

124. Ikeda, T.; Boero, M. *J. Chem. Phys.* **2012,** *137*, 041101.

125. Schwenk, C. F.; Hofer, T. S.; Rode, B. M. *J. Phys. Chem. A* **2004,** *108*, 1509.

126. Chang, R. *Chemistry*. 1994.

127. Lide, D. R. *CRC Handbook of Chemistry and Physics*. 2003.

128. Lumsdon, D. G.; Fraser, A. R. *Environ. Sci. Technol.* **2005,** *39*, 6624.

129. Iskrenova-Tchoukova, E.; Kalinichev, A. G.; Kirkpatrick, R. J. *Langmuir* **2010,** *26*, 15909.

130. Samadfam, M.; Niitsu, Y.; Sato, S.; Ohashi, H. *Radiochim. Acta* **1996,** *73*, 211.

131. Rusin, P. A.; Quintana, L.; Brainard, J. R.; Strietelmeier, B. A.; Tait, C. D.; Ekberg, S. A.; Clark, D. L. *Environ. Sci. Technol.* **1994,** *28*, 1686.

132. Ashraf, M. A.; Rehman, M. A.; Maah, M. J.; Yusoff, I. *Crit. Rev. Environ. Sci. Technol.* **2014,** *44*, 1740.

133. Xiangke, W.; Wenming, D.; Jinzhou, D.; Zuyi, T. *Nucl. Chem.* **1999,** *240*, 783.

134. Comans, R. N. J.; Haller, M.; Preter, P. D. *Geochim. Cosmochim. Acta* **1991,** *55*, 433.

135. van Bergeijk, K. E.; Noordijk, H.; Lembrechts, J.; Frissel, M. J. *J. Environ. Radioact.* **1992,** *15*, 265.

136. Lee, M. H.; Lee, C. W. *J. Environ. Radioact.* **1999,** *47*, 253.

137. Zhang, M. L.; Ren, A.; Shao, D.; Wang, X. *J. Radioanal. Nucl. Chem.* **2006,** *268*, 33.

138. Hille, B. *Ion Channels of Excitable Membranes*. 2001.

139. Guharay, F.; Sachs, F. *J. Physiol.* **1984,** *352*, 685.

140. Nelson, M. T.; Patlak, J. B.; Worley, J. F.; Standen, N. B. *Am. J. Physion-cell Ph.* **1990,** *259*, C13.

141. Doyle, D. A.; Cabral, J. M.; Pfuetzner, R. A.; Kuo, A.; Gulbis, J. M.; Cohen, S. L.; Chait, B. T.; MacKinnon, R. *Science* **1998,** *280*, 69.

142. Jiang, Y.; Lee, A.; Chen, J.; Cadene, M.; Chait, B. T.; MacKinnon, R. *Nature* **2002,** *417*, 515.

143. Jiang, Y.; Lee, A.; Chen, J.; Ruta, V.; Cadene, M.; Chait, B. T.; MacKinnon, R. *Nature* **2003,** *423*, 33.

144. Payandeh, J.; Scheuer, T.; Zheng, N.; Catterall, W. A. *Nature* **2011,** *475*, 353.

145. Zhang, X.; Ren, W.; DeCaen, P.; Yan, C.; Tao, X.; Tang, L.; Wang, J.; Hasegawa, K.; Kumasaka, T.; He, J. *Nature* **2012,** *486*, 130.

146. Heginbotham, L.; Abramson, T.; MacKinnon, R. *Science* **1992,** *258*, 1152.

147. Heginbotham, L.; Lu, Z.; Abramson, T.; MacKinnon, R. *Biophys. J.* **1994,** *66*, 1061.

148. Derebe, M. G.; Sauera, D. B.; Zenga, W.; Alam, A.; Shia, N.; Jiang, Y. *Proc. Natl. Acad.*

Sci. U. S. A. **2011,** *108*, 598.

149. Shi, N.; Ye, S.; Alam, A.; Chen, L.; Jiang, Y. *Nature* **2006,** *440*, 570.

150. Alam, A.; Jiang, Y. *Nat. Struct. Mol. Biol.* **2009,** *16*, 35.

151. Noskov, S. Y.; Roux, B. *J. Gen. Physiol.* **2007,** *129*, 135.

152. Vora, T.; Bisset, D.; Chung, S. H. *Biophys. J.* **2008,** *95*, 1600.

153. Shen, R.; Guo, W. *Biochim. Biophys. Acta, Biomembr.* **2009,** *1788*, 1024.

154. Shen, R.; Guo, W.; Zhong, W. *Biochim. Biophys. Acta, Biomembr.* **2010,** *1798*, 1474.

155. Furini, S.; Domene, C. *Biophys. J.* **2011,** *101*, 1623.

156. Furini, S.; Domene, C. *Biophys. J.* **2012,** *103*, 2106.

157. Furini, S.; Domene, C. *Biophys. J.* **2013,** *105*, 1737.

158. Shen, R.; Guo, W. *J. Phys. Chem. Lett.* **2012,** *3*, 2887.

159. Wang, Y.; Chamberlin, A. C.; Noskov, S. Y. *J. Phys. Chem. B* **2014,** *118*, 2041.

160. Dudev, T.; Lim, C. *J. Am. Chem. Soc.* **2009,** *131*, 8092.

161. Dudev, T.; Lim, C. *J. Am. Chem. Soc.* **2010,** *132*, 2321.

162. Varma, S.; Rempe, S. B. *J. Am. Chem. Soc.* **2008,** *130*, 15405.

163. Fowler, P. W.; Tai, K.; Sansom, M. S. P. *Biophys. J.* **2008,** *95*, 5062.

164. Alam, A.; Jiang, Y. *Nat. Struct. Mol. Biol.* **2009,** *16*, 30.

165. Grimme, S.; Antony, J.; Ehrlich, S.; Krieg, H. *J. Chem. Phys.* **2010,** *132*, 154104.

166. Bostick, D. L.; Brooks, C. L. *Proc. Natl. Acad. Sci. U. S. A.* **2007,** *104*, 9260.

167. Varma, S.; Sabo, D.; Rempe, S. B. *J. Mol. Biol.* **2008,** *376*, 13.

168. Liao, R. Z.; Siegbahn, P. E. *Chemical Science* **2015,** *6*, 2754.

169. Dudev, T. *Computational Chemistry* **2014,** *2*, 19.

170. Varma, S.; Rempe, S. B. *Biophys. J.* **2007,** *93*, 1093.

171. Morokuma, K. *J. Chem. Phys.* **1971,** *55*, 1236.

172. Ziegler, T.; Rauk, A. *Theor. Chim. Acta* **1977,** *46*, 1.

173. Van Lenthe, E.; van Leeuwen, R.; Baerends, E. J.; Snijders, J. G. *Int. J. Quantum Chem.* **1996,** *57*, 281.

174. te Velde, G.; Bickelhaupt, F. M.; Baerends, E. J.; Gisbergen, v. S. J. A.; Fonseca Guerra, C.; Snijders, J. G.; Ziegler, T. *J. Comput. Chem.* **2001,** *22*, 931.

175. Zhang, Y.; Voth, G. A. *J. Chem. Theory Comput.* **2011,** *7*, 2277.

176. Lindorff-Larsen, K.; Maragakis, P.; Piana, S.; Eastwood, M. P.; Dror, R. O.; Shaw, D. E.

PLoS One **2012,** *7,* e32131.

177. Jorgensen, W. L.; Jenson, C. *J. Comput. Chem.* **1998,** *19*, 1179.

178. Bonomi, M.; Branduardi, D.; Bussi, G.; Camilloni, C.; Provasi, D.; Raiteri, P.; Donadio, D.; Marinelli, F.; Pietrucci, F.; Broglia, R. A.; Parrinello, M. *Comput. Phys. Commun.* **2009,** *180*, 1961.

179. Moradi, M.; Tajkhorshid, E. *J. Phys. Chem. Lett.* **2013,** *4*, 1882.

180. Laio, A.; Rodriguez-Fortea, A.; Gervasio, F. L.; Ceccarelli, M.; Parrinello, M. *J. Phys. Chem. B* **2005,** *109*, 6714.

181. Babin, V.; Roland, C.; Darden, T. A.; Sagui, C. *J. Chem. Phys.* **2006,** *125*, 204909.

182. Autieri, E.; Sega, M.; Pederiva, F.; Guella, G. *J. Chem. Phys.* **2010,** *133*, 095104.

183. Varma, S.; Rempe, S. B. *Biophys. Chem.* **2006,** *124*, 192.

184. Rao, J. S.; Dinadayalane, T. C.; Leszczynski, J.; Sastry, G. N. *J. Phys. Chem. A* **2008,** *112*, 12944.

185. Soper, A. K.; Weckstrom, K. *Biophys. Chem.* **2006,** *124*, 180.

186. Glezakou, V. A.; Chen, Y.; Fulton, J. L.; Schenter, G. k.; Dang, L. X. *Theor. Chem. Acc.* **2006,** *115*, 86.

187. Whitfield, T. W.; Verma, S.; Harder, E.; Lamoureux, G.; Rempe, S. B.; Roux, B. *J. Chem. Theory Comput.* **2007,** *3,* 2068.

188. Carrillo-Tripp, M.; Saint-Martin, H.; Ortega-Blake, I. *J. Chem. Phys.* **2003,** *118*, 7062.

189. Sadhu, B.; Sundararajan, M.; Bandyopadhyay, T. *J. Phys. Chem. B* **2015,** *119*, 10989.

190. Kim, I.; Allen, T. W. *Proc. Natl. Acad. Sci. U. S. A.* **2011,** *108*, 17963.

191. Kopfer, D. A.; Song, C.; Gruene, T.; Sheldrick, G. M.; Zachariae, U.; de Groot, B. L. *Science* **2014,** *346*, 352.

192. Smart, O. S.; Goodfellow, J. M.; Wallace, B. A. *Biophys. J.* **1993,** *65*, 2455.

193. Bostick, D. L.; Brooks, C. L. *J. Am. Chem. Soc.* **2010,** *132*, 13185.

194. Bostick, D. L.; Arora, K.; Brooks, C. L. *Biophys. J.* **2009,** *96*, 3887.

195. Thomas, M.; Jayatilaka, D.; Corry, B. *Biophys. J.* **2011,** *100*, 60.

196. Yu, H.; Noskov, S. Y.; Roux, B. *Proc. Natl. Acad. Sci. U. S. A.* **2010,** *107*, 20329.

197. Noskov, S. Y.; Berneche, S.; Roux, B. *Nature* **2004,** *431*, 830.

198. Forman, S. L.; Fettinger, J. C.; Pieraccini, S.; Gottarelli, G.; Davis, J. T. *J. Am. Chem. Soc.* **2000,** *122*, 4060.

199. Dudev, T.; Lim, C. *Annu. Rev. Biophys.* **2008,** *37*, 97.

200. Thomas, M.; Jayatilaka, D.; Corry, B. *Biophys. J.* **2007,** *93*, 2635.

201. Alam, A.; Shi, N.; Jiang, Y. *Proc. Natl. Acad. Sci. U. S. A.* **2007,** *104*, 15334.

202. Eisenman, G. *Biophys. J.* **1962,** *2*, 259.

203. Noskov, S. Y.; Berneche, S.; Roux, B. *Nature* **2004,** *431* (7010), 830-834.

204. Sadhu, B.; Sundararajan, M.; Bandyopadhyay, T. *The Journal of Physical Chemistry B* **2015,** *119* (40), 12783-12797.

205. Patel, S.; Davis, J. E.; Bauer, B. A. *Journal of the American Chemical Society* **2009,** *131* (39), 13890-13891.

206. Leontyev, I. V.; Stuchebrukhov, A. A. *J. Chem. Theory Comput.* **2012,** *8*, 3207.

207. Leontyev, I. V.; Stuchebrukhov, A. A. *Journal of Chemical Theory and Computation* **2012,** *8* (9), 3207-3216.

208. Kohagen, M.; Lepšík, M.; Jungwirth, P. *The Journal of Physical Chemistry Letters* **2014,** *5* (22), 3964-3969.

209. Shi, N.; Ye, S.; Alam, A.; Chen, L.; Jiang, Y. Atomic structure of a Na+- and K+-conducting channel. *Nature* **2006,** *440* (7083), 570-574.

210. Alam, A.; Shi, N.; Jiang, Y. *Proceedings of the National Academy of Sciences* **2007,** *104* (39), 15334-15339.

211. Alam, A.; Jiang, Y. *Nat Struct Mol Biol* **2009,** *16* (1), 35-41.

212. Ahlrichs, R.; Bar, M.; Baron, H. P.; Bauernschmitt, R.; Bocker, S.; Ehrig, M.; Eichkorn, K.; Elliot, S.; Furche, F.; Haase, F.; Haser, M.; Horn, H.; Huber, C.; Huniar, U.; Kattannek, M.; Kolmel, C.; Koolwitz, M.; May, K.; Ochsenfeld, C.; Ohm, H.; Schafer, A.; Schneider, U.; Treutler, O.; von Arnim, M.; Weigend, F.; Weis, P.; Weiss, H. *TURBOMOLE V6.3.1*. 2011.

213. Perdew, J. P. *Phys. Rev. B: Condens. Matter Mater. Phys.* **1986,** *33*, 8822.

214. Neese, F. *WIREs Comput. Mol. Sci.* **2012,** *2*, 73.

215. Klamt, A.; Schüürmann, G. *J. Chem. Soc., Perkin Trans. 2* **1993**, 799.

216. Sadhu, B.; Sundararajan, M.; Bandyopadhyay, T. *The Journal of Physical Chemistry B* **2015,** *119* (34), 10989-10997.

217. Chaudhari, M. I.; Soniat, M.; Rempe, S. B. *The Journal of Physical Chemistry B* **2015,** *119* (28), 8746-8753.

218. Todorova, T.; Hünenberger, P. H.; Hutter, J. *Journal of Chemical Theory and Computation*

2008, *4* (5), 779-789.

219. Rudolph, W. W.; Irmer, G. *Dalton Transactions* **2013,** *42* (11), 3919-3935.

220. Hess, B.; Bekker, H.; Berendsen, H. J. C.; Fraaije, J. G. E. M. *J. Comput. Chem.* **1997,** *18*, 1463.

221. Barducci, A.; Bussi, G.; Parrinello, M. *Phys. Rev. Lett.* **2008,** *100*, 020603.

222. Pidcock, E.; Moore, G. R. *JBIC Journal of Biological Inorganic Chemistry* **2001,** *6* (5), 479-489.

223. Egorov, V. N.; Povinec, P. P.; Polikarpov, G. G.; Stokozov, N. A.; Gulin, S. B.; Kulebakina, L. G.; Osvath, I. *Journal of Environmental Radioactivity* **1999,** *43* (2), 137-155.

224. Ticknor, K.; Cho, Y. *Journal of Radioanalytical and Nuclear Chemistry* **1990,** *140* (1), 75-90.

225. Handl, J. In *Radiochimica Acta*, 1996; Vol. 72, p 33.

226. Maleknia, S.; Brodbelt, J. *Journal of the American Chemical Society* **1992,** *114* (11), 4295-4298.

227. Bocchi, C.; Careri, M.; Casnati, A.; Mori, G. *Analytical Chemistry* **1995,** *67* (23), 4234-4238.

228. Ji, H.-F.; Dabestani, R.; Brown, G. M.; Sachleben, R. A. *Chemical Communications* **2000,** (10), 833-834.

229. Casnati, A.; Pochini, A.; Ungaro, R.; Ugozzoli, F.; Arnaud, F.; Fanni, S.; Schwing, M.-J.; Egberink, R. J. M.; de Jong, F.; Reinhoudt, D. N. *Journal of the American Chemical Society* **1995,** *117* (10), 2767-2777.

230. Ghidini, E.; Ugozzoli, F.; Ungaro, R.; Harkema, S.; Abu El-Fadl, A.; Reinhoudt, D. N. *Journal of the American Chemical Society* **1990,** *112* (19), 6979-6985.

231. Asfari, Z.; Bressot, C.; Vicens, J.; Hill, C.; Dozol, J.-F.; Rouquette, H.; Eymard, S.; Lamare, V.; Tournois, B. *Analytical Chemistry* **1995,** *67* (18), 3133-3139.

232. Chakraborty, S.; Dutta, R.; Wong, B. M.; Ghosh, P. *RSC Advances* **2014,** *4* (107), 62689-62693.

233. Chakraborty, S.; Dutta, R.; Arunachalam, M.; Ghosh, P. *Dalton Transactions* **2014,** *43* (5), 2061-2068.

234. A. Gale, P.; L. Sessler, J.; Kral, V. *Chemical Communications* **1998,** (1), 1-8.

235. Gale, P. A.; Hursthouse, M. B.; Light, M. E.; Sessler, J. L.; Warriner, C. N.; Zimmerman,

R. S. *Tetrahedron Letters* **2001,** *42* (38), 6759-6762.

236. Turner, B.; Shterenberg, A.; Kapon, M.; Botoshansky, M.; Suwinska, K.; Eichen, Y. *Chemical Communications* **2002,** (7), 726-727.

237. Turner, B.; Shterenberg, A.; Kapon, M.; Suwinska, K.; Eichen, Y. *Chemical Communications* **2001,** (1), 13-14.

238. Custelcean, R.; Delmau, L. H.; Moyer, B. A.; Sessler, J. L.; Cho, W.-S.; Gross, D.; Bates, G. W.; Brooks, S. J.; Light, M. E.; Gale, P. A. *Angewandte Chemie* **2005,** *117* (17), 2593-2598.

239. Miyaji, H., Sato, W. and Sessler, Jonathan L. *Angew. Chem., Int. Ed.* **2000,** *112*.

240. Anzenbacher, P.; Try, A. C.; Miyaji, H.; Jursíková, K.; Lynch, V. M.; Marquez, M.; Sessler, J. L.. *Journal of the American Chemical Society* **2000,** *122* (42), 10268-10272.

241. Sessler, J. L.; Gross, D. E.; Cho, W.-S.; Lynch, V. M.; Schmidtchen, F. P.; Bates, G. W.; Light, M. E.; Gale, P. A. *Journal of the American Chemical Society* **2006,** *128* (37), 12281-12288.

242. Boda, A.; Sheikh, M. A. *The Journal of Physical Chemistry A* **2012,** *116* (33), 8615-8623.

243. Hill, S. E.; Feller, D.; Glendening, E. D. *The Journal of Physical Chemistry A* **1998,** *102* (21), 3813-3819.

244. Sundararajan, M.; Solomon, R. V.; Ghosh, S. K.; Venuvanalingam, P. *RSC Advances* **2011,** *1* (7), 1333-1341.

245. Kříž, J.; Dybal, J.; Makrlík, E.; Sedláková, Z. *Chemical Physics* **2012,** *400*, 19-28.

246. Dinesh Kumar, C.; Sharma, B.; Soujanya, Y.; Chary, V. N.; Patpi, S. R.; Kantevari, S.; Sastry, G. N.; Prabhakar, S. *Physical Chemistry Chemical Physics* **2014,** *16* (32), 17266-17271.

247. Narbutt, J.; Wodynski, A.; Pecul, M. *Dalton Transactions* **2015,** *44* (6), 2657-2666.

248. Verma, P. K.; Pathak, P. N.; Kumari, N.; Sadhu, B.; Sundararajan, M.; Aswal, V. K.; Mohapatra, P. K. *J. Phys. Chem. B* **2014,** *118*, 14388.

249. Verma, P. K.; Kumari, N.; Pathak, P. N.; Sundararajan, M.; Aswal, V. K.; Mohapatra, P. K.; Sadhu, B. *J. Phys. Chem. A* **2014,** *118*, 3996.

250. Verma, P. K.; Pathak, P. N.; Mohapatra, P. K.; Aswal, V. K.; Sadhu, B.; Sundararajan, M. *J. Phys. Chem. B* **2013,** *117*, 9821.

251. Austin, J. P.; Sundararajan, M.; Vincent, M. A.; Hillier, I. H. *Dalton Transactions* **2009,** (30), 5902-5909.

252. Wåhlin, P.; Danilo, C.; Vallet, V.; Réal, F.; Flament, J.-P.; Wahlgren, U. *Journal of Chemical Theory and Computation* **2008,** *4* (4), 569-577.

253. Leininger, T.; Nicklass, A.; Küchle, W.; Stoll, H.; Dolg, M.; Bergner, A. *Chemical Physics Letters* **1996,** *255* (4), 274-280.

254. Whitten, J. L. *J. Chem. Phys.* **1973,** *58*, 4496.

255. Baerends, E. J.; Ellis, D. E.; Ros, P. *Chem. Phys.* **1973,** *2*, 41.

256. Dunlap, B. I.; Connolly, J. W. D.; Sabin, J. R. *J. Chem. Phys.* **1979,** *71*, 4993.

257. Van Alsenoy, C. *J. Comput. Chem.* **1988,** *9*, 620.

258. Eichkorn, K.; Treutler, O.; Öhm, H.; Häser, M.; Ahlrichs, R. *Chem. Phys. Lett.* **1995,** *240*, 283.

259. teVelde, G.; Bickelhaupt, F. M.; Baerends, E. J.; Van Gisbergen, S. J. A.; Guerra, C. F.; Snijders, J. G.; Ziegler, T. *J. Comput. Chem.* **2001,** *22*, 931.

260. Pardue, D. B.; Gustafson, S. J.; Periana, R. A.; Ess, D. H.; Cundari, T. R. *Computational and Theoretical Chemistry* **2013,** *1019*, 85-93.

261. Bader, R. F. W. *Atoms in molecules: a quantum theory*. 1990; Vol. 2.

262. Bader, R. F. W. *J. Phys. Chem. A* **2009,** *113*, 10391.

263. Pandey, K. K.; Patidar, P.; Bariya, P. K.; Patidar, S. K.; Vishwakarma, R. *Dalton Transactions* **2014,** *43* (26), 9955-9967.

264. Topol, I. A.; Tawa, G. J.; Burt, S. K.; Rashin, A. A. *J. Chem. Phys.* **1999,** *111*, 10998.

265. Dang, L. X.; Garrett, B. C. *The Journal of Chemical Physics* **1993,** *99* (4), 2972-2977.

266. Pichierri, F. *Journal of Molecular Structure: THEOCHEM* **2002,** *581* (1–3), 117-127.

267. Wu, Y.-D.; Wang, D.-F.; Sessler, J. L. *The Journal of Organic Chemistry* **2001,** *66* (11), 3739-3746.

268. Steiner, T. *Acta Crystallographica Section B* **1998,** *54* (4), 456-463.

269. Gopikrishnan, C. R.; Jose, D.; Datta, A. *AIP Advances* **2012,** *2* (1), 012131.

270. Wintergerst, M. P.; Levitskaia, T. G.; Moyer, B. A.; Sessler, J. L.; Delmau, L. H. *Journal of the American Chemical Society* **2008,** *130* (12), 4129-4139.

271. Matta, C. F.; Castillo, N.; Boyd, R. J. *The Journal of Physical Chemistry A* **2005,** *109* (16), 3669-3681.

272. Dieter Cremer, E. K. *Croat. Chem. Acta* **1984,** *57*, 1259-1281.

273. Rozas, I.; Alkorta, I.; Elguero, J. *Journal of the American Chemical Society* **2000,** *122* (45), 11154-11161.

274. Blasius, E.; Klein, W.; Schön, U. *Journal of Radioanalytical and Nuclear Chemistry* **1985,**

89 (2), 389-398.

275. Zhang, A.; Hu, Q.; Chai, Z. *Separation Science and Technology* **2009,** *44* (9), 2146-2168.

276. Casnati, A.; Barboso, S.; Rouquette, H.; Schwing-Weill, M.-J.; Arnaud-Neu, F.; Dozol, J.-F.; Ungaro, R. *Journal of the American Chemical Society* **2001,** *123* (49), 12182-12190.

277. Arnaud-Neu, F.; Barrett, G.; Fanni, S.; Marrs, D.; McGregor, W.; McKervey, M. A.; Schwing-Weill, M.-J.; Vetrogon, V.; Wechsler, S. *Journal of the Chemical Society, Perkin Transactions 2* **1995,** (3), 453-461.

278. Gupta, V. K.; Ludwig, R.; Agarwal, S. Strontium(II) Sensor Based on a Modified Calix[6]arene in PVC Matrix. *Analytical Sciences* **2005,** *21* (3), 293-296.

279. Sadhu, B.; Sundararajan, M.; Velmurugan, G.; Venuvanalingam, P. *Dalton Trans.* **2015,** *44*, 15450.

280. Sieffert, N.; Wipff, G. *The Journal of Physical Chemistry A* **2006,** *110* (3), 1106-1117.

281. Chaumont, A.; Wipff, G. *The Journal of Physical Chemistry B* **2010,** *114* (43), 13773-13785.

282. Ahlrichs, R., Armbruster, M.K., Bachorz, R.A., Bär, M., Baron, H.P., Bauernschmitt, R., Bischoff, F.A., Böcker, S., Crawford, N., Deglmann, P. and Della Sala, F. TURBOMOLE 6.6, a development of University of Karlsruhe and Forschungszentrum Karlsruhe GmbH, 1989–2007, TURBOMOLE GmbH, since 2007.**2014**.

283. Mikheev, N. B.; Spytsin, V. I.; Dyachkova, R. A.; Auerman, L. N. *J. Phys. Colloques.* **1979,** *40*, C4-230.

284. Gorden, A. E. V.; DeVore, M. A.; Maynard, B. A. *Inorg. Chem.* **2013,** *52*, 3445.

285. Drew, M. G. B.; Iveson, P. B.; Hudson, M. J.; Liljenzin, J. O.; Spjuth, L.; Cordier, P. Y.; Enarsson, A.; Hill, C.; Madic, C. *J. Chem. Soc., Dalton Trans.* **2000,** *5*, 821.

286. Afsar, A.; Harwood, L. M.; Hudson, M. J.; Distler, P.; John, J. *Chem. Commun.* **2014,** *50*, 15082.

287. Street, K.; Seaborg, G. T. *J. Am. Chem. Soc.* **1950,** *72*, 2790.

288. Bhattacharyya, A.; Mohapatra, P. K.; Manchanda, V. K. *Solvent Extr. Ion Exch.* **2006,** *24*, 1.

289. Foreman, M. R.; Hudson, M. J.; Drew, M. G.; Hill, C.; Madic, C. *Dalton Trans.* **2006,** *13*, 1645.

290. Panak, P. J.; Geist, A. *Chem. Rev.* **2013,** *113*, 1199.

291. Hill, C.; Madic, C.; Baron, P.; Ozawa, M.; Tanaka, Y. *J. Alloys Compd.* **1998,** *271*, 159.

292. Dam, H. H.; Reinhoudt, D. N.; Verboom, W. *Chem. Soc. Rev.* **2007,** *36*, 367.

293. Steed, J. W.; Turner, D. R.; Wallace, K. *Core concepts in supramolecular chemistry and nanochemistry*. 2007.

294. Chen, K.; Feng, X.; Liang, L. L.; Zhang, Y. Q.; Zhu, Q. J.; Xue, S. F.; Tao, Z. *Cryst. Growth Des.* **2011,** *11*, 5712.

295. Feng, X.; Du, H.; Chen, K.; Xiao, X.; Luo, S. X.; Xue, S. F.; Zhang, Y. Q.; Zhu, Q. J.; Tao, Z.; Zhang, X. Y.; Wei, G. *Cryst. Growth Des.* **2010,** *10*, 2901.

296. Kushwaha, S.; Rao, S. A.; Sudhakar, P. P. *Inorg. Chem.* **2012,** *51*, 267.

297. Chen, K.; Liang, L. L.; Liu, H. J.; Zhang, Y. Q.; Xue, S. F.; Tao, Z.; Xiao, X.; Zhu, Q. J.; Lindoy, L. F.; Wei, G. *CrystEngComm* **2012,** *14*, 7994.

298. Chen, K.; Liang, L. L.; Zhang, Y. Q.; Zhu, Q. J.; Xue, S. F.; Tao, Z. *Inorg. Chem.* **2011,** *50*, 7754.

299. Thuéry, P. *Inorg. Chem.* **2009,** *48*, 4497.

300. Shaikh, M.; Mohanty, J.; Sundararajan, M.; Bhasikuttan, A. C.; Pal, H. *J. Phys. Chem. B* **2012,** *116*, 12450.

301. Khorwal, V.; Sadhu, B.; Dey, A.; Sundararajan, M.; Datta, A. *J. Phys. Chem. B* **2013,** *117*, 8603.

302. Sayed, M.; Sundararajan, M.; Mohanty, J.; Bhasikuttan, A. C.; Pal, H. *J. Phys. Chem. B* **2015,** *119*, 3046.

303. Schreckenbach, G.; Shamov, G. A. *Acc. Chem. Res.* **2010,** *43*, 19.

304. Lan, J. H.; Shi, W. Q.; Yuan, L. Y.; Li, J.; Zhao, Y. L.; Chai, Z. F. *Coord. Chem. Rev.* **2012,** *256*, 1406.

305. Bhattacharyya, A.; Ansari, S. A.; Gadly, T.; Ghosh, S. K.; Mohapatra, M.; Mohapatra, P. K. *Dalton Trans.* **2015,** *44*, 6193.

306. Zaiter, A.; Amine, B.; Bouzidi, Y.; Belkhiri, L.; Boucekkine, A.; Ephritikhine, M. *Inorg. Chem.* **2014,** *53*, 4687.

307. Dolg, M.; Stoll, H.; Savin, A.; Preuss, H. *Theor. Chim. Acta* **1989,** *75*, 173.

308. Kűchle, W.; Dolg, M.; Stoll, H.; Preuss, H. *J. Chem. Phys.* **1994,** *100*, 7535.

309. Cao, X.; Heidelberg, D.; Ciupka, J.; Dolg, M. *Inorg. Chem.* **2010,** *49*, 10307.

310. Brown, M. A.; Vila, F.; Sterrer, M.; Thürmer, S.; Winter, B.; Ammann, M.; Rehr, J.; van

Bokhoven, J. A. *J. Phys. Chem. Lett.* **2012,** *3*, 1754.

311. Martin, R. L.; Hay, P. J.; Pratt, L. R. *J. Phys. Chem. A* **1998,** *102*, 3565.

312. Shamov, G. A.; Schreckenbach, G. *J. Phys. Chem. A* **2005,** *109*, 10961.

313. Gutowski, K. E.; Dixon, D. A. *J. Phys. Chem. A* **2006,** *110*, 8840.

314. Bryantsev, V. S.; Diallo, M. S.; Goddard, W. A. *J. Phys. Chem. B* **2008,** *112*, 9709.

315. Mülliken, R. S. *J. Chem. Phys.* **1955,** *23*, 1833.

316. Nalewajski, R. F.; Mrozek, J. *Int. J. Quantum Chem.* **1994,** *51*, 187.

317. Nalewajski, R. F.; Mrozek, J.; Michalak, A. *Int. J. Quantum Chem.* **1997,** *61*, 589.

318. Wiberg, K. B. *Tetrahedron* **1968,** *24*, 1083.

319. Glendening, E. D.; Landis, C. R.; Weinhold, F. *J. Comput. Chem.* **2013,** *34*, 1429.

320. Fonseca Guerra, C.; Snijders, J. G.; te Velde, G.; Baerends, E. *J. Theor. Chem. Acc.* **1998,** *99*, 391.

321. Huang, Q. R.; Kingham, J. R.; Kaltsoyannis, N. *Dalton Trans.* **2015,** *44*, 2554.

322. Chang, C.; Pelissier, M.; Durand, P. *Phys. Scr.* **1986,** *34*, 394.

323. Heully, J. L.; Lindgren, I.; Lindroth, E.; Lundquist, S.; Martensson-Pendrill, A. M. *J. Phys. B: At. Mol. Phys.* **1986,** *19*, 2799.

324. van Lenthe, E.; Baerends, E. J.; Snijders, J. G. *J. Chem. Phys.* **1993,** *99*, 4597.

325. van Lenthe, E.; Baerends, E. J.; Snijders, J. G. *J. Chem. Phys.* **1996,** *105*, 6505.

326. Knope, K. E.; Soderholm, L. *Chem. Rev.* **2013,** *113*, 944.

327. Allen, P. G.; Bucher, J. J.; Shuh, D. K.; Edelstein, N. M.; Craig, I. *Inorg. Chem.* **2000,** *39*, 595.

328. Stumpf, T.; Hennig, C.; Bauer, A.; Denecke, M. A.; Fanghänel, T. *Radiochim. Acta* **2004,** *92*, 133.

329. Gerkin, R. E.; Reppart, W. J. *Acta Crystallogr., Sect. C: Cryst. Struct. Commun.* **1984,** *40*, 781.

330. D’Angelo, P.; Martelli, F.; Spezia, R.; Filipponi, A.; Denecke, M. A. *Inorg. Chem.* **2013,** *52*, 10318.

331. Wiebke, J.; Moritz, A.; Cao, X.; Dolg, M. *Phys. Chem. Chem. Phys.* **2007,** *9*, 459.

332. Zhang, J.; Heinz, N.; Dolg, M. *Inorg. Chem.* **2014,** *53*, 7700.

333. Kuta, J.; Clark, A. E. *Inorg. Chem.* **2010,** *49*, 7808.

334. Clark, A. E. *J. Chem. Theory Comput.* **2008,** *4*, 708.

335. David, F. H.; Vokhmin, V. *New J. Chem.* **2003,** *27*, 1627.

336. Heinz, N.; Zhang, J.; Dolg, M. *J. Chem. Theory Comput.* **2014,** *10*, 5593.

337. D'Angelo, P.; Spezia, R. *Chem. - Eur. J.* **2012,** *18*, 11162.

338. Wang, C. Z.; Shi, W. Q.; Lan, J. H.; Zhao, Y. L.; Wei, Y. Z.; Chai, Z. F. *Inorg. Chem.* **2013,** *52*, 10904.

339. Ni, X. L.; Xiao, X.; Cong, H.; Liang, L. L.; Cheng, C.; Cheng, X. J.; Ji, N. N.; Zhu, Q. J.; Xue, S. F.; Tao, Z. *Chem. Soc. Rev.* **2013,** *42*, 9480.

340. Zhao, Y.; Liang, L. L.; Chen, K.; Zhang, T.; Xiao, X.; Zhang, Y. Q.; Tao, Z.; Xue, S. F.; Zhu, Q. Z. *CrystEngComm* **2013,** *15*, 7987.

341. Zhang, Y. Q.; Zhu, Q. J.; Xue, S. F.; Tao, Z. *Molecules* **2007,** *12*, 1325.

342. Michalak, A.; DeKock, R. L.; Ziegler, T. *J. Phys. Chem. A* **2008,** *112*, 7256.

343. Lan, J. H.; Shi, W. Q.; Yuan, L. Y.; Zhao, Y. L.; Li, J.; Chai, Z. F. *Inorg. Chem.* **2011,** *50*, 9230.